IN SEARCH OF WATER VAPOR ON JUPITER: LABORATORY MEASUREMENTS OF THE MICROWAVE PROPERTIES OF WATER VAPOR AND SIMULATIONS OF JUPITER'S MICROWAVE EMISSION IN SUPPORT OF THE JUNO MISSION

A Dissertation
Presented to
The Academic Faculty

by

Bryan Mills Karpowicz

In Partial Fulfillment
of the Requirements for the Degree
Doctor of Philosophy in the
School of Earth and Atmospheric Sciences

Georgia Institute of Technology
May 2010

IN SEARCH OF WATER VAPOR ON JUPITER: LABORATORY MEASUREMENTS OF THE MICROWAVE PROPERTIES OF WATER VAPOR AND SIMULATIONS OF JUPITER'S MICROWAVE EMISSION IN SUPPORT OF THE JUNO MISSION

Approved by:

Professor Paul G. Steffes,
Committee Chair
School of Electrical and Computer Engineering
Georgia Institute of Technology

Professor Gary Gimmestad
School of Earth and Atmospheric Sciences
School of Electrical and Computer Engineering
Georgia Institute of Technology

Professor Paul G. Steffes, Advisor
School of Electrical and Computer Engineering
Georgia Institute of Technology

Professor Carol Paty
School of Earth and Atmospheric Sciences
Georgia Institute of Technology

Professor Judith A. Curry
School of Earth and Atmospheric Sciences
Georgia Institute of Technology

Professor Josef Dufek
School of Earth and Atmospheric Sciences
Georgia Institute of Technology

Date Approved: November 24, 2009

Dedicated in Honour of Professor Derek M. Cunnold ,

I hope this work would meet your standards. Your wisdom, good humour, and insights will be deeply missed.

ACKNOWLEDGEMENTS

This thesis is the culmination of years of hard work, however, I am indebted to a number of people as this work required not only a number of technical and scientific breakthroughs, but required physical, mental, and emotional exertion which no one person could withstand alone. First I must thank my Advisor Prof. Paul G. Steffes for his seemingly endless supply of enthusiasm, and support. One could not ask for a better advisor in terms of professional, academic, technical, or personal guidance. He has always been quick to lend a hand whether of a scientific/technical challenge, or helping to lift a few 100 kg gas cylinders up two flights of stairs. I'm also indebted to members of my thesis committee: Prof. Judith Curry, Prof. Gary Gimmestad, Prof. Carol Paty, and Prof. Josef Dufek for their time, patience and careful review of my thesis. I'm grateful to the Juno Mission and the support received to conduct the ultra-high pressure measurements by NASA Contract NNM06AA75C from the Marshall Space Flight Center supporting the Juno Mission Science Team, under Subcontract 699054X from the Southwest Research Institute. I'm also grateful for support received to develop the Localized Radiative Transfer model under the NASA Planetary Atmospheres Program (Grant NNG06GF34G).

The unusually large scale of this project required quite a bit of technical as well as hard labor. I thank Tom Flach from Hays Fabrication and Welding for his hard work in designing, manufacturing, and hydro-testing the 1200 lbs pressure vessel which allowed these experiments to be conducted both safely and reliably. The facilities planning required to conduct the experiments went smoothly in part thanks to Bob House of ECE, and Bob Goodman TRC Worldwide Engineering, Inc. Help from the ECE machine shop, in particular Louis Boulanger was extremely helpful when problems arose in assembly of various system components. Richard Turner came up with some elegant solutions to moving, and protecting gas bottles from the elements,

and I greatly appreciate his effort and craftsmanship. I thank Dr. Thomas R. Hanley for both his technical expertise, and his assistance in assembling the pressure vessel, and EZEE shed (which I assure the reader, there was nothing easy about its assembly). I'm also indebted to him for his hard work in the development of the microwave opacity measurement system. I also thank Kiruthika Devaraj for her time and effort in lending a hand in assembling the EZEE shed, and lending a hand when lifting the many gas bottles needed to conduct the experiments. I am also indebted to a number of previous group members have made a number contributions along in development of hardware, software, and general laboratory improvements including: Dr. Priscilla N. Mohammed, Dr. James P. Hoffman, and Dr. David R. Deboer.

The complex nature of dealing with water vapor, and non-ideal gases was quite a challenge. I appreciate the insight, and suggestions given by Dr. Eric Lemmon of NIST in developing an equation of state for H_2-H_2O. Glenn Orton was extremely helpful in comparing radiative transfer models, and providing *ab-initio* calculations of collisionally induced absorption from H_2-CH_4-He. I also appreciate Dr. Philip Rosenkranz of MIT sharing his latest edition of his microwave water vapor opacity model.

Thanks are also in order to member of Dr. Durgin's lab, especially Dr. Josh Griffin for spotting and repairing the EZEE shed, when a strong wind would damage it on occasion. I thank Brian Bennet and Tony Tingler in ECE shipping for their help and extra effort in transporting some of the larger, and more unusual pieces of equipment to our lab. I also thank Sharon Fennell for her hard work in quickly processing the various equipment orders, and travel expense statements over the years.

Last but not least I thank my family and friends for their love and support over my somewhat extended stay in as a graduate student in academia.

Table of Contents

LIST OF TABLES

LIST OF FIGURES

SUMMARY

This research has involved the conduct of a series of laboratory measurements of the centimeter-wavelength opacity of water vapor along with the development of a hybrid radiative transfer ray-tracing simulator for the atmosphere of Jupiter which employs a model for water vapor opacity derived from the measurements. For this study an existing Georgia Tech high-sensitivity microwave measurement system (*Hanley and Steffes*, 2007) has been adapted for pressures ranging from 12-100 bars, and a corresponding temperature range of 293-525°K. Water vapor is measured in a mixture of hydrogen and helium. Using these measurements which covered a wavelength range of 6–20 cm, a new model is developed for water vapor absorption under Jovian conditions. In conjunction with our laboratory measurements, and the development of a new model for water vapor absorption, we conduct sensitivity studies of water vapor microwave emission in the Jovian atmosphere using a hybrid radiative transfer ray-tracing simulator. The approach has been used previously for Saturn (*Hoffman*, 2001), and Venus (*Jenkins et al.*, 2001).

This model has been adapted to include the antenna patterns typical of the NASA Juno Mission microwave radiometer (NASA/Juno -MWR) along with Jupiter's geometric parameters (oblateness), and atmospheric conditions. Using this adapted model we perform rigorous sensitivity tests for water vapor in the Jovian atmosphere. This work will directly improve our understanding of microwave absorption by atmospheric water vapor at Jupiter, and improve retrievals from the Juno microwave radiometer. Indirectly, this work will help to refine models for the formation of Jupiter and the entire solar system through an improved understanding of the planet-wide abundance of water vapor which will result from the successful opreation of the Juno Microwave Radiometer (Juno-MWR).

CHAPTER I

INTRODUCTION

There are a vast number of challenges our society must face in order to improve our lives here on Earth, and better understand the fundamental underpinnings of how our planetary system, and planetary systems in general, function. The key lies in understanding how each system works, identifying the key mechanisms, and by studying the composition of Jupiter, inferring the origin and history of the solar system. Earth and planetary remote sensing provides us with a unique tool to better observe changes in our own planet, planets within our solar system, and even planets extending outside our solar system. These tools are by no means perfect. We must continue to improve the enabling technologies, and improve planetary models to better reflect both what is observed and what is physically meaningful. The NASA New Frontiers Mission Juno provides a unique opportunity to develop new technologies, and improve our understanding of Jupiter using detailed models of its composition, dynamics, and microwave absorption which allow for a correct interpretation of Jupiter's microwave emission spectrum.

1.1 Background and Motivation

For centuries astronomers have looked towards the outer planets in search of answers regarding the origins of the solar system. Today astronomers and planetary scientists still look towards the outer planets as a laboratory for understanding the origins of the solar system, in particular planetary formation. Among the outer planets, Jupiter stands out as being both the largest in size, and the most challenging for planetary scientists in the understanding of its formation. While most planetary scientists favor the core accretion model for formation of Jupiter (*Pollack et al.*, 1996), the time scale

required for accumulation of a sufficient gaseous envelope extends beyond what would be expected for the lifetime of the solar nebula. An alternative formation process which has been advocated in *Boss* (1998, 2002) is that of gravitational instability. Using this process a gas giant such as Jupiter could be formed on a much shorter time scale; however, if a planet such as Jupiter has an enrichment of heavy elements far beyond that of the solar nebula, this would present difficulties for the gravitational instability model.

While satellite observations of the abundance of gaseous species in Jupiter's atmosphere have been made in an attempt to improve knowledge of the formation process, the latest observations by the Galileo entry probe have presented more questions than answers regarding Jupiter's formation. Galileo's *in-situ* probe showed a depletion of oxygen relative to solar abundance, while other species such as carbon, nitrogen, and sulfur showed an enrichment of about three times solar abundance (using the values given by *Anders and Grevesse* (1989) which was the standard for solar composition at the time of the Galileo Probe entry). A depletion of oxygen associated with a depletion in water abundance, along with an enhancement of carbon, nitrogen and sulfur is hard to explain on a global scale for Jupiter. Unfortunately, the Galileo probe entered the Jovian atmosphere through a "hot spot", which resulted in values atypical for the planet on a global scale (*Young*, 2003).

While initial modeling studies have been performed which show that it is possible to retrieve deep water vapor abundance in Jupiter's atmosphere using a multi-channel radiometer as proposed for the Juno mission (*Janssen et al.*, 2005), there are a number of factors which will limit the accuracy of this approach. Previous laboratory measurements of the microwave opacity of water vapor under pressures and temperatures representative of Jupiter have been conducted in a nitrogen atmosphere, and not a helium-hydrogen atmosphere (*Ho et al.*, 1966). While models for water vapor absorption have been extrapolated (*Goodman*, 1969) to a hydrogen-helium atmosphere, far

more accurate measurements are necessary to accurately retrieve the Jovian water vapor abundance (*de Pater et al.*, 2005). In addition the radiative transfer model used by *Janssen et al.* (2005), which is the foundation for this mission, does not currently account for Jupiter's oblateness, or for the antenna patterns of the radiometer.

To address these limiting factors to mission success, a series of laboratory measurements have been conducted, and a radiative transfer simulator with the most accurate model for microwave absorption by water vapor in a H_2/He atmosphere under Jovian conditions has been developed. For this study the existing Georgia Tech high-sensitivity microwave measurement system (*Hanley and Steffes*, 2007) has been upgraded to withstand pressures ranging from 12–100 bars, and a corresponding temperature range of 293–525° K. Water vapor is measured in a mixture of hydrogen, and helium. Using these measurements which cover a wavelength range of 6–20 cm, a new model for water vapor absorption under Jovian conditions has been developed. In conjunction with our laboratory measurements, and the development of a new model for water vapor absorption, sensitivity studies and simulated retrievals of water vapor using a radiative transfer simulator are presented. The approach has been used previously for Saturn (*Hoffman*, 2001), and Venus (*Jenkins et al.*, 2001).

1.2 Organization and Research Objectives

This dissertation includes seven topics: theoretical discussion of the microwave absorption properties of gaseous and cloud/aerosol constituents, design and measurement procedures for measuring the microwave absorption properties of water vapor under Jovian conditions, discussion of pure and mixtures of non-ideal gases in association with a model for the H_2O/H_2/He ternary mixture, development of an empirically derived model for H_2O opacity under Jovian conditions, a discussion of the thermodynamic properties in Jupiter's atmosphere, a description of the microwave radiative transfer model/simulator, and simulations along with sensitivity analysis of Jupiter's

microwave emission as observed from the Microwave Radiometer (MWR) aboard the soon-to-be-launched NASA Juno mission.

In Chapter 2 a description of the theory of microwave absorption and refraction by gases in the Jovian system are discussed. A brief discussion of how aerosol/cloud particles absorb microwave radiation is also presented. This chapter discusses models of absorption for gases in the Jovian atmosphere which have been developed by others, along with providing a reference frame for the new H_2O absorption model developed in this thesis.

Chapter 3 describes the upgraded Georgia Tech high-sensitivity microwave measurement system. The theory of microwave measurements within the system is briefly described, along with detailed the upgrades which allowed for measurements in the pressure range from 12 to 100 bars, and in the temperature range from 333 to 525°K.

In Chapter 4 properties of non-ideal pure gases, and non-ideal gas mixtures are discussed. Previous measurements regarding the thermodynamic properties of the H_2/H_2O/He system are discussed. A new model empirical model for the ternary mixture of H_2/He/H_2O is developed based upon a few measurements conducted using the Georgia Tech system, along with thermodynamic measurements available in published literature.

Chapter 5 provides a summary of the microwave opacity data obtained, and presents the new microwave opacity model for H_2O vapor under Jovian conditions. The model includes the effects of compressibility of the H_2/He/H_2O mixture under test. The total error budget of all instruments, and their impact upon the accuracy of the microwave absorption model are discussed. The temperature, and pressure regimes in which the model remains valid are also discussed.

Chapter 6 describes the new model Thermochemical model of the Jovian atmosphere including the compressibility of the ternary mixture of H_2, He and H_2O. The non-ideal effects of the H_2/He/H_2O mixture and its importance in studies of Jovian

atmospheres are discussed. A cloud/aerosol sedimentation scheme following *Ackerman and Marley* (2001) is described, and utilized to explore the range of possible cloud bulk densities in the Jovian atmosphere.

In Chapter 7 the theory of radiative transfer, and ray tracing is discussed, along with providing a detailed description of the radiative transfer simulator. The methodology uses the absorption, and refractivity models for gasses and cloud materials discussed in Chapter 2. The details of how these absorption, and refractivity models are combined to simulate microwave emission in the Jovian atmosphere are discussed.

Chapter 8 utilizes the radiative transfer model to simulate the microwave emission from Jupiter as viewed from the Juno MWR. A survey of recent studies regarding the composition of the Jovian atmosphere is presented. This survey is used as a guide to evaluate the possible range of values for constituent abundances. The impact of the new microwave absorption model for water vapor is discussed, along with discussion of the sensibility of water vapor in the Jovian atmosphere from the Juno MWR.

Chapter 9 summarizes our findings and presents suggestions for future work. The contributions of this author to the field of laboratory measurements of the microwave properties of H_2O, and to the modeling of Jupiter's atmosphere are discussed.

CHAPTER II

CENTIMETER-WAVE ABSORPTION, EMISSION, AND REFRACTION OF GASES AND LIQUIDS

Theories of electromagnetic absorption, emission, and refraction of materials all are fundamentally a way of accounting for how electromagnetic energy interacts in or between media. Refraction is a process which can be thought of in simplest terms. On example is that of a car traveling along a beachside road. If the car veers off the road with one wheel on the pavement, and the other on the sand, it will have a tendency to change its direction without the aid of the driver. Refraction of electromagnetic radiation occurs when there is a change in the dielectric or magnetic properties of the media in which the electromagnetic wave is propagating. This change in material properties in turn alters the speed of the wave, and leads to a bending, or change in direction of the propagating electromagnetic wave.

Absorption or emission from a material is a slightly more complicated process. One can first think of electrons in orbital locations within an atom whereby an electron transitions from one orbital state to another. This simple absorption or emission process can be shown to occur at discrete wavelengths via,

$$\nu_o = \frac{E_u - E_l}{h} \tag{2.1}$$

where ν_o is the frequency of the absorbed/emitted electromagnetic energy, E_u and E_l represent the upper and lower energy states of the atom. While this simple theory indicates that absorption or emission can take place only at discrete wavelengths, this is overly-simplistic when describing absorption or emission from a distribution of moving and colliding molecules such as in a gas. While equation 2.1 does not give the complete absorption spectrum of a molecule, it provides a useful starting point

in the strong, discrete spectral regions of absorption/emission commonly referred to as absorption lines. To complicate matters further, the processes that govern these lines are far more complex than the simple electron transition for an atom. While the electron transition does play a role in absorption/emission spectra, electron transitions are typically important at shorter wavelengths (e.g. Ultra-Violet and visible spectra). The two processes which are of most concern in the microwave spectrum are rotation, and vibration of molecules. Rotational transitions occur when a molecule either has or may acquire an unequal distribution of charge, or dipole moment. Vibrational transitions occur when a molecule has an asymmetry about it which allows for a change (vibration, or oscillation) in the dipole moment.

While discrete energy transitions account for some of the absorption structure within a molecules absorption spectrum, it only accounts for processes within an individual molecule. To account for interactions between molecules, one must consider its line shape, or distribution of its energy as a function of frequency. Several effects can contribute to the line broadening; the key effects in the microwave regime are Doppler and pressure broadening. The Doppler broadening occurs due to motions of the molecule relative to the applied electromagnetic field. While this effect is considerable at low pressures, it becomes negligible at high temperatures and pressures. This leaves the pressure broadening effect. Unfortunately, this effect has more than one model and the best fit for a particular molecule, or combination of molecules must be determined via experimental methods.

One of the earliest line shape models was that of *Lorentz* (1915). This line shape can be written as

$$F_L(\nu_j, \nu) = \frac{1}{\pi}\left[\frac{\Delta\nu}{(\nu_j - \nu)^2 + \Delta\nu^2} - \frac{\Delta\nu}{(\nu_j + \nu)^2 + \Delta\nu^2}\right], \tag{2.2}$$

where $\Delta\nu$ is the linewidth at half-maximum, ν_j is the frequency of the line center, and ν is the frequency of an incident electromagnetic field.

The work of *Debye* (1929) showed that under certain conditions polar molecules

could not be modeled well with a Lorentz line shape. This led to the work of *van Vleck and Weisskopf* (1945) who used

$$F_{VVW}(\nu_j,\nu)=\frac{1}{\pi}\frac{\nu}{\nu_j}\left[\frac{\Delta\nu}{(\nu_j-\nu)^2+\Delta\nu^2}+\frac{\Delta\nu}{(\nu_j+\nu)^2+\Delta\nu^2}\right], \tag{2.3}$$

Gross (1955) simplified the Lorentz expression by assuming a Maxwell distribution in place of a Boltzmann distribution for molecular velocities. The lineshape is of the form

$$F_G(\nu_j,\nu)=\frac{1}{\pi}\left[\frac{4\nu\nu_j\Delta\nu}{(\nu_j^2-\nu^2)+4\nu^2\Delta\nu^2}\right], \tag{2.4}$$

where $\Delta\nu$ is the is the linewidth at half-maximum, ν_j is the frequency of the line center, and ν is the frequency of the incident electromagnetic field.

Finally, the Ben-Rueven lineshape which is particularly important in studies involving ammonia (NH_3) is

$$F_{BR}(\nu_j,\nu)=\frac{2}{\pi}\left(\frac{\nu}{\nu_j}\right)^2\frac{(\Delta\nu-\zeta)\nu^2+(\Delta\nu+\zeta)[(\nu_j+\delta)^2+\Delta\nu^2-\zeta^2]}{[\nu^2-(\nu_j+\delta)^2-\gamma^2+\zeta^2]^2+4\nu^2\Delta\nu^2}, \tag{2.5}$$

where $\Delta\nu$ is the linewidth at half-maximum, ν_j is the frequency of the line center, ν is the frequency of an incident electromagnetic field, δ is a line shift parameter, and ζ is a line-to-line coupling element.

2.1 H_2-He-CH_4 Continuum Absorption

Since molecular hydrogen, helium, and methane have no detectable lines in a neutral atmosphere, a model used for Collisionally Induced Absorption (CIA) between H_2, He, and CH_4 has been adopted which is similar to that presented in *Orton et al.* (2007). Data from Tables 2, and 3 of *Orton et al.* (2007) can be used to develop a model for CIA absorption using a 2D interpolation scheme as a function of density and temperature. Data produced using a finer frequency step was provided by Orton (*Private Communication*), and includes a grid for the CIA from He and CH_4. The table is provided via electronic download using `http://users.ece.gatech.edu/~psteffes/palpapers/h2h2/`.

2.2 Absorption Formalisms Using the JPL Poynter–Pickett Catalog

Several commonly used formalisms for centimeter- and millimeter-wavelength absorption from gaseous species make use of the JPL Poynter-Pickett line catalog. The catalog has a wealth of information regarding the absorption lines of several molecules. Species which have microwave absorption models which make use of the Poyter-Pickett catalog include NH_3, and PH_3. Regardless of the catalog used, the absorption coefficient (in units of cm^{-1}) for a particular molecule at a given frequency is calculated by,

$$\alpha = \sum DA_j \pi \Delta\nu_j F_j(\nu, \nu_{oj}, ...) \tag{2.6}$$

where ν is the frequency, and for the line j,D is a correction term which unless otherwise stated is unity, A_j is the line center absorption, $\Delta\nu_j$ is the line-width, and F_j is the line-shape function.

The line center absorption (cm^{-1}) is calculated using:

$$A_j = \frac{NS_j(T)}{\pi\Delta\nu_j} \tag{2.7}$$

where N is the number density, $S_j(T)$ is the intensity of the line j. The value for line intensity is calculated using:

$$S(T) = S(300)\left(\frac{300}{T}\right)^n \frac{\exp(-hcE_l/kT) - \exp(-hcE_h/kT)}{\exp(-hcE_l/300k) - \exp(-hcE_h/300k)} \tag{2.8}$$

assuming energy spacings are small compared to kT, $S(T)$ is approximated by:

$$S(T) \approx S(300)\left(\frac{300}{T}\right)^{n+1} \exp\left(-\frac{hc}{k}E_l\left(\frac{1}{T} - \frac{1}{300}\right)\right) \tag{2.9}$$

where n=1 (for a linear molecule) or 3/2 (for a non linear molecule), E_l and E_h are the lower and upper state energies (both in units of cm^{-1}).

The linewidth is calculated as,

$$\Delta\nu_j = \sum_i \Delta\nu_{ij}^o P_i \left(\frac{300}{T}\right)^{\xi_{ij}} \quad \text{(GHz)} \tag{2.10}$$

where $\Delta\nu^o_{ij}$ is the line broadening parameter for gas i and line j in GHz/bar, P_i is the partial pressure of the gas i in bars, and $\xi_{i,j}$ is the line broadening parameter temperature dependence for gas i and line j.

2.2.1 H_2S Absorption Formalism

The most accurate H_2S absorption model available at wavelengths relevant to the Juno mission is that of *Deboer and Steffes* (1994). The model of *Deboer and Steffes* (1994) was developed based upon laboratory measurements of H_2S. The formalism uses the BR lineshape, and sets the coupling term (ζ) equal to the linewidth $\Delta\nu_j$. Values for $\nu^o_{H_2,j}$, $\nu^o_{He,j}$, and $\nu^o_{H_2S,j}$ are 1.96, 1.20 and 5.78 GHz/bar, repsectively. Values for $\nu^o_{H_2S,j}$ are modified to 5.38, 6.82, 5.82, and 5.08 GHz/bar for the 168, 216, 300, and 393 GHz lines, respectively. The value for the pressure shift term is found by,

$$\delta = 1.28 P_{H_2S} \quad \text{(GHz)} \tag{2.11}$$

where P_{H_2S} is the partial pressure from H_2S. Finally the line broadening parameter $\xi_{i,j}$ is set to 0.7 for all lines and gases.

Verification of the model performance was tested by reproducing results presented in *DeBoer* (1995). In Figure 2.12 in *DeBoer* (1995) the opacity due to H_2S absorption is plotted from 1 to 100 GHz for a pressure 5.84 bars, a temperature of 212°K, and mixing ratios of 79.03%, 8.98%, and 11.99% for H_2, He, and H_2S. A comparison between the present work and that of *DeBoer* (1995) is presented in Figure 2.1, and agrees quite well with Figure 2.12 of *DeBoer* (1995).

2.2.2 PH_3 Absorption Formalism

While Phosphine is not found in large quantities in the Jovian atmosphere, it has been found to be a very opaque in the microwave region, and should be considered. The *Hoffman and Steffes* (2001) absorption model is based upon extensive laboratory measurements and is appropriate for microwave observations of Jupiter. The model

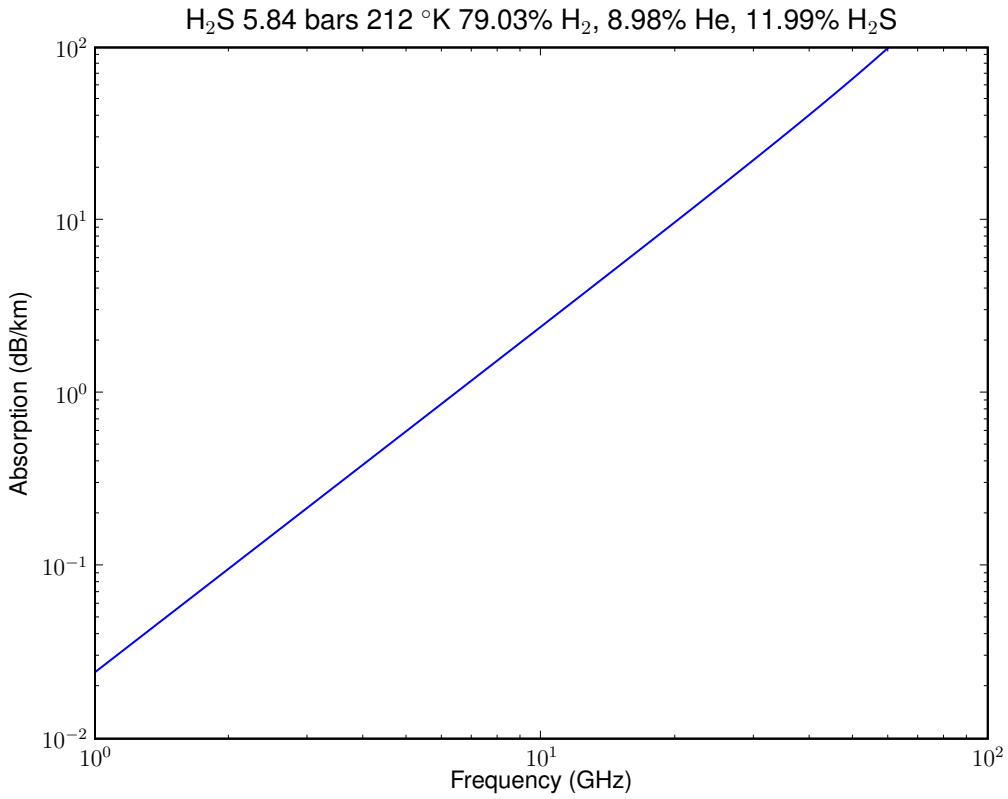

Figure 2.1: Absorption due to H_2S under the conditions used in *DeBoer* (1995) Figure 2.12.

uses a VVW lineshape with values in equation 2.10 set to the following: ξ_{ij} values are set to 1.0 for Phosphine, and 0.75 for gases Helium, and Hydrogen, $\Delta\nu^o_{ij}$ is set to the values given in Table 2.1. Additional parameters are archived on the Planetary Atmospheres Lab (including the line intensities, and line centers) website.

Table 2.1: The *Hoffman and Steffes* (2001) PH_3 absorption parameters.

Ellastic Collision Lines (J,K)	Intensity Weighting	$\Delta\nu^o_{ij}$ H_2 (GHz/bar)	$\Delta\nu^o_{ij}$ He (GHz/bar)	$\Delta\nu^o_{ij}$ PH_3 (GHz/bar)
K=6, or K=3, J<8	2.76	1.4121	0.7205	0.4976
8<J≤26, K=3	36.65	0.5978	0.3050	3.1723
Otherwise	1	3.2930	1.6803	4.2157

2.2.3 NH_3 Absorption Formalism

The radiative transfer model used for our study employs the NH_3 absorption model of *Hanley et al.* (2009). The model of *Hanley et al.* (2009) uses a BR lineshape with the coupling term found by

$$\zeta_j = 1.262 P_{H_2} \left(\frac{300}{T}\right)^{0.7964} + 0.3 P_{He} \left(\frac{300}{T}\right)^{2/3} + 0.5296 P_{NH_3} \left(\frac{295}{T}\right)^{1.554} \Delta\nu^o_j, \quad (2.12)$$

where P_{H_2}, P_{He},and P_{NH_3} are the partial pressures (in bars) from hydrogen, helium and ammonia, repectively. The available self broadening parameters ($\Delta\nu^o_j$) are taken from *Poynter and Kakar* (1975). The pressure broadened linewidth is given as

$$\Delta\nu_j = 1.640 \left(\frac{300}{T}\right)^{0.7756} P_{H_2} + 0.75 \left(\frac{300}{T}\right)^{2/3} P_{He} + 0.852 \left(\frac{295}{T}\right) P_{NH_3} \Delta\nu^o_j, \quad (2.13)$$

where again P_{H_2}, P_{He},and P_{NH_3} are the partial pressures (in bars) from hydrogen, helium and ammonia, repectively. Again, the self broadening parameters when available ($\Delta\nu^o_j$) are taken from *Poynter and Kakar* (1975). When unavailable, the value for $\Delta\nu^o_j$ are found by using the J,K transitions associated with those lines via

$$\Delta\nu^o_j(J,K) = 25.923 \frac{K}{\sqrt{J(J+1)}} \quad (2.14)$$

where $\Delta\nu_j^o$ is units of MHz/torr.

The pressure shift term is given by

$$\delta = -0.0498\Delta\nu \tag{2.15}$$

in units of (GHz).

Finally, *Hanley et al.* (2009) use an additional multiplicative correction term D, which is taken as 0.9301.

2.3 H_2O Absorption

Prior to this work only three models have been proposed for the microcwave and millimeter-wavelength opacity from water vapor in a Jovian atmosphere: the *DeBoer* (1995) model, the *DeBoer* (1995) model with corrections from *de Pater et al.* (2005), and the *Goodman* (1969) model.

The *Goodman* (1969) model is an adaptation of the work of *Ho et al.* (1966) for an H_2-He atmosphere. Its formalism is much simpler in that only the 22.23515 GHz ($0.74\,\mathrm{cm}^{-1}$) line and the continuum of absorption strongest around 4496.9 GHz ($150\,\mathrm{cm}^{-1}$) are considered. The formalism is the following given in units of cm^{-1}

$$\begin{aligned}\alpha_{H_2O} &= P_{H_2O}\left(\frac{273}{T}\right)^{13/3}\nu^2 \\ &\times\left(1.073\times10^{-8}\left[\frac{\Delta\nu_1}{(\nu-0.74)^2+\Delta\nu_1^2}+\frac{\Delta\nu_1}{(\nu+0.74)^2+\Delta\nu_1^2}\right]\right. \\ &\left.+17.20\times10^{-8}\Delta\nu_1\right)\end{aligned} \tag{2.16}$$

where,

$$\Delta\nu_1 = 0.1\left(\frac{P}{760}\right)\left(\frac{273}{T}\right)^{2/3}[0.810X_{H_2}+0.35X_{He}] \tag{2.17}$$

where T is temperature in °K, ν is wavenumber in cm^{-1}, P is pressure in torr, X_{H_2} is the mole fraction of hydrogen, and X_{He} is the mole fraction of helium.

The DeBoer formalism as corrected in *de Pater et al.* (2005) uses a gross line shape and is derived from the formalism given in *Ulaby et al.* (1981), with a substitution

from *Goodman* (1969). The original formalism given in *DeBoer* (1995) over estimated the opacity contribution from water vapor by orders of magnitude, knowing the origin of the corrected formalism, is therefore of some importance. The formalism starts out with that of *Ulaby et al.* (1981) :

$$\begin{aligned}\alpha_{H_2O} &= 2\nu^2\rho_v\left(\frac{300}{T}\right)^{5/2}\sum_{i=1}^{10}A_i\exp(-E_i'/T)\left[\frac{\gamma_i}{(\nu_i^2-\nu^2)^2+4\nu^2\gamma_i^2}\right] \\ &\quad +4.69\times10^{-6}\rho_v\left(\frac{300}{T}\right)^{2.1}\left(\frac{P}{1000}\right)\nu^2 \end{aligned} \tag{2.18}$$

where α_{H_2O} is the absorption coefficient in dB/km, ν is the frequency in GHz, ρ_v is the density of water vapor in $\frac{\mathrm{g}}{\mathrm{m}^3}$ and T is the temperature in Kelvin. The equation in *Ulaby et al.* (1981) is given in term of water vapor density, however, *de Pater et al.* (2005) apply the necessary conversion factors. First, one must substitute partial pressure of water vapor for density

$$\rho_v = \frac{P_{H_2O}}{R_{H_2O}T}\quad\left(\frac{\mathrm{g}}{\mathrm{m}^3}\right) \tag{2.19}$$

whereP_{H_2O} is the partial pressure of water vapor in Pascal, R_{H_2O} is the specific gas constant of water vapor, and T is the temperature in Kelvin. One must be careful to apply the correct conversion factors such that P_{H_2O} is in units of bars, and the values for water vapor density remain in units of $\frac{\mathrm{g}}{\mathrm{m}^3}$.

$$\rho_v = \frac{P_{H_2O}(\mathrm{bars})\left[\frac{1\times10^5\,\frac{\mathrm{N}}{\mathrm{m}^2}}{1\,\mathrm{bar}}\right]}{0.4615\left[\frac{\mathrm{Nm}}{\mathrm{gK}}\right]T} \tag{2.20}$$

Applying the above to equation 2.18, the formalism becomes

$$
\begin{aligned}
\alpha_{H_2O} &= 2\nu^2 \frac{P_{H_2O}(\text{bars}) \left[\frac{1\times10^5 \frac{\text{N}}{\text{m}^2}}{1\,\text{bar}}\right]}{0.4615 \left[\frac{\text{Nm}}{\text{gK}}\right] T} \left(\frac{300}{T}\right)^{5/2} \times \\
&\quad \sum_{i=1}^{10} A_i \exp(-E_i'/T) \left[\frac{\gamma_i}{(\nu_i^2-\nu^2)^2+4\nu^2\gamma_i^2}\right] \\
&\quad +4.69\times10^{-6} \frac{P_{H_2O}(\text{bars}) \left[\frac{1\times10^5 \frac{\text{N}}{\text{m}^2}}{1\,\text{bar}}\right]}{0.4615 \left[\frac{\text{Nm}}{\text{gK}}\right] T} \left(\frac{300}{T}\right)^{2.1} \times \\
&\quad (0.81P_{H_2}+0.35P_{He})\nu^2
\end{aligned} \tag{2.21}
$$

with the equation now expressed in terms of water vapor partial pressure in place of density. Finally, the *Goodman* (1969) term $(0.81P_{H_2}+0.35P_{He})$ is used in place of total pressure, a factor of $\frac{\pi}{4}$ is introduced, and values of T are combined into the $\left(\frac{300}{T}\right)$ terms where the equation is now in the appropriate form.

$$
\begin{aligned}
\alpha_{H_2O} &= \frac{1}{300}\frac{\pi}{4} 2\nu^2 \frac{P_{H_2O}(\text{bars}) \left[\frac{1\times10^5 \frac{\text{N}}{\text{m}^2}}{1\,\text{bar}}\right]}{0.4615 \left[\frac{\text{Nm}}{\text{gK}}\right] T} \left(\frac{300}{T}\right)^{7/2} \times \\
&\quad \sum_{i=1}^{10} A_i \exp(-E_i'/T) \left[\frac{\frac{4\gamma_i}{\pi}}{(\nu_i^2-\nu^2)^2+4\nu^2\gamma_i^2}\right] \\
&\quad +\frac{1}{300} 4.69\times10^{-6} \frac{P_{H_2O}(\text{bars}) \left[\frac{1\times10^5 \frac{\text{N}}{\text{m}^2}}{1\,\text{bar}}\right]}{0.4615 \left[\frac{\text{Nm}}{\text{gK}}\right] T} \left(\frac{300}{T}\right)^{3.1} \left(\frac{P}{1000}\right) \nu^2 \quad (\text{dB/km})
\end{aligned} \tag{2.22}
$$

After multiplying through by all constants, the formalism becomes

$$
\begin{aligned}
\alpha_{H_2O} &= 1134.5 P_{H_2O} \left(\frac{300}{T}\right)^{7/2} \\
&\quad \times \sum_{i=1}^{10} A_i \exp\left(\frac{-E_i'}{T}\right) \frac{4\nu^2\gamma_i/\pi}{(\nu_{o,i}-\nu^2)^2+4\nu^2\gamma_i^2} \\
&\quad +3.39\times10^{-3} \left(\frac{300}{T}\right)^{3.1} \times (0.81P_{H_2}+0.35P_{He})\nu^2\,(\text{dB/km}),
\end{aligned} \tag{2.23}
$$

which is the formalism as given in *de Pater et al.* (2005). The terms in equation 2.23 are: ν frequency in GHz, A_i the absorption at line i, E_i' is a term representing quantum energy transition state at line i, $\nu_{o,i}$ the line center frequency for line i, T is temperature in °K , P_{H_2O}, P_{H_2}, and P_{He}, are the partial pressures in bars of water vapor, hydrogen, and helium, respectively. The value for the line width γ_i is given by,

$$\gamma_i = \gamma_{H_2,i} P_{H_2} \left(\frac{300}{T}\right)^{\xi_{H_2,i}} + \gamma_{He,i} P_{He} \left(\frac{300}{T}\right)^{\xi_{He,i}} + \gamma_{H_2O,i} P_{H_2O} \left(\frac{300}{T}\right)^{\xi_{H_2O,i}} \quad \text{(GHz)} \tag{2.24}$$

where $\gamma_{H_2,i}$,$\gamma_{He,i}$, and $\gamma_{H_2O,i}$ are the line broadening parameters for hydrogen, helium and water vapor, respectively. The values of $\xi_{H_2,i}$, $\xi_{He,i}$, and $\xi_{H_2O,i}$ are the linewidth temperature dependence terms for hydrogen, helium, and water vapor, respectively. The partial pressures of hydrogen, helium, and water vapor are P_{H_2}, P_{He}, and P_{H_2O} in bars. The value T is the temperature in °K. The table of parameters for the 10 water vapor lines are given in Table 2.2. The Table is essentially taken from *Ulaby et al.* (1981), with additional parameters for H_2 and He taken from *Dutta et al.* (1993).

Table 2.2: The *DeBoer* (1995) water vapor model parameters as corrected by *de Pater et al.* (2005)

Line Number (i)	$\nu_{o,i}$ (GHz)	E_i'	A_i	γ_{i,H_2}	$\gamma_{i,He}$	γ_{i,H_2O}	ξ_{i,H_2}	$\xi_{i,He}$	ξ_{i,H_2O}
1	22.23515	644	1.0	2.935	0.67	10.67	0.9	0.515	0.626
2	183.31012	196	41.9	2.40	0.71	11.64	0.95	0.49	0.649
3	323	1850	334.4	2.395	0.67	9.59	0.9	0.515	0.420
4	325.1538	454	115.7	2.395	0.67	11.99	0.9	0.49	0.619
5	380.1968	306	651.8	2.39	0.63	12.42	0.85	0.54	0.630
6	390	2199	127.0	2.395	0.67	9.16	0.9	0.515	0.330
7	436	1507	191.4	2.395	0.67	6.32	0.9	0.515	0.290
8	438	1070	697	2.395	0.67	8.34	0.9	0.515	0.360
9	442	1507	590.2	2.395	0.67	6.52	0.9	0.515	0.332
10	448	412	973.1	2.395	0.67	11.57	0.9	0.515	0.510

2.4 Cloud Absorption

The absorption from cloud particles in the Rayleigh limit (where the size parameter $X = \frac{2\pi r}{\lambda} << 1$), is a far more simple expression than for cases in the Mie regime

$(X > 1)$. The absorption efficiency in the Rayleigh limit is given as,

$$Q_a = 4XIm(-K) \tag{2.25}$$

where,

$$K = \frac{\epsilon - 1}{\epsilon + 2} \tag{2.26}$$

where ϵ is the permitivity of the particle. Next, solving for the absorption cross section,

$$\sigma_a = 4\pi r^2 XIm(-K) \tag{2.27}$$

where r is particle radius. The absorption coefficient is then found by:

$$\alpha_{cloud} = \int_0^\infty \sigma_a(r) n(r) dr \tag{2.28}$$

where $n(r)$ is the particle size distribution. Considering the volume fraction occupied by the particle distribution,

$$f = \int_0^\infty \frac{4\pi r^3}{3} n(r) dr \tag{2.29}$$

The value for absorption coefficient can be written as:

$$\alpha_{cloud} = \frac{6\pi}{\lambda} Im(-K) f \tag{2.30}$$

The volume fraction occupied by the particle size distribution can then be calculated as,

$$f = \frac{D}{\rho} \tag{2.31}$$

where D is the cloud bulk density, and ρ is the density of the cloud material. Next the value of $Im(-K)$ simlifies to

$$Im(-K) = 3\left(\frac{\epsilon''}{(\epsilon' + 2) + (\epsilon'')^2}\right) \tag{2.32}$$

Substituting this along with the volume fraction, the equation for α_{cloud} simplifies to

$$\alpha_{cloud} = \frac{18\pi}{\lambda} \frac{D}{\rho} \left(\frac{\epsilon''}{(\epsilon' + 2)^2 + (\epsilon'')^2}\right) \quad (\mathrm{cm}^{-1}) \tag{2.33}$$

where D is cloud bulk density in $\frac{g}{cm^3}$, ρ is particle mass density (density of material) in $\frac{g}{cm^3}$, ϵ' is the real part of the dielectric constant, and ϵ'' is the imaginary part of the dielectric constant. The particle mass density, or the density of the cloud material is assumed to be that of water ($1\,\frac{g}{cm^3}$). For cloud materials such as ammonia ice, the material density could be as low as $0.84\,\frac{g}{cm^3}$ (*Ackerman and Marley*, 2001), for ammonium hydrosulfide $1.17\,\frac{g}{cm^3}$ (*Weast and Astle*, 1979), and for water ice $0.93\,\frac{g}{cm^3}$ (*Ackerman and Marley*, 2001). By using equation 2.33 we are slightly overstating the opacity of the ammonium hydrosulfide clouds, while understating the opacity of the ammonia, and water ice clouds. As shown in Figures A.7 and A.8, the effect of including the appropriate densities is minimal both in terms of brightness temperature, and limb darkening. In Figure A.9, the ammonia content of the H_2O-NH_3 solution cloud is shown along with the cloud bulk densities for the enhanced ammonia case. It is clear the H_2O-NH_3 solution cloud will have a fraction of the solution cloud that is composed of ammonia (D_{NH_3}/D_{cloud}) that is at most 0.0002. This a negligibly small amount, and it is safe to assume that the material density will be essentially that of water.

Many sources which give dielectric properties of cloud materials give values of dielectric properties expressed in terms of refractive index ($n = n' + jn''$). Expressing such values in terms of dielectric constant is simply

$$\epsilon' = (n')^2 + (n'')^2 \tag{2.34}$$

for the real part of the dielectric constant, and

$$\epsilon'' = 2n'n'' \tag{2.35}$$

for the imaginary part of the dielectric constant, where n' is the real part of the refractive index, and n'' is the imaginary part of the refractive index.

All clouds besides the H_2O-NH_3 cloud use constant values as a function of frequency for ϵ' and ϵ'', and are presented in Table 2.3. For H_2O-NH_3 cloud, we use a

formalism for pure water from *Ulaby et al.* (1986), where the real part of the dielectric constant is given as,

$$\epsilon'_w = \epsilon_{t_\infty} + \frac{\epsilon_{w_o} - \epsilon_{w_\infty}}{1 + (2\pi f \tau_w)^2} \tag{2.36}$$

where f is in Hz, and τ_w is in seconds. The imaginary part is

$$\epsilon''_w = \frac{2\pi f \tau_w (\epsilon_{w_o} - \epsilon_{w_\infty})}{1 + (2\pi f \tau_w)^2} \tag{2.37}$$

The value for τ_w, the relaxation time is a function of temperature expressed by,

$$\begin{aligned} \tau_w(T) &= \frac{1}{2\pi}\left((1.1109 \times 10^{-10}) - (3.824 \times 10^{-12})T + (6.938 \times 10^{-14})T^2\right. \\ &\quad \left. -(5.096 \times 10^{-16})T^3)\right) \text{(seconds)} \end{aligned} \tag{2.38}$$

where T is expressed in °C. The values for high frequency limit of ϵ_w, ϵ_{w_∞} is taken to be 4.9. The static dielectric constant ϵ_{w_o} is a function of temperature given by

$$\epsilon_{w_o}(T) = 88.045 - 0.4147T + 6.295 \times 10^{-4}T^2 + 1.075 \times 10^{-5}T^3 \tag{2.39}$$

where T is in °C. While it is shown in Figure A.9 that the amount of ammonia contained in the H_2O-NH_3 cloud is small, it could have an effect upon both the real and imaginary parts of the dielectric constant. Also, the formulation for liquid water refractive index has been shown to work well for clouds on Earth, but there has been no measurement of the dielectric properties of water under deep Jovian conditions. Future measurements under Jovian conditions would certainly help reduce uncertainties in absorption from the H_2O–NH_3 solution cloud.

2.5 Refraction in Planetary Atmospheres

Refraction in the microwave regime has played a significant role in our understanding of the outer planets. Active microwave sensing using radio occultation techniques has provided insight into the composition, and temperature structure of the outer planets (*Lindal et al.*, 1987; *Lindal et al.*, 1985, 1981). In the field of passive radio astronomy, and radiometry, the role of refraction is often overlooked in the development of

radiative transfer models. Here we present the formalisms used to compute refractive index for Jovian planets.

The refractive indices of gases often approach values close to 1, however, small changes in refractive index can significantly alter the distribution of electromagnetic energy of a propagating wave. For convenience, the refractive index is often expressed in terms of refractivity defined as

$$N_i = 10^6(1 - n_i) \tag{2.40}$$

where n_i is the refractive index of a constituent i at an atmospheric level. Often times a value for refractivity is associated with a specific temperature and pressure. To compute the refractivity under different atmospheric conditions, this value must be corrected for temperature and pressure. The value for refractivity under atmospheric conditions may be computed as

$$N_i = N_i' \left(\frac{P_i}{P'}\right) \left(\frac{T_i}{T'}\right) \tag{2.41}$$

where N_i' is the refractivity value associated with conditions of pressure P', and temperature T', P_i is the partial pressure of the atmospheric constituent, and T_i is the temperature of the atmospheric constituent. If one knows the refractivities of each constituent in an atmosphere, the total refractivity at each level can be computed as

$$N_t = \sum_{i=1}^{M} N_i \tag{2.42}$$

where i the constituent at a level in the atmosphere, and M is the number of constituents in the atmosphere at a given level.

2.6 Refractivity of H_2, He, and CH_4

The three most abundant constituents in Jovian atmospheres are H_2, He, and CH_4. Given these three constituents play such a dominant role in terms of composition, it is necessary to include their refractivity profiles in a ray tracing radiative transfer

model. A summary of different refractivity values and their associated values of pressure and temperature are given in Table 2.4. The work of *Hoffman* (2001) only included refractivity from H_2 and He using the values presented in *DeBoer* (1995). Since many radio occultation studies (*Mohammed*, 2005; *Lindal et al.*, 1987; *Lindal et al.*, 1985, 1981) use values presented in *Essen* (1953), we will use these values for all of our sensitivity analysis, unless otherwise stated. Laboratory measurements presented in *Spilker* (1990) are used given that measurements were conducted under Jovian conditions using a fairly precise method to measure refractivity using a cavity resonator.

2.7 Refractivity of Water Vapor

Following CH_4, water vapor is the next most abundant constituent deep in the atmospheres of Jovian planets. Given this information it would be wise to consider the refractivity contributions from water vapor. Many Earth based GPS occultations use an expression derived from *Thayer* (1974) which is expressed as,

$$N = K_1 \frac{P_d}{T} + K_2 \frac{P_w}{T} + K_3 \frac{P_w}{T^2} \tag{2.43}$$

where P_d is the partial pressure of dry air in mbar, P_w is the partial pressure of water vapor in mbar, and T is the temperature in °K. The values K_1, K_2, and K_3 are empirically derived constants with values of 77.6, 64.8, and 3.776×10^5. While this formula is widely used, there is one major inaccuracy in its derivation. The value of K_2 was derived by extrapolating its value from infrared to radio wavelengths. The strong contributions from several water vapor lines in the infrared invalidate this derivation (*Rüeger*, 2002). The "Best Available" values for K_1, K_2, and K_3 are 77.674 $\pm$0.013 K/mbar, 71.97 $\pm$10.5 K/mbar, and 375406 $\pm$3000 K^2/mbar, repspectively (*Rüeger*, 2002). For Earth's atmosphere *Rüeger* (2002) also includes a term for CO_2's contribution to refractivity. For Jovian planets we ignore the contribution from dry

air and use

$$N_w = K_2 \frac{P_w}{T} + K_3 \frac{P_w}{T^2} \tag{2.44}$$

where P_w is the partial pressure of water vapor, and T is the temperature in °K. We use 71.97 K/mbar, and 375406 K^2/mbar for K_2, and K_3, respectively.

2.8 Solution Cloud Refractivity

While it is known that cloud refractivity plays a role in propagation studies, very few consider the role of ray-bending in microwave radiometry. One of the more widely used cloud refractivity (used for fogs and small particles on Earth) models is that of *Liebe et al.* (1993). In this work, we will only consider refractivity of the H_2O-NH_3 solution cloud. For simplicity, and to test against results presented in *Liebe et al.* (1993) the expression for the permittivity of water is calculated by their Double-Debye relaxation model expressed as,

$$\epsilon_w = \epsilon_o - \nu \frac{\epsilon_o - \epsilon_1}{\nu + j\gamma_1} + \frac{\epsilon_1 - \epsilon_2}{\nu + j\gamma_2} \tag{2.45}$$

where ν is the frequency in GHz, ϵ_o is the static dielectric constant, ϵ_1 and ϵ_2 are high frequency dielectric constants, and finally γ_1 and γ_2 are the two relaxation frequencies. The static and high frequency dielectric constants are given by,

$$\epsilon_o = 77.66 = 103.3(\theta - 1) \tag{2.46}$$

$$\epsilon_1 = 0.0671\epsilon_o \tag{2.47}$$

$$\epsilon_2 = 3.52 \tag{2.48}$$

The value θ is given by,

$$\theta = 300/T \tag{2.49}$$

where T is the value for temperature in °K. Values for the relaxation frequencies are given by,

$$\gamma_1 = 20.20 - 146(\theta - 1) + 316(\theta - 1)^2 \tag{2.50}$$

$$\gamma_2 = 39.8\gamma_1 \tag{2.51}$$

where both γ_1 and γ_2 are both in units of GHz. The refractivity is then calculated using:

$$N_w = 1.5\frac{D'}{\rho}Re\left(\frac{\epsilon_w - 1}{\epsilon_w + 2}\right) \tag{2.52}$$

where D' is the particle density in $\frac{\text{g}}{\text{m}^3}$, ρ is the density of the material in $\frac{\text{g}}{\text{cm}^3}$. It should be noted that the discrepancy in units is intentional ($\frac{\text{g}}{\text{m}^3}$ vs. $\frac{\text{g}}{\text{cm}^3}$) to preserve appropriate units in the formulation of *Liebe et al.* (1993).

Table 2.3: Cloud Dielectric Properties studies with values presented in terms of refractive index are denoted with unit n, and studies with values presented in terms of dielectric constant are denoted with a unit ϵ

Cloud composition	Real (n'/ϵ')	Imaginary (n''/ϵ'')	Unit (n/ϵ)	Source
Ammonia Ice @1300 cm^{-1}	1.48	8.73×10^{-4}	n	*Howett et al.* (2007)
NH_4SH ice @1300 cm^{-1}	2.72	7.83×10^{-4}	n	*Howett et al.* (2007)
H_2O ice @30 GHz	3.15	1×10^{-3}	ϵ	*Matsuoka et al.* (1996)

Table 2.4: Refractivity values used in recent studies. Values marked with a * are used for sensitivity analysis unless otherwise stated.

Constituent	N'	P (bars)	T (°K)	Source
H_2*	136	1.01325	273	*Essen* (1953)
H_2	124	1	293	*DeBoer* (1995)
He *	35	1.01325	273	*Essen* (1953)
He	35.83	1	293	*DeBoer* (1995)
CH_4*	440	1.01325	273	*Spilker* (1990)

CHAPTER III

EXPERIMENT DESIGN AND THEORY

The Planetary Atmospheres Lab at Georgia Tech has a long history of providing the planetary science community with precise laboratory measurements of the absorption coefficients for microwave opaque gases. While the cavity resonator method used to in these measurements of microwave opacity is similar to *Hanley and Steffes* (2007), the system used for this study required several newly-developed components to operate under the extreme conditions required to simulate the deep Jovian atmosphere. Throughout the study, instruments were either upgraded or added to improve knowledge of water vapor concentration, temperature, pressure, and even mass flow of hydrogen. In this chapter the basic microwave measurement theory is presented. In addition, the unique instrumentation used is highlighted, and the benefit provided by each instrument is presented.

3.1 Using a Cavity Resonator to Measure Microwave Opacity and Refractivity in a Laboratory

The microwave energy propagation can be represented as a plane wave with propagation in the $+z$ direction using

$$E(z) = Re\left[E_o \exp(-\alpha z - j\beta z)\exp(j2\pi\nu t)\right] \tag{3.1}$$

$$H(z) = Re\left[H_o \exp(-\alpha z - j\beta z)\exp(j2\pi\nu t)\right], \tag{3.2}$$

where E_o and H_o are the amplitudes of the electric and magnetic fields, j is represents the imaginary unit ($\sqrt{-1}$), α is the attenuation coefficient, β is the phase constant, ν is frequency, and t is time. The phase constant can be represented as

$$\beta = \frac{2\pi}{\lambda}, \tag{3.3}$$

where λ is wavelength. The two electromagnetic properties which govern the transmission of electromagnetic waves in a medium are electric permittivity (ϵ), and magnetic permeability (μ). For a medium which is non-ferrous, μ is usually taken to be μ_o ($4\pi\times10^{-7}\,\frac{\mathrm{H}}{\mathrm{m}}$), and has only has a real part. The value of ϵ, however, usually contains a real and imaginary part ($\epsilon = \epsilon' + j\epsilon''$). Using the dielectric properties of an arbitrary medium, the attenuation, and phase constants are represented by

$$\alpha = 2\pi\nu\sqrt{\frac{\mu\epsilon'}{2}\left(\sqrt{1+\left(\frac{\epsilon''}{\epsilon'}\right)^2}-1\right)} \tag{3.4}$$

$$\beta = 2\pi\nu\sqrt{\frac{\mu\epsilon'}{2}\left(\sqrt{1+\left(\frac{\epsilon''}{\epsilon'}\right)^2}+1\right)} \tag{3.5}$$

where α is in $\frac{\text{nepers}}{\mathrm{m}}$, and β is in units of $\frac{\text{radians}}{\mathrm{m}}$ (*Ramo et al.*, 1965). The ratio of α to β gives

$$\frac{\alpha}{\beta} = \sqrt{\frac{\sqrt{1+\left(\frac{\epsilon''}{\epsilon'}\right)^2}-1}{\sqrt{1+\left(\frac{\epsilon''}{\epsilon'}\right)^2}+1}}\,. \tag{3.6}$$

Equation 3.6 can be simplified further if one considers the loss tangent. The loss tangent is defined as,

$$\tan(\delta) = \left(\frac{\epsilon''}{\epsilon'}\right) = \frac{1}{Q_{gas}}\,, \tag{3.7}$$

where Q_{gas} is the unitless quality factor for a gas. The loss tangent ($\frac{\epsilon''}{\epsilon'}$) is usually far less than unity for most microwave opaque gases. Using this approximation combined with equation 3.6 the value for the ratio of α to β becomes

$$\frac{\alpha}{\beta} \approxeq \frac{\epsilon''}{2\epsilon} = \frac{1}{2Q_{gas}}\,. \tag{3.8}$$

This approximation leads to a straightforward equation for the absorption coefficient by substituting the phase constant (β in Equation 3.3) into Equation 3.8 which yields

$$\alpha = \frac{\pi}{\lambda}\frac{1}{Q_{gas}}\,. \tag{3.9}$$

The unitless value Q_{gas} is measured by using a microwave resonator. There are a variety of microwave resonators including rectangular (e.g., a microwave oven), Fabry-Perot, and cylindrical cavity resonators. Cylindrical cavity resonators tend to be the most popular for high-pressure microwave spectroscopy out of convenience, since their shape is compatible with pressure vessels constructed out of cylindrical sections of thick-walled pipe. In fact, some studies have used the body of the pressure vessel itself as the microwave resonator (*Ho et al.*, 1966; *Morris and Parsons*, 1970). In the present work a well characterized cylindrical cavity resonator is used. The resonator was most recently used by *Hanley et al.* (2009) to measure the microwave opacity of ammonia up to the 12 bar level in the Jovian atmosphere. Figure 3.1 shows the cavity resonator used prior to installation in the current high-pressure system. The quality factor of a resonance within a microwave resonator is defined by

$$Q^m_{resonance} = \frac{2\pi f_o \times \text{Energy Stored}}{\text{Average Power Loss}} \tag{3.10}$$

where f_o is the center frequency of a resonance characterized by a peak in the frequency response of the resonator (*Matthaei et al.*, 1980). The measured quality factor ($Q^m_{resonance}$) is found by taking the center frequency and dividing it by its half-power bandwidth

$$Q^m_{resonance} = \frac{f_o}{\text{Bandwidth}} \ . \tag{3.11}$$

The quality factor of a resonator loaded with a test gas can be expressed as

$$\frac{1}{Q^m_{loaded}} = \frac{1}{Q_{gas}} + \frac{1}{Q_{vacuum}} + \frac{1}{Q_{probe\,1}} + \frac{1}{Q_{probe\,2}} \tag{3.12}$$

where Q^m_{loaded} is the measured quality factor of the resonator loaded with a test gas, Q_{gas} is the quality factor of the gas, Q_{vacuum} is the quality factor of the resonator under vacuum, and $Q_{probe\,1}$ and $Q_{probe\,2}$ are the coupling losses from the two probes (loop antennas) in the resonator (*Matthaei et al.*, 1980). Given that the resonator is essentially symmetric, and the coupling probes are essentially the same size and

dimensions it is assumed that $Q_{probe\,1}$=$Q_{probe\,2}$. This value is now referred to as $Q_{coupling}$ and is determined by measuring the transmission losses in the system, or transmissivity of the system $t = 10^{-S/10}$ where S is the insertion loss of the resonator in decibels (dB) at the frequency of a resonance. Using the following relations, the value of $Q_{coupling}$ is found via

$$t = \left(2\frac{Q^m}{Q_{coupling}}\right)^2 \tag{3.13}$$

$$\frac{1}{Q_{coupling}} = \frac{\sqrt{t}}{2Q^m} \ , \tag{3.14}$$

where Q^m is a measured quality factor (*Matthaei et al.*, 1980).The value for Q_{vacuum} is related to the measured quality factor under vacuum (Q^m_{vacuum}) conditions by

$$\frac{1}{Q^m_{vacuum}} = \frac{1}{Q_{vacuum}} + \frac{1}{Q_{probe\,1}} + \frac{1}{Q_{probe\,2}} \ . \tag{3.15}$$

After substitution of Equation 3.14 into Equations 3.12 and 3.15, the value of Q_{gas} is given by

$$\frac{1}{Q_{gas}} = \frac{1-\sqrt{t_{loaded}}}{Q^m_{loaded}} - \frac{1-\sqrt{t_{vacuum}}}{Q^m_{vacuum}} \ , \tag{3.16}$$

where t_{loaded} and t_{vacuum} are the transmissivity values of the loaded and vacuum measurements. One could directly calculate Q_{gas} assuming that the center frequency of a resonance does not change with the addition of a test gas. It is known, however, that this is not the case. An effect known as dielectric loading which is related to the refractive index of a gas present will change the center frequency of the resonance. This effect can be compensated by using a tunable resonator (e.g., *Ho et al.*, 1966; *Morris and Parsons*, 1970), however, in doing this the coupling properties of the resonator can change, resulting in a error prone measurement of Q_{gas}. In place of a measurement of Q under vacuum conditions (Q^m_{vacuum}), one can measure the Q in the presence of a microwave transparent gas with the same refractive index as the test gas. The amount of microwave transparent gas added can be used to tune the center frequency of the resonator. This allows for a "frequency matched" value

replacing the term in Equation 3.16. The resulting expression in dB/km making the appropriate substitution converting from Nepers/km to dB/km (1 Neper/km= 2 optical depths km^{-1}=2×10log$_{10}(e)$ ≅ 8.686 dB/km) yields the expression used for calculating absorption

$$\alpha = 8.686\,\frac{\pi}{\lambda}\left(\frac{1-\sqrt{t_{loaded}}}{Q^m_{loaded}} - \frac{1-\sqrt{t_{matched}}}{Q^m_{matched}}\right)\ \left(\frac{\mathrm{dB}}{\mathrm{km}}\right), \tag{3.17}$$

where the wavelength λ has units of km (*DeBoer and Steffes*, 1996a).

The dielectric loading of a resonance also gives information regarding the refractive index of a gas. For most gases the index of refraction (n) is usually close to unity. As a result the refractivity of a gas is given by multiplying the residual $n-1$ by 10^6, or

$$N = 10^6(n-1), \tag{3.18}$$

where N is the refractivity of a gas. The measurement of refractivity uses the dielectric loading principle discussed previously, and is calculated by a more direct method than absorption. The refractivity is measured using

$$N = 10^6\,\frac{f_{vacuum} - f_{gas}}{f_{gas}}\ , \tag{3.19}$$

where f_{vacuum} is the center frequency of a resonance measured under vacuum, and f_{gas} is the center frequency measured with a test gas (*Tyler and Howard*, 1969).

The center frequencies of a TE or TM mode resonance in a cylindrical cavity resonator is calculated using

$$f_{TE(N,M,L)} = \frac{c}{2\pi\sqrt{\mu_r\epsilon_r}}\sqrt{\left(\frac{p_{n,m}}{r}\right)^2 + \left(\frac{\pi L}{h}\right)^2} \tag{3.20}$$

$$f_{TM(N,M,L)} = \frac{c}{2\pi\sqrt{\mu_r\epsilon_r}}\sqrt{\left(\frac{q_{n,m}}{r}\right)^2 + \left(\frac{\pi L}{h}\right)^2}, \tag{3.21}$$

where c is the speed of light (cm/s), μ_r and ϵ_r are the real parts of the relative permeability and permittivity of the medium contained inside the resonator, r and h

are the interior radius and height of the resonator (cm), $q_{n,m}$ is the m$^{\text{th}}$ zero of the n$^{\text{th}}$ order bessel function, and $p_{n,m}$ is the first derivative of the m$^{\text{th}}$ zero, n$^{\text{th}}$ order bessel function of the first kind (*Pozar*, 1998). In this work only TE modes are measured due to their high quality factors. In fact most TM modes have been intentionally suppressed to further reduce interference with the neighboring TE modes (*Hanley*, 2007).

There are five uncertainties for measuring the absorptivity: instrumentation errors and electrical noise (Err_{inst}), errors in dielectric matching (Err_{diel}), errors in transmissivity measurement (Err_{trans}), errors due to resonance asymmetry (Err_{asym}), and errors in the measurement conditions resulting from uncertainty in temperature, pressure, mixing ratio, and compressibility (Err_{cond}). The computation of errors is described in more detail in the work of *Hanley and Steffes* (2007); *Hanley* (2007), however, a brief overview of how these errors are computed in the current work is of some interest.

The instrumentation errors considered in Err_{inst} are limited to instrumentation errors associated with the microwave test equipment. Two parameters of interest in calculating Err_{inst} are the error in measuring the center frequency of a resonance (Err_o) and the error in measuring the bandwidth of a resonance (Err_Δ). The instrument used in these experiments is the same Agilent E5071C-ENA Vector Network Analyzer used in *Hanley* (2007). The value for Err_o (3σ error) is calculated following *Hanley* (2007)

$$Err_o = f_{measured}\left(5 \times 10^{-8} + 5 \times 10^{-7} \times years\,since\,calibrated\right)\ \text{(Hz)}, \qquad (3.22)$$

with the measured frequency given in Hz. Agilent does not provide an error calculation for its E5071C-ENA Vector Network Analyzer, therefore the approach of *Hanley* (2007) is followed using

$$Err_\Delta = \sqrt{2}BW_{measured}\left(5 \times 10^{-8} + 5 \times 10^{-7} \times years\,since\,calibrated\right)\ \text{(Hz)}, \quad (3.23)$$

with the measured bandwidth given in Hz, and Err_Δ is a 3σ error.

One final source of error that must be accounted for before calculating Err_{inst} is the uncertainty in the mean of the measurement population Err_n. For each resonance 30 sweeps are taken, the standard deviations of the bandwidths measured for the 30 sweeps are computed, and Err_n is computed for each resonance as

$$Err_n = \frac{2.045}{\sqrt{30}} s_n, \tag{3.24}$$

where s_n is the standard deviation of the Bandwidth measurement of a resonance over 30 sweeps. For further details on computing Err_n see *Hanley* (2007).

The worst case error for instrumentation is given by

$$Err_{inst} = \pm \frac{8.686\pi}{\lambda} Err_\psi \ \left(\frac{\text{dB}}{\text{km}}\right) \tag{3.25}$$

with λ is the wavelength (km), and Err_ψ is calculated as

$$Err_\psi = \sqrt{\Gamma_l^2 + \Gamma_m^2 - 2(\Gamma_l \Gamma_m)} \ . \tag{3.26}$$

The remaining terms in Equation 3.26 are calculated using

$$\Gamma_i^2 = \frac{\gamma_i^2}{f_{o,i}^2} \left[\frac{Err_o^2}{Q_i^2} + Err_\Delta^2 + Err_{N_i}^2 + \frac{2Err_o Err_\Delta}{Q_i} \right], i = l, m, \tag{3.27}$$

$$\Gamma_l \Gamma_m = -\frac{\gamma_l \gamma_m}{f_{o,l} f_{o,m}} \left[\frac{Err_o^2}{Q_l Q_m} + Err_\Delta^2 + \frac{Err_o Err_\Delta}{Q_l} + \frac{Err_o Err_\Delta}{Q_m} \right] \tag{3.28}$$

$$Q_i = \frac{f_{o,i}}{BW_i}, i = l, m \tag{3.29}$$

where subscripts l and m represent loaded and matched cases, and γ, f_o, and BW represent the $1 - \sqrt{t}$ terms from Equation 3.17, the resonance center frequency, and resonance bandwidth, respectively. Values for Err_o and Err_Δ are scaled by factor of $\frac{2}{3}$ to yield 2σ uncertainties.

Errors in dielectric matching (Err_{diel}) result from imprecise alignment of the center frequency of the matched measurement with that of the loaded measurement. Even though the gas used for matching is lossless, the Quality factor measured can vary

slightly. The magnitude of this effect is calculated by comparing the Quality factors for three vacuum measurements to the matched Quality factor

$$\left(\frac{dQ}{df}\right)_i = \left|\frac{Q_{vacuum,i} - Q_{matched}}{f_{vacuum,i} - f_{matched}}\right|, \text{ for i = 1, 2, and 3.} \tag{3.30}$$

The maximum of the three values is then used to to calculate a dQ value

$$dQ = \left(\frac{dQ}{df}\right)_{max} |f_{loaded} - f_{matched}| \ , \tag{3.31}$$

where f_{loaded} and $f_{matched}$ are the center frequencies of the resonance under loaded and matched conditions, respectively. The error in dielectric matching is then computed by propagating ±dQ through Equation 3.17

$$Err_{diel} = \left|8.686\,\frac{\pi}{\lambda}\left[\left(\frac{1-\sqrt{t_{loaded}}}{Q^m_{loaded}+dQ} - \frac{1-\sqrt{t_{matched}}}{Q^m_{matched}}\right) - \left(\frac{1-\sqrt{t_{loaded}}}{Q^m_{loaded}-dQ} - \frac{1-\sqrt{t_{matched}}}{Q^m_{matched}}\right)\right]\right|. \tag{3.32}$$

Perhaps the largest uncertainty in these measurements comes from the process of disconnecting and reconnecting cables during the transmissivity measurements. The error is found by taking the appropriate statistics about the measured transmissivity. The cables to the resonator are disconnected from the resonator and then connected in a thru configuration, the transmissivity is measured. The cables are disconnected and reconnected, the transmissivity is measured again, and the process is repeated a third time to generate 3 samples. The error in measured transmissivity is given by

$$Err_{mt} = \frac{4.303}{\sqrt{3}} s_n \tag{3.33}$$

where s_n is the standard deviation of the transmissivity measurements. While Err_{mt} takes into account the variation in the cables which can be connected and reconnected, it does not account for the cables within the pressure vessel which can not be removed.

To account for the additional uncertainty from those cables a value of 0.5 dB is assumed, the resulting value for the uncertainty in insertion loss is

$$Err_{insertion\,loss} = \sqrt{Err_{mt}^2 + 0.5^2}. \tag{3.34}$$

The error in insertion loss is used to find the error in transmissivity

$$Err_{t,i} = \frac{1}{2}\left(10^{-(S_i - Err_{insertion\,loss})} - 10^{-(S_i + Err_{insertion\,loss})}\right),\ i = l, m \tag{3.35}$$

where subscript i represents the loaded and matched cases and S is the insertion loss of the resonator. This is used to map the 2σ uncertainty in opacity which gives

$$Err_{trans} = \frac{8.686}{2}\frac{\pi}{\lambda}\left(\frac{\sqrt{t_l - Err_{t,l}} - \sqrt{t_l + Err_{t,l}}}{Q^m_{loaded}} - \frac{\sqrt{t_m - Err_{t,m}} - \sqrt{t_l + Err_{t,m}}}{Q^m_{matched}}\right) \tag{3.36}$$

The final source of uncertainty is that which arises from the asymmetry of a resonance. This is accounted for by first calculating the bandwidth based upon higher and lower halves of the resonance

$$BW_h = 2(f_h - f_c) \tag{3.37}$$

$$BW_l = 2(f_c - f_l) \tag{3.38}$$

where BW_h and BW_l are the equivalent full bandwidths based on assuming symmetry of the high and low sides of the resonance, f_h is the frequency at the half power point on the upper portion of the resonance, f_l is the frequency at the half power power point on the lower portion of the resonance, and f_c is the center frequency. The difference between opacities calculated using BW_h and BW_l are treated as a 2σ error defined as Err_{asym} and is expressed as

$$Err_{asym} = \left|8.686\,\frac{\pi}{\lambda}\left[\left(\frac{1-\sqrt{t_{loaded}}}{Q^m_{loaded}(BW_h)} - \frac{1-\sqrt{t_{matched}}}{Q^m_{matched}(BW_h)}\right) - \left(\frac{1-\sqrt{t_{loaded}}}{Q^m_{loaded}(BW_l)} - \frac{1-\sqrt{t_{matched}}}{Q^m_{matched}(BW_l)}\right)\right]\right|, \tag{3.39}$$

where $Q^m_{loaded}(BW_h)$ and $Q^m_{loaded}(BW_l)$ are the loaded quality factors evaluated using the bandwidth computed using the higher and lower half of the resonance, respectively. The values $Q^m_{matched}(BW_h)$, and $Q^m_{matched}(BW_l)$ are the matched quality factors computed using the higher and lower half of the resonance, respectively.

The uncertainty in measurement conditions Err_{cond} can only be computed if the pressure, temperature, concentration and compressibility dependences of the refractive and absorbing properties of the test gas mixture are known. Since this is rarely the case, their effects are excluded from the measurement uncertainty with inclusion of the conditional uncertainties separately. Finally, the 95% confidence measurement uncertainty is calculated as

$$Err_\alpha = \sqrt{Err^2_{inst} + Err^2_{diel} + Err^2_{trans} + Err^2_{asym}} \; . \tag{3.40}$$

While the theoretical computation of refractivity using an ideal resonator as given in Equation 3.19 is relatively simple, the actual calculation, and propagating errors using a resonator that can deform with temperature and pressure is slightly more complex. The extensive set of measurements conducted allows us to model the temperature dependence of the cavity resonator under vacuum conditions. *Hanley* (2007) showed that the height (h) and radius (r) of the cavity resonator can be represented as

$$r_T = a_o + a_1 T + a_2 T^2 \text{ (cm)} \tag{3.41}$$

$$h_T = b_o + b_1 T \text{ (cm)}, \tag{3.42}$$

where a_i, and b_i are empirically derived coefficients. These coefficients are derived using all the conducted vacuum measurements and fitting Equation 3.20 with the values of a_i, and b_i as free parameters. The derived parameters are given in Table 3.1. A plot of the residuals between the actual data points and the empirically derived equation is shown in Figure 3.2. The spread in residual values increases for the 500

and 525°K data points comes from a less precise control of temperature at higher temperatures. The overall correlation coefficient (R^2) is 0.999999916598402.

Table 3.1: Empirically derived coefficients for Equations 3.41 and 3.42

i	a	b
0	12.993000651099409	25.635264739431314
1	0.000498685501301	0.000412843042129
2	-0.000000332586042	-

Although a uniform pressure exists in the pressure vessel, and the resonator is contained within that pressure vessel, the dimensions of the resonator have been shown to change with pressure in *Hanley* (2007). The changes are accounted for using

$$r_P = r_T \left(1 - \frac{P}{E}(1-\nu)\right) \tag{3.43}$$

$$h_P = h_T \left(1 + \frac{2P\nu}{E}\right) \ , \tag{3.44}$$

where P is the pressure in bars, ν (0.29) is Poisson's ratio, E is the Young's modulus (1.93×10^6 bars). The values for the resonator dimensions r_P,h_P, r_T, and h_T are propagated through Equation 3.20 to obtain frequencies adjusted for pressure and temperature (f_P and f_T). The two are combined in a correction term f_{PTcorr} which is represented by

$$f_{PTcorr} = f_P - f_T. \tag{3.45}$$

The correction term is combined with Equation 3.19 giving the expression used to compute refractivity:

$$N = 10^6 \frac{f_{vac} - f_{gas} - f_{PTcorr}}{f_{gas}}. \tag{3.46}$$

An uncertainty associated with the pressure temperature correction (Δf_{PTcorr}) is computed by adding 0.5°K to the temperature used in Equations 3.41 and 3.42, and by taking the difference between the computed f_{PTcorr} and that with an increase in

Figure 3.1: Microwave Cavity resonator used for all experiments.

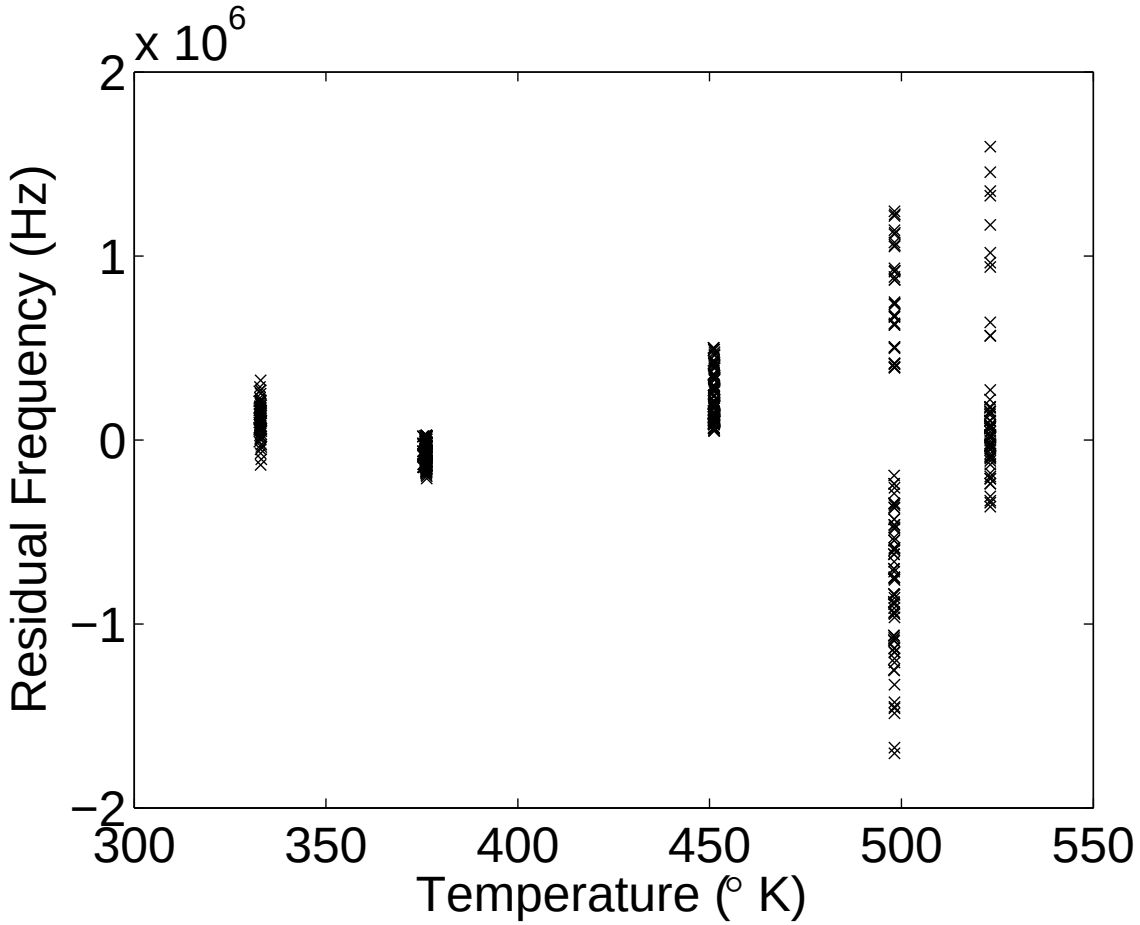

Figure 3.2: Residual values between measured vacuum center frequencies and the empirically derived equation for center frequencies of the cavity resonator.

0.5°K. The overall uncertainty is computed using

$$\Delta N = 10^6 \frac{\sqrt{\Delta f_{vac}^2 + \Delta f_{gas}^2 + \Delta f_{PTcorr}^2}}{f_{gas}} \tag{3.47}$$

where Δf_{vac} is the uncertainty in the frequency of the resonator at vacuum, and Δf_{gas} is the uncertainty associated with the center frequency of the resonator loaded by the test gas.

3.2 The Ultra-High Pressure System

The Ultra-High Pressure System is shown in schematic form in Figure 3.3. The system is composed of a pressure vessel custom built by Hays Fabrication and Welding located in Springfield, Ohio, a water reservoir made of a 304 stainless steel pipe 18" long and 1.5" in diameter, a Grieve®industrial oven model AB-650 (maximum temperature 650°F), two Matheson®3030 regulators (580 for Ar/He, and 350 for H_2), two Omega®DPG7000 pressure gauges (one rated from 0-15 psi, the other rated to 300 psi), an Omega®(subcontracted by Omega-Dyne®) PX1009L0-1.5KAV pressure transducer capable of measuring up to 1500 psi at 600°F, and an Omega® $\frac{1}{4}$" NPT thermocouple probe (TC-T-NPT-G-72). All the valves shown in Figure 3.3 with a blue dot are high temperature valves made by Swagelok®(SS-1RS6-PK) rated to 315°C at a maximum pressure of 215 bars, otherwise valves are rated to 93°C at a maxium pressure of 295 bars (SS-1RS6).

The custom pressure vessel was designed with two $\frac{1}{2}$" NPT input ports for gas delivery, one $\frac{1}{4}$" NPT port for the thermocouple, and two CF-1.33" Flanges for microwave feedthroughs. The pressure vessel was hydro-tested by Hays Fabrication and Welding with all input flanges, and feedthroughs at a pressure of 1450 psi. In place of a standard rubber or viton O-ring a composite (glass fiber/NBR) KLINGERsil®C-4430 is used to seal the pressure vessel along with 20 nuts 2-3/8" in diameter torqued to 1300 lb-ft of torque using a hand torque wrench (325 ft-lbs) and a 4x torque multiplier. The vessel is constructed out of a 12" section of schedule 100 pipe which is 14"

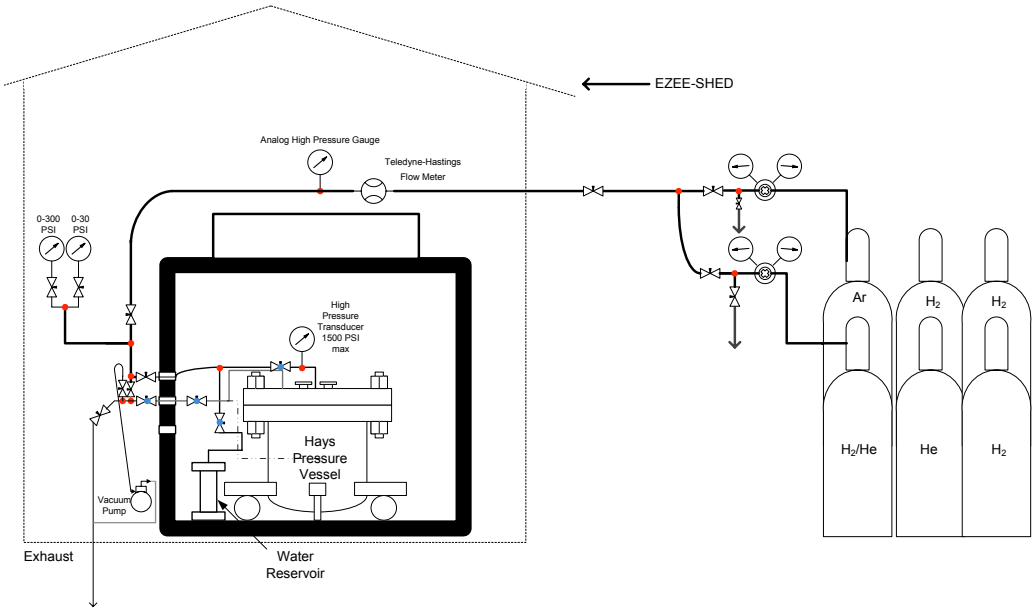

Figure 3.3: The Georgia Tech Ultra-High Pressure System.

in diameter (outer dimension). On one end an elliptical head is welded to the bottom giving the vessel a maximum interior height of 18-1/8". The top is a ANSI class 900 flange 4" thick, with a top plate which is 3-5/8" thick The vessel has a volume of 32.3 liters, and weighs approximately 1200 lbs.

The two most critical (and heaviest) elements of the Ultra-High Temperature Pressure System (the pressure vessel and oven) are shown in Figure 3.4. The weight of the pressure vessel (1200 lbs) and the shipping weight of the oven (1630 lbs) far exceeded the load capacity of the laboratory floor. Therefore, it was necessary to employ a civil engineer (Bob Goodman of TRC Worldwide Engineering®) to evaluate potential locations on the Van Leer 4^{th} floor roof (adjacent to the 5^{th} floor Laboratory). After careful analysis it was determined that a concrete pad on which a decommissioned crane once stood, would be the ideal location for a load far exceeding 2800 lbs. Once the equipment was procured, it was lifted onto the 4^{th} floor roof via a crane rented from Southway Crane. After delivery of the pressure vessel to the 4^{th} floor roof, a

Figure 3.4: The Grieve oven (AB-650) and the Custom Hays Fabrication and Welding Pressure Vessel.

steel shed (Arrow EZEE®Shed 86) was erected to protect the oven. A photograph of the system in assembly is shown in Figure 3.5. In addition to the EZEE®shed, a 1 Ton capacity gantry crane (Harbor Freight®Model 41188), and a 1 chain lift (Harbor Frieght/ Central Machinery®Model 00996) was procured and assembled. This enabled one person to disassemble the pressure vessel (remove the top) and insert the microwave resonator. After the microwave resonator was inserted, the top was replaced along with the 20 nuts each fastened with an applied torque of 1300 lb-ft.

Over the course of the measurement campaign, several relatively minor changes were made to the system described above. First, the $\frac{1}{4}$" thermocouple probe (TC-T-NPT-G-72) was replaced by a high temperature thermometer / hygrometer (JLC international®EE33-MFTI-9205-HA07-D05-AB6-T52) for experiments conducted below 525 °K, and after November 11, 2008. The high temperature thermometer / hygrometer was inserted into the $\frac{1}{2}$" exhaust port of the pressure vessel. In place of the $\frac{1}{4}$" thermocouple probe, a $\frac{1}{4}$" line was used as a replacement exhaust port (shown as a dotted line in Figure 3.3). For measurements at 525 °K and above the thermometer / hygrometer was replaced by a high precision Omega®Resistance Temperature Detector (RTD) (PR-11-2-100-1/8-9-E), with a Swagelok®$\frac{1}{8}$" Swagelok®tube to $\frac{1}{2}$" NPT adapter (SS-200-1-8BT).

Figure 3.5: The Ultra-High Pressure system in assembly.

Also, during measurements at 500-525 K, it became apparent that the microwave coaxial cables made by Astrolab® did not meet the manufacturer specifications. In fact, one of the cables oozed solder between the cable SMA nut and the Ceramtec® feedthrough in effect cold-soldering the cable to the feedthrough. The thread on the feedthrough was slightly damaged, however, a small adapter with low insertion loss was placed over the feedthrough to prevent further damage to the Ceramtec® feedthrough's thread. The CobraFlex® cable was damaged upon removal, due to the sma nut seizing against the cable body resulting in a tear in the outer conductor. For a few measurements at 500° K this cable was repaired and used in the system with no degradation in measurement errors, however, it was necessary on several occasions to repair the cable (resolder the broken end). Given the tedious nature of having to repair this cable, and the poor temperature performance of the Astrolab CobraFlex ®, a "homemade" solution was required. The Astrolab® cable assemblies were replaced with sections of Times Microwave M17/86-00001 (formerly known as RG-225), along

with Type-N connectors (PE4060 and PE4062) from Pasternack Enterprises® and solder with a high-temperature solder.

3.3 The Data Acquisition System

While developing the data acquisition and microwave systems for the atmospheric simulator, two major factors were considered: pressure, and temperature ratings. A schematic of the cables, and measurement devices used is shown in Figure 3.6 . The microwave resonator shown in Figure 3.6 has been used in several studies, most recently it has been used in studies by *Hanley* (2007) and *Hanley and Steffes* (2007). The resonator is a cylindrical cavity resonator with an interior height of 25.75 cm, and an interior radius of 13.12 cm. The resonator is connected to Ceramtec®feedthroughs within the pressure vessel, by SiO_2 microwave cables (Times Microwave®). They were selected to withstand the highest temperatures possible 600°C (1000°C without the connector). This was done to minimize the need to replace the cables within the pressure vessel (applying 1300 lb-ft of torque to 20 bolts is quite labor intensive). On the exterior of the pressure vessel two SMA Ceramtec feedthroughs (16545-01-CF) both rated to 103 bars and 350°C are used. Both Ceramtec®feedthroughs are backed by fully annealed copper gaskets made by Kurt J. Lesker Company®(Part # VZCUA19). While it would have been ideal to also use SiO_2 cables exterior to the pressure vessel within the oven (from a temperature performance aspect), there are two problems with this concept. First, for our application it would have been cost prohibitive. Second, the wear due to several cycles of connecting, and reconnecting the cables would likely damage SiO_2 cables. Instead two 4 ft sections of CobraFlex®cables with a PTFE dielectric rated to 250°C from Astrolab®were used to connect the microwave feeedthroughs to the SMA to type N panel mounts to the outside of the oven. Two sections of 80' length of Andrews®CNT 600 microwave cable

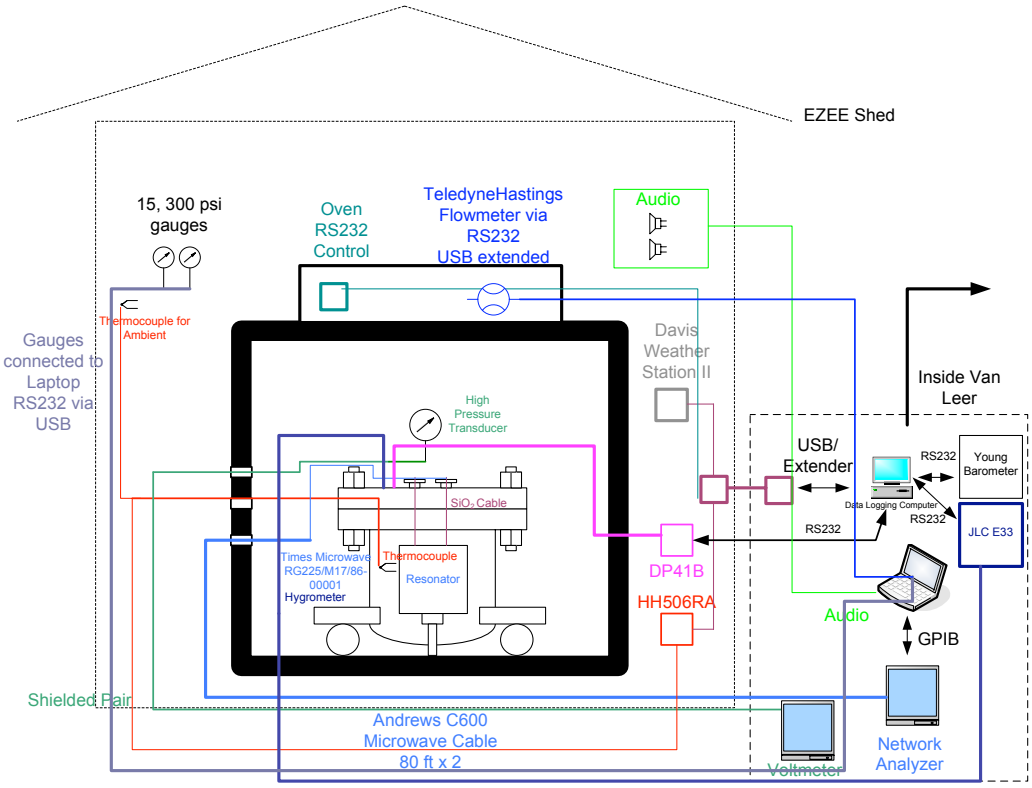

Figure 3.6: The microwave and data acquisition system.

are connected to the type N bulkheads on the oven back to the Agilent®E5071C network analyzer. The CNT 600 cable is not exposed to an extreme environment, thus its maximum operating temperature of 85°C is sufficient for our application. Use of the long microwave cable extension is required to ensure temperature stability of the Agilent®E5071C network analyzer by placing it within the laboratory environment. The S parameters measured by the network analyzer are read in via GPIB to the data acquisition computer.

In addition to the microwave measurement system, there are the pressure and temperature measurement systems. Both systems make use of an extended USB bus which allows the data acquisition computer to remain inside the laboratory. The temperature measurement system is composed of an Omega®HH506RA temperature

reader connected to two type T thermocouples (one connected inside the pressure vessel and one on the pipes for ambient temperature). The temperature reader is connected to an RS-232/USB converter which is then connected to the USB bus within the EZEE shed. The Omega®DPG7000 pressure gauges are read via two USB webcams connected to the USB bus. Finally the voltage from the high pressure transducer is read in via a shielded twisted pair back into the laboratory where the voltage is read in by an HP 34401A multimeter. The data acquisition computer reads in the voltage from the multimeter via GPIB. For calibration purposes in the initial setup, a Davis®Weather Station II, with a barometer placed within the EZEE®shed, and connected to the USB bus via an RS232/USB converter was used to measure barometric pressure to a precision of ± 1.7 mbar. However, a strong storm on August 1, 2008 resulted in some damage to the EZEE®shed, along with the functionality of the Davis®Weather Station II. A Young®61202L barometric pressure sensor was purchased to replace the Davis®Weather Station II. To prevent further damage, and keep the sensor operating under conditions which maximize its precision (± 0.3 mbar at 20 °C), the sensor is placed inside the laboratory and connected to a computer via RS232 .

As time went on, our knowledge of available sensors accumulated. We discovered that an affordable line of pressure gauges which measured absolute pressure (rather than pressure relative to ambient), with the same precision as the Omega®DPG7000 series were available. The GE Sensing®/Druck®DPI-104 gauge has a 0.05% of full scale precision, has the option to be powered externally, and has an RS-232 interface for data acquisition. The DPG7000 series gauges required correction for local atmospheric pressure, replacing AAA batteries on a regular basis, and only display pressure (the only data acquisition interface is the experimenter). While the improvements over the DPG7000 series gauges may appear to be mostly a matter of convenience, the switch from relative to absolute pressure eliminates any uncertainty or error when

correcting the relative measurements to obtain absolute pressure.

3.4 Experimental Determination of System Volume

A critical parameter for these experiments is the volume occupied by the test gas. In previous works using the Georgia Tech microwave measurement system constituents were always treated as ideal gases (e.g. *Hanley et al.*, 2009; *Mohammed and Steffes*, 2003; *Hoffman and Steffes*, 2001; *Joiner and Steffes*, 1991a). Unfortunately, the ideal gas law breaks down under high pressure, especially for gases such as H_2 and water vapor. To further add to this complexity mixtures have non-ideal interactions which vary as a function of their mole fraction, especially the components H_2 and water vapor (*Seward et al.*, 2000; *Rabinovich*, 1995; *Seward and Franck*, 1981). This renders the use of partial pressures alone to determine concentration useless. The volume occupied by the gas mixture under test in the pressure vessel must be determined to the highest precision possible such that the initial amount of water vapor added to the system can be determined. One may think that this should be a straightforward and simple task, a number of experiments have proven otherwise.

A Teledyne-Hastings flowmeter with a flow "totalizer" function was purchased in part to allow for a simple determination of the system volume. Several tests were conducted at approximately 375, and 450 °K. With each test the system was initially evacuated using a vacuum pump, and a small amount of hydrogen was added to the system (each test approximately up to 1 bar of pressure). A low pressure of hydrogen was used such that the ideal gas law would hold. During the tests, the operator needed to be extremely careful not to exceed the maximum flowrate of 10 Standard Liters per Minute (SLM). The "totalized" flow from the flowmeter outputs in Standard Liters (SL), which is converted to moles of H_2

$$n_{H_2} = \frac{1}{M_{H_2}} \frac{V_{H_2} P_{STP}}{R_{H_2} T_{STP}}, \tag{3.48}$$

Table 3.2: Instruments used and associated precision.

Instrument	Range (°C)	Measurement Parameter	Precision (3σ)
Omega®DPG7000*	-18–65	Pressure (Vacuum–15 psig)	±0.05 % FS
Omega®DPG7000*	-18–65	Pressure (Ambient–300 psig)	±0.05 % FS
Omega®PX1009L0-1.5KAV	-18.3–343.3	Pressure (0–1500 psia)	±0.06 % FS
Omega®HH506RA	-20–60	Temperature (-200–400°C)	±(0.05% rdg + 0.3°C)
Omega®PR-11-2-100-1/8-9-E	-50–450	Temperature (-50-450°C)	±(0.15 + 0.002 rdg)°C
Omega®DP41B	0–50	Temperature (-200–900°C)	± 0.2°C
Type T Thermocouple	-200–400	Temperature (-200–400°C)	Greater of ± 1.0° C or 0.75 % rdg
Agilent®E5071C	∼20	S parameters	See Discussion
HP®34401A multimeter	∼20	Voltage (output from Tranducer)	±(0.0050% rdg + 0.0035% range)
Davis®Weather Station II **	-20–60	Barometric Pressure (mbars)	±1.7 mbar @ 20°C
Young®61202L	∼20	Barometric Pressure (mbars)	±0.3 mbar @ 20°C
JLC®EE33-MFTI	-40-180	Humidity (RH%)	±(1.5%+ 0.015*RH)
JLC®EE33-MFTI	-40-180	Temperature (°C)	±0.3–0.5°C
GE sensing®/Druck®DPI-104	-10–50	Pressure (0–30 psia)	±0.05 % FS
GE sensing®/Druck®DPI-104	-10–50	Pressure (0–300 psia)	±0.05 % FS
Teledyne-Hastings®HFM-I-401	-20–70	Flowrate (0-10 slm), operates up to 1500psi	±(0.2% FS +0.5% rdg)

* Replaced in favor of DPI-104.

** Replaced with Young®61202L.

where n_{H_2} is the number of moles, M_{H_2} is the molar mass of hydrogen (2.01594 $\frac{\text{grams}}{\text{mol}}$), V_{H_2} is the number of Standard Liters measured by the flowmeter, P_{STP} is the pressure under standard conditions (1.01325 bars), R_{H_2} is the specific gas constant for Hydrogen (0.041243648124 $\frac{\text{L bar}}{\text{gram K}}$), and T_{STP} is the temperature under standard conditions (273.15°K). The total volume of the system can then be found via the ideal gas law:

$$V = \frac{n_{H_2} RT}{P}, \tag{3.49}$$

Only two reliable experiments to determine the pressure vessel volume were conducted with the flowmeter: one experiment with a pressure of 1.1138 bars at a temperature of 373.55°K, and another with a pressure of 1.6801 bars at 445.03°K. The volume found using Equation 3.49 for the 373.55°K experiment was 32.71 Liters, and at 445.03 the volume was found to be 32.91 Liters. The stated accuracy of the flowmeter is 0.2% of full scale+0.5% of the flow reading. While there is no stated accuracy of the "totalizer" function of the flowmeter, we estimate this accuracy to be at the 1% level. At first glance this would seem to be a sufficient measure of volume, however, the ability to measure "totalized" flow has some challenges. The flowmeter's totalizer function has a tendency to over state the flow rate below 0.2 SLM. This effect is clearly visible in viewing Figures 3.7 and 3.8 where the totalized flow continues to increase more than what one would expect given the relatively small pressure increase. For this reason in each experiment, the totalized flow was taken to be the value before the flow dropped below the 0.2 SLM threshold.

The relatively large uncertainty in the volume estimate using this method (both the accuracy of the flowmeter, and the need for a 0.2 SLM cutoff), was a motivation to employ a second method to determine the pressure vessel's volume. Other laboratory studies which require a precise measure of system volume often employ a water vaporization technique (e.g., *Seward and Franck*, 1981). This method involves injecting a known mass, or volume of pure liquid water into the system, and heating the system to the temperature at which tests are typically performed. The pressure

is then measured and compared with either a steam table, or a standard equation of state. In this test, the water reservoir depicted in Figure 3.3 was replaced by a small section of 3/8" pipe. A vacuum was drawn in the system to ensure no ambient air was present during the test. The small section of 3/8" pipe was then filled with distilled water, and a valve behind the pipe was slowly turned until the water level in the 3/8" section of pipe dropped. The section of pipe was then re-filled with distilled water using a 100 mL graduated cylinder , and the amount of liquid added to the system was recorded. This process was repeated until 12 mL of distilled water was added. Using this method we estimate the error in measured liquid volume to be ± 0.5 mL. The oven was then turned on, and the temperature of the system was brought to 376.52°K. The pressure of the system was measured using a small buffer of Argon (0.9943 bars), once the valve to the pressure vessel was opened the pressure measured 0.6379 bars. Using the equation of state given by *Wagner and Pruß* (2002), the volume occupied by the water vapor comes to 32.326 Liters. With the largest uncertainty being that of the liquid water measurement (± 0.5 mL) the range of likely values associated with this measurement is 30.979 to 33.673 Liters. While this error is slightly larger than the stated accuracy of the flowmeter, our confidence in this method, and given that previous studies *Seward and Franck* (1981) prefer the water vaporization technique outweighs the statistical error of the instrumentation. It should also be pointed out the result using the water vapor vaporization technique falls within the error bars of the volume measurement using the flow meter technique.

System availability limited the number of volume experiments which could be conducted. Ideally multiple measurements of volume at each measurement temperature would be conducted, and a more statistical error estimate could be derived. Instead the one volume system measurement taken using the water vaporization technique is extrapolated for higher temperatures. A second effect which can only be modeled, is the volume increase of the pressure vessel due to the elasticity of the metal. This

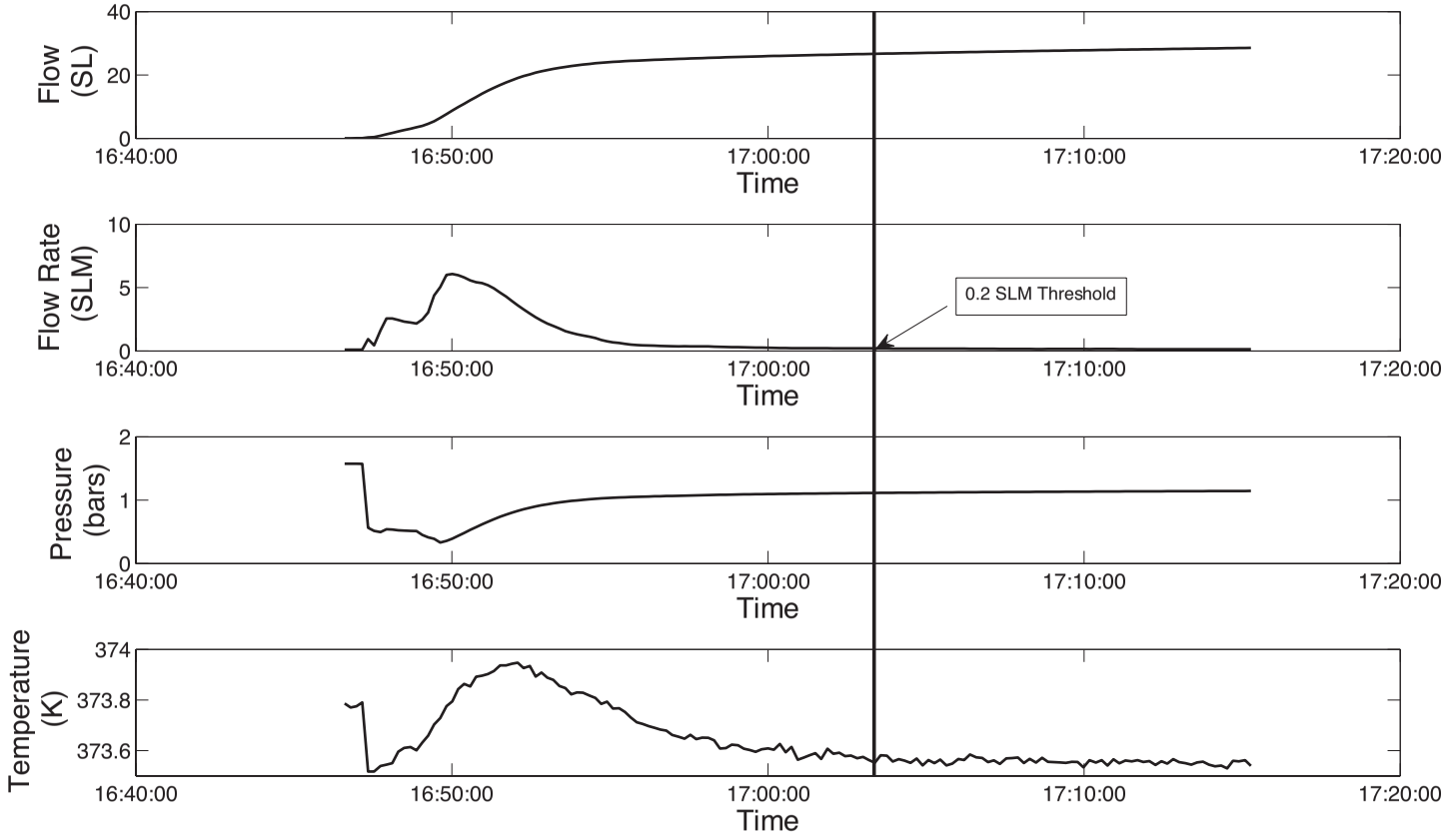

Figure 3.7: Data from the 373.55°K/1.1138 bar volume experiment.

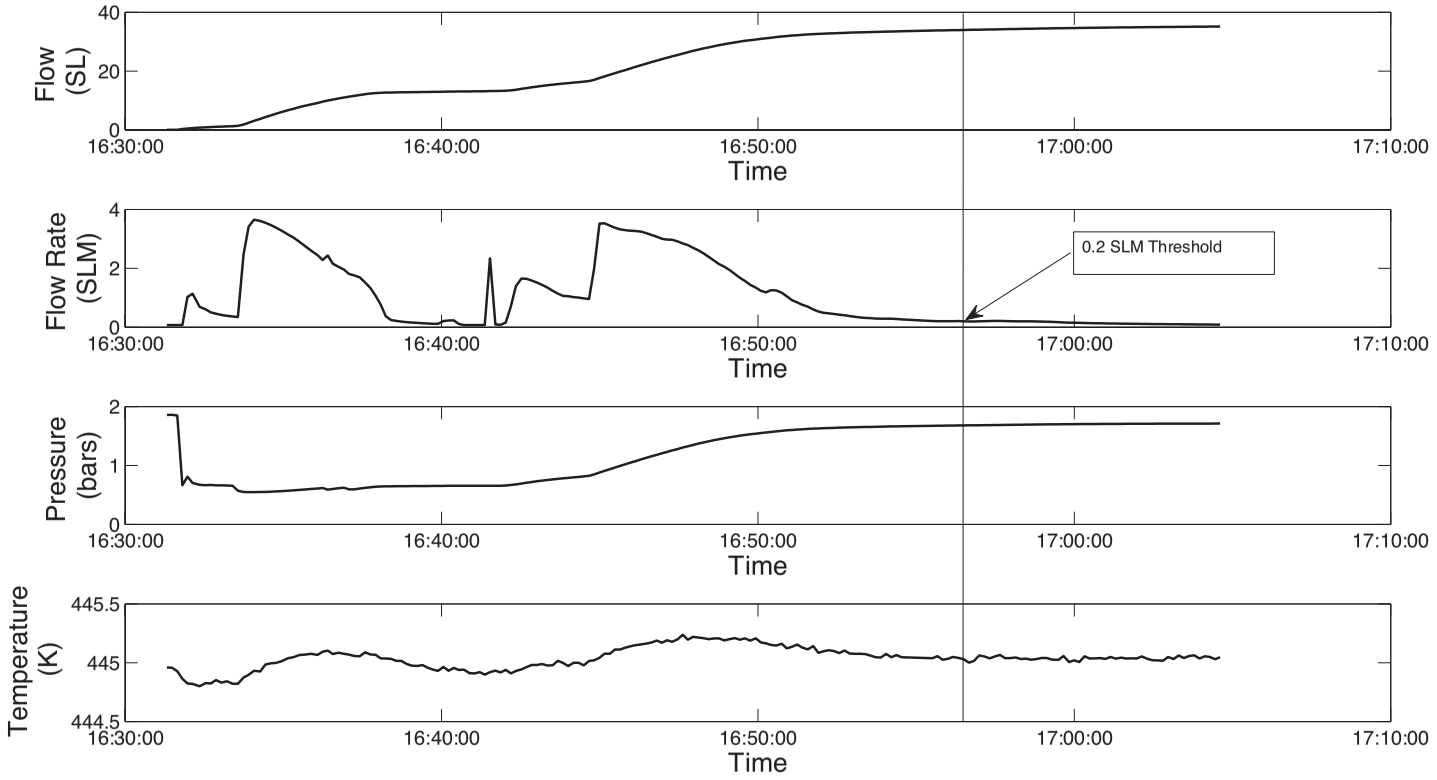

Figure 3.8: Data from the 445.03°K/1.6801 bar volume experiment.

Table 3.3: Values for the Young's modulus of carbon steel at various temperatures.

Temperature (°F)	Young's Modulus (10^6psi)
-100	30.3
70	29.4
200	28.8
300	28.3
400	27.9
500	27.3
600	26.5

can be achieved using the material properties of the pressure vessel combined with elasticity theory

$$V = V_o(1 + \alpha(T - T_o) + \beta(P - P_o)), \tag{3.50}$$

where V_o is the volume of the pressure vessel under reference conditions, T_o is the reference temperature in kelvins, P_o is the reference pressure in bars, T is the test temperature in Kelvins, P is the test pressure in bars, α is the volumetric thermal expansion coefficient of carbon steel (3.672×10^{-5}), β is the pressure expansion coefficient of a thick walled cylinder (*Zander and Thomas*, 1979). The pressure expansion coefficient for a thick walled cylinder ignoring end effects can be computed using

$$\beta = \frac{1}{E}\frac{3(1-2\nu) + 2(1+\nu)k^2}{k^2 - 1}, \tag{3.51}$$

where E is Young's modulus in bars, ν is the Poisson's ratio (0.303 for mild carbon steel), and k is the ratio of the inside to outside diameter of the pressure vessel $\left(\frac{14}{12.125}\right)$ (*Kell and Whalley*, 1965). The Young's modulus for mild carbon steel has a slight temperature dependence. Values from Table 3.3 are converted to units of bars, and Kelvin. The value for E is found by linearly interpolating the scaled values from Table 3.3 using test temperature T (*ASME*, 2007).

One last consideration made to correct the volume as a function of temperature is the the decrease in gas volume resulting from thermal expansion of the the cavity resonator. Exact dimensions of the exterior of the cavity resonator are unknown.

The cavity is an imperfect cylinder, and is bored off center at a slight pitch. This results in cavity walls with varying thickness from about 1/4" to 1/8". The length of the cylindrical part of the resonator is 10", with the exterior diameter being 10.4" and the interior diameter is approximately 10". The end plates of the resonator are 11.25" in diameter, and 0.375" thick. Combining all components the stainless steel of the resonator occupies approximately 2.27 Liters of volume at room temperature. The volume of the resonator must be expressed in terms of the reference temperature (376.52085°K), in place of room temperature (293.15°K). Using a volumetric thermal expansion coefficient for stainless steel (5.22×10^{-5}), the approximate volume of the resonator at the reference temperature is 2.270118494 Liters. Equation 3.50 is modified to include the effects from thermal expansion from the resonator via

$$V = V_o(1 + \alpha(T - T_o) + \beta(P - P_o)) - \alpha_r(T - T_o)V_r, \tag{3.52}$$

where α_r is the volumetric thermal expansion coefficient for stainless steel (5.22×10^{-5}), and V_r is the volume of the resonator at the reference temperature (2.270118494 Liters).

The validity of the thick walled cylinder approximation for the pressure vessel was tested via finite element analysis performed using COMSOL®. The simulation used an approximate geometry from the schematic drawings provided by Hays Fabrication and Welding®, and assumed that elements were constructed out of a uniform piece of carbon steel. The simulation uses symmetry and only uses 1/4 section of the pressure vessel as shown in Figure 3.9. Results showing the change in volume due to thermal loading along with a 100 bar loading are shown in Figure 3.10. As a comparison, the effects using an equivalent thick walled cylinder approximation with a volumetric thermal expansion coefficient are also shown. It is clear that the thick walled cylinder approximation produces a larger change in volume than indicated by the COMSOL®results. A second COMSOL®analysis was preformed considering only thermal loading of the pressure vessel. These results along with results performing an analysis using a volumetric thermal expansion coefficient are shown in Figure

3.11. Again, it is clear that the COMSOL®analysis produces results which indicate a change in volume which is slightly smaller than the analysis in Equation 3.50 would indicate. It is also clear that thermal loading effects are far more important than pressure loading effects in terms of changing the volume of the pressure vessel. These results from COMSOL®are deemed sufficient in verifying our assumption of a thick walled cylinder.

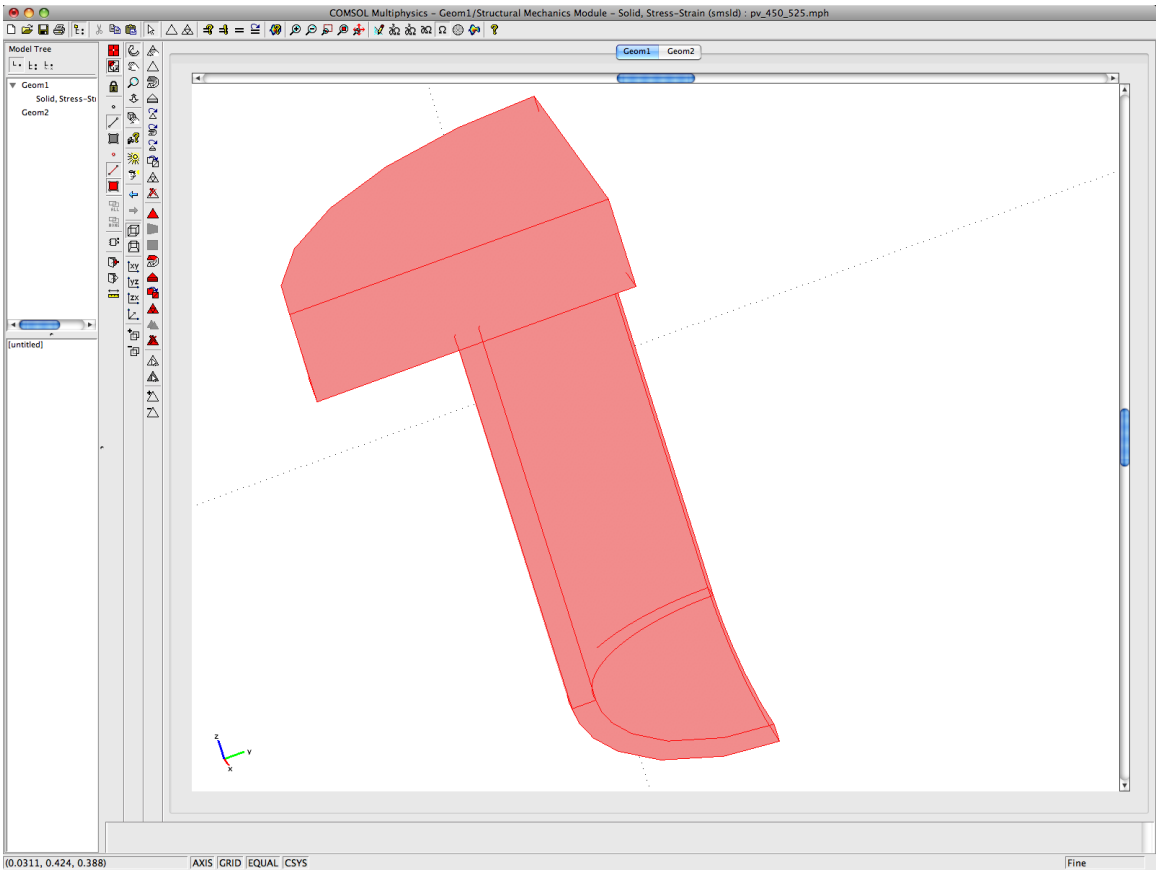

Figure 3.9: Screen shot from COMSOL®simulation showing the geometry used in the Pressure vessel analysis.

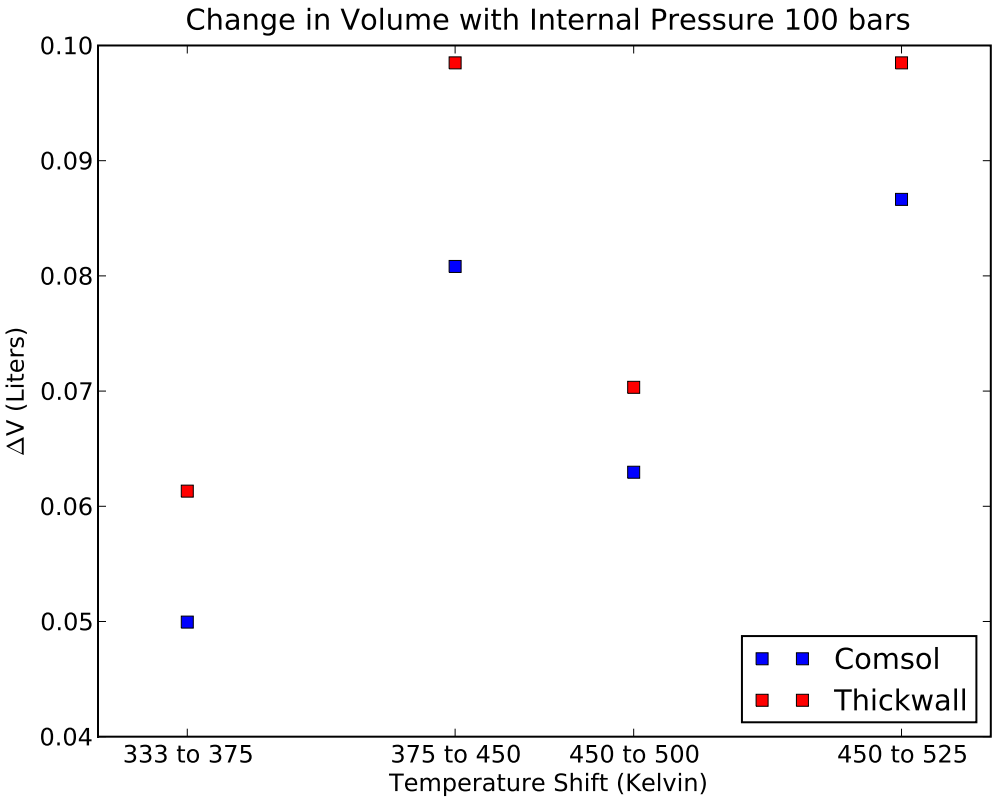

Figure 3.10: Change in volume due to thermal loading and pressure loading.

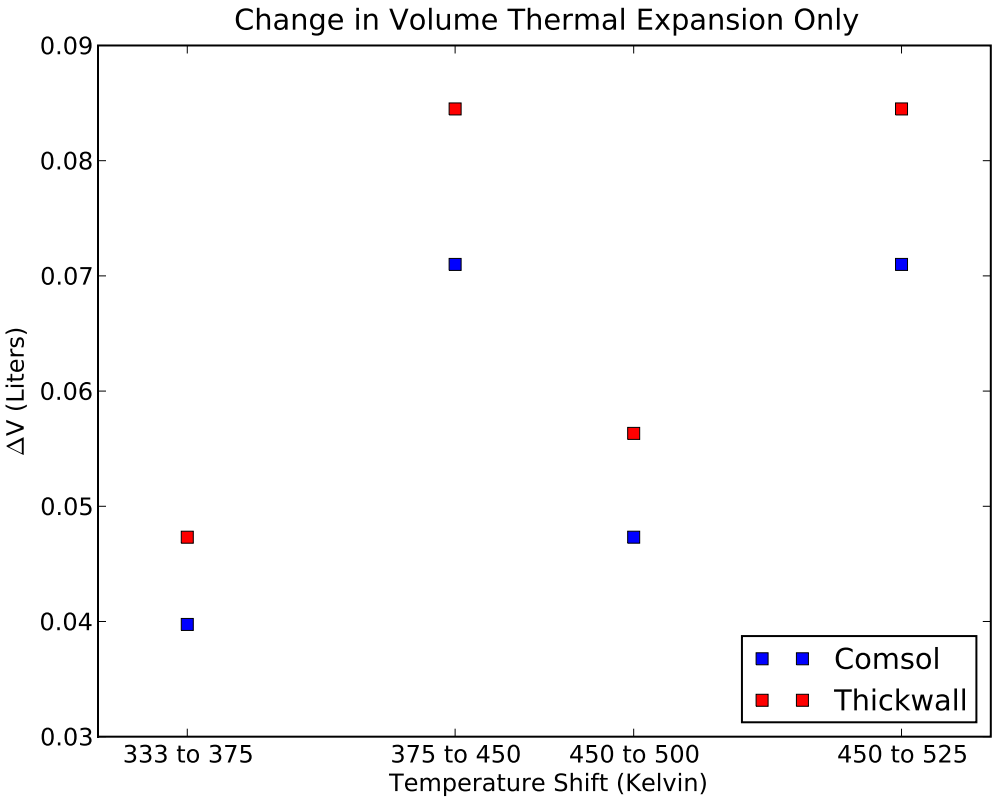

Figure 3.11: Change in volume due to thermal loading alone.

CHAPTER IV

COMPRESSIBILITY OF PURE FLUIDS AND MIXTURES

Many studies of the outer planets have assumed all components in the gaseous state can be treated using the ideal gas law. Extensive thermodynamic measurements conducted over the years have allowed for well-constrained equations of state for pure gases. The current standard equation of state for H_2 indicates that at pressures of 100 bars the deviation from the ideal gas assumption approaches 6 %. If one considers the measurements of *Seward et al.* (2000) and *Seward and Franck* (1981) containing mixtures of H_2 and H_2O, and observes that such mixtures exhibit large excess volume, one should conclude that the ideal gas law is rendered useless in our experiments, and perhaps even for the Jovian atmosphere depending upon the mole fraction of H_2O present. Measurements conducted under deep Jovian conditions must account for the compressibility of such mixtures. In the conducted experiments, the vapor pressure and associated density of pure water can be derived from a well known equation of state. Without an accurate equation of state of the H_2O-H_2-He mixture, the estimates of mole fraction of helium and hydrogen in our experiments would be inaccurate, even if one accurately measures the pressure after hydrogen and helium are added. This is due to two complex effects which are neglected while assuming a gas (or mixture of gases) are ideal: the volume of molecules individual moleucules, and forces between molecules are non-zero. Fortunately, there are measurements and physically based fitting procedures, which can be used to accurately account for these effects, and are the focus of this chapter.

4.1 The Basic Equation of State: Relationship between Pressure, Temperature and Density

The most simple equation of state is that of the ideal gas law, which is written as

$$PV = nRT, \tag{4.1}$$

where P is the pressure, V is the volume, n is the molar density, R is the specific gas constant, and T is the absolute temperature. It may also be written as,

$$P = \rho RT, \tag{4.2}$$

where ρ is the density of the gas. The ideal gas law holds under two conditions. The first is that each molecule occupies volume which may be considered infinitesimal. The second is that the distance between each molecule is sufficiently large as to eliminate the attraction or repulsion between molecules (commonly known as van der Waals forces). A first order approximation to account for these forces can be written in the form of the van der Waals equation of state where,

$$\left(P + \frac{n^2 a}{V^2}\right)(V - nb) = nRT, \tag{4.3}$$

where a is a measure of the attraction between molecules, and b is the volume occupied by each molecule. While the above equation provides a simple intuitive way to account for real gas behavior, it is rarely accurate for real gases. Over the years a number of expressions have been developed to account for non-ideal gas behavior. Many equations start with a simple assumption that a gas has a compressibility factor given as

$$Z = \frac{PV}{nRT} = \frac{P}{\rho RT} \tag{4.4}$$

or,

$$Z = 1 + Z_{residual}(\delta, \tau), \tag{4.5}$$

where $Z_{residual}$ is a function of normalized temperature τ, and normalized density δ. The values of τ and δ are usually defined by

$$\tau = \frac{T_c}{T} \tag{4.6}$$

and

$$\delta = \frac{\rho}{\rho_c}, \tag{4.7}$$

where T_c and ρ_c are the values for temperature and density at the critical point of a particular gas/fluid.

By definition, a gas with a compressibility of unity can be considered ideal. Equations which explicitly derive pressure for a given density and temperature are often called pressure explicit equations of state. The most accurate among these equations is the so-called modified Benedict Webb Ruben equation or mBWR (*Span*, 2000). The compressibility can be written in a compact form (as and equation of state)

$$Z(\tau,\delta) = 1 + \sum_{i=1}^{N_{poly}} n_i \tau^{t_i} \delta^{d_i} + \sum_{i=N_{poly}+1}^{N_{poly}+N_{exp}} n_i \tau_i^{t_i} \delta^{d_i} \exp\left(-\delta^2\right). \tag{4.8}$$

However, older studies which utilize the mBWR equation often write this expression in a less compact form

$$\begin{aligned} P &= \rho RT + \rho^2(n_1 T + n_2 T^{1/2} + n_3 + n_4/T + n_5/T^2) \\ &\quad + \rho^3(n_6 T + n_7 + n_8/T + n_9/T^2) + \rho^4(n_{10} T + n_1 1 + n_{12}/T) \\ &\quad + \rho^5 n_{13} + \rho^6(n_{14}/T + n_{15}/T^2) + \rho^7 n_{16}/T + \rho^8(n_{17}/T + n_{18}/T^2) + \rho^9 n_{19}/T^2 \\ &\quad + \rho^3(n_{20}/T^2 + n_{21}/T^3)\exp(-\gamma\rho^2) + \rho^5(n_{22}/T^2 + n_{23}/T^4)\exp(-\gamma\rho^2) \\ &\quad + \rho^7(n_{24}/T^2 + n_{25}/T^3)\exp(-\gamma\rho^2) + \rho^9(n_{26}/T^2 + n_{27}/T^4)\exp(-\gamma\rho^2) \\ &\quad + \rho^{11}(n_{28}/T^2 + n_{29}/T^3)\exp(-\gamma\rho^2) + \rho^{13}(n_{30}/T^2 + n_{31}/T^3 + n_{32}/T^4)\exp(-\gamma\rho^2), \end{aligned} \tag{4.9}$$

where $\gamma = 1/\rho_c^2$. The equation of state for Helium (He^4) is of this form, and the values for n_i are shown in Table 4.1.

Table 4.1: mBWR coefficients for Helium (*McCarty*, 1990).

Order (i)	n_i
1	$0.4558980227431\times10^{-4}$
2	$0.1260692007853\times10^{-2}$
3	$-0.7139657549318\times10^{-2}$
4	$0.9728903861441\times10^{-2}$
5	$-0.1589302471562\times10^{-1}$
6	$0.1454229259623\times10^{-5}$
7	$-0.4708238429298\times10^{-4}$
8	$0.1132915232587\times10^{-2}$
9	$0.2410763742104\times10^{-2}$
10	$-0.5093547838381\times10^{-8}$
11	$0.2699726927900\times10^{-5}$
12	$-0.3954146691114\times10^{-4}$
13	$0.1551961438127\times10^{-8}$
14	$0.1050712335785\times10^{-7}$
15	$-0.5501158366750\times10^{-7}$
16	$-0.1037673478521\times10^{-9}$
17	$0.6446881346448\times10^{-12}$
18	$0.3298960057071\times10^{-10}$
19	$-0.3555585738784\times10^{-12}$
20	$-0.6885401367690\times10^{-2}$
21	$0.9166109232806\times10^{-2}$
22	$-0.6544314242937\times10^{-5}$
23	$-0.3315398880031\times10^{-4}$
24	$-0.2067693644676\times10^{-7}$
25	$0.3850153114958\times10^{-7}$
26	$-0.1399040626999\times10^{-10}$
27	$-0.1888462892389\times10^{-11}$
28	$-0.4595138561035\times10^{-14}$
29	$0.6872567403738\times10^{-14}$
30	$-0.6097223119177\times10^{-18}$
31	$-0.7636186157005\times10^{-17}$
32	$0.3848665703556\times10^{-17}$

The Helmholtz energy form of the equation of state has become a more popular form for equations of state (*Span*, 2000). While equations of state in the pressure explicit form are more attractive in terms of being intuitive, they can become cumbersome when trying to fit measurements of various thermodynamic parameters (the mBWR equation being a prime example). The Helmholtz energy of a substance is defined as

$$a(T,\rho) = a^o(T,\rho) + a^r(T,\rho), \tag{4.10}$$

where a is the Helmholtz energy, a^o is the ideal part of the Helmholtz energy, and a^r is the residual part of the Helmholtz energy. The ideal part of the Helmholtz energy is found via

$$a^o(T,\rho) = u^o(T) - Ts^o(T,\rho), \tag{4.11}$$

where u^o represents the ideal part of the specific internal energy, and s^o is the ideal part of the specific entropy. Equations of state using Helmholtz energy typically represent the equation of state in terms of the normalized (or reduced) Helmholtz energy expressed as (*Span*, 2000)

$$\alpha = \frac{a^o}{RT} + \frac{a^r}{RT} = \alpha^o + \alpha^r. \tag{4.12}$$

The ideal part of the Normalized Helmholtz Energy (NHE) can be found by two methods depending upon the reference. Some studies give the ideal part explicitly in the form

$$\alpha_o = \ln(\delta) + n_1^o + n_2^o\tau + n_3^o \ln(\tau) + \sum_{i=4}^{N_{terms}} n_i^o \ln\left(1 - \exp(-\gamma_i^o\tau)\right) \tag{4.13}$$

The water equation of state (*Wagner and Pruß*, 2002) uses this form, and the coefficients associated with it are given in Table 4.2.

Other studies (*McCarty*, 1990; *Setzmann and Wagner*, 1991; *Leachman*, 2007) give an equation for c_p^o/R, which can be integrated to find α^o. The equation for c_p^o/R

Table 4.2: Terms and Coefficients for the ideal part of the Normalized Helmholtz Energy of Water (H_2O (*Wagner and Pruß*, 2002).

Order (i)	n_i^o	γ_i^o
1	-8.32044648201	
2	6.6832105268	
3	3.00632	
4	0.012436	1.28728967
5	0.97315	3.53734222
6	1.27950	7.74073708
7	0.96956	9.24437796
8	0.24873	27.5075105

is typically given in the form

$$\frac{c_p^o}{R} = \sum_{i=1}^{N_{power}} n_i^o T^{t_i} + \sum_{i=N_{power}+1}^{N_{power}+N_{exp}} \nu_i \frac{{u_i}^2}{T} \frac{\exp(u_i/T)}{(\exp(u_i/T)-1)^2} \tag{4.14}$$

The expression for α_o is found using (*Span*, 2000)

$$\alpha^o = \frac{h_o \tau}{RT_c} - \frac{s_o}{R} - 1 + \ln\left(\frac{\delta/\delta_o}{\tau/\tau_o}\right) - \frac{\tau}{R}\int_{\tau_o}^{\tau} \frac{c_p^o}{\tau^2} d\tau + \frac{1}{R}\int_{\tau_o}^{\tau} \frac{c_p^o}{\tau} d\tau \tag{4.15}$$

where h_o and s_o are the enthalpy and entropy at a reference state. This reference state taken at the normal boiling point of the fluid T_o and ρ_o, or their equivalent normalized (reduced) parameters τ_o, and δ_o, respectively. These values have been computed using NIST's REFPROP (*Lemmon et al.*, 2007). The values for each fluid of interest are given in Table 4.5. For gases/fluids which have equations in this form, the expression for the ideal part of the Helmholtz energy (e.g., hydrogen, helium,

methane) simplifies to

$$\begin{aligned}\alpha^o &= \frac{-s_o}{R} - 1 - \ln(\frac{\rho_o}{\rho_c}\frac{To}{Tc}) + n_1^o + n_1^o \ln(T_o) - n_1^o \ln(T_c) \\ &\quad - \ln(\tau) + \ln(\delta) + n_1^o \ln(\tau) \\ &\quad + \tau\left(\frac{h_o}{RT_c} - n_1^o \frac{T_o}{T_c}\right) \\ &\quad + \sum_{i=1}^{N_{exp}} \nu_i \frac{u_i}{T_o} \frac{\exp(\frac{u_i}{T_o})}{(\exp(\frac{u_i}{T_o}) - 1)} - \nu_i \ln\left(\exp\left(\frac{u_i}{T_o}\right) - 1\right) \\ &\quad + \tau \sum_{i=1}^{N_{exp}} \frac{-\nu_i \frac{u_i}{Tc}}{(\exp(\frac{u_i}{T_o}) - 1)} \end{aligned} \tag{4.16}$$

For the case of helium, this simplifies further with no exponential terms ($N_{exp} = 0$), owing to the fact it is a mono-atomic gas with a $\frac{c_p^o}{R}$ of $\frac{5}{2}$. The coefficients necessary to compute α^o for hydrogen and methane are given in Tables 4.3 and Table 4.4, respectively.

Table 4.3: Terms and Coefficients for the ideal part of the Normalized Helmholtz Energy of H_2 (*Leachman*, 2007).

Order (i)	n_i^o	t_i	ν_i	ui
1	2.5	0.0		
2			1.616	531
3			-0.4117	751
4			-0.792	1989
5			0.758	2484
6			1.217	6859

For the residual part of the NHE can be found by two methods depending upon the referenced equation of state. Some studies use an explicit Helmholtz formalism with the form (i.e., hydrogen, water, methane)

$$\begin{aligned}\alpha^r &= \sum_{i=1}^{N_{poly}} n_i \delta^{d_i} \tau^{t_i} + \sum_{j=1}^{N_{exp}} n_j \delta^{d_j} \tau^{t_j} \exp(-\delta^{c_j}) \\ &\quad + \sum_{k=1}^{N_{gauss}} n_k \delta^{d_k} \tau^{t_k} \exp(-\alpha_k'(\delta - \epsilon_k)^2 - \beta_k(\tau - \gamma_k)^2) + \sum_{l=1}^{N_{crit}} n_l \Delta^{b_l} \delta\psi \end{aligned} \tag{4.17}$$

Table 4.4: Terms and Coefficients for the ideal part of the Normalized Helmholtz Energy of CH_4 (*Setzmann and Wagner*, 1991).

Order (i)	n_i^o	t_i	ν_i	ui
1	4.0016	0.0		
2			0.84490000×10^{-2}	648.0
3			4.6942000	1957.0
4			3.4865000	3895.0
5			1.6572000	5705.0
6			1.4115000	15080.0

with critical parameters

$$\Delta = \theta^2 + B_l \left((\delta - 1)^2\right)^{a_l} \tag{4.18}$$

$$\theta = (1 - \tau) + A_l \left((\delta - 1)^2\right)^{\frac{1}{2\beta_l}} \tag{4.19}$$

$$\psi = \exp(-C_l(\delta - 1)^2 - D_l(\tau - 1)^2), \tag{4.20}$$

where N_{poly} is the number of polynomial terms, N_{exp} is the number of exponential terms, N_{gauss} is the number of gaussian terms, N_{crit} is the number of critical terms. The terms necessary to compute the residual Helmholtz energy for normal Hydrogen are provided in Table 4.6 (*Leachman*, 2007). The Helmholtz formalism for water is perhaps the most complicated using all terms in Equation 4.17. Tables with the necessary coefficients to compute the residual Helmholtz energy of water are given in Tables 4.7, 4.8, 4.9, and 4.10. The coefficients for methane are not important for our laboratory measurements, however, it is an important constituent in the Jovian atmosphere. Table 4.11 gives the coefficients necessary to compute the residual Helmholtz energy of methane.

In this work only helium is the only pure substance which has an equation of state with a form other than the explicit Helmholtz energy form. By utilizing the

expression for the mBWR given in *Younglove and McLinden* (1994)

$$\begin{aligned}\alpha_r &= \frac{1}{RT}\sum_{i=1}^{19}\frac{n'_i}{i}\rho^i \\ &\quad -\frac{1}{2RT}(n'_{20}+n'_{21})\rho_c^2(\exp(-\delta^2)-1) \\ &\quad -\frac{1}{2RT}(n'_{22}+n'_{23})\rho_c^4(\exp(-\delta^2)(\delta^2+1)-1) \\ &\quad -\frac{1}{2RT}(n'_{24}+n'_{25})\rho_c^6(\exp(-\delta^2)(\delta^4+2\delta^2+2)-2) \\ &\quad -\frac{1}{2RT}(n'_{26}+n'_{27})\rho_c^8(\exp(-\delta^2)(\delta^6+3\delta^4+6\delta^2+6)-6) \\ &\quad -\frac{1}{2RT}(n'_{28}+n'_{29})\rho_c^{10}(\exp(-\delta^2)(\delta^8+4\delta^6+12\delta^4+24\delta^2+24)-24) \\ &\quad -\frac{1}{2RT}(n'_{30}+n'_{31}+n'_{32})\rho_c^{12}(\exp(-\delta^2)(\delta^{10}+5\delta^8+20\delta^6+60\delta^4+120\delta^2+120) \\ &\quad -120), \end{aligned} \tag{4.21}$$

where n'_i represents each term after it has been multiplied by the appropriate power of T in the pressure explicit form of the mBWR (which can be transformed into a δ). By carefully multiplying out each term, and keeping track of powers of δ, and τ, the above can be used to adapt the mBWR EOS to that of a standard Helmholtz energy equation of state with polynomial, and exponential terms. The resulting expression involves 80 terms derived from the original 32 coefficient mBWR. While many of those terms include density terms with a power of zero, this shows that while still physical, the mBWR was developed as a fitting tool, and it is not the most efficient or compact form possible. It is quite likely that a new Helmholtz expression could be derived with fewer terms, yet fit the data from *McCarty* (1990). Work is currently underway at NIST to develop such an expression (*Lemmon and Arp*, 2009).

Table 4.5: Reference values for enthalpy and entropy for pure fluids of interest (*Lemmon et al.*, 2007).

Fluid	T_o (°K)	ρ_o (mol/L)	h_o (J/mol)	s_o (J/mol/K)
H_2 (normal)	273.15	0.00044031564828974387	7206.9069892047	143.4846187346
He	4.230359714841141	31.163394763964778	108.78863197310453	3.6929233790579463
CH_4	111.66720547358069	26.326811491312679	8295.6883966242294	28.384819963016852

Table 4.6: Terms and Coefficients for the residual part of the Normalized Helmholtz Energy of H_2 (*Leachman*, 2007).

Order (i,j,k)	$n_{i,j,k}$	$t_{i,j,k}$	$d_{i,j,k}$	$c_{i,j,k}$	$\alpha'_{i,j,k}$	$\beta_{i,j,k}$	$\gamma_{i,j,k}$	$\epsilon_{i,j,k}$
Polynomial								
(i)								
1	-6.93643	0.6844	1					
2	0.01	1	4					
3	2.1101	0.989	1					
4	4.52059	0.489	1					
5	0.732564	0.803	2					
6	-1.34086	1.1444	2					
7	0.130985	1.409	3					
Exponential								
(j)								
1	-0.777414	1.754	1	1				
2	0.351944	1.311	3	1				
Gaussian								
(k)								
1	-0.0211716	4.187	2		1.685	0.171	0.7164	1.506
2	0.0226312	5.646	1		0.489	0.2245	1.3444	0.156
3	0.032187	0.791	3		0.103	0.1304	1.4517	1.736
4	-0.0231752	7.249	1		2.506	0.2785	0.7204	0.67
5	0.0557346	2.986	1		1.607	0.3967	1.5445	1.6620

Table 4.7: Terms and Coefficients for the residual part of the Normalized Helmholtz Energy of H_2O (polynomial terms) (*Wagner and Pruß*, 2002).

Order (i)	n_i	t_i	d_i
1	$0.12533547935523\times10^{-1}$	-0.5	1.0
2	$0.78957634722828\times10^{1}$	0.875	1.0
3	$-0.87803203303561\times10^{1}$	1.0	1.0
4	0.31802509345418	0.5	2.0
5	-0.26145533859358	0.75	2.0
6	$-0.78199751687981\times10^{-2}$	0.375	3.0

Table 4.8: Terms and Coefficients for the residual part of the Normalized Helmholtz Energy of H_2O (exponential terms) (*Wagner and Pruß*, 2002).

Order (j)	n_j	t_j	d_j	c_j
1	$0.88089493102134\times10^{-2}$	1.0	4.0	0.0
2	-0.66856572307965	4.0	1.0	1.0
3	0.20433810950965	6.0	1.0	1.0
4	$-0.66212605039687\times10^{-4}$	12.0	1.0	1.0
5	-0.19232721156002	1.0	2.0	1.0
6	-0.25709043003438	5.0	2.0	1.0
7	0.16074868486251	4.0	3.0	1.0
8	$-0.40092828925807\times10^{-1}$	2.0	4.0	1.0
9	$0.39343422603254\times10^{-6}$	13.0	4.0	1.0
10	$-0.75941377088144\times10^{-5}$	9.0	5.0	1.0
11	$0.56250979351888\times10^{-3}$	3.0	7.0	1.0
12	$-0.15608652257135\times10^{-4}$	4.0	9.0	1.0
13	$0.11537996422951\times10^{-8}$	11.0	10.0	1.0
14	$0.36582165144204\times10^{-6}$	4.0	11.0	1.0
15	$-0.13251180074668\times10^{-11}$	13.0	13.0	1.0
16	$-0.62639586912454\times10^{-9}$	1.0	15.0	1.0
17	-0.10793600908932	7.0	1.0	2.0
18	$0.17611491008752\times10^{-1}$	1.0	2.0	2.0
19	0.22132295167546	9.0	2.0	2.0
20	-0.40247669763528	10.0	2.0	2.0
21	0.58083399985759	10.0	3.0	2.0
22	$0.49969146990806\times10^{-2}$	3.0	4.0	2.0
23	$-0.31358700712549\times10^{-1}$	7.0	4.0	2.0
24	-0.74315929710341	10.0	4.0	2.0
25	0.47807329915480	10.0	5.0	2.0
26	$0.20527940895948\times10^{-1}$	6.0	6.0	2.0
27	-0.13636435110343	10.0	6.0	2.0
28	$0.14180634400617\times10^{-1}$	10.0	7.0	2.0
29	$0.83326504880713\times10^{-2}$	1.0	9.0	2.0
30	$-0.29052336009585\times10^{-1}$	2.0	9.0	2.0
31	$0.38615085574206\times10^{-1}$	3.0	9.0	2.0
32	$-0.20393486513704\times10^{-1}$	4.0	9.0	2.0
33	$-0.16554050063734\times10^{-2}$	8.0	9.0	2.0
34	$0.19955571979541\times10^{-2}$	6.0	10.0	2.0
35	$0.15870308324157\times10^{-3}$	9.0	10.0	2.0
36	$-0.16388568342530\times10^{-4}$	8.0	12.0	2.0
37	$0.43613615723811\times10^{-1}$	16.0	3.0	2.0
38	$0.34994005463765\times10^{-1}$	22.0	4.0	2.0
39	$-0.76788197844621\times10^{-1}$	23.0	4.0	2.0
40	$0.22446277332006\times10^{-1}$	23.0	5.0	3.0
41	$-0.62689710414685\times10^{-4}$	10.0	14.0	3.0
42	$-0.55711118565645\times10^{-9}$	50.0	3.0	3.0
43	-0.19905718354408	44.0	6.0	3.0
44	0.31777497330738	46.0	6.0	4.0
45	-0.11841182425981	50.0	6.0	6.0

Table 4.9: Terms and Coefficients for the residual part of the Normalized Helmholtz Energy of H_2O (gaussian terms) (*Wagner and Pruß*, 2002).

Order(k)	n_k	t_k	d_k	c_k	α'_k	β_k	γ_k	ϵ_k
1	$-0.31306260323435\times10^{2}$	0.0	3.0	6.0	20	150	1.21	1
2	$0.31546140237781\times10^{2}$	1.0	3.0	6.0	20	150	1.21	1
3	$-0.25213154341695\times10^{4}$	4.0	3.0	6.0	20	250	1.25	1

Table 4.10: Terms and Coefficients for the residual part of the Normalized Helmholtz Energy of H_2O (critical terms) (*Wagner and Pruß*, 2002).

Order (l)	n_l	β_l	a_l	b_l	B_l	C_l	D_l	A_l
1	-0.14874640856724	0.3	3.5	0.85	0.2	28	700	0.32
2	0.31806110878444	0.3	3.5	0.95	0.2	32	800	0.32

Table 4.11: Terms and Coefficients for the residual part of the Normalized Helmholtz Energy of Methane (*Setzmann and Wagner*, 1991).

Order (i,j,k)	$n_{i,j,k}$	$t_{i,j,k}$	$d_{i,j,k}$	$c_{i,j,k}$	$\alpha'_{i,j,k}$	$\beta_{i,j,k}$	$\gamma_{i,j,k}$	$\epsilon_{i,j,k}$
Polynomial (i)								
1	$0.43679010280\times10^{-1}$	-0.5	1.0					
2	0.67092361990	0.5	1.0					
3	$-0.17655778590\times10^{1}$	1.0	1.0					
4	0.85823302410	0.5	2.0					
5	$-0.12065130520\times10^{1}$	1.0	2.0					
6	0.51204672200	1.5	2.0					
7	$-0.40000107910\times10^{-3}$	4.5	2.0					
8	$-0.12478424230\times10^{-1}$	0.0	3.0					
9	$0.31002697010\times10^{-1}$	1.0	4.0					
10	$0.17547485220\times10^{-2}$	3.0	4.0					
11	$-0.31719216050\times10^{-5}$	1.0	8.0					
12	$-0.22403468400\times10^{-5}$	3.0	9.0					
13	$0.29470561560\times10^{-6}$	3.0	10.0					
Exponential (j)								
1	0.18304879090	0.0	1.0	1				
2	0.15118836790	1.0	1.0	1				
3	-0.42893638770	2.0	1.0	1				
4	$0.68940024460\times10^{-1}$	0.0	2.0	1				
5	$-0.14083139960\times10^{-1}$	0.0	4.0	1				
6	$-0.30630548300\times10^{-1}$	2.0	5.0	1				
7	$-0.29699067080\times10^{-1}$	2.0	6.0	1				
8	$-0.19320408310\times10^{-1}$	5.0	1.0	2				
9	-0.11057399590	5.0	2.0	2				
10	$0.99525489950\times10^{-1}$	5.0	3.0	2				
11	$0.85484378250\times10^{-2}$	2.0	4.0	2				
12	$-0.61505556620\times10^{-1}$	4.0	4.0	2				
13	$-0.42917924230\times10^{-1}$	12.0	3.0	3				
14	$-0.18132072900\times10^{-1}$	8.0	5.0	3				
15	$0.34459047600\times10^{-1}$	10.0	5.0	3				
16	$-0.23859194500\times10^{-2}$	10.0	8.0	3				
17	$-0.11590949390\times10^{-1}$	10.0	2.0	4				
18	$0.66416936020\times10^{-1}$	14.0	3.0	4				
19	$-0.23715495900\times10^{-1}$	12.0	4.0	4				
20	$-0.39616249050\times10^{-1}$	18.0	4.0	4				
21	$-0.13872920440\times10^{-1}$	22.0	4.0	4				
22	$0.33894895990\times10^{-1}$	18.0	5.0	4				
23	$-0.29273787530\times10^{-2}$	14.0	6.0	4				
Gaussian (k)								
1	$0.93247999460\times10^{-4}$	2.0	2.0	2	20.0	200	1.07	1
2	$-0.62871715180\times10^{1}$	0.0	0.0	2	40.0	250	1.11	1
3	$0.12710694670\times10^{2}$	1.0	0.0	2	40.0	250	1.11	1
4	$-0.64239534660\times10^{1}$	2.0	0.0	2	40.0	250	1.11	1

4.2 Quantities Derived from the Helmholtz Energy, and its derivatives

A wide variety of thermodynamic parameters can be derived from the fundamental Helmholtz energy. Some of these thermodynamic parameters are given in Table 4.12. Thermodynamic parameters have been measured for a variety of purposes for some gasses, and liquids, which allow one to constrain a Helmholtz formalism. While it not necessary to express an equation of state in terms of its Helmoholtz energy (i.e., the EOS for Helium is in an mBWR form), it is still necessary to either integrate the EOS as done in *Span* (2000), take a term by term reduction as done in this work, or have redundant routines to calculate a variety of thermodynamic parameters as done in NIST's REFPROP. Each individual component's EOS has been fitted using numerous thermodynamic measurements. Table 4.12 shows that each parameter has a variety of partial derivatives associated with it. These partial derivatives are not computationally intensive, however, their expressions are somewhat complex. The values of the derivatives of the ideal and residual Helmholtz energy are given in Tables 4.13, and 4.14. When an equation of state has a series of critical terms associated with it (i.e. water), additional derivatives in Table 4.13 are computed using the derivatives given in Table 4.15.

4.3 Using Helmholtz formalisms to describe mixtures of Gases and Fluids

An additional complication which must be considered at high temperatures and pressures deep within the Jovian atmosphere is the interaction between gases in a mixture. This implies that Dalton's Law of partial pressures fails to hold in addition to the breakdown of the ideal gas law. The method used follows *Kunz et al.* (2006) which starts by modifying the critical density and temperature (sometimes referred to as

Table 4.12: Themodynamic parameters expressed as functions of Helmholtz energy and partial derivatives with respect to τ and δ.

Pressure	$P(\delta,\tau) = \rho RT\left(1+\delta\frac{d\alpha^r}{d\delta}\right)$
Internal Energy	$u(\delta,\tau) = RT\tau\left(\frac{\alpha^o}{d\tau}+\frac{\alpha^r}{d\tau}\right)$
Entropy	$s(\delta,\tau) = R\tau\left(\frac{\alpha^o}{d\tau}+\frac{\alpha^r}{d\tau}\right)-\alpha^o-\alpha^r$
Enthalpy	$h(\delta,\tau) = RT\left(1+\tau\left(\frac{\alpha^o}{d\tau}+\frac{\alpha^r}{d\tau}\right)+\delta\frac{d\alpha^r}{d\delta}\right)$
Isochoric heat capacity	$c_v(\delta,\tau) = -R\tau^2\left(\frac{d^2\alpha^o}{d\tau^2}+\frac{d^2\alpha^r}{d\tau^2}\right)$
Isobaric heat capacity	$c_p(\delta,\tau) = c_v(\delta,\tau)+R\left(\frac{\left(1+\delta\frac{d\alpha^r}{d\delta}-\delta\tau\frac{dd\alpha^r}{d\tau d\delta}\right)^2}{1+2\delta\frac{d\alpha^r}{d\delta}+\delta^2\frac{d^2\alpha^r}{d\delta^2}}\right)$
Second Virial Coefficient	$B(\tau) = \frac{1}{\rho_c}\lim_{\delta\to 0}\frac{d\alpha^r}{d\delta} = \frac{1}{\rho_c}\frac{d\alpha^r}{d\delta}(\frac{1\times10^{-8}}{\rho_c},\tau)$
Third Virial Coefficient	$C(\tau) = \frac{1}{\rho_c^2}\lim_{\delta\to 0}\frac{d^2\alpha^r}{d\delta^2} = \frac{1}{\rho_c^2}\frac{d^2\alpha^r}{d\delta^2}\left(\frac{1\times10^{-8}}{\rho_c},\tau\right)$
Speed of Sound	$w(\delta,\tau) = \sqrt{RT\left(1+2\delta\frac{d\alpha^r}{d\delta}+\delta^2\frac{d^2\alpha^r}{d\delta^2}-\frac{\left(1+\delta\frac{d\alpha^r}{d\delta}-\delta\tau\frac{dd\alpha^r}{d\tau d\delta}\right)^2}{\tau^2\left(\frac{d^2\alpha^o}{d\tau^2}+\frac{d^2\alpha^r}{d\tau^2}\right)}\right)}$

Table 4.13: Partial derivatives of the ideal part of the Helmholtz Energy.

Derivative	Expression
$\frac{d\alpha^o}{d\tau} =$	$n_2^o+\frac{n_3^o}{\tau}+\sum_{i=4}^{N_{exp,o}} n_i^o\gamma_i^o\left(\left(1-\exp(-\gamma_i^o\tau)\right)^{-1}-1\right)$
$\frac{d^2\alpha^o}{d\tau^2} =$	$-\frac{n_3^o}{\tau^2}-\sum_{i=4}^{N_{exp,o}} n_i^o\left(\gamma_i^o\right)^2\exp(-\gamma_i^o\tau)\left(1-\exp(-\gamma_i^o\tau)\right)^{-2}$
$\frac{d\alpha^o}{d\tau} =$	$\frac{h_o}{RT_c}-n_1^o\frac{T_o}{T_c}+\frac{n_1^o}{\tau}-\frac{1}{\tau}+\sum_{i=1}^{N_{exp,o}}\nu_i\frac{1}{\tau}\frac{u_i}{T_c/\tau}\frac{\exp(\frac{-u_i}{T_c/\tau})}{1-\exp(\frac{-u_i}{T_c/\tau})}-\sum_{i=1}^{N_{exp,o}}\frac{1}{T_c}\frac{v_iu_i}{\exp(u_i/T_o)-1)}$
$\frac{d^2\alpha^o}{d\tau^2} =$	$\frac{1-\left(n_1^o+\sum_{i=1}^{N_{exp,o}}\frac{\left(\frac{u_i}{T}\right)^2\exp\left(-\frac{u_i}{T}\right)}{\left(1-\exp\left(\frac{-u_i}{T}\right)\right)^2}\right)}{\tau^2}$

Table 4.14: Partial derivatives of the residual part of the Helmholtz Energy.

Derivative	Expression
$\frac{d\alpha^r}{d\delta} =$	$\sum_{i=1}^{N_{poly}} n_i d_i \delta^{d_i-1}\tau^{t_i}$
	$+\sum_{j=1}^{N_{exp}} n_j \exp(-\delta^{c_j})\left(\delta^{d_j-1}\tau^{t_j}(d_j - c_j\delta^{c_j})\right)$
	$+\sum_{k=1}^{N_{gauss}} n_k \delta^{d_k}\tau^{t_k}\exp\left(-\alpha'_k(\delta-\epsilon_k)^2 - \beta_k(\tau-\gamma_k)^2\right)\left(\frac{d_k}{\delta} - 2\alpha'_k(\delta-\epsilon_k)\right)$
	$+\sum_{l=1}^{N_{crit}} n_l\left(\Delta^{b_l}\left(\psi + \delta\frac{d\psi}{d\delta}\right) + \frac{d\Delta^{b_l}}{d\delta}\delta\psi\right)$
$\frac{d^2\alpha^r}{d\delta^2} =$	$\sum_{i=1}^{N_{poly}} n_i d_i(d_i-1)\delta^{(d_i-2)}\tau^{t_i}$
	$+\sum_{j=1}^{N_{exp}} n_j \exp(-\delta^{c_j})\left(\delta^{d_j-2}\tau^{t_j}\left((d_j - c_j\delta^{c_j})(d_j - 1 - c_j\delta^{c_j}) - c_j^2\delta^{c_j}\right)\right)$
	$+\sum_{k=1}^{N_{gauss}} n_k \tau^{t_k}\exp(-\alpha'_k(\delta-\epsilon_k)^2 - \beta_k(\tau-\gamma_k)^2)$
	$\times\left(-2\alpha'_k\delta^{d_k} + 4\alpha_k^2\delta^{d_k}(\delta-\epsilon_k)^2 - 4d_k\alpha_k\delta^{d_k-1}(\delta-\epsilon_k) + d_k(d_k-1)\delta^{d_k-2}\right)$
	$+\sum_{l=1}^{N_{crit}} n_l\left(\Delta^{b_l}\left(2\frac{d\psi}{d\delta} + \delta\frac{d^2\psi}{d\delta^2}\right) + 2\frac{d\Delta^{b_l}}{d\delta}\left(\psi + \delta\frac{d\psi}{d\delta}\right) + \frac{d^2\Delta^{b_l}}{d\delta^2}\delta\psi\right)$
$\frac{d\alpha^r}{d\tau} =$	$\sum_{i=1}^{N_{poly}} n_i t_i \delta^{d_i}\tau^{t_i-1}$
	$+\sum_{j=1}^{N_{exp}} n_j t_j \delta^{d_j}\tau^{t_j-1}\exp(-\delta^{c_j})$
	$+\sum_{k=1}^{N_{gauss}} n_k \delta^{d_k}\tau^{t_k}\exp(-\alpha'_k(\delta-\epsilon_k)^2 - \beta_k(\tau-\gamma_k)^2)\left(\frac{t_k}{\tau} - 2\beta_k(\tau-\gamma_k)\right)$
	$+\sum_{l=1}^{N_{crit}} n_l\delta\left(\frac{d\Delta^{b_l}}{d\tau}\psi + \Delta^{b_l}\frac{d\psi}{d\tau}\right)$
$\frac{d^2\alpha^r}{d\tau^2} =$	$\sum_{i=1}^{N_{poly}} n_i t_i(t_i-1)\delta^{d_i}\tau^{t_i-2}$
	$+\sum_{j=1}^{N_{exp}} n_j t_j(t_j-1)\delta^{d_j}\tau^{t_j-2}\exp(-\delta^{c_j})$
	$+\sum_{k=1}^{N_{gauss}} n_k \delta^{d_k}\tau^{t_k-2}\exp(-\alpha'_k(\delta-\epsilon_k)^2 - \beta_k(\tau-\gamma_k)^2)$
	$\times\left(\left(\frac{t_k}{\tau} - 2\beta_k(\tau-\gamma_k)\right)^2 - \frac{t_k}{\tau^2} - 2\beta_k\right)$
	$+\sum_{l=1}^{N_{crit}} n_l\delta\left(\frac{d^2\Delta^{b_l}}{d\tau^2}\psi + 2\frac{d\Delta^{b_l}}{d\tau}\frac{d\psi}{d\tau} + \Delta^{b_l}\frac{d^2\psi}{d\tau^2}\right)$
$\frac{d^2\alpha^r}{d\tau d\delta} =$	$\sum_{i=1}^{N_{poly}} n_i d_i t_i \delta^{d_i-1}\tau^{t_i-1}$
	$+\sum_{j=1}^{N_{exp}} n_j t_j \delta^{d_j-1}\tau^{t_j-1}(d_j - c_j\delta^{c_j})\exp(-\delta^{c_j})$
	$+\sum_{k=1}^{N_{gauss}} n_k \delta^{d_k}\tau^{t_k}\exp(-\alpha'_k(\delta-\epsilon_k)^2 - \beta_k(\tau-\gamma_k)^2)$
	$\times\left(\frac{d_k}{\delta} - 2\alpha_k(\delta-\epsilon_k)\right)\left(\frac{t_k}{\tau} - 2\beta_k(\tau-\gamma_k)\right)$
	$+\sum_{l=1}^{N_{crit}} n_l\left(\Delta^{b_l}\left(\frac{d\psi}{d\tau} + \delta\frac{d^2\psi}{d\delta d\tau}\right) + \delta\frac{d\Delta^{b_l}}{d\delta}\frac{d\psi}{d\tau} + \frac{d\Delta^{b_l}}{d\tau}\left(\psi + \delta\frac{d\psi}{d\delta}\right) + \frac{d^2\Delta^{b_l}}{d\delta d\tau}\delta\psi\right)$

Table 4.15: Partial Derivatives for Critical Parameters used in Helmholtz equations of state.

Derivative	Expression
$\frac{d\psi}{d\delta} =$	$-2C_l(\delta-1)\psi$
$\frac{d^2\psi}{d\delta^2} =$	$\left(2C_l(\delta-1)^2-1\right)2C_l\psi$
$\frac{d\psi}{d\tau} =$	$-2D_l(\tau-1)\psi$
$\frac{d^2\psi}{d\tau^2} =$	$\left(2D_l(\tau-1)^2-1\right)2D_l\psi$
$\frac{d^2\psi}{d\delta d\tau} =$	$4C_lD_l(\delta-1)(\tau-1)\psi$
$\frac{d\Delta}{d\delta} =$	$(\delta-1)\left(A_l\theta\frac{2}{\beta_l}\left((\delta-1)^2\right)^{1/2\beta_l-1}+2B_la_l\left((\delta-1)^2\right)^{a_l-1}\right)$
$\frac{d^2\Delta}{d\delta^2} =$	$\frac{1}{\delta-1}\frac{d\Delta}{d\delta}+(\delta-1)^2$
	$\Big[4B_la_l(a_l-1)\left((\delta-1)^2\right)^{a_l-2}$
	$+2A_l^2\left(\frac{1}{\beta}\right)^2\left(\left((\delta-1)^2\right)^{1/2\beta_l-1}\right)^2$
	$+A_l\theta\frac{4}{\beta_l}\left(\frac{1}{2\beta_l}-1\right)\left((\delta-1)^2\right)^{1/2\beta_l-1}\Big]$
$\frac{d\Delta^{b_l}}{d\delta} =$	$b_l\Delta^{b_l-1}\frac{d\Delta}{d\delta}$
$\frac{d^2\Delta^{b_l}}{d\delta^2} =$	$b_l\left(\Delta^{b_l-1}\frac{d^2\Delta}{d\delta^2}+(b_l-1)\Delta^{b_l-2}\left(\frac{d\Delta}{d\delta}\right)^2\right)$
$\frac{d\Delta^{b_l}}{d\tau} =$	$-2\theta b_l\Delta^{b_l-1}$
$\frac{d^2\Delta^{b_l}}{d\tau^2} =$	$2b_l\Delta^{b_l-1}+4\theta^2b_l(b_l-1)\Delta^{b_l-2}$
$\frac{d^2\Delta^{b_l}}{d\delta d\tau} =$	$-A_lb_l\frac{2}{\beta_l}\Delta^{b_l-1}(\delta-1)\left((\delta-1)^2\right)^{1/2\beta_l-1}-2\theta b_l(b_l-1)\Delta^{b_l-2}\frac{d\Delta}{d\delta}$

"reducing parameters") using

$$\frac{1}{\rho_{c,mix}} = \sum_{i=1}^{N} X_i^2 \frac{1}{\rho_{c,i}} + \sum_{i=1}^{N-1} \sum_{j=i+1}^{N} 2X_i X_j \beta_{\nu,ij} \gamma_{\nu,ij} \frac{X_i + X_j}{\beta_{\nu,ij}^2 (X_i + X_j)} \frac{1}{8} \left(\frac{1}{\rho_{c,i}^{1/3}} + \frac{1}{\rho_{c,j}^{1/3}} \right)^3 \tag{4.22}$$

and,

$$T_{c,mix} = \sum_{i=1}^{N} X_i^2 T_{c,i} + \sum_{i=1}^{N-1} \sum_{j=i+1}^{N} 2X_i X_j \beta_{T,ij} \gamma_{T,ij} \frac{X_i + X_j}{\beta_{T,ij}^2 (X_i + X_j)} \sqrt{T_{c,i} T_{c,j}} \ , \tag{4.23}$$

where N is the number of gases present in the mixture, X represents the mole fraction of each individual component (accompanied by the appropriate offset index i, and j to include interactions between all components), $\beta_{\nu,ij}$ and $\gamma_{\nu,ij}$ are empirically interaction terms associated with density, and $\beta_{T,ij}$ and $\gamma_{T,ij}$ are the empirically derived interaction terms associated with temperature (*Kunz et al.*, 2006). The subscript ν along with the use of inverse density in equation 4.22 comes from a derivation based upon specific volume ($\nu = \frac{1}{\rho}$), and is kept to be consistent with literature. These modified values are *only* applied to to calculate modified τ, and δ for the *residual* part of the Helmholtz energy and its associated derivatives. The ideal part of the Helmholtz energy and its associated derivatives are computed using the equation appropriate for the component, and weighting it by the mole fraction of each component. While the interaction between components in a mixture can be modeled using 4.22 and 4.23, other mixtures require a second interaction term. The residual part of the Helmholtz energy is modified to include an excess departure function using

$$\alpha_r = \sum_{i=1}^{N} X_i \alpha_i^r(\delta, \tau) + \alpha^E(\delta, \tau, X) \tag{4.24}$$

where α_r is the modified Helmholtz energy for the mixture, α_i^r is the residual Helmholtz energy from each component, and α^E is the excess term computed using

$$\alpha^E(\delta, \tau, X) = \sum_{i=1}^{N-1} \sum_{j=i+1}^{N} X_i X_j F_{i,j} \left(\sum_{k=1}^{N_{poly}} N_k \delta^{d_k} \tau^{t_k} + \sum_{l=1}^{N_{exp}} N_l \delta^{d_l} \tau^{t_l} \exp(-\delta^{c_l}) \right) \tag{4.25}$$

Table 4.16: Interaction parameters used for the calculation of the excess Helmholtz energy for the H_2-CH_4 mixture.

k	N_k	d_k	t_k	$\beta_{\nu,ij}$	$\gamma_{\nu,ij}$	$\beta_{T,ij}$	$\gamma_{T,ij}$
				1.0	1.018702573	1.0	1.352643115
1	0.25157134971934	1	2.000				
2	$0.62203841111983\times10^{-2}$	3	1.000				
3	$0.88850315184396\times10^{-1}$	3	1.750				
4	$0.35592212573239\times10^{-1}$	4	1.400				

where F_{ij} is an empirical factor which is set to 1, but for some groups of mixtures this can be adjusted in place of deriving new values of $N_{k,l}$, $d_{k,l}$, and $t_{k,l}$ for a given mixture. The number and value of the terms in equation 4.25 are typically found for mixtures of gases by fitting large data sets of experimental data.

While FORTRAN code is available through NIST's REFPROP to fit such mixtures, in its current form this code is rather difficult to follow, and use effectively. In place of REFPROP, a new Python implementation was developed. Extensive care was taken to ensure that parameters calculated with the Python implementation matched precisely the values calculated with NIST's implementation for each constituent and for mixtures. Currently there is no H_2O-H_2 mixture available in REFPROP, so it was necessary to test mixture calculations with another mixture. Given that it is important in the Jovian atmosphere, the GERG 2004 mixture of H_2-CH_4 (*Kunz et al.*, 2006) was used to validate the Python implementation for gas mixtures. The parameters for the H_2-CH_4 mixture are given in Table 4.16.

Unfortunately, for the most important interaction in our system H_2-H_2O, there are only a few available measurements to constrain such an equation, especially along the parameter space of most interest in our experiments pressure, density (specific volume), and temperature (also known as pVT measurements). The ultra high pressure system developed for microwave opacity measurements was not designed specifically

for pVT measurements. Despite this, it was necessary to use the system in this capacity to make a few measurements which could be used to better constrain equations 4.22, 4.23, 4.24, and 4.25.

4.4 pVT measurements of Pure H_2 and H_2-H_2O mixtures

As described in Chapter 3, extensive lengths were taken to best estimate the volume of the ultra-high pressure system. Knowledge of the system volume is critical in measurements involving pressure Volume and Temperature (pVT), and in our measurements is likely the largest source of error. Three series of pVT measurements were conducted in this work: a series of measurements of Pure H_2 at a temperature of ∼375°K, a series of measurements of Pure H_2 at a temperature of ∼450°K, and a series of measurements with an H_2-H_2O mixture at ∼375°K, and ∼450°K.

Two measurements of pure H_2 were conducted both as a verification for our measurement technique, and as a method to calibrate the pressure transducer using higher precision/lower pressure gauges. The procedure for each measurement was essentially identical. A vacuum was drawn in the system, followed by the slow addition of H_2 into the pressure vessel while recording the "Totalized Flow" as indicated by the mass flow meter (see Figures 3.7 and 3.8). After an amount of H_2 was added to the system, the system was allowed to settle and thermally equilibrate. After a period of a few hours, a pressure reading was taken by either reading the value off the DPI104 300 psi gauge for pressure less than 20 bars (along with recording the transducer voltage for calibration), or by recording the transducer voltage at pressures greater than 20 bars. The data from the two experiments are shown in Tables 4.17 and 4.18. The density in each table is computed by taking the number of moles as calculated using Equation 3.48, and dividing by the system volume using Equation 3.52. The value for the theoretical density given in each table is the density computed using the reference equation of state for H_2 (*Leachman*, 2007) combined with the measured pressure and

temperature. *Seward and Franck* (1981) claimed a maximum deviation of 0.4 % from the work of *Michels et al.* (1959). The results in Tables 4.17 and 4.18 indicate a maximum which is greater; however, we maintain that this data is useful given that most of the deviations are between 1-2 %. It should be pointed out that this may be a unfair comparison given that it is unclear that whether the 0.4 % deviation given in *Seward and Franck* (1981) is in terms of pressure, or density. Given the error propagation which could arise from all instruments required to make these measurements combined with uncertainty in the system volume, we find the 1-3 % deviation between measured and predicted density to be in surprisingly good agreement. It should be noted that in this work the decimal places included in all tables extend far past the instrument precision, and uncertainty (See Table 3.2). This is done in the hopes that better calibrations, or techniques in the future may allow for interpretations past the current instrument, or measurement uncertainty.

The measurement of pVT measurement of the H_2-H_2O mixture was conducted in a slightly different manner. The oven was pre-heated to a temperature of approximately 375°K. Approximately 1 bar of water vapor was added to the pressure vessel by drawing a vacuum in the system, shutting all valves in the interior of the oven, then slowly opening valve to the water reservoir. The system was allowed to stabilize after a number of hours. Once the system temperature and water vapor reading indicated by the EE33 hygrometer stabilized, a small buffer of H_2 (1.4701 bars) was added so as to precisely measure the pressure of water vapor in the system. The final pressure was recorded as 1.0640 bars. The reference equation of state for pure H_2O (*Wagner and Pruß*, 2002) combined with the pressure and temperature measurement were used to compute the density of water present. The density is then multiplied by the system volume to find the number of moles of H_2O as shown in Table 4.19. After measuring the amount of water vapor present in the system, H_2 was added (with the number of moles recorded by the mass flow meter), until the total pressure approached 20 bars.

The valves interior to the oven were shut, and the system was allowed to stabilize once more. A small buffer of hydrogen again was used to measure the 19.826 bar pressure. One final addition of H_2 resulted in a measurement at approximately 75 bars as indicated by the pressure transducer. After the 75 bar measurement was taken, the oven temperature was set to ∼450°K. Once the system reached a stable point the pressure and temperature were recorded as shown in Table 4.19. Note that in Table 4.19 the density decreases by approximately 0.01 $\frac{g}{L}$ owing to the increase in volume due to thermal expansion of the pressure vessel.

Table 4.17: Measured and predicted molar densities for pVT measurements at approximately 375°K.

Pressure (bars)	Temperature (Kelvin)	Density Measured (mol/L)	Density Theory (mol/L)	% Diff (%)
19.621	376.583838	0.610146323459678	0.620557986102	1.68
60.2077428212589	376.861914	1.84379399866837	1.86516461123	1.15

Table 4.18: Measured and predicted molar densities for pVT measurements at approximately 450°K.

Pressure (bars)	Temperature (Kelivn)	Density Measured (mol/L)	Density Theory (mol/L)	%Difff (%)
9.37	447.048682	0.246141696877912	0.251064353847	1.96
18.628	447.706152	0.488340817787976	0.49641064593	1.62
27.5995522535781	447.396826	0.711002641182661	0.733161401532	3.02
38.267015234775	447.701025	0.996709531283615	1.01122345323	1.43
47.535357455937	447.701025	1.24589349328939	1.25119048615	0.42
56.8786821648432	447.795752	1.50692467973713	1.49088043793	-1.08

Table 4.19: Measured Pressure, Temperature, density data for H_2-H_2O mixture

T (°K)	P (bars)	Moles H_2	Moles H_2O	Density (g/L)
376.204932	19.826	18.663980319129138	1.126616830674388	1.79167542485
377.726416	75.059974199647826	74.965164072252165	1.126616830674388	5.30095092818
446.697607	87.860145913789353	74.965164072252165	1.126616830674388	5.28857731271

4.5 Development of an equation of state for H_2-H_2O mixtures

An equation of state that accurately represents how pressure, density, and temperature relate in the H_2-H_2O system is critical in both interpreting our lab measurements, and will be critical for understanding the microwave emission from Jupiter as viewed from the Juno MWR. Surprisingly, there are very few measurements of the H_2-H_2O system in the temperature, and pressure regime relevant for the deep Jovian atmosphere. Data sets available used to constrain our H_2-H_2O equation of state are shown in Figure 4.1.

The largest data set is that of *Lancaster and Wormald* (1990), however, the data available is in the form of Excess Enthalpy. Excess Enthalpy is defined as

$$h^E(p,T,x) = h_{mix}(p,T,X) - \sum_{i=1}^{N_{comp}} X_i h_i(p,T) \tag{4.26}$$

where h_{mix} is the enthalpy measured for a given mixture, X_i is the mole fraction of component i, p is the pressure of the mixture, and T is the temperature of the mixture (*Wormald*, 1977). It is important to note that $h_i(p,T)$ is the enthalpy computed for a pure component under the *total* pressure of the *mixture*. Excess enthalpy is defined as the enthalpy of the mixture less the enthalpy of each constituent computed at the *total* pressure of the *mixture* weighted by mole fraction. The enthalpy of each pure component and the mixture is calculated using the enthalpy equation given in Table 4.12. In fitting the available data, there are two derivatives of the Helmholtz energy that are being constrained. When fitting excess enthalpy data both the residual Helmholtz energy derivative with respect to reduced temperature ($\frac{d\alpha_r}{d\tau}$), and reduced density ($\frac{d\alpha_r}{d\delta}$) are constrained. The Helmholtz energy derivative that is of most interest in this work is $\frac{d\alpha_r}{d\delta}$, since it is the only derivative term necessary to relate density and temperature to pressure (see Table 4.12). Therefore, the best source of data to

constrain the mixture terms for a H_2-H_2O mixture is a pVT measurement. Unfortunately, very few pVT measurements have been conducted in the desired pressure temperature space with *Seward and Franck* (1981), and *Gillespie and Wilson* (1980) being the only studies besides this work to conduct and report any pVT values. It is unfortunate that a number of measurements in *Seward and Franck* (1981) are plotted in a 3D space, and little information can accurately extracted with exception to values near the critical point presented in Table I of their paper. *Seward et al.* (2000) presented values of second and third virial coefficients based upont pVT measurements, however, they do not give the explicit pVT values used to derive these virial coefficients. Virial coefficients can be used to constrain an H_2-H_2O mixture, however, the original data could provide more information, and would serve as a better constraint for an equation of state. Finally *Rabinovich* (1995) give cross second virial coefficients (B_{12}) which can be converted to virial coefficients via

$$B = X_{H_2O}^2 B_{H_2O} + X_1 X_2 B_{12} + X_2^2 B_{H_2}, \tag{4.27}$$

where B_{H_2O} is the virial coefficient for pure water, B_{H_2} is the virial coefficient of pure H_2, and X is the mole fraction (*Hodges et al.*, 2004). The cross virial coefficients of *Rabinovich* (1995) are said to be based upon the data of *Namiot* (1991), however, an English translation of the original work could not be found. Unfortunately, *Rabinovich* (1995) doesn't give values of mole fraction associated with each value of B_{12}. One could use arbitrary values of mole fraction, however, the propagation of errors in computing B_{12} often leads to a spread of data points with large error which discussed in detail in *Hodges et al.* (2004). For this reason, no attempt was made to fit the data provided by *Rabinovich* (1995).

The general fitting process utilized the Levenberg-Marquardt approach (*Press et al.*, 1992) combined with Equations from Table 4.12, Equation 4.24, and the derivatives associated with Equation 4.24 taken from Table 4.14. Details of the

Levenberg-Marquardt approach is published at length elsewhere, and the implementation "leastsq" function in the Python library SciPy was used to derive a best fit for the data set.

The optimized interaction parameters are shown in Table 4.20. The resulting equation of state fits most of the available data within measurement errors. The excess enthalpy computed with the equation of state for H_2-H_2O with data superimposed from *Lancaster and Wormald* (1990) is shown in Figures 4.2 and 4.3. The data from *Lancaster and Wormald* (1990) is shown with an error bar corresponding to the stated error of 2 %. Most of the data falls within these error bars, however, given the inherent difficulty in measuring the H_2-H_2O system a 2 % error bar may over state the precision of this measurement. The percent difference or error between the equation of state and measurements of pVT are shown in Figure 4.4. The measurements used below 600°K are those conducted in this work (a copy of *Gillespie and Wilson* (1980) could not be found), whereas those above 600°K are from *Seward and Franck* (1981). Finally the residual between computed and measured Second and Third Virial Coefficients from *Seward et al.* (2000) are shown in Figures 4.5 and 4.6, respectively. The fit for the H_2-H_2O equation of state is quite reasonable when one considers that all the measurements used have varying sources of error, and the somewhat limited data set available to constrain the equation. Given that this fit is within reason, the equation can be used to better estimate the amount of hydrogen contained in mixtures of hydrogen and water vapor. All measurements of microwave opacity were conducted by measuring total pressure of any given mixture, and therefore need to be corrected to account for the density of each constituent in the mixture.

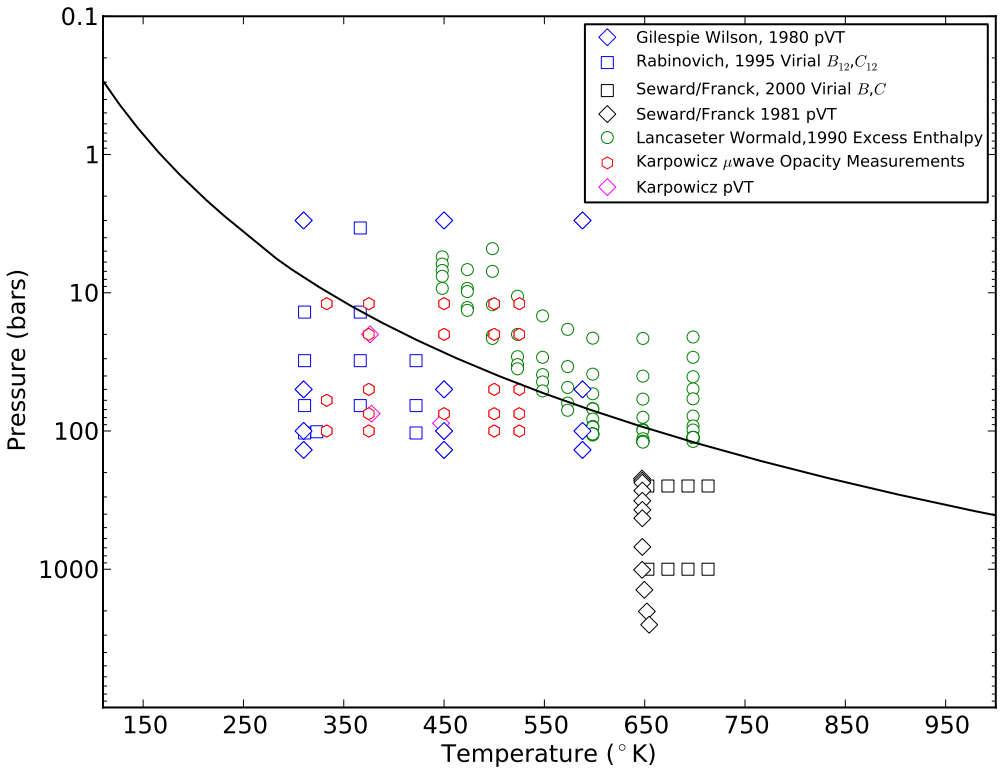

Figure 4.1: Available thermodynamic data in P-T space along with a Jupiter temperature pressure profile.

Table 4.20: Interaction parameters used for the calculation of the excess Helmholtz energy for the H_2-H_2O mixture.

N_l	d_l	t_l	c_l
8.43730166×10^{-2}	1.01325950	29.6892622	0.157106640
1.20304163×10^{-2}	0.875427966	5.66963126	-0.123114242
4.85353759	2.25904893	-0.472763978	1.07298418
-9.45732780	1.73721803	5.68600592	0.751254725

$\beta_{\nu,ij}$	$\gamma_{\nu,ij}$	$\beta_{T,ij}$	$\gamma_{T,ij}$
-68.4724158	2.76510561	-172.902015	3.36805346

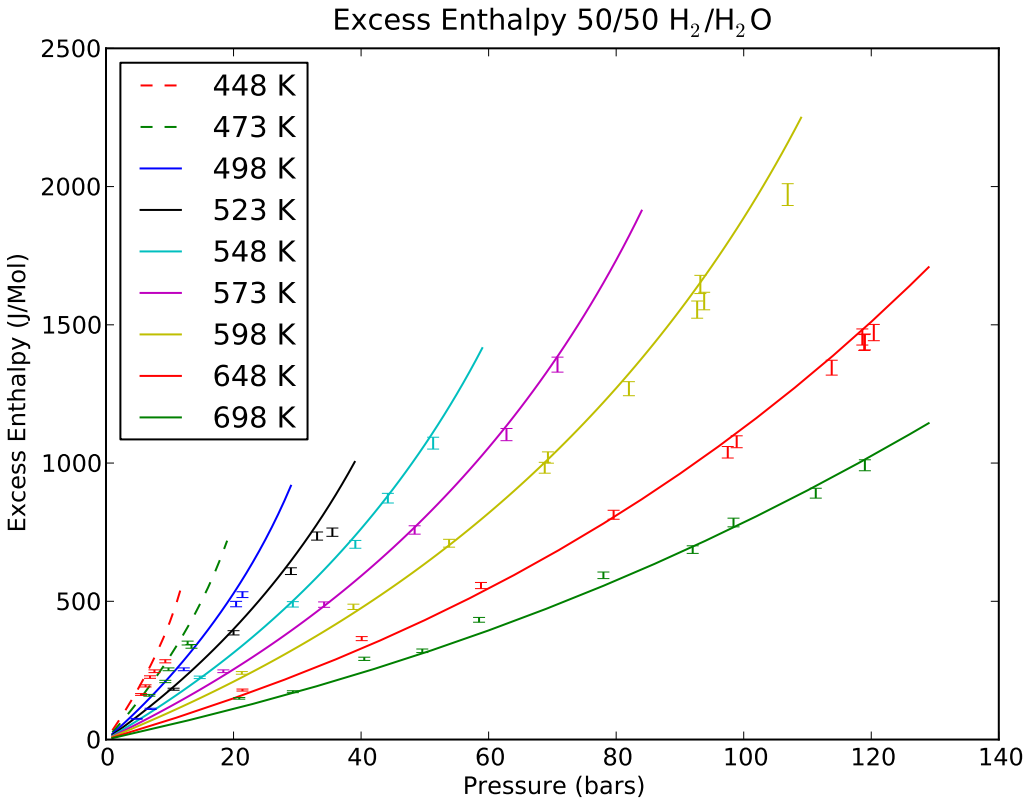

Figure 4.2: Excess Enthalpy computed using an equal mole fraction of hydrogen to water vapor with data points from *Lancaster and Wormald* (1990).

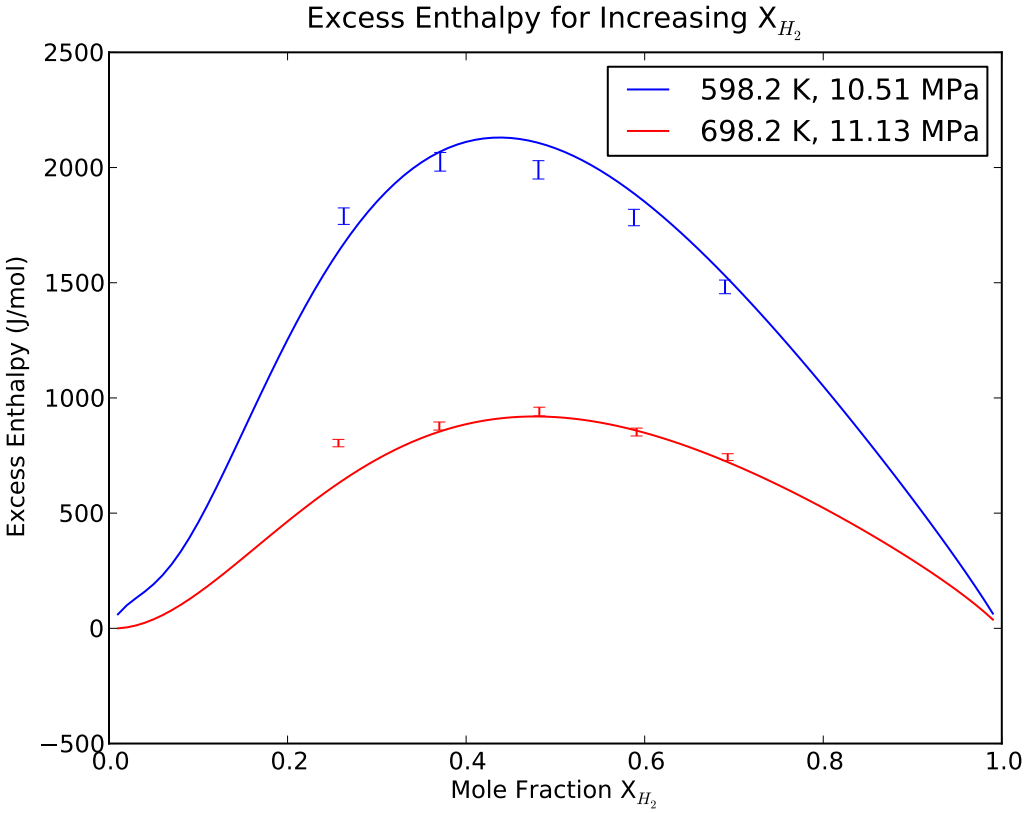

Figure 4.3: Excess Enthalpy computed using a variable mole fraction of H_2 with data points from *Lancaster and Wormald* (1990).

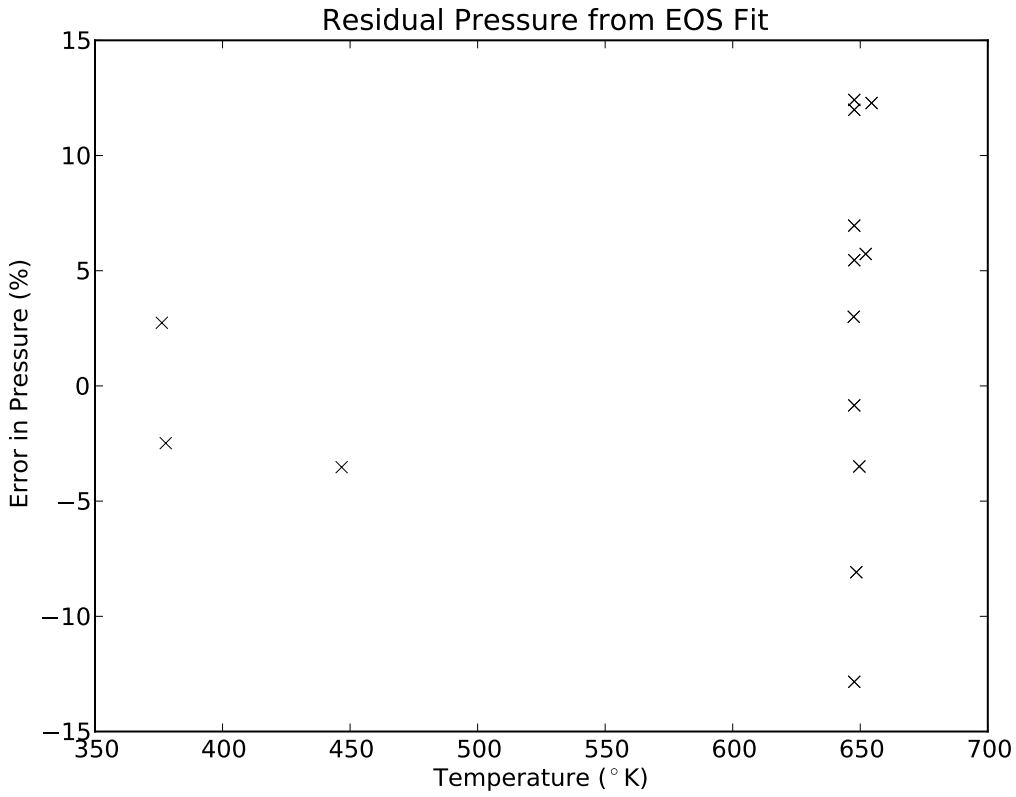

Figure 4.4: Residual Pressure (%Error) between the H_2-H_2O equation of state and measurements.

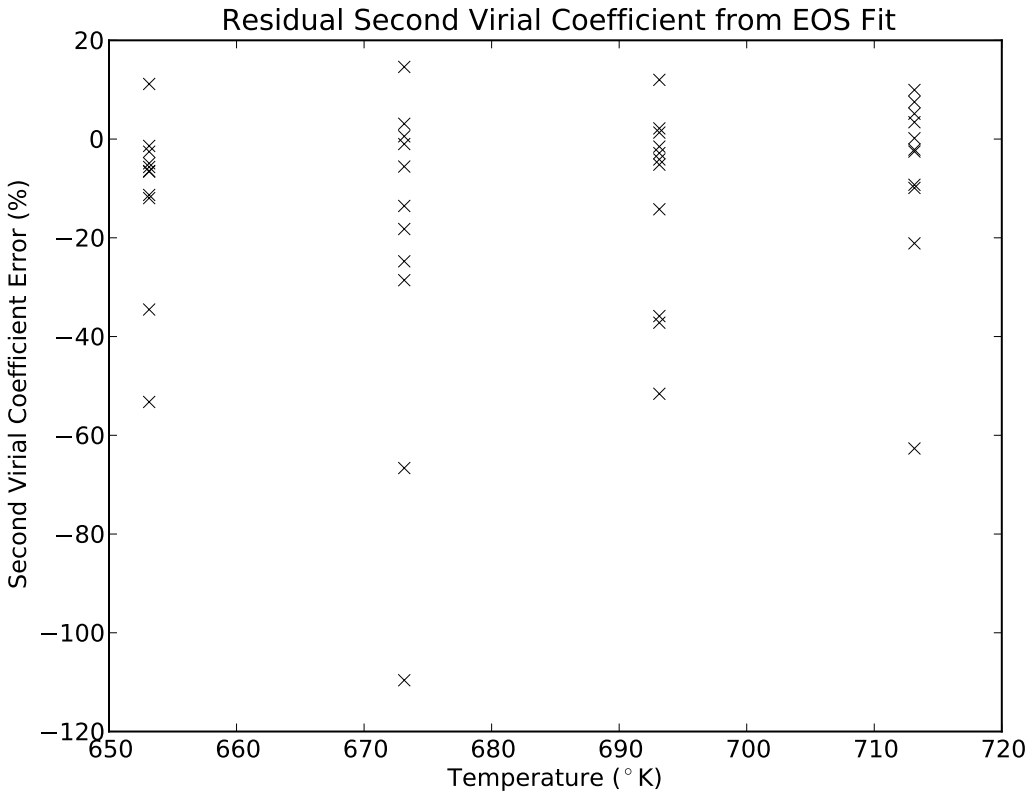

Figure 4.5: Residual Second Virial Coefficients (%Error) between the H_2-H_2O equation of state and measurements.

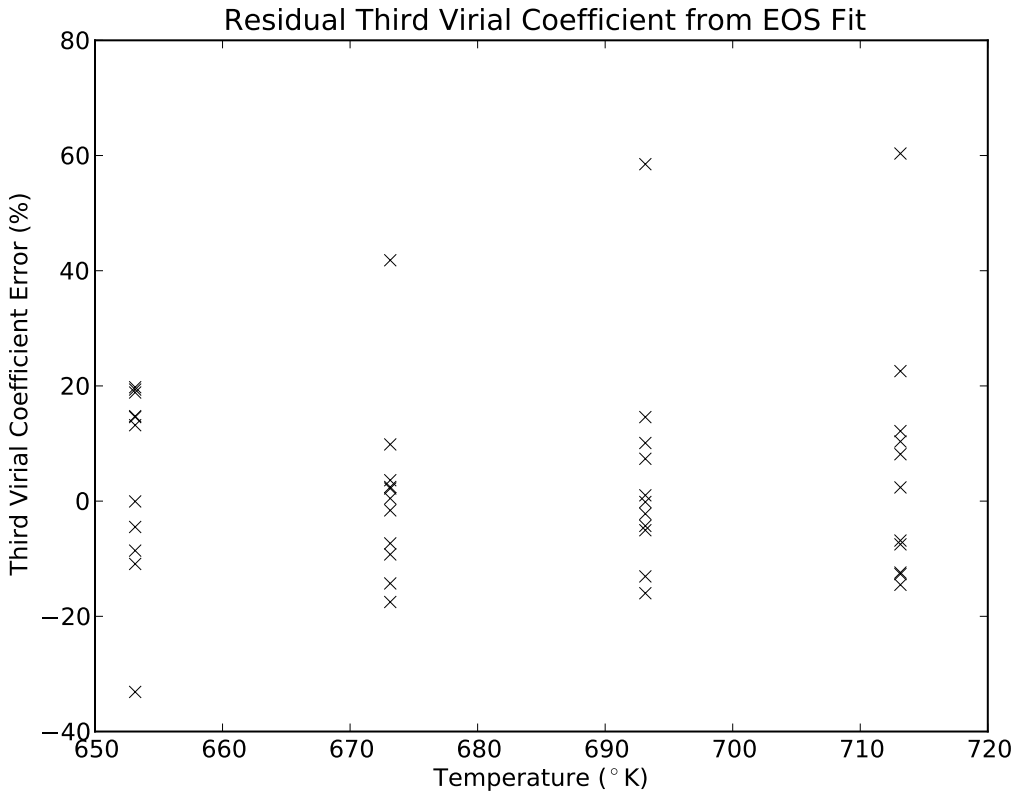

Figure 4.6: Residual Third Virial Coefficients (%Error) between the H_2-H_2O equation of state and measurements.

CHAPTER V

NEW ABSORPTION MODEL FOR WATER VAPOR

One of the primary goals of this work has been to develop a new model for the microwave absorption from water vapor verified by an extensive set of laboratory experiments which simulate the deep Jovian atmosphere. In this chapter several aspects of the new absorption model are discussed including: a brief discussion of the measurement process, discussion regarding the new opacity model, the data fitting approach, and finally a comparison between previous water vapor models to the new one presented in this work. The new model is based upon an extensive set of laboratory measurements, and will be critical to the future success of the NASA Juno mission, in particular, the performance of the Microwave Radiometer (MWR).

5.1 The Measurement Process

The measurement process involved an extensive series of measurements under deep Jovian conditions with temperatures in the range 333-525°K, and pressures up to 100 bars. A possible dry Jovian adiabatic temperature-pressure overlayed with pressure-temperature measurement points are shown in Figure 5.1. As shown in Figure 5.1, there is an extensive number of measurement points (each involving hundreds of data points) covering a wide range of temperature and pressure.

The measurement process is quite involved, time consuming, and often tedious. While extensive lengths have been taken to automate processes, the experimenter still must be actively involved in each stage in the process. The first step in the process involves drawing a vacuum in the system. This can take on the order of 8-24 hours depending upon what constituents were in the high pressure system prior to drawing a vacuum. If the system contained only argon prior to operating the vacuum pump,

8 hours was sufficient. If a mixture of gas containing any amount of water vapor was present, the vacuum pump was allowed to run for at least 24 hours. While the vacuum pump is drawing a vacuum, the experimenter must periodically monitor the temperature within the pressure vessel, and make slight adjustments to the temperature to ensure the temperature is constant just prior to taking a vacuum measurement of the microwave resonator response. While there is a computer control of temperature, there are a number of factors which contribute to a fluctuation in temperature within the pressure vessel. First, the thermocouple for the temperature controller is in the air stream of the oven, not inside the pressure vessel. This allows the oven to control the temperature within a short period of time, but is not necessarily the temperature within the pressure vessel. Second, the high pressure system and oven are outdoors (covered by a steel EZEE shed), and are subject to large ambient temperature swings which result in a temperature offset. This offset in temperature is a combined effect of the temperature controller response and of radiation of heat from pipes and small orifices in the oven (for cable feedthroughs etc). The observed trend is that for a increase in ambient temperature of a few °C, the oven will decrease in temperature between 0.2-0.5°, with the opposite being true for a decrease in ambient temperature. Once the experimenter has determined that the temperature is stable, a measurement is taken of the spectral response of the microwave resonator. The quality factor from the vacuum measurement is used to compute an error budget as described in Chapter 3.

Once a measurement of the microwave resonator's spectral response has been taken, the experimenter quickly opens the oven, closes off valves which admit/vent gas to the pressure vessel (inside the over), and opens the valve to the water reservoir shown in Figure 3.3. The water reservoir was filled with distilled water, ACS Reagent Grade with ASTM D 1193 specifications for reagent water, type II (manufactured by Ricca Chemical Company). The experimenter closely monitors either the

pressure reading from the transducer or the hygrometer, and closes the valve to the water reservoir once the desired water vapor pressure (always below the saturation vapor pressure) is reached. The experimenter quickly closes the door to the oven and monitors both the hygrometer reading (when available), temperature and the center frequency of a few key resonances. Stabilization of the hygrometer reading and the center frequencies of the resonances (approximately 6-8 hours) indicates that the water vapor is well mixed within the pressure vessel, and a second measurement of the spectral response of the resonator is taken. This spectral response is used to compute Q^m_{loaded} in Equation 3.17 over several resonances in the resonator, and is used to compute the microwave opacity of pure water vapor at the center frequencies of those resonances.

After completing the measurement of pure water vapor, the experimenter conducts what is referred to as a "buffer measurement" of the water vapor pressure. While there is a measurement of water vapor pressure made by the transducer, and hygrometer (when available), this measurement is not as precise as one can make with either the DPG-7000, or the DPI-104 vacuum/pressure gauges. The "buffer measurement" technique loads a small section of pipe with a gas at a pressure slightly greater than the pressure indicated by either the transducer, or hygrometer. The experimenter then quickly opens the door to the oven, opens the valve to the pressure vessel, and records the pressure from the pure water vapor (plus a minute correction for the neutral gas in the buffering) indicated by the DPG-7000 or DPI-104 gauges. The experimenter then adds Hydrogen/and Helium to the pressure vessel until the next desired pressure is reached. Once the desired pressure is reached the experimenter shuts the valve inside the oven, and closes the door to the oven. The experimenter then waits another 6-8 hours waiting for the system to stabilize before taking another measurement of the resonators spectral response. The process described is repeated with a direct measurement of pressure using the transducer once the pressure limit

of either the DPI-104, or DPG-7000 (approximately 20 bars) is exceeded.

Once the maximum pressure in an experiment has been reached, the experimenter reverses the process by venting the gas mixture, giving a second group of measurements. By assuming no preferential venting of one constituent, the reduced pressure mixtures would have a constant mixing ratio of water vapor, and hydrogen/helium. Unfortunately, some of these measurements did seem to indicate a preferential venting of hydrogen/helium vs. water and were omitted when constructing a model for water vapor opacity. The measurements are useful in some cases as points of verification. Once all the desired pressures have been reached, the remaining gas is vented, and a vacuum is drawn in the system. A second measurement of the system's spectral response is taken after 24 hours under vacuum conditions.

The next step in the process is to dielectrically match the center frequencies of the measured resonances using a microwave transparent gas. In all of the experiments, argon was used due to its high refractivity reducing the amount of gas necessary to match each pressure. The process involves reading the measurement taken of the resonator's spectral response under a given pressure, and adding argon until the center frequency of the resonator is matched. The experimenter must wait a few hours when adding large amounts of argon such that the system stabilizes allowing for thermal gradients to work their way out of the system. Once the system is thermally stable, the experimenter carefully adds or removes gas to precisely match the center frequency. This process is aided by a series of tones produced by the data acquisition computer to help the experimenter reach the center frequency. The measured spectral response of each resonance is used to compute $Q^m_{matched}$ in Equation 3.17. Once all resonances are matched for a previously measured pressure, the process is repeated allowing the system to thermally stabilize. Once all resonances have been matched over all pressure conditions, the system is again vacuumed, and measurements of the resonator properties are again taken.

The final step in the measurement process is to measure the transmissivity of the resonators, which requires that the experimenter open the oven, disconnect the microwave cables from the resonator and connect a female-to-female sma adapter (thru load) in place of the resonator. The experimenter then closes the oven door, and waits until the temperature stabilizes within the oven. Once the oven reaches the desired temperature the spectral response is measured and used to compute t_{loaded}, and $t_{matched}$ in Equation 3.17. The entire process has been refined, and reduced to a 1 week time frame. Earlier measurements took up to 2 weeks due to inefficient scheduling of experiments.

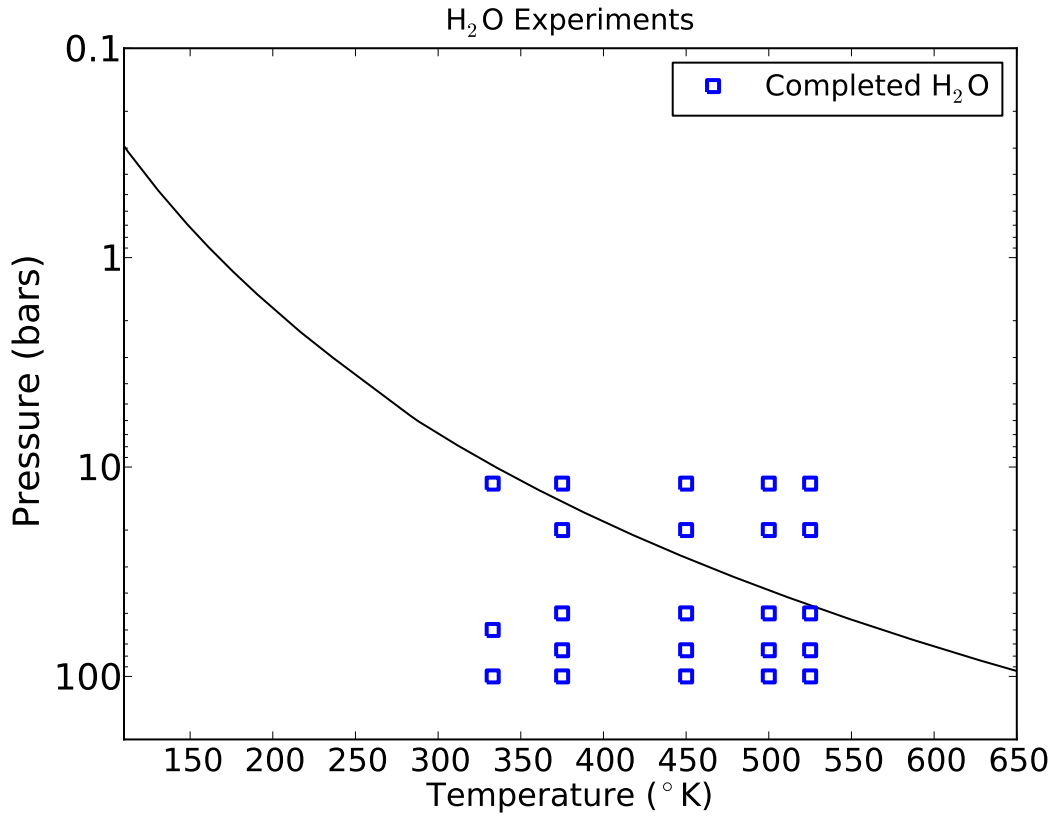

Figure 5.1: Dry Jovian adiabatic temperature-pressure profile along with T-P space of microwave opacity measurements.

5.2 Ultra-High Pressure Measurement Data Set

The ultra-high pressure measurement data set for water vapor is the result of many hours repeating the process described in Section 5.1. After careful analysis the data has been reduced to 17 measurement data sets. The measurement conditions for each experiment are summarized in Table 5.1. While conducting measurements three different mixtures of broadening gases were used. The first used water combined with a hydrogen/helium mixture premixed with a mole fraction of 13.5% helium (the Jovian abundance as measured by *von Zahn et al.* (1998)). This mixture was used for experiments 1 and 2, and for a few pressures in experiments 7, 8, and 9. The second type of mixture was for a pure mixture of Helium up to either 6 or 13 bars pressure, with remaining pressures using pure hydrogen. Finally, a measurement of water vapor in pure hydrogen was conducted to better decouple the interactions between hydrogen-water, and helium-water broadening.

As mentioned in Section 5.1, the data points taken while decreasing pressure were omitted owing to preferential venting of hydrogen/helium vs. water vapor, and are considered valid data points, but are not used for fitting. Also, Experiment 17 is included in the data set only as a verification, and is not used for fitting owing to the low opacity, and scatter in the data set. The data set is available for download as an excel spreadsheet using the following url: `http://users.ece.gatech.edu/~psteffes/palpapers/karpowicz_data/water_data/h2o_data.xls`. The data organized with "tabs" and is split by experiment, valid data flags, omitted data flags, and data used for development of the new microwave opacity model.

5.3 Development of a New Centimeter-Wave Opacity model

The new opacity model which is optimized using the highest quality data from our extensive measurement data set starts with a modification of the *Rosenkranz* (1998) model for water vapor. *Rosenkranz* (1998) was chosen as a starting point owing to

Table 5.1: Summary of Experiments conducted using the ultra-high pressure measurement system.

Experiment	Temperature(°K)	Max Pressure (bars)	Hydrogen-Helium mixture	Water Vapor Pressure (bars)
1	376.1	21.2	Factory H_2-He Pre-mix 13.5% He	0.328
2	376.2	86.0	Factory H_2-He Pre-mix 13.5% He	0.322
3	376.3	96.1	846.5 $\frac{g}{m^3}$ He	0.396
4	376.2	99.6	1691.4 $\frac{g}{m^3}$ He	0.384
5	376.2	96.6	1658.8 $\frac{g}{m^3}$ He	0.363
6	376.2	99.6	H_2 Only	0.444
7	451.2	101.1	Factory Pre-mix up to 20 bars	1.358
8	451.2	99.3	Factory Pre-mix up to 20 bars	0.701
9	523.2	90.6	Factory Pre-mix up to 40 bars	3.290
10	523.1	88.7	1077.9 $\frac{g}{m^3}$ He	1.856
11	498.2	87.8	H_2 Only	2.504
12	498.2	87.4	1250.1 $\frac{g}{m^3}$ He	0.923
13	498.1	92.4	590.2 $\frac{g}{m^3}$ He	2.106
14	451.1	91.7	H_2 Only	1.149
15	451.2	91.7	879.9 $\frac{g}{m^3}$ He	1.388
16	451.1	89.1	1386.8 $\frac{g}{m^3}$ He	0.744
17	333.0	82.1	1928.6 $\frac{g}{m^3}$ He	0.175

the fact that it is frequently used for microwave remote sensing studies of Earth, and its relatively simple form allowed for a high quality fit for our data set. It may be possible to adapt models such as the MT_CKD (*Payne et al.*, 2010) which have a strong physical basis, however, the model is also constrained by field measurements of Earth's atmosphere which may not provide the best information regarding the Jovian atmosphere. An updated version of the *Rosenkranz* (1998) model was provided by Dr. Philip Rosenkranz, and was heavily modified to fit our measurements. The model includes lines from the HITRAN database (*Rothman et al.*, 2009) up to 916 GHz. The line centers, line intensities, line widths and temperature exponents are given in Table 5.2. The contributions for line absorption is computed using

$$\alpha_{lines} = n_w \sum_{i=1}^{15} I_{o,i} \theta^{2.5} \exp(E_{o,i}(1-\theta)) F_{VVW}(\nu_i, \nu, \Delta\nu_i) \qquad (\mathrm{km}^{-1}) \qquad (5.1)$$

where n_w is the number density of water molecules in molecules per cubic centimeter weighted by the isotope fraction from O^{16} (0.997317), $I_{o,i}$ is the line intensity, $E_{o,i}$ is the temperature coefficient, θ is the standard $\frac{300}{T}$ where T is in degrees Kelvin, and

F_{VVW} is the van Vleck-Weisskopf line shape given in Equation 2.3. The value of $\Delta\nu_i$ is computed using

$$\Delta\nu_i = P_{ideal,H_2O}\theta^{x_{H_2O,i}}\Delta\nu_{H_2O,i} + P_{ideal,H_2}\theta^{x_{H_2,i}}\Delta\nu_{H_2,i} + P_{ideal,He}\theta^{x_{H_2,i}}\Delta\nu_{H_2,i} \quad (5.2)$$

where $x_{H_2O,i}$ $x_{H_2,i}$ and $x_{He,i}$ are the temperature exponents for water vapor, hydrogen, and helium, respectively. Likewise, the parameters $\Delta\nu_{H_2O,i}$ $\Delta\nu_{H_2,i}$ and $\Delta\nu_{H_2O,i}$ are the line broadening parameters for water vapor, hydrogen, and helium, respectively. The values for P_{ideal,H_2O} P_{ideal,H_2} and $P_{ideal,He}$ are the *ideal* pressures which are computed from *density* of each constituent present. In the case of our experiments this is the density as computed by the equation of state developed in Chapter 4, including interaction parameters for H_2-H_2O. Once the density is computed the ideal pressure is computed as

$$P_{ideal,gas} = \frac{\rho_{gas}}{M_{gas}} R_{gas} T \quad \text{(bars)} \quad (5.3)$$

where ρ_{gas} is the density of the gas in grams per cubic meter, M_{gas} is the molecular weight of the gas (in grams per mol), R_{gas} is the ideal gas constant for the gas, and T is the Temperature in Kelvin. The value for R_{gas} is the generally accepted value of 8.314472×10^{-5} $\frac{m^3\,bar}{K\,mol}$ for H_2 and H_2O, however, the equation of state for helium requires the use of the older value 8.314310×10^{-5} $\frac{m^3\,bar}{K\,mol}$.

The broadening parameters for H_2 and He are taken from *de Pater et al.* (2005), and are given in Table 5.3.

While the line contributions are important, they are quite insignificant in the frequency range where our measurements were conducted. The feature which dominates in this frequency regime is the continuum absorption defined as:

$$\alpha_{continuum} = \alpha_{c,w} + \alpha_{c,f} \quad (5.4)$$

where $\alpha_{c,w}$ is the continuum term from the water density, and $\alpha_{c,f}$ is the continuum term dependent upon the foreign gas present. The continuum term from water vapor

Table 5.2: Self broadening line parameters for water vapor.

Line (GHz)	Line Intensities ($I_{i,o}$)	Line widths (GHz/mbar)	Temperature Exponent (x_{H_2O})	Temperature Coefficient ($E_{o,i}$)
22.2351	0.1314×10^{-13}	0.01349	0.61	2.144
183.3101	0.2279×10^{-11}	0.01466	0.85	0.668
321.2256	0.8058×10^{-13}	0.01057	0.54	6.179
325.1529	0.2701×10^{-11}	0.01381	0.74	1.541
380.1974	0.2444×10^{-10}	0.01454	0.89	1.048
439.1508	0.2185×10^{-11}	0.009715	0.62	3.595
443.0183	0.4637×10^{-12}	0.00788	0.50	5.048
448.0011	0.2568×10^{-10}	0.01275	0.67	1.405
470.8890	0.8392×10^{-12}	0.00983	0.65	3.597
474.6891	0.3272×10^{-11}	0.01095	0.64	2.379
488.4911	0.6676×10^{-12}	0.01313	0.72	2.852
556.9360	0.1535×10^{-8}	0.01405	1.0	0.159
620.7008	0.1711×10^{-10}	0.011836	0.68	2.391
752.0332	0.1014×10^{-8}	0.01253	0.84	0.396
916.1712	0.4238×10^{-10}	0.01275	0.78	1.441

Table 5.3: Hydrogen and Helium line broadening parameters for water vapor.

Line (GHz)	$\Delta\nu_{H_2}$ (GHz/bar)	$\Delta\nu_{He}$ (GHz/bar)	x_{H_2}	x_{He}
22.2351	2.395	0.67	0.900	0.515
183.3101	2.400	0.71	0.950	0.490
321.2256	2.395	0.67	0.900	0.515
325.1529	2.395	0.67	0.900	0.490
380.1974	2.390	0.63	0.850	0.540
439.1508	2.395	0.67	0.900	0.515
443.0183	2.395	0.67	0.900	0.515
448.0011	2.395	0.67	0.900	0.515
470.8890	2.395	0.67	0.900	0.515
474.6891	2.395	0.67	0.900	0.515
488.4911	2.395	0.67	0.900	0.515
556.9360	2.395	0.67	0.900	0.515
620.7008	2.395	0.67	0.900	0.515
752.0332	2.395	0.67	0.900	0.515
916.1712	2.395	0.67	0.900	0.515

is defined as

$$\alpha_{c,w} = C_w P^2_{ideal,H_2O} \theta^{x_{w,continuum}} + C'_w P^{n_{continuum}}_{ideal} \theta^{x'_{continuum}} \quad (\mathrm{km}^{-1}) \tag{5.5}$$

where C_w is an empirically derived constant (1.8×10^{-8} in the latest version of *Rosenkranz* (1998)), $x_{continuum}$ is the temperature exponent of the continuum (7.5 in the latest version of *Rosenkranz* (1998)), C'_w is an additional empirically derived constant along with empirically derived $n_{continuum}$ and $x'_{continuum}$. The second term does not appear in *Rosenkranz* (1998), however, it was necessary to fit pure water vapor data with pressures exceeding 2 bars. The foreign gas contribution is defined as

$$\alpha_{c,f} = C_f P^2_{f,ideal} \theta^3 \quad (\mathrm{km}^{-1}) \tag{5.6}$$

where C_f is an empirically derived constant (5.43×10^{-10} in in the latest version of *Rosenkranz* (1998)). In this work C_f is derived in two parts one derived with respect to H_2 and the other due to He. This results in a modified value for $\alpha_{c,f}$ defined as

$$\alpha_{c,f} = C_{H_2} P^2_{ideal,H_2} \theta^3 + C_{He} P^2_{ideal,He} \theta^3 \quad (\mathrm{km}^{-1}) \tag{5.7}$$

where C_{H_2} and C_{He} are empirically derived constants based upon our measurements. The total absorption due to water vapor is then written as

$$\alpha_{H_2O} = 4.342945(\alpha_{lines} + \alpha_{continuum}) \quad \left(\frac{\mathrm{dB}}{\mathrm{km}}\right) \tag{5.8}$$

with the necessary empirically derived constants summarized in Table 5.4. The number of digits extending past the decimal point are not an indication of precision. They are included to allow for future interpretation and decoupling between the water vapor absorption model and the equation of state derived in Chapter 4.

5.4 Data Fitting Process

The model presented in Section 5.3 was derived based upon an extensive laboratory measurement data set. The data set used to fit the opacity model was only a

Table 5.4: Empirically derived constants for the new H_2O water vapor model.

C_w	$4.36510480961\times\ 10^{-7}$
C'_w	$2.10003048186\times\ 10^{-26}$
$x_{continuum}$	13.3619799812
$n_{continuum}$	6.76418487001
$x'_{continuum}$	0.0435525417274
C_{H_2}	$5.07722009423\times 10^{-11}$
C_{He}	$1.03562010226\times 10^{-10}$

subset of the data taken. The three primary reasons for omitting data points for the model fit were: spread in data points at lower frequency resonances due to the limited sensitivity, possible preferential venting of H_2/He when taking measurements while decreasing pressure in the system (data taken after the maximum pressure was reached), and the elimination of experiment 17 owing to scatter in its data points and its limited value in a model for a Jovian atmosphere. The spread in data points at lower frequency resonances arose primarily due to the low opacity values when smaller quantities of water vapor were measured. When opacity values approached the sensitivity threshold of $10^{-2}\ \frac{\text{dB}}{\text{km}}$ for the $\sim$1.5 GHz and $\sim$1.8 GHz resonances, quite a bit of scatter was observed. The possible preferential venting of H_2 can be observed when comparing data points, and model curves in for experiments conducted after the maximum pressure for the experiment was reached. Once the compromised data points had been omitted, the process of fitting the data points began with the pure water vapor data set, or the first pressure in experiments 1-16. The method used a Levenberg-Marquardt optimization technique with a minimization function of

$$\chi^2 = \frac{(s \times (\alpha_{meas} - \alpha_{model}))^2}{Err^2_{\alpha,meas}} \tag{5.9}$$

where s is an adjustable scale factor, α_{meas} is the measured absorption coefficient, α_{model} is the absorption coefficient for the model undergoing optimization, and $Err_{\alpha,meas}$ is the measurement error for the measured absorption coefficient. The scale factor

s was adjusted to "balance" data points in experiments 1-6 which had larger measurement errors, to better optimize data taken at ∼375°K. The value of s was set to 10 for experiments 1-6,and a value of unity for all other experiments. The pure water data set was initially fit without the C'_w in Equation 5.5, however, experiments 9 and 11 fit poorly due to the large amount of water vapor. The C'_w term was added and optimized adjusting values of s for experiments 9 and 11 such that they would be weighted more than data points with less opacity. The inclusion of the C'_w term significantly improved the fit for experiments 9 and 11 without compromising the quality of fit for the remaining experiments. Once the pure water vapor data was fit, the values for C_{He} were fit using data taken with a mixture of H_2O and Helium only. This involved the second pressure in experiments 5, 10, 12, 13, 15, and 16. Next, the data using a mixture of hydrogen and water vapor was used to optimize C_{H_2} using all data in experiments 6, 11, and 14. Finally C_{He} and C_{H2} were optimized together using all experiments from 1 to 16.

5.5 Model Performance

The optimized model performed quite well when considering the relatively low level of opacity observed in these experiments. The results from all experiments superimposed over the new model (black), *DeBoer* (1995) (blue), and *Goodman* (1969) (red) are shown in Figures 5.2 -5.136. Data from Experiment 17 is shown in Figures 5.133-Figures 5.135 for verification of the model, and was not used to fit the expression. Some scatter can be observed for small water vapor abundances as in Experiment 4 (Figures 5.26-5.31), however, for large water vapor abundances as in Experiment 9 (Figures 5.64-5.72), both the scatter and error bars reduce to almost negligible values. The model reproduces the data set quite well, and in viewing Table 5.5, the model results lie within the 2σ error bars of the measurement for 488 out of a total of 929 fitted data points. The model performance surpasses any previously-used Jovian

water vapor opacity model, and the use of either the *DeBoer* (1995) or *Goodman* (1969) models should be discontinued.

Table 5.5: Performance of the model in the current work versus existing Jovian opacity models.

Model	Data Points within 2σ (counts)	Maximum Deviation $\left(\frac{\text{dB}}{\text{km}}\right)$	Minimum Deviation $\left(\frac{\text{dB}}{\text{km}}\right)$	Mean Deviation $\left(\frac{\text{dB}}{\text{km}}\right)$
This Work	488	0.79229	0.000108	0.07584
DeBoer (1995)	157	3.03188	0.00062	0.37493
Goodman (1969)	200	3.01434	0.00015	0.21504
Total	929			

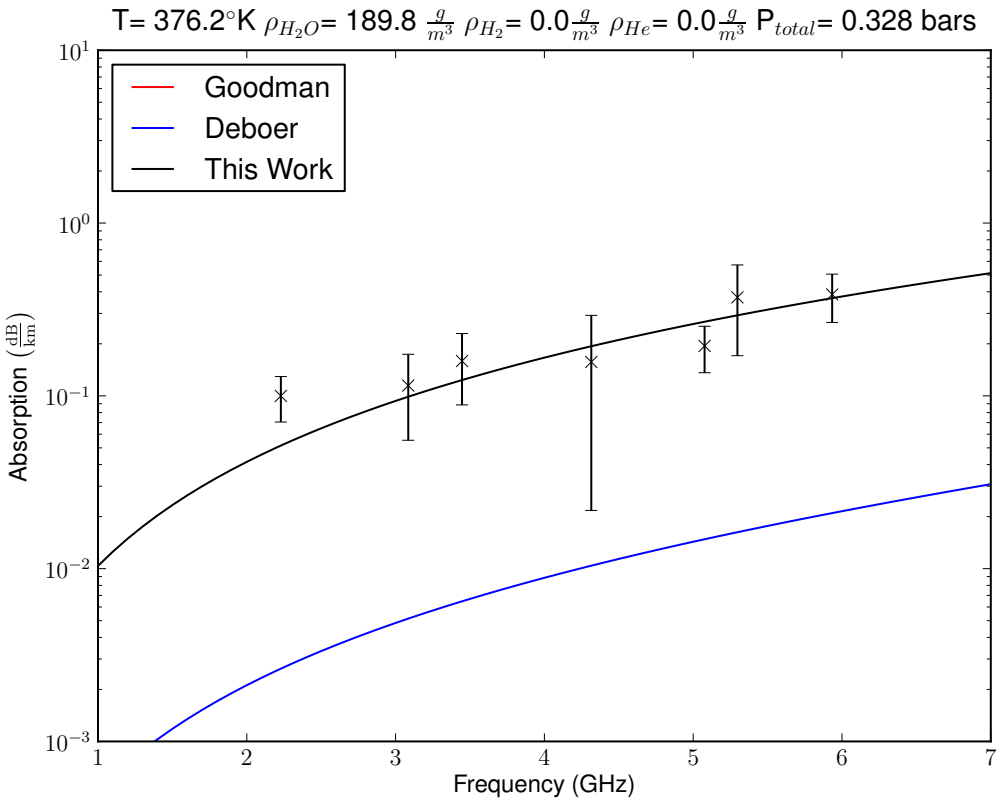

Figure 5.2: Experiment 1 with pure water vapor.

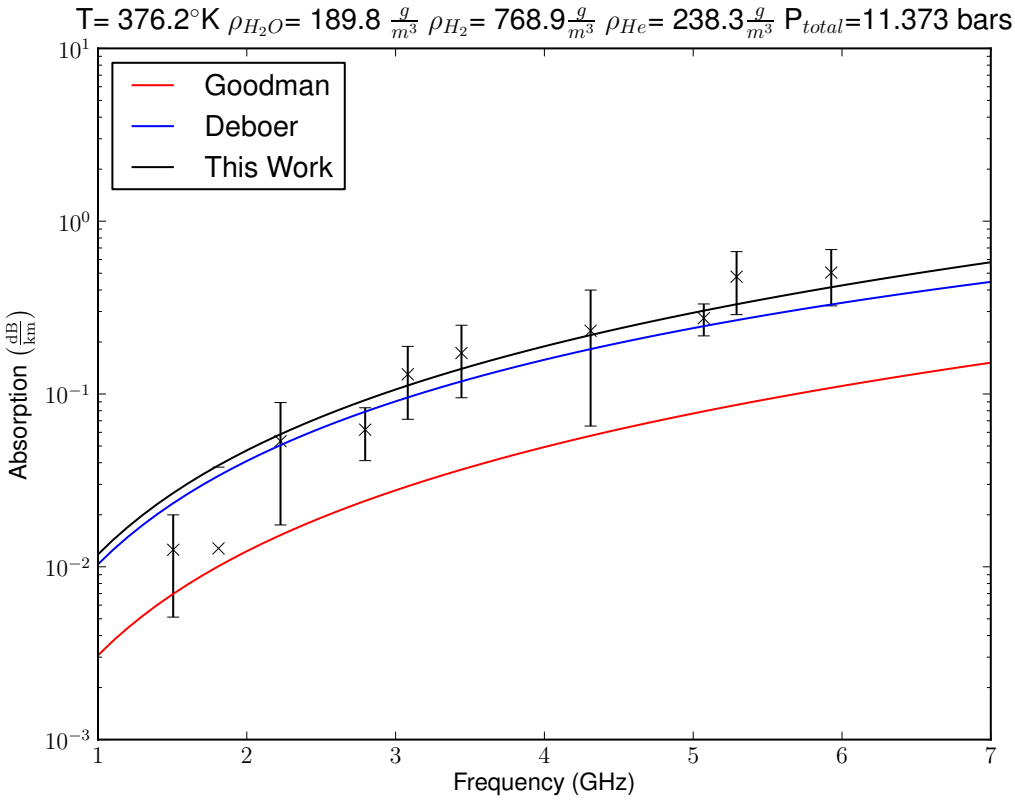

Figure 5.3: Experiment 1 with Factory H_2/He mixture 11.3 bars total pressure .

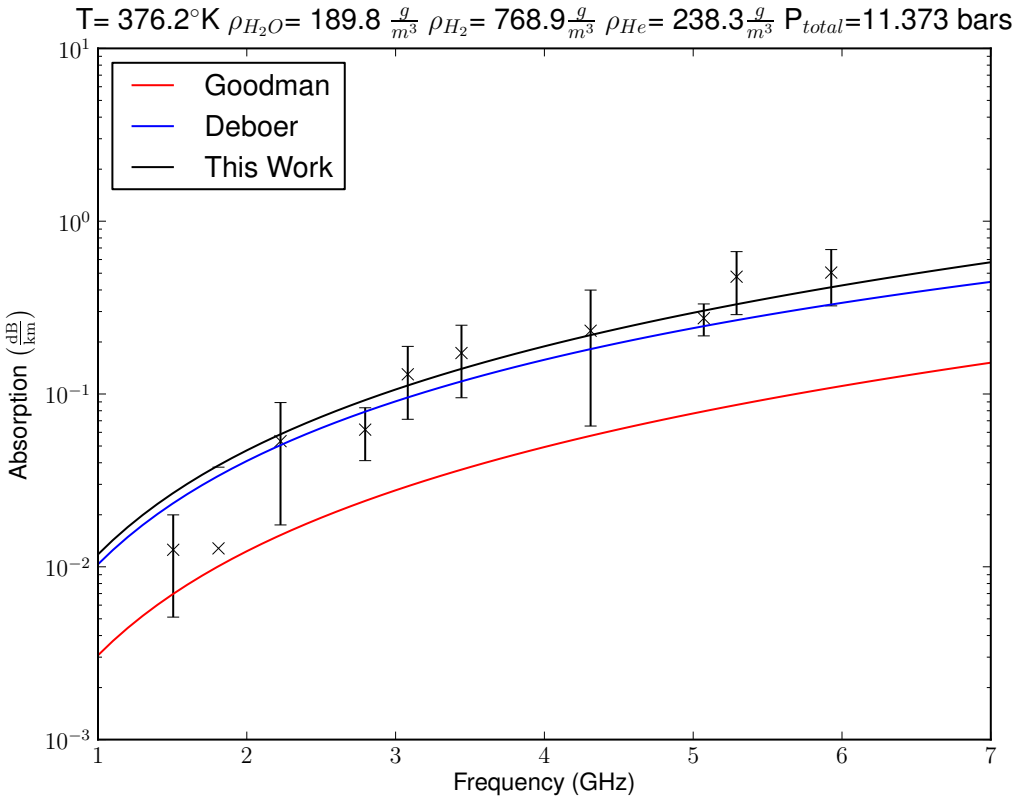

Figure 5.4: Experiment 1 with Factory H_2/He mixture 21.2 bars total pressure .

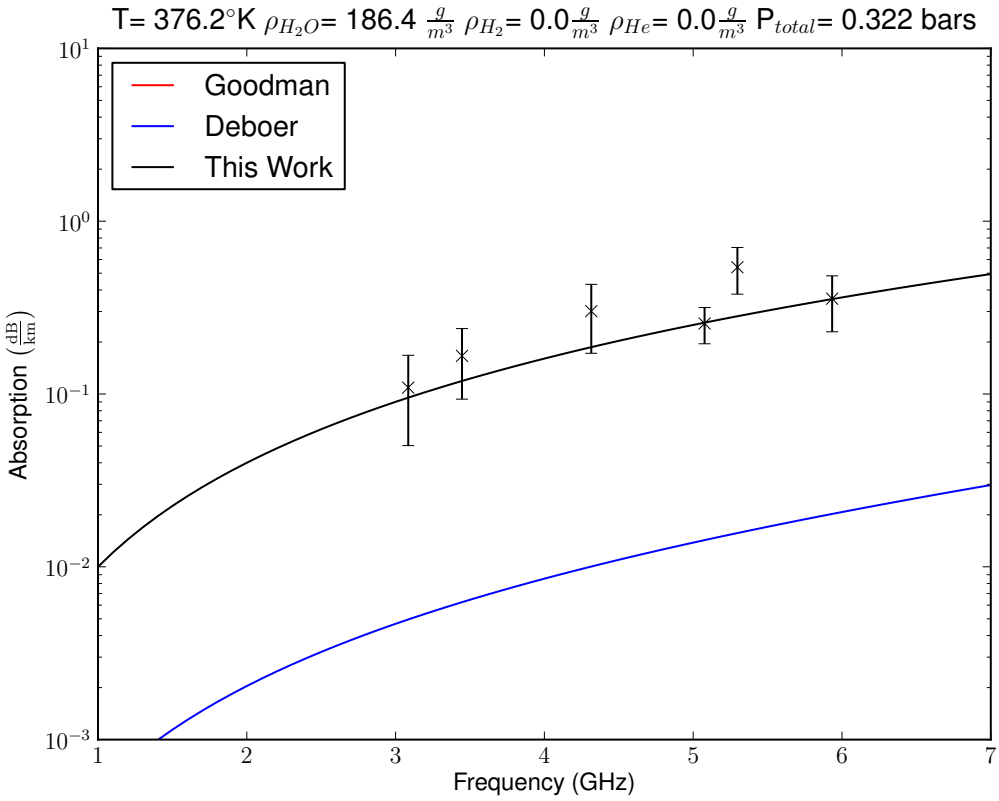

Figure 5.5: Experiment 2 pure water vapor.

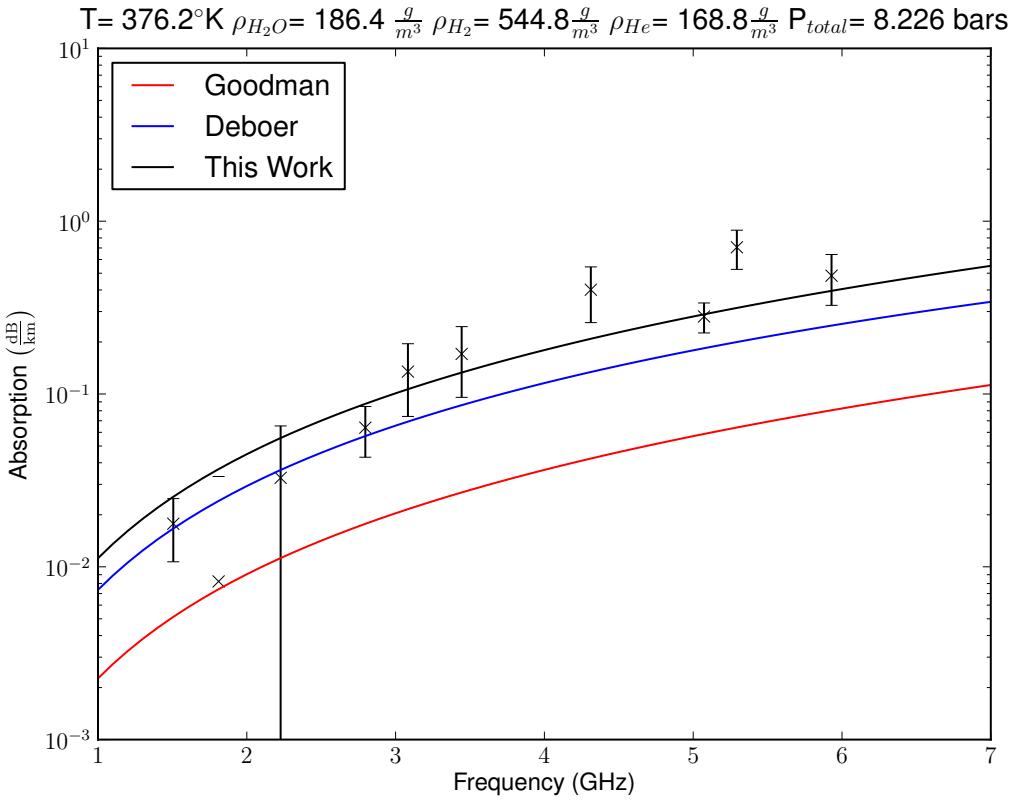

Figure 5.6: Experiment 2 with Factory H_2/He mixture 8.2 bars total pressure.

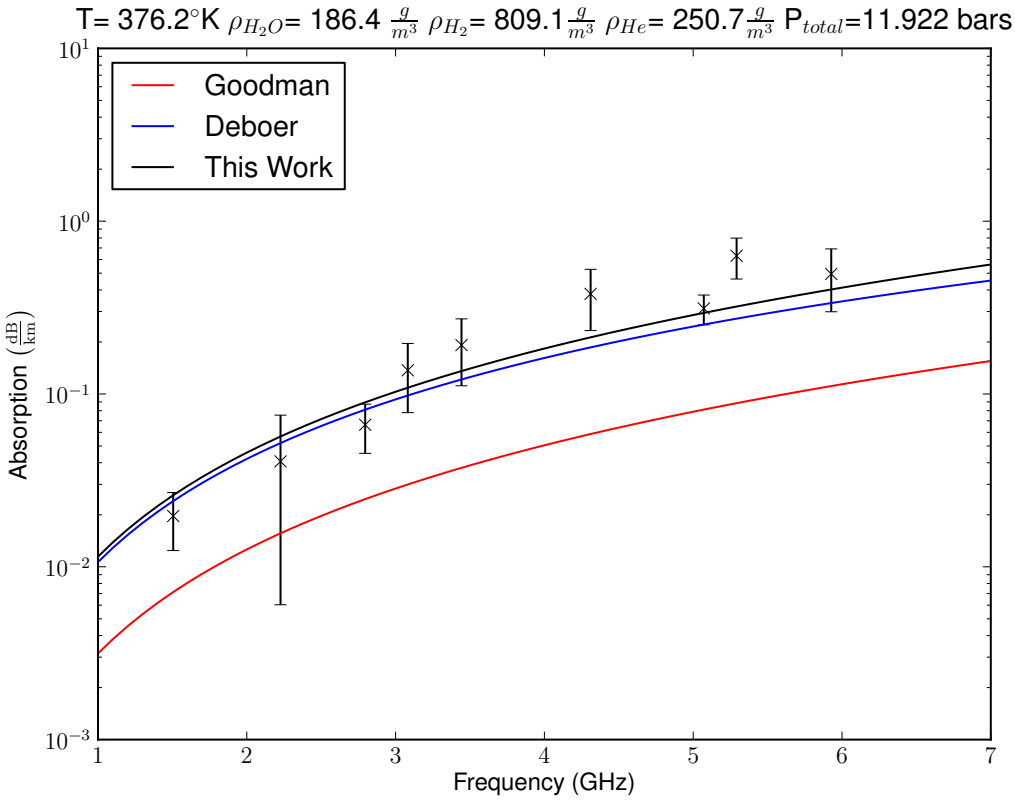

Figure 5.7: Experiment 2 with Factory H_2/He mixture 11.9 bars total pressure

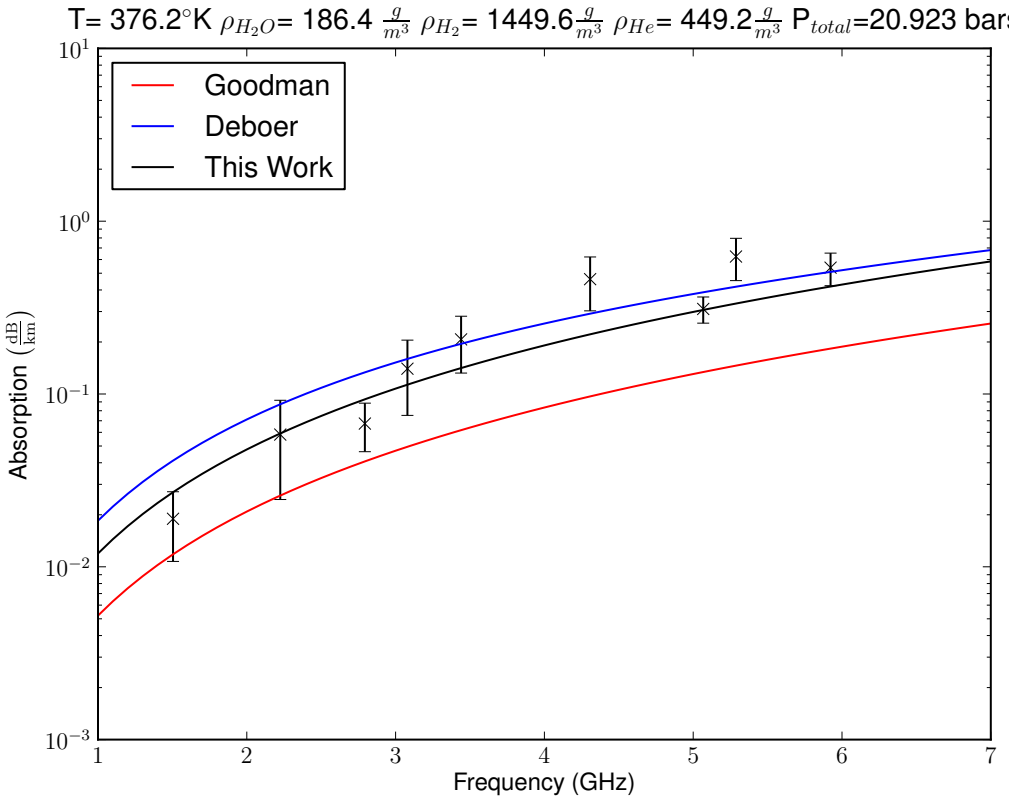

Figure 5.8: Experiment 2 with Factory H_2/He mixture 20.9 bars total pressure .

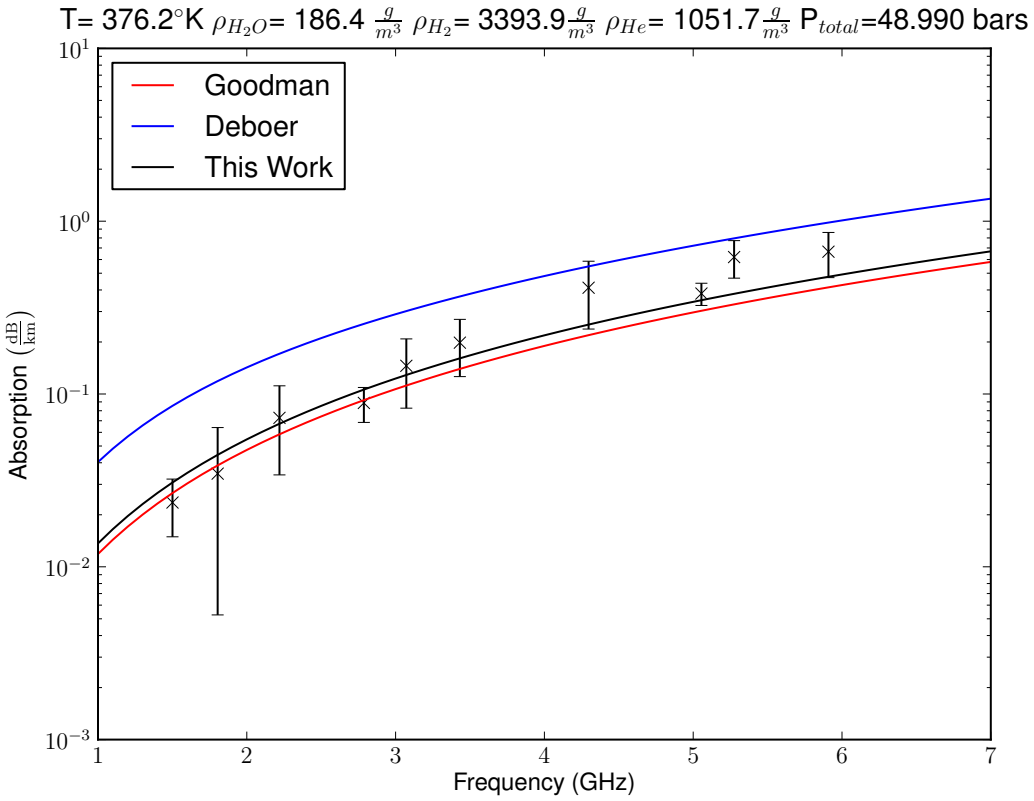

Figure 5.9: Experiment 2 with Factory H_2/He mixture 48.9 bars total pressure.

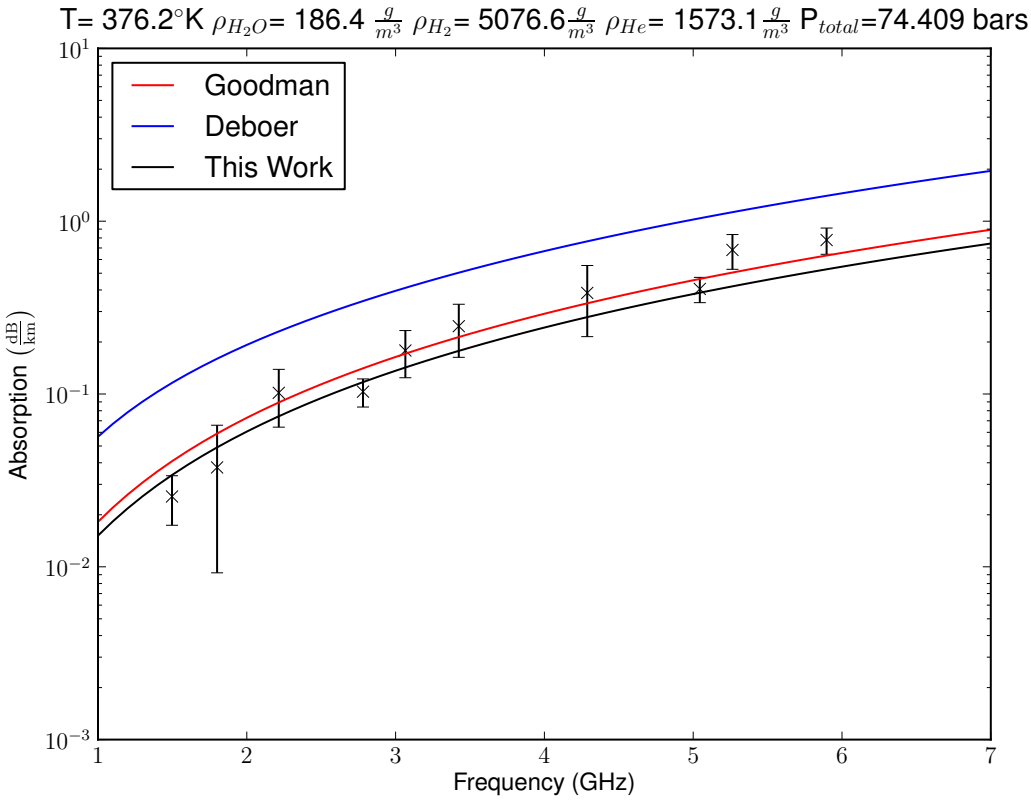

Figure 5.10: Experiment 2 with Factory H_2/He mixture 74.4 bars total pressure .

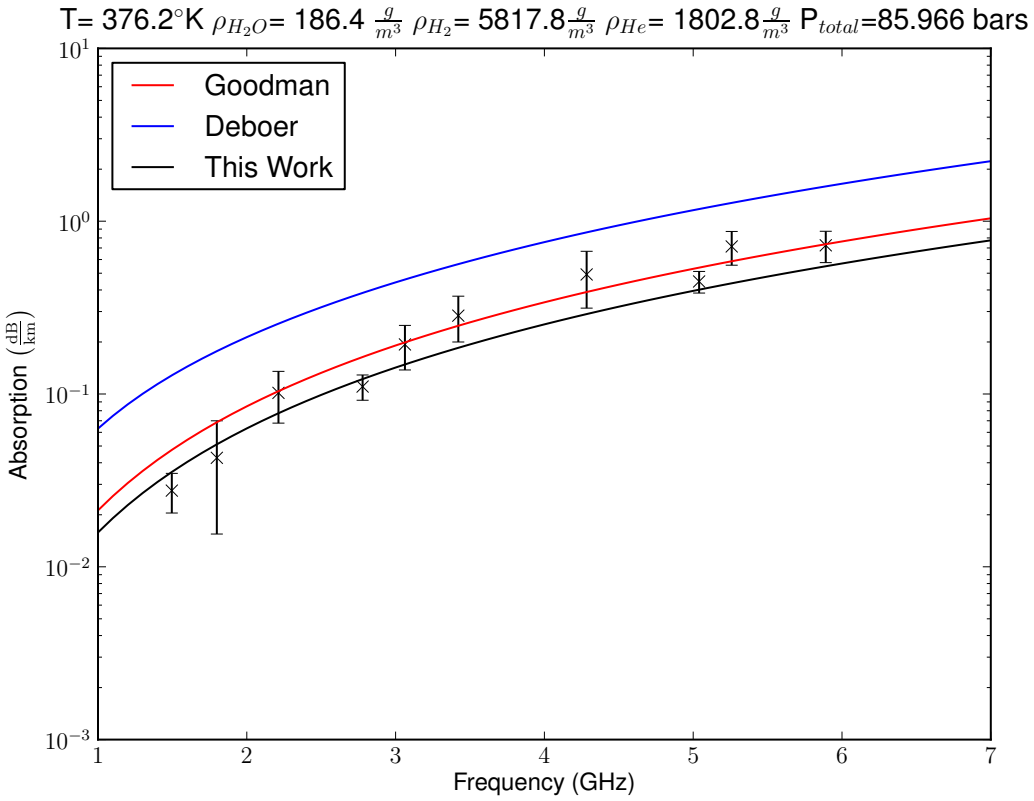

Figure 5.11: Experiment 2 with Factory H_2/He mixture 86 bars total pressure.

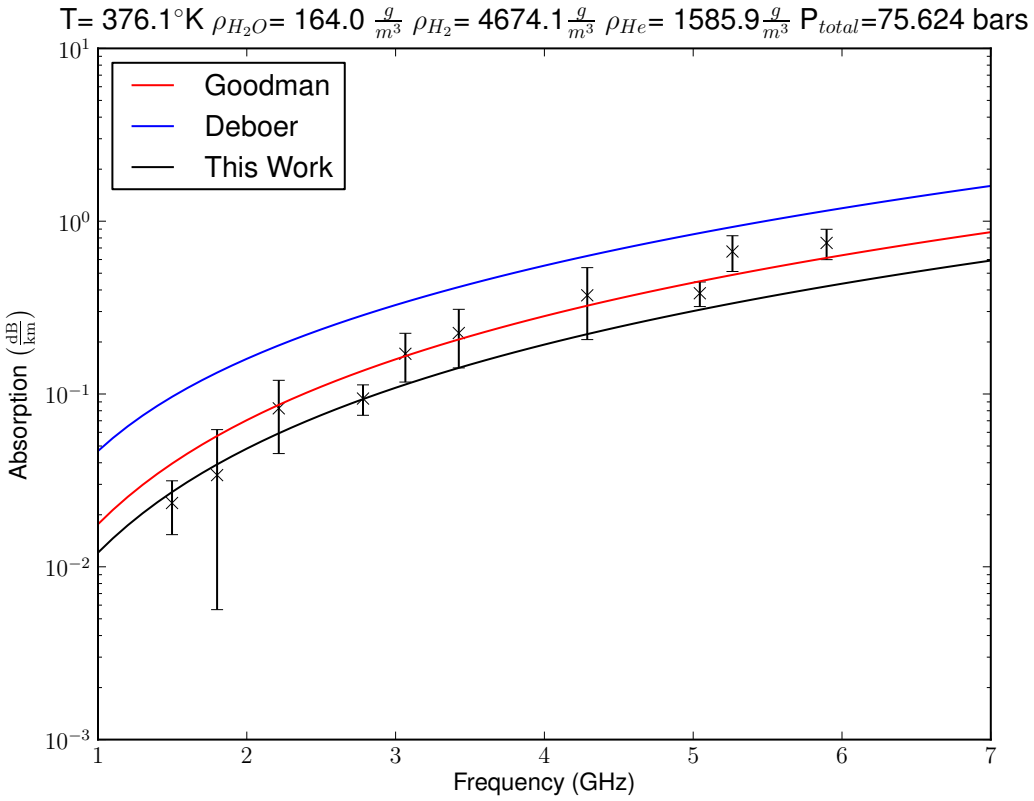

Figure 5.12: Experiment 2 with Factory H_2/He mixture 75.6 bars (after max pressure) .

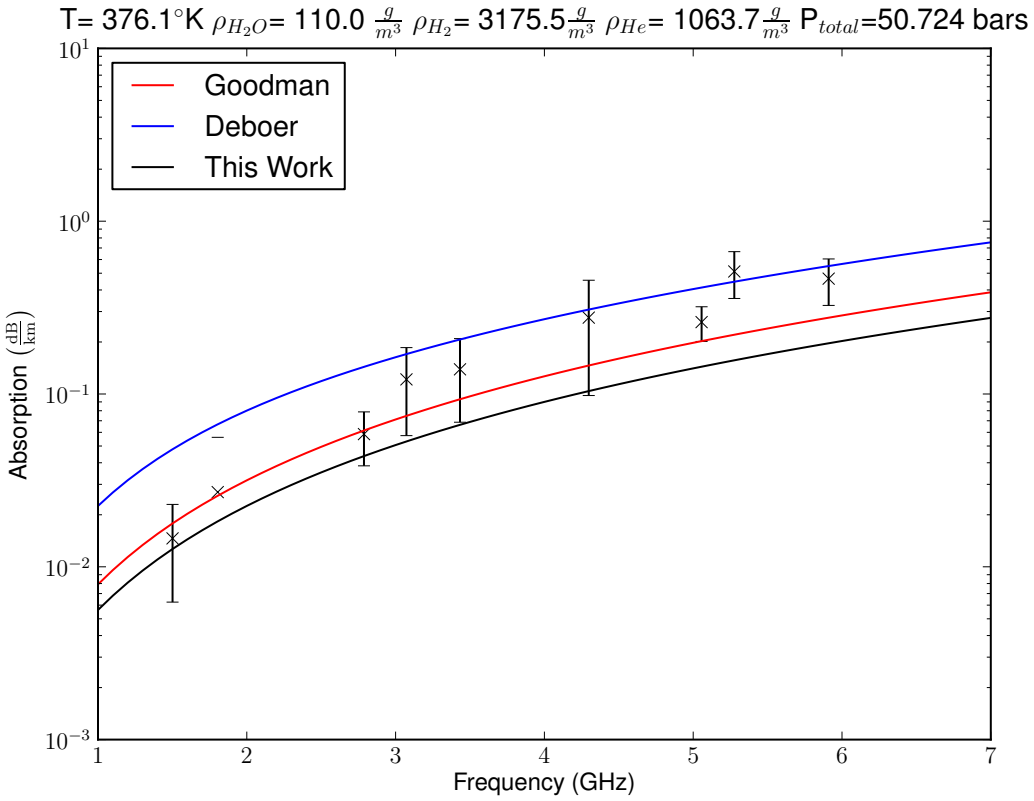

Figure 5.13: Experiment 2 with Factory H_2/He mixture 50.7 bars (after max pressure).

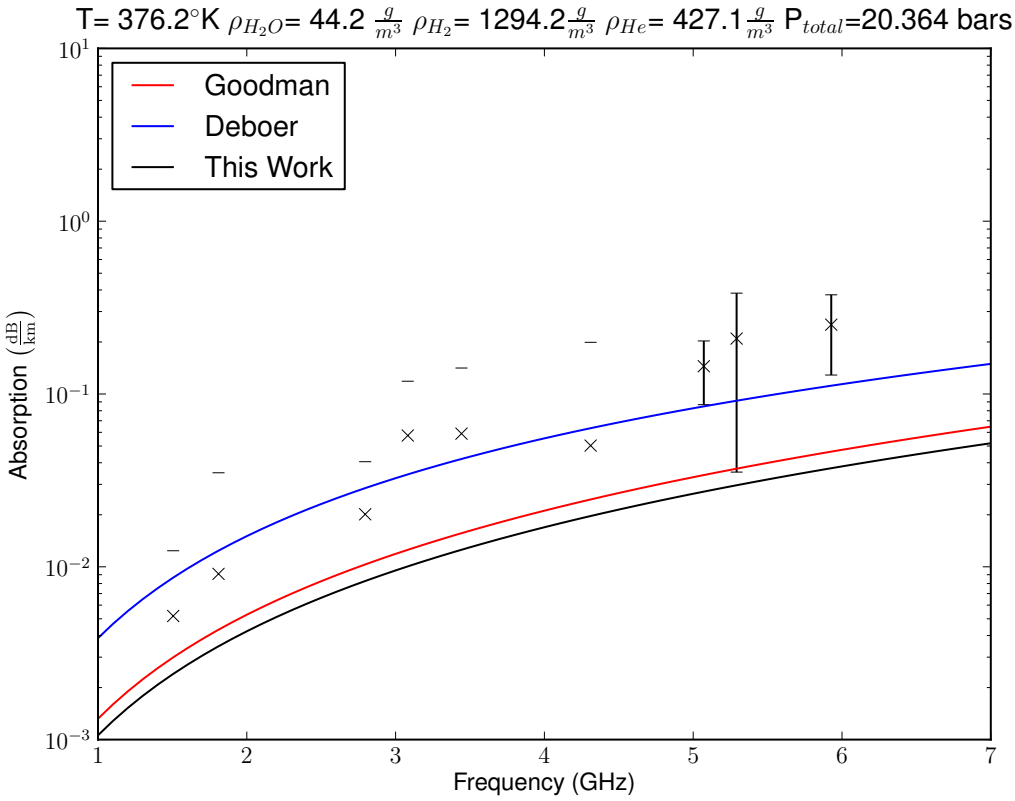

Figure 5.14: Experiment 2 with Factory H_2/He mixture 20.3 bars (after max pressure).

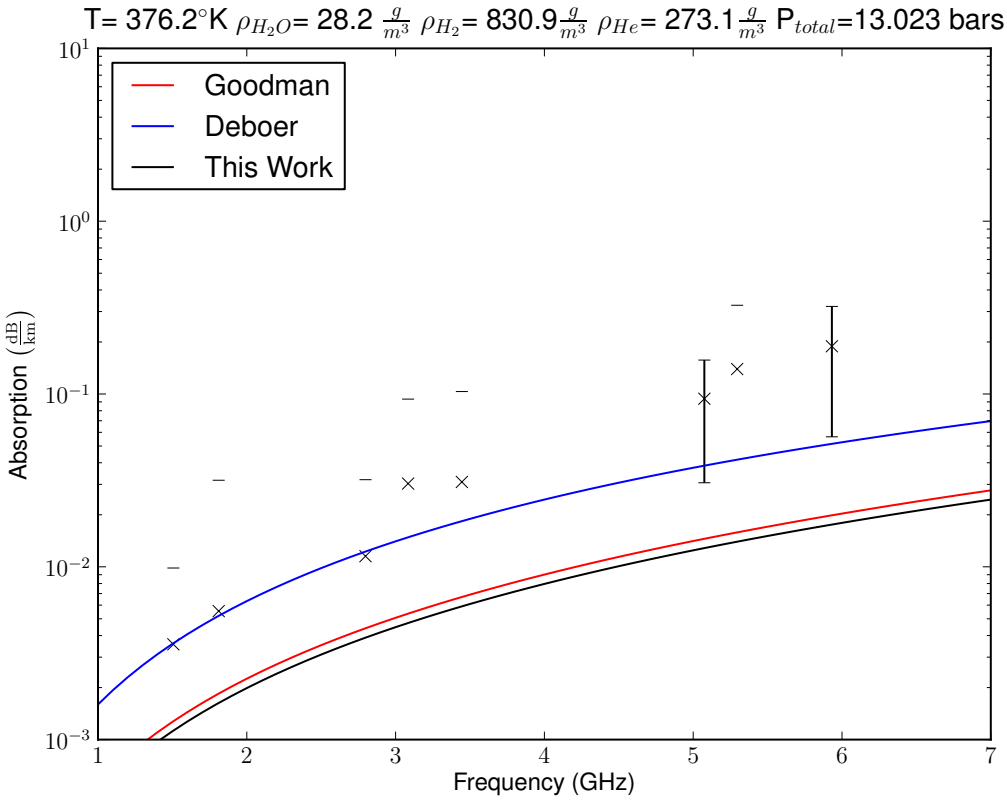

Figure 5.15: Experiment 2 with Factory H_2/He mixture 13 bars (after max pressure).

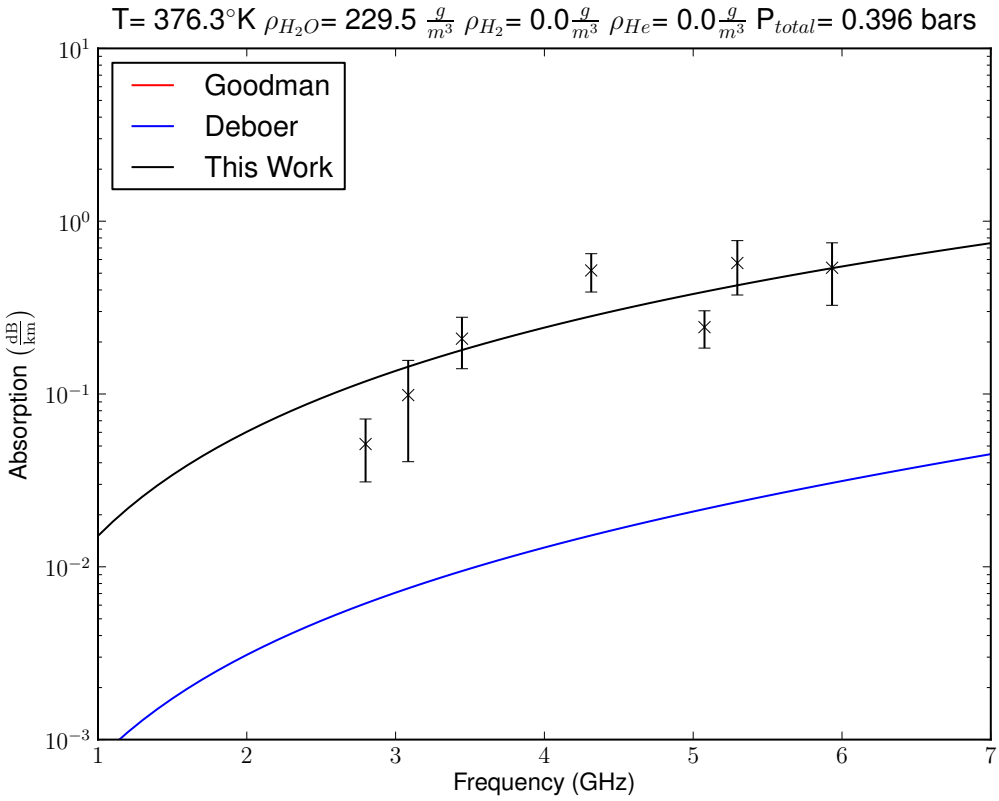

Figure 5.16: Experiment 3 with pure water vapor.

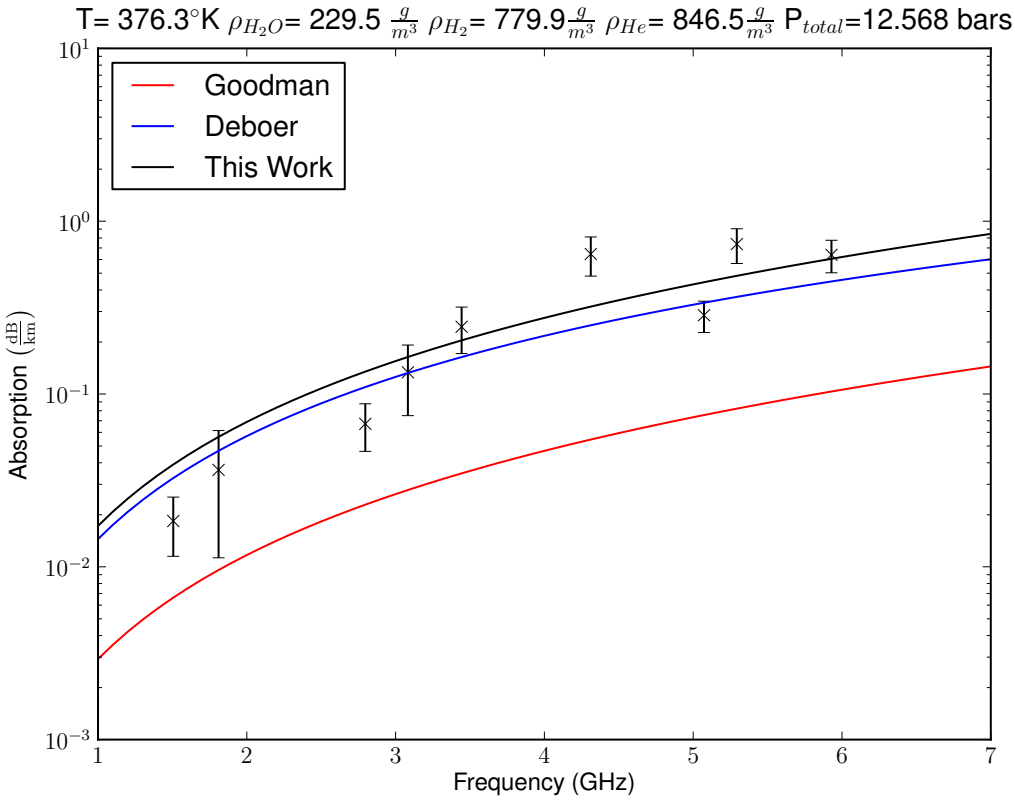

Figure 5.17: Experiment 3 with H_2/He mixture 12.5 bars total pressure

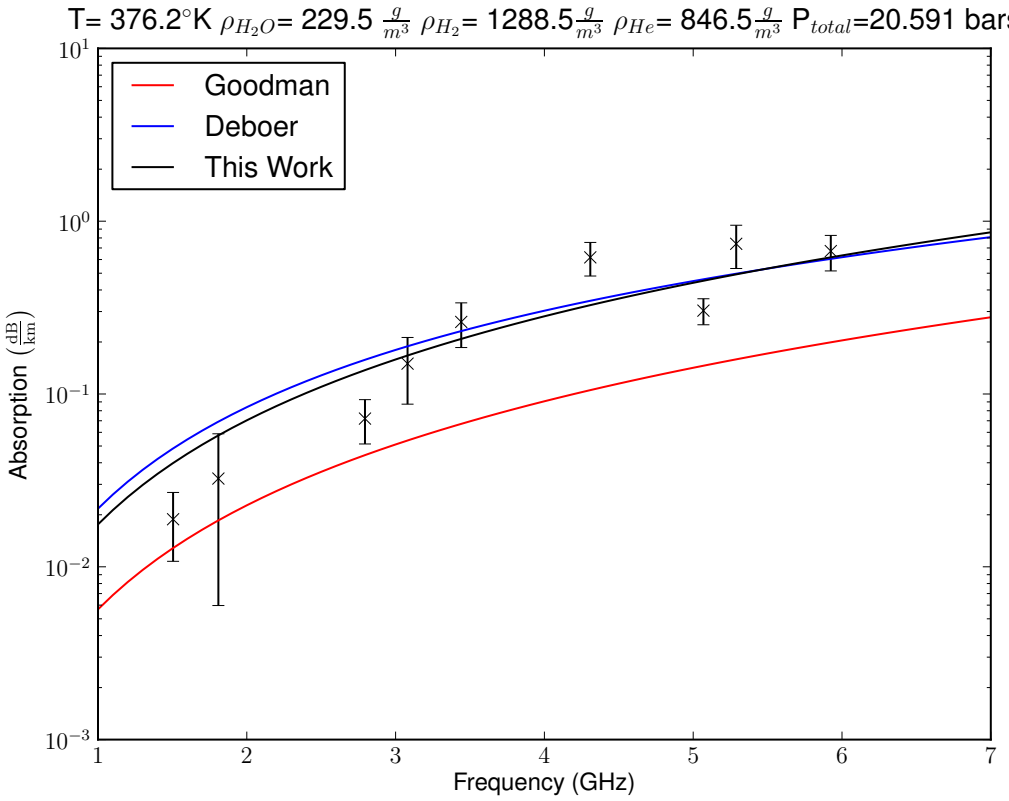

Figure 5.18: Experiment 3 with H_2/He mixture 20.5 bars total pressure

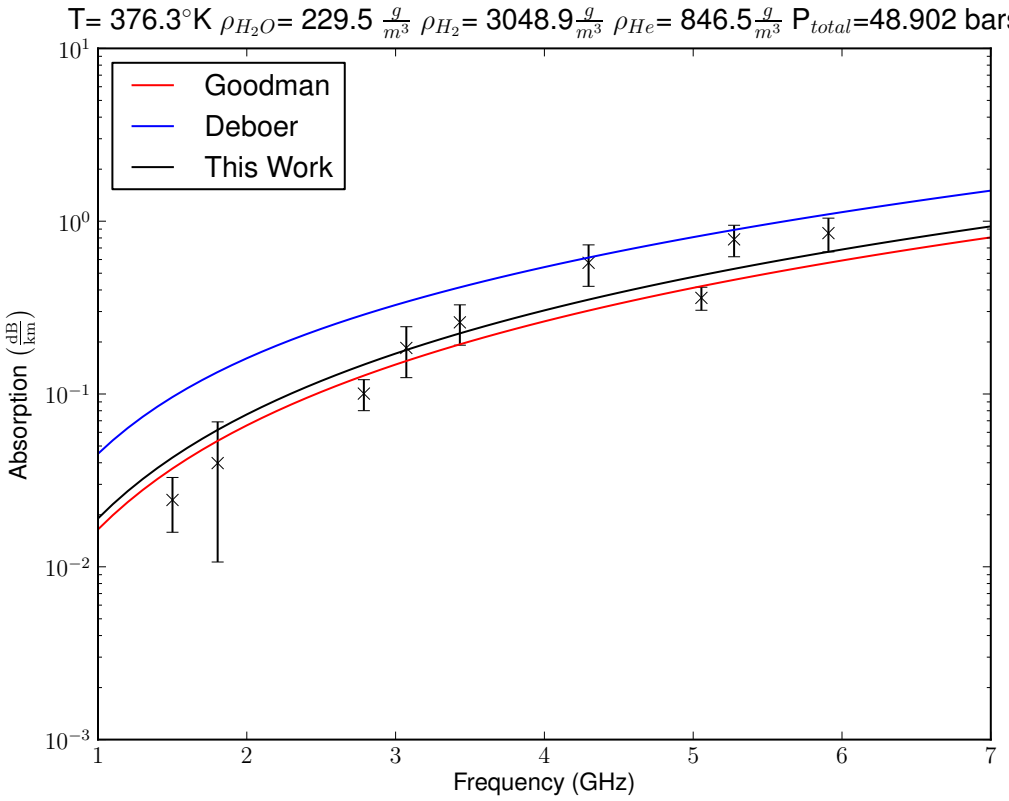

Figure 5.19: Experiment 3 with H_2/He mixture 48.9 bars total pressure.

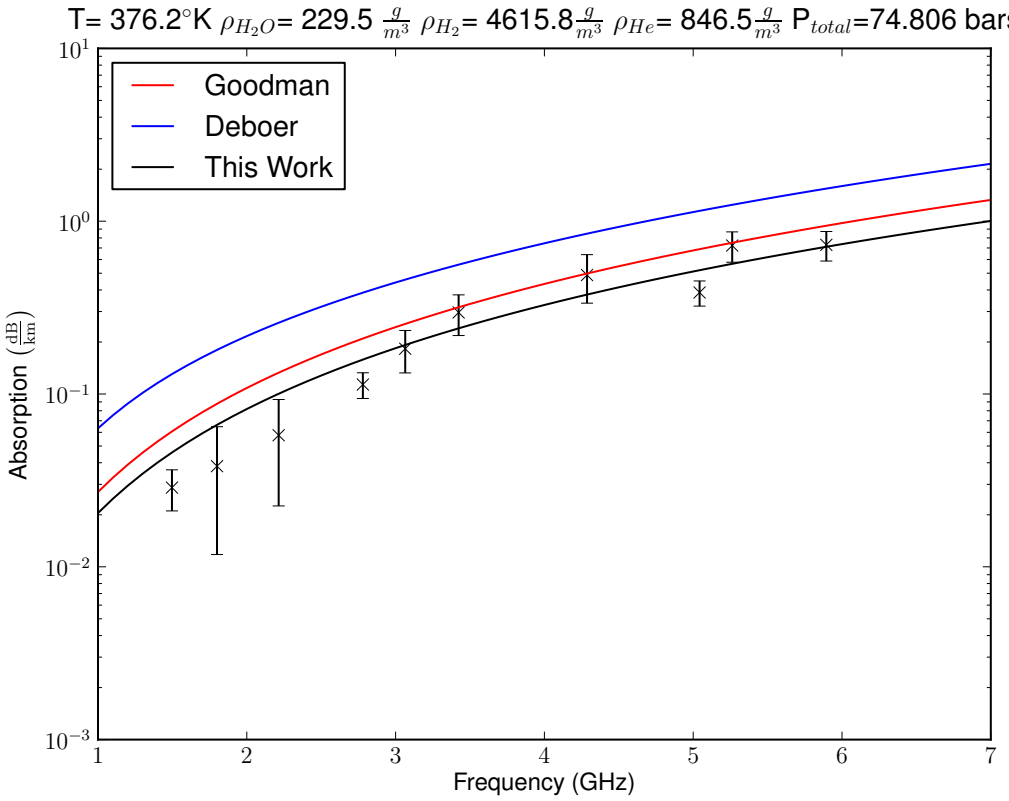

Figure 5.20: Experiment 3 with H_2/He mixture 74.8 bars total pressure.

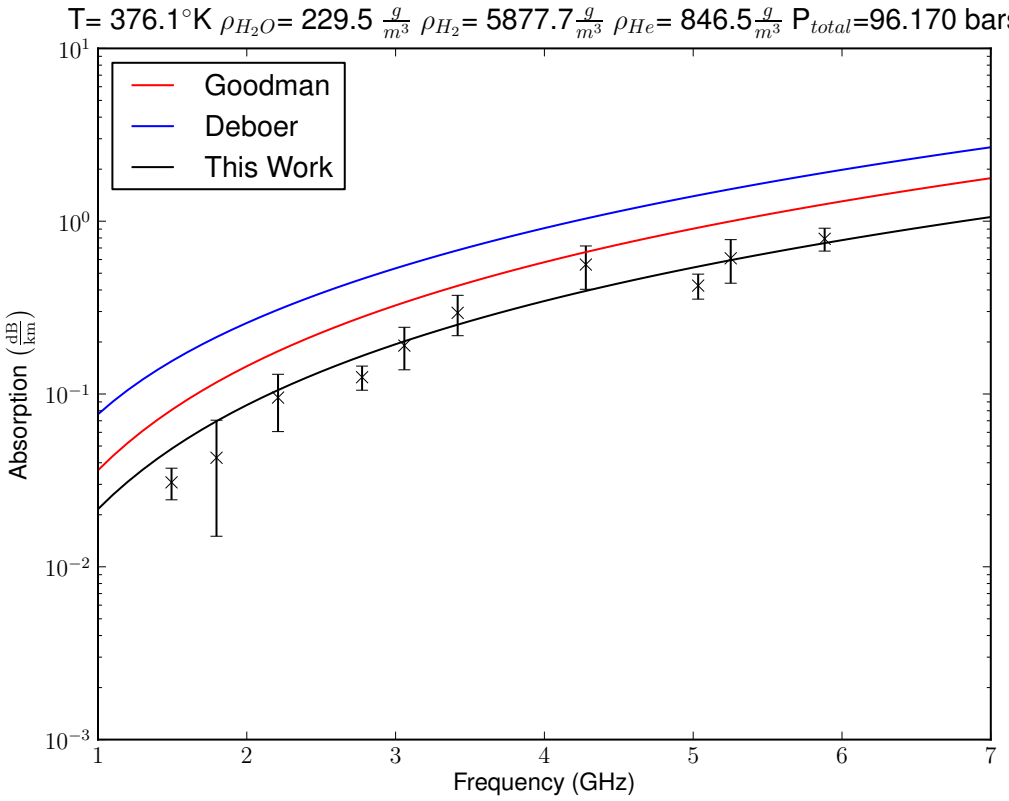

Figure 5.21: Experiment 3 with H_2/He mixture 96.1 bars total pressure.

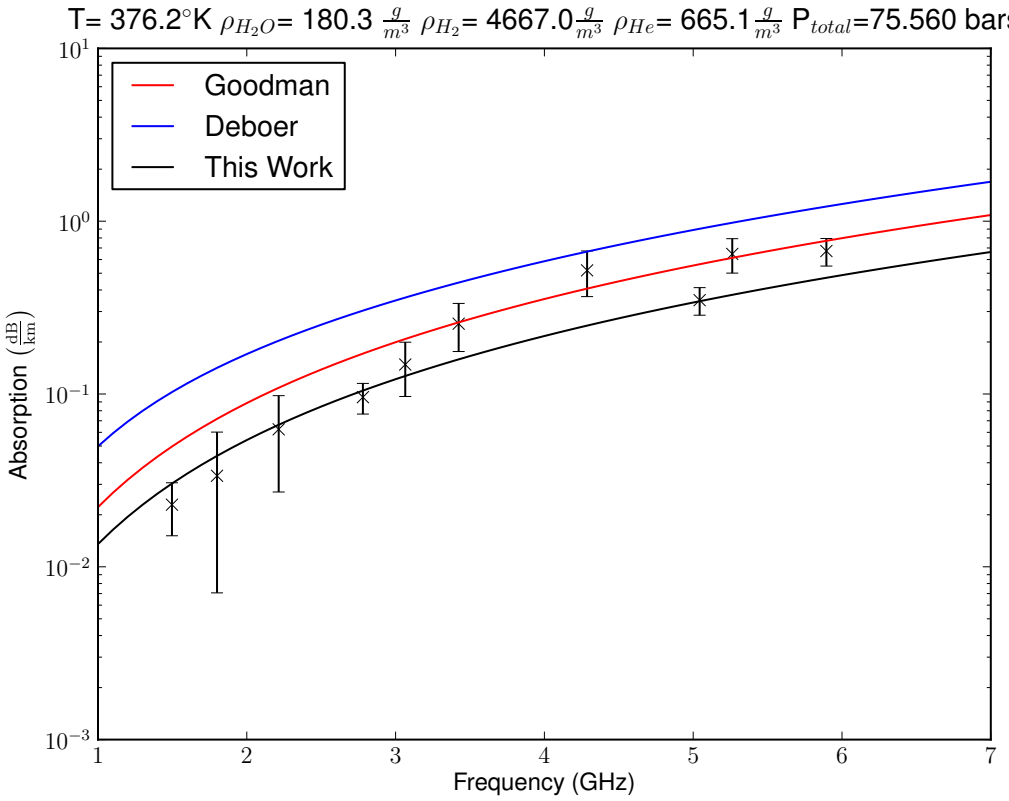

Figure 5.22: Experiment 3 with H_2/He mixture 75.6 bars total pressure (after maximum pressure).

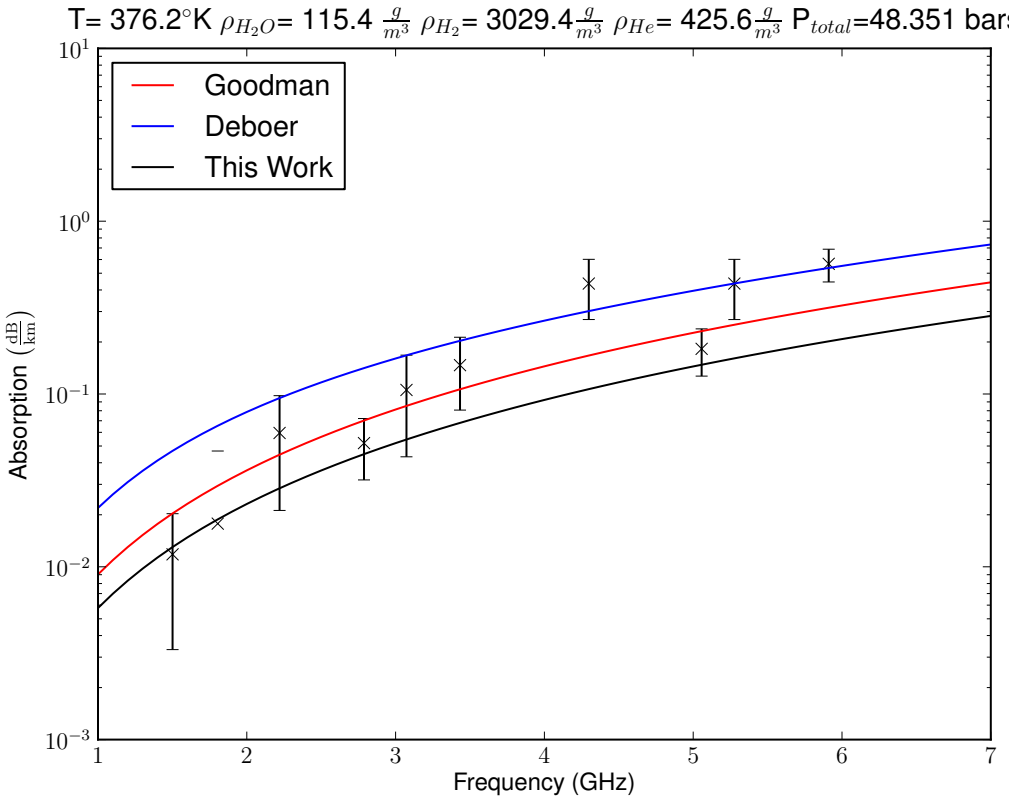

Figure 5.23: Experiment 3 with H_2/He mixture 48.4 bars total pressure (after maximum pressure).

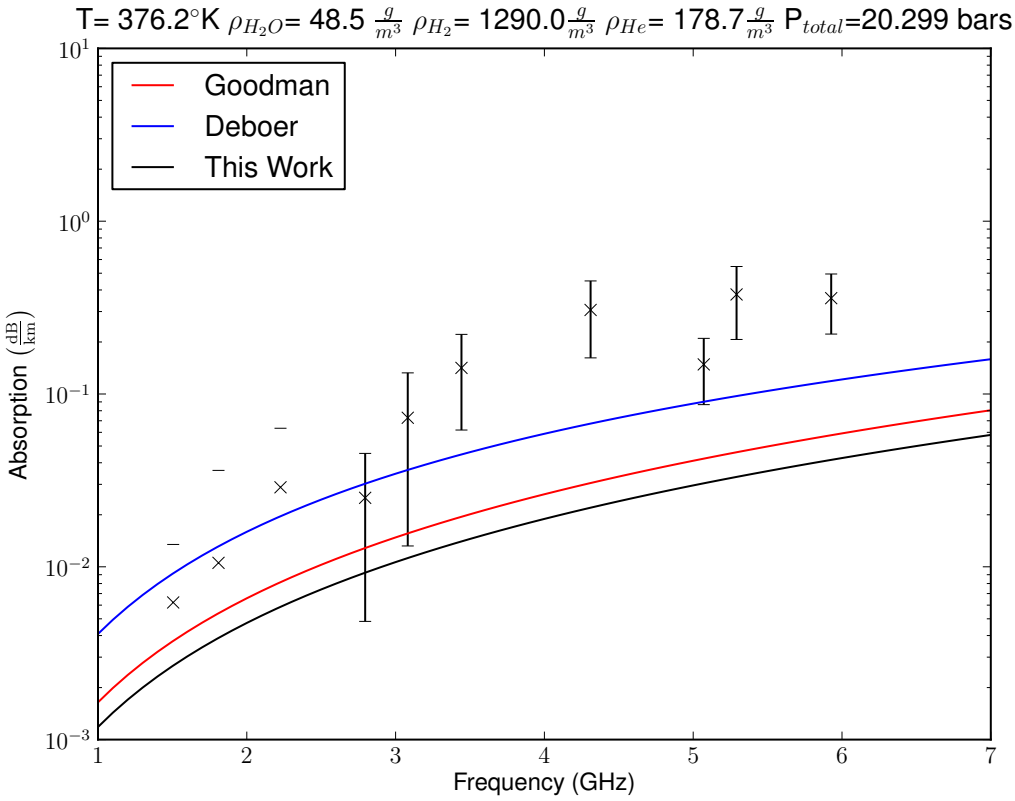

Figure 5.24: Experiment 3 with H_2/He mixture 20.3 bars total pressure (after maximum pressure).

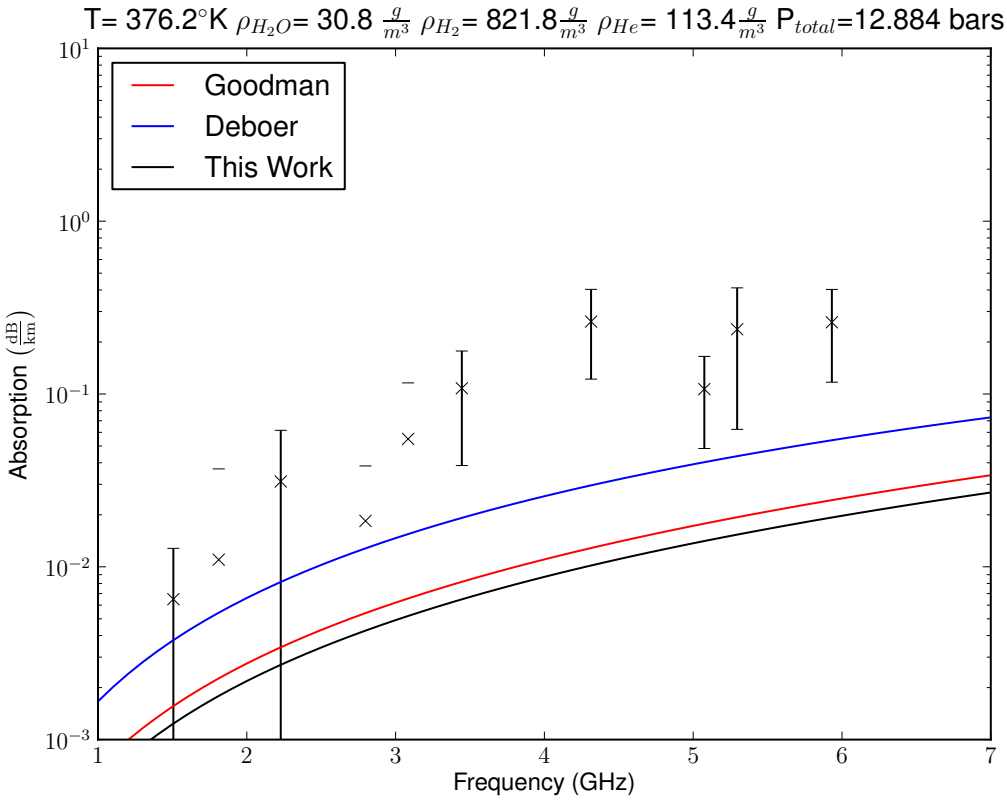

Figure 5.25: Experiment 3 with H_2/He mixture 12.9 bars total pressure (after maximum pressure).

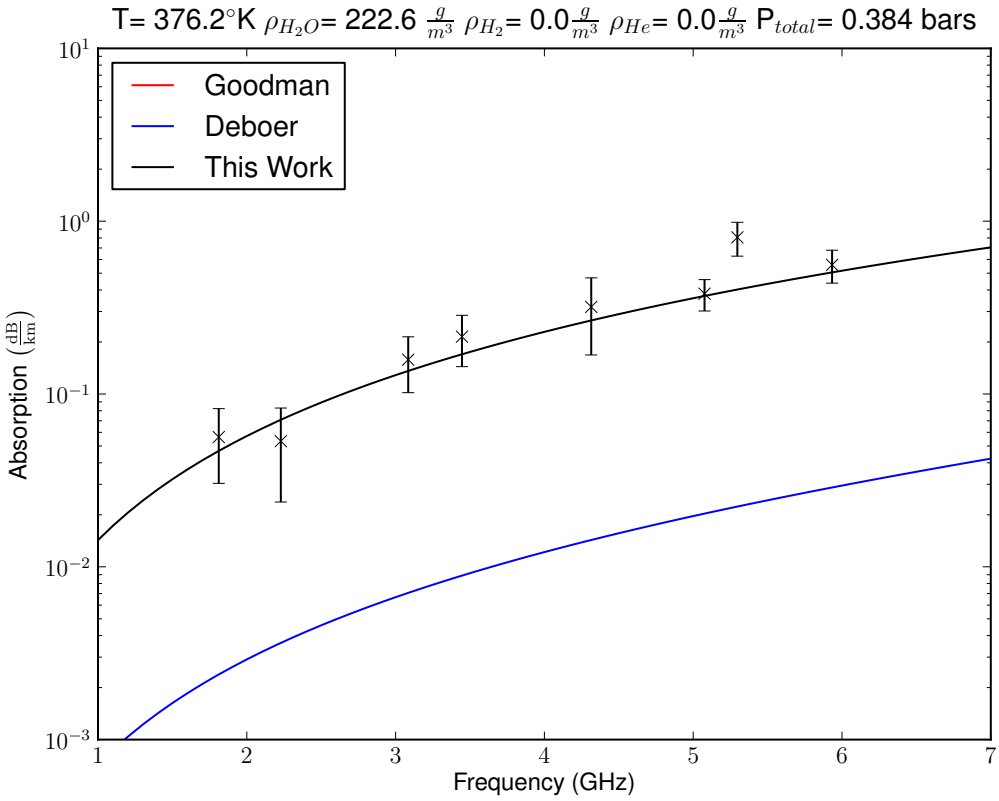

Figure 5.26: Experiment 4 with pure water vapor.

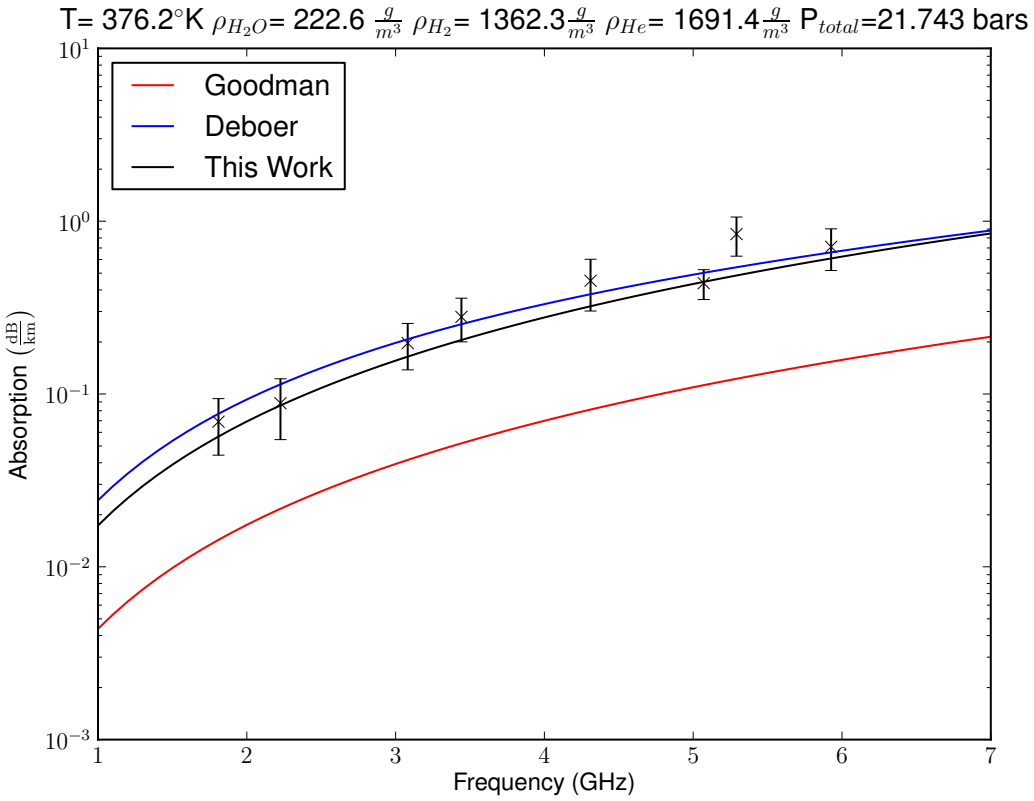

Figure 5.27: Experiment 4 with H_2/He mixture 21.7 bars total pressure

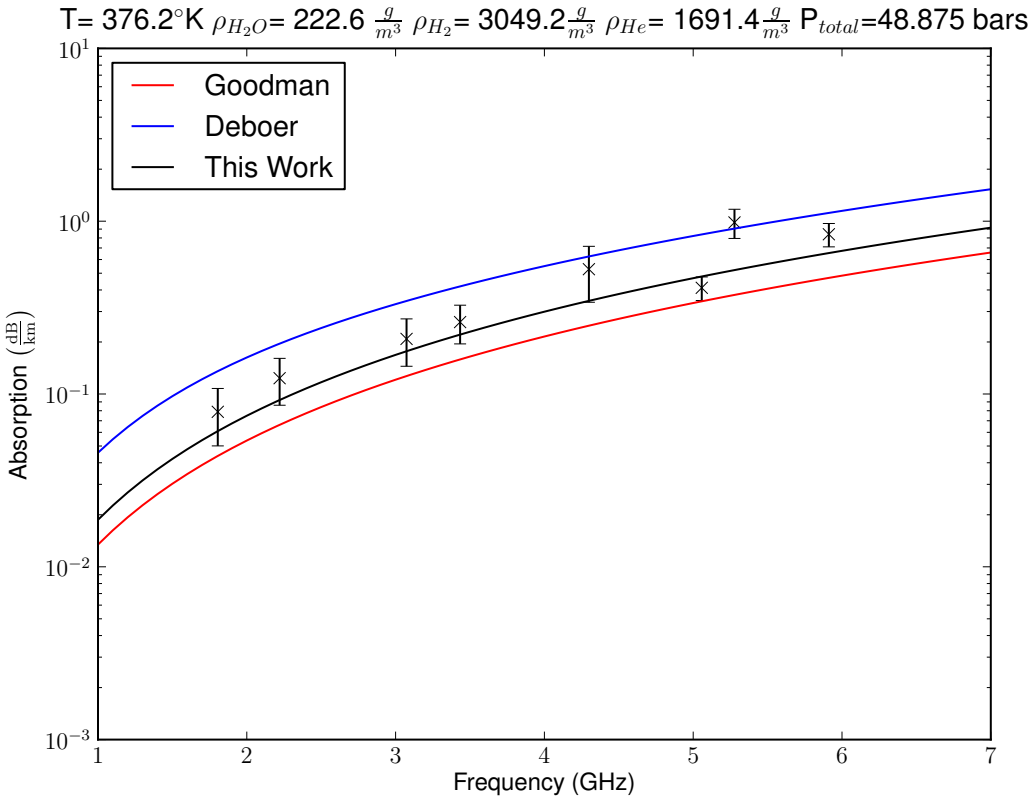

Figure 5.28: Experiment 4 with H_2/He mixture 48.9 bars total pressure.

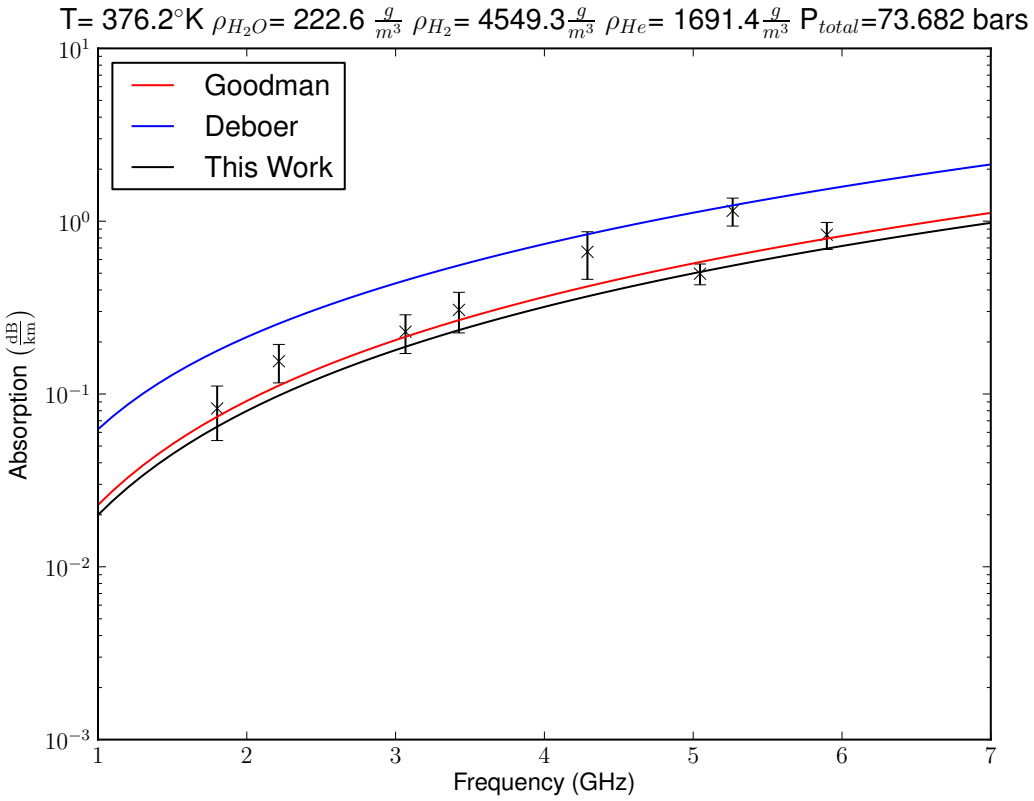

Figure 5.29: Experiment 4 with H_2/He mixture 73.7 bars total pressure.

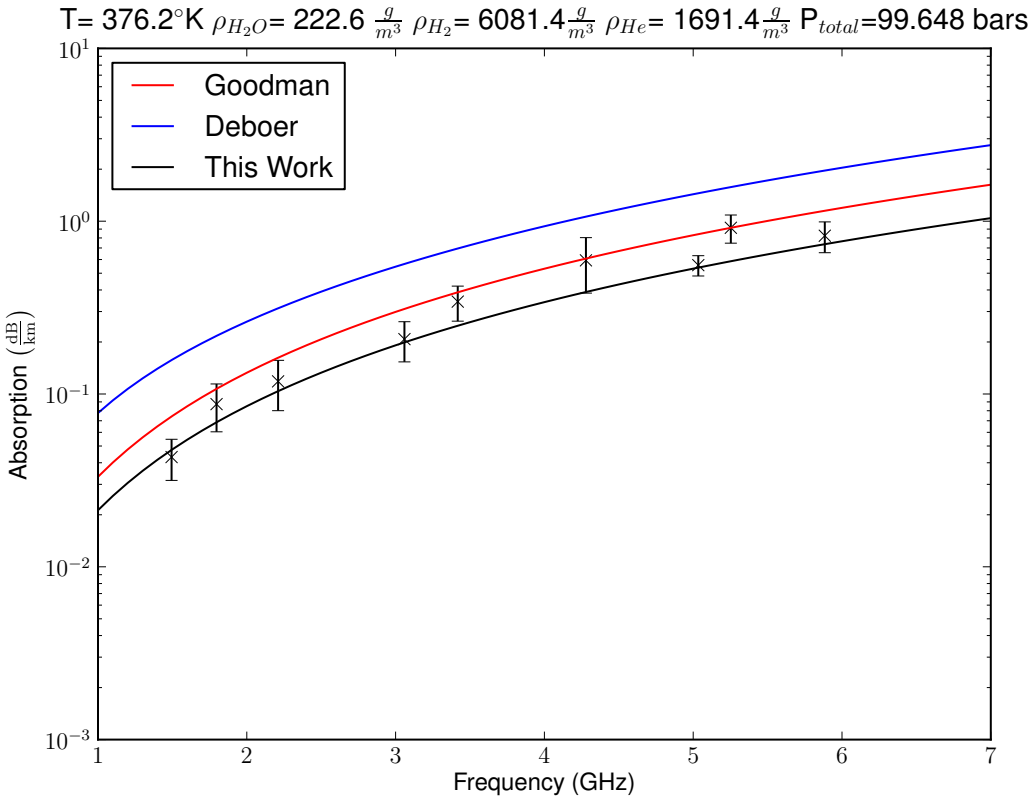

Figure 5.30: Experiment 4 with H_2/He mixture 99.6 bars total pressure .

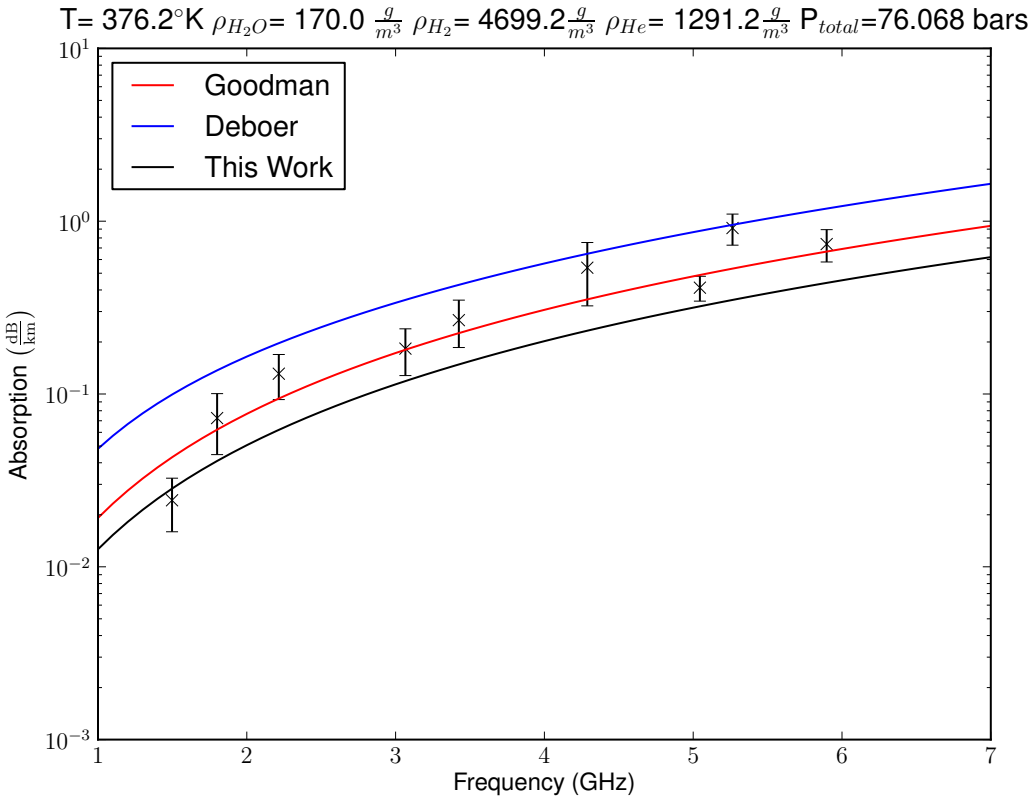

Figure 5.31: Experiment 4 with H_2/He mixture 76.1 bars total pressure (after maximum pressure).

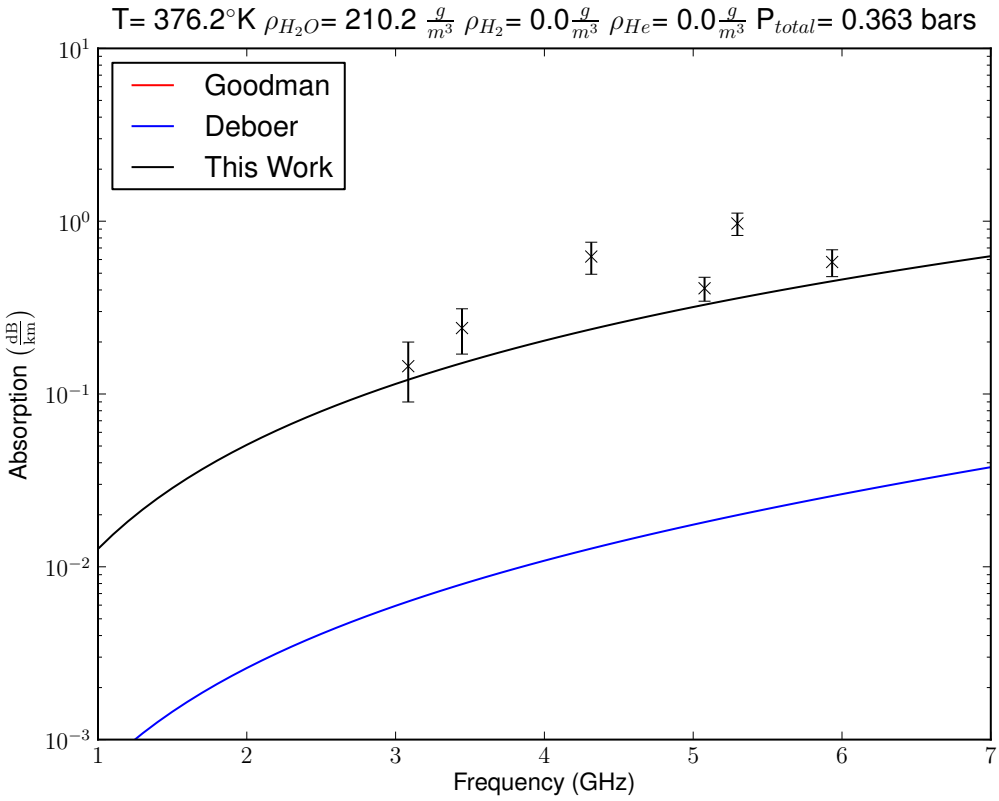

Figure 5.32: Experiment 5 with pure water vapor.

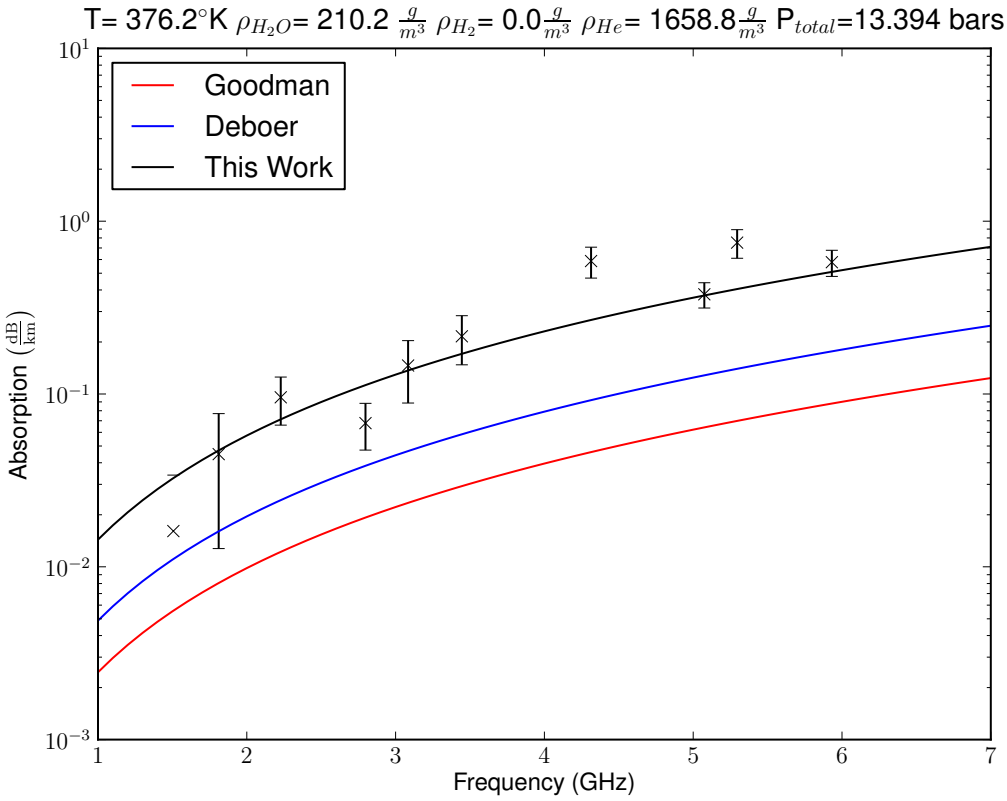

Figure 5.33: Experiment 5 with He mixture 13.4 bars total pressure

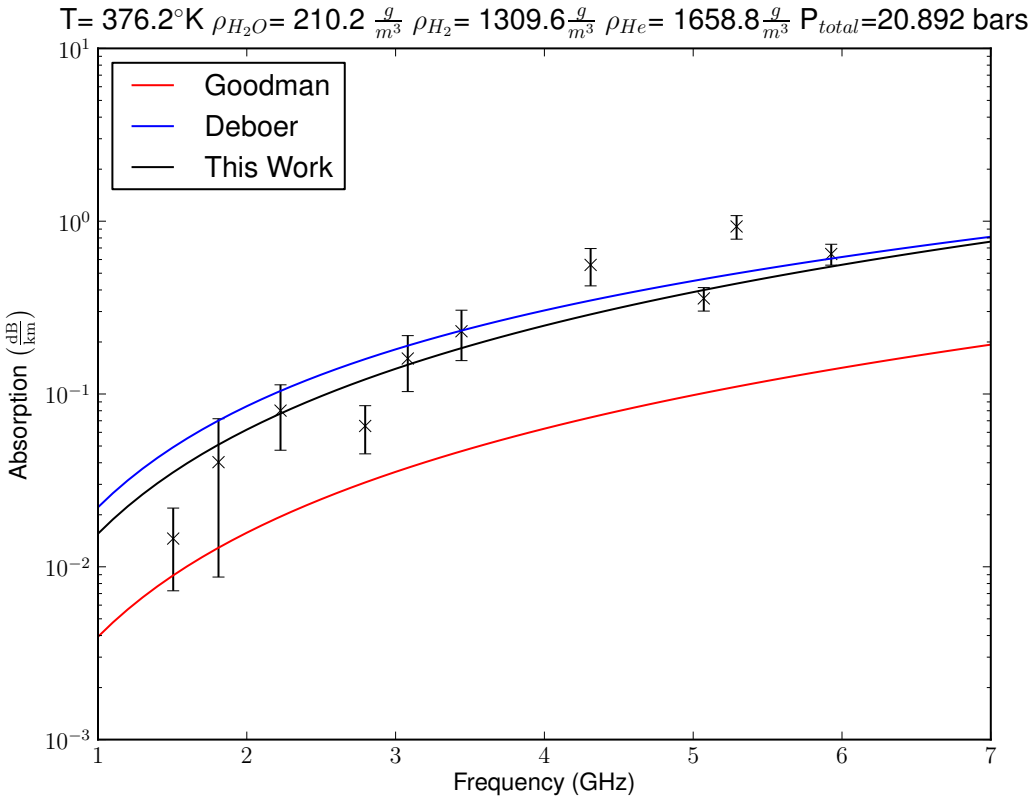

Figure 5.34: Experiment 5 with H_2/He mixture 20.9 bars total pressure

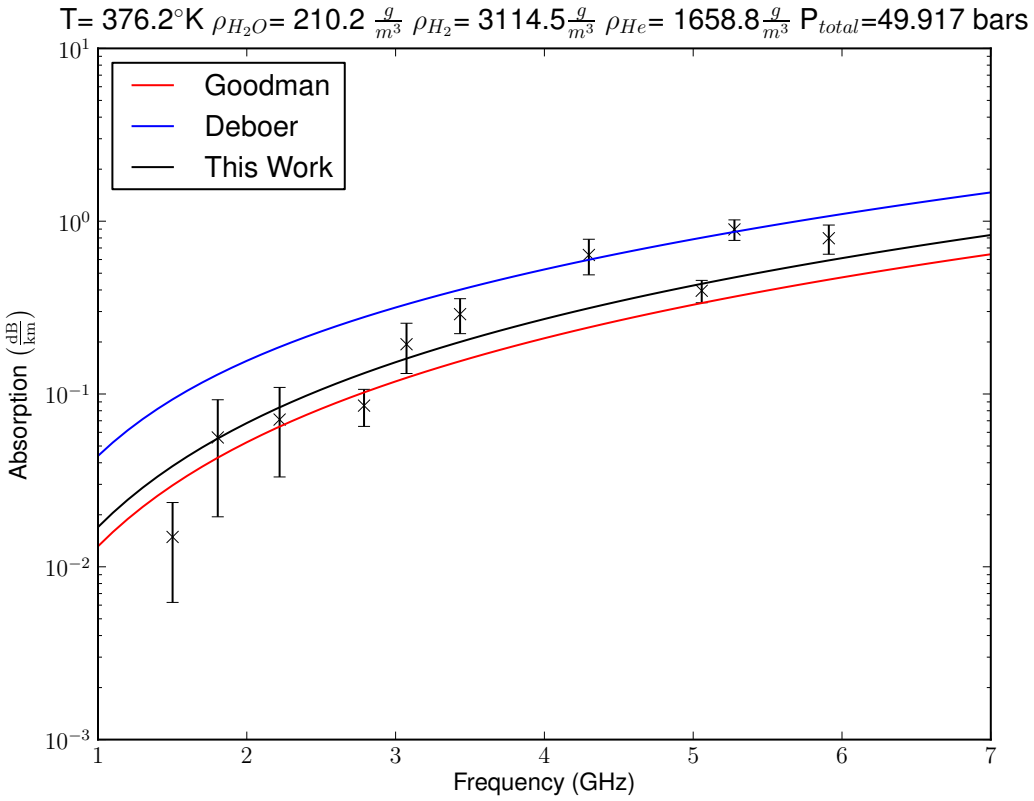

Figure 5.35: Experiment 5 with H_2/He mixture 49.9 bars total pressure.

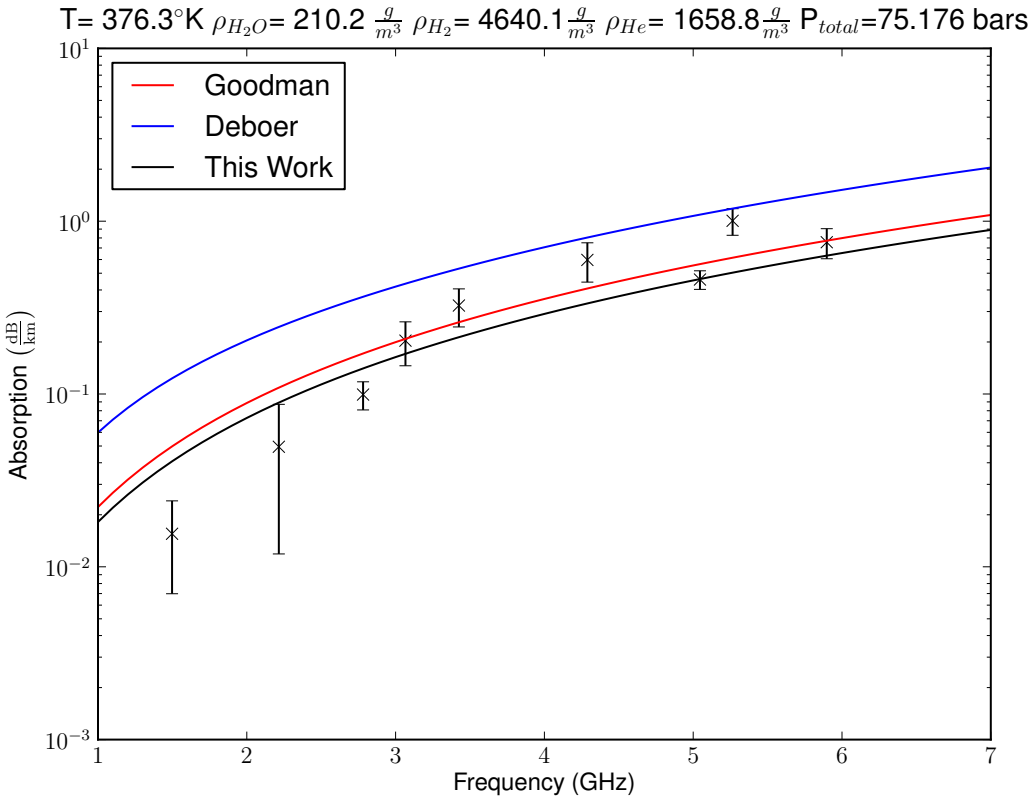

Figure 5.36: Experiment 5 with H_2/He mixture 75.1 bars total pressure.

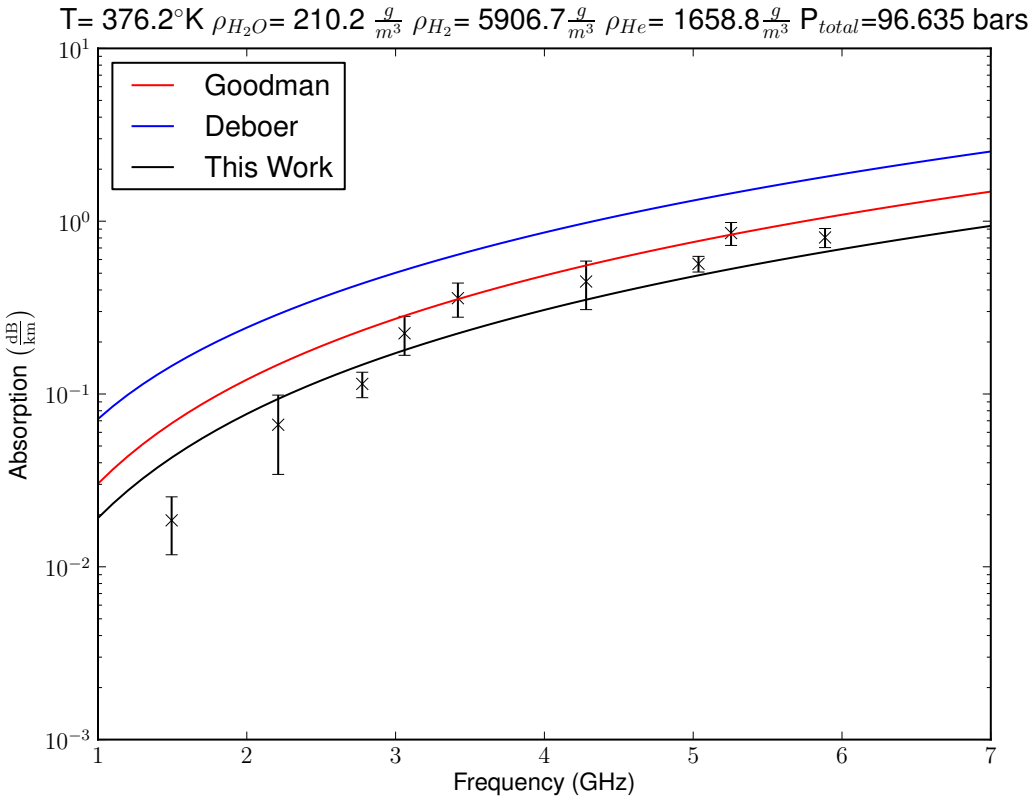

Figure 5.37: Experiment 5 with H_2/He mixture 96.6 bars total pressure.

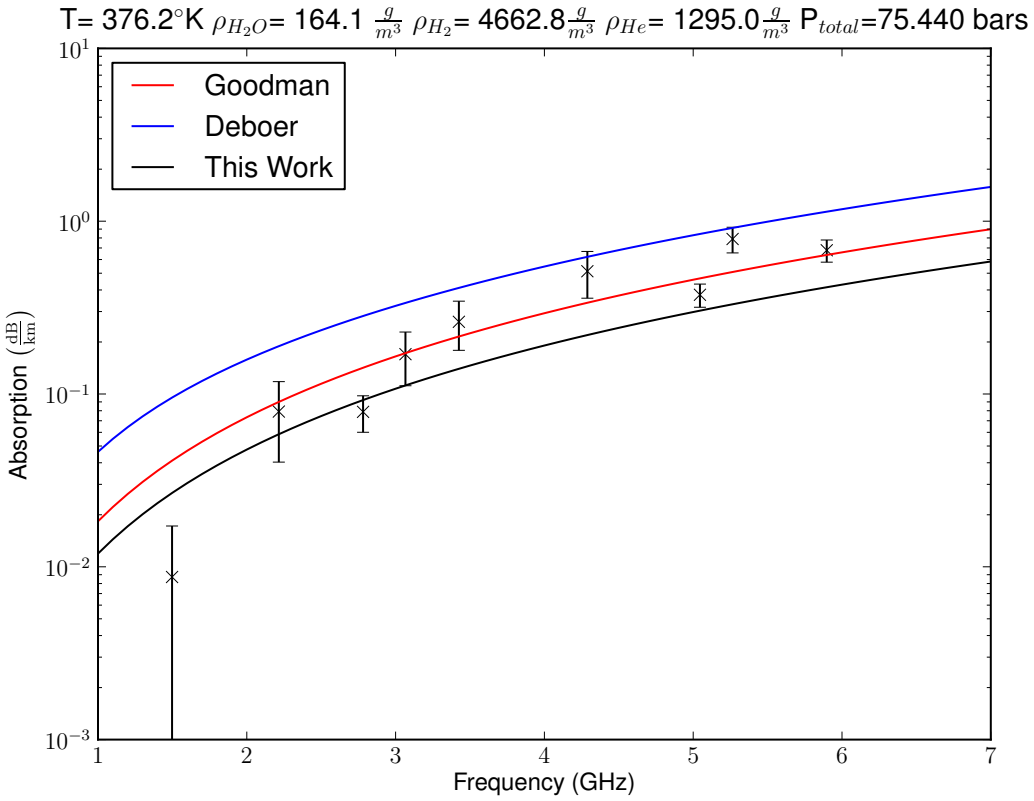

Figure 5.38: Experiment 5 with H_2/He mixture 75.4 bars total pressure (after maximum pressure).

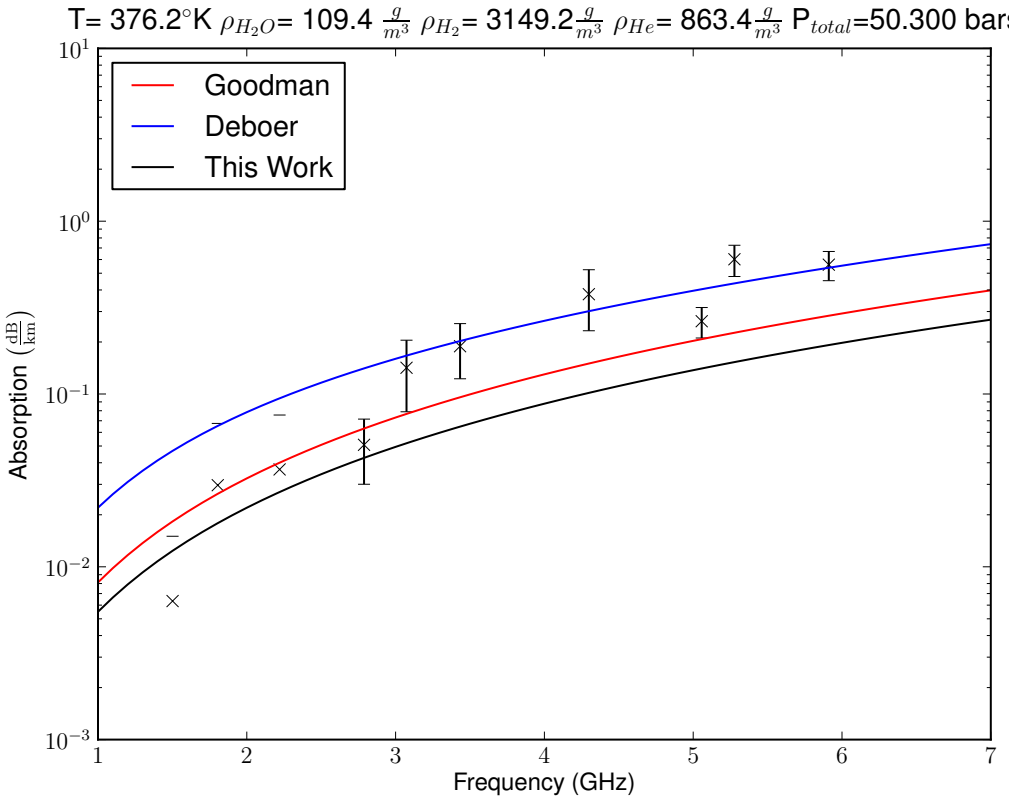

Figure 5.39: Experiment 5 with H_2/He mixture 50.3 bars total pressure (after maximum pressure).

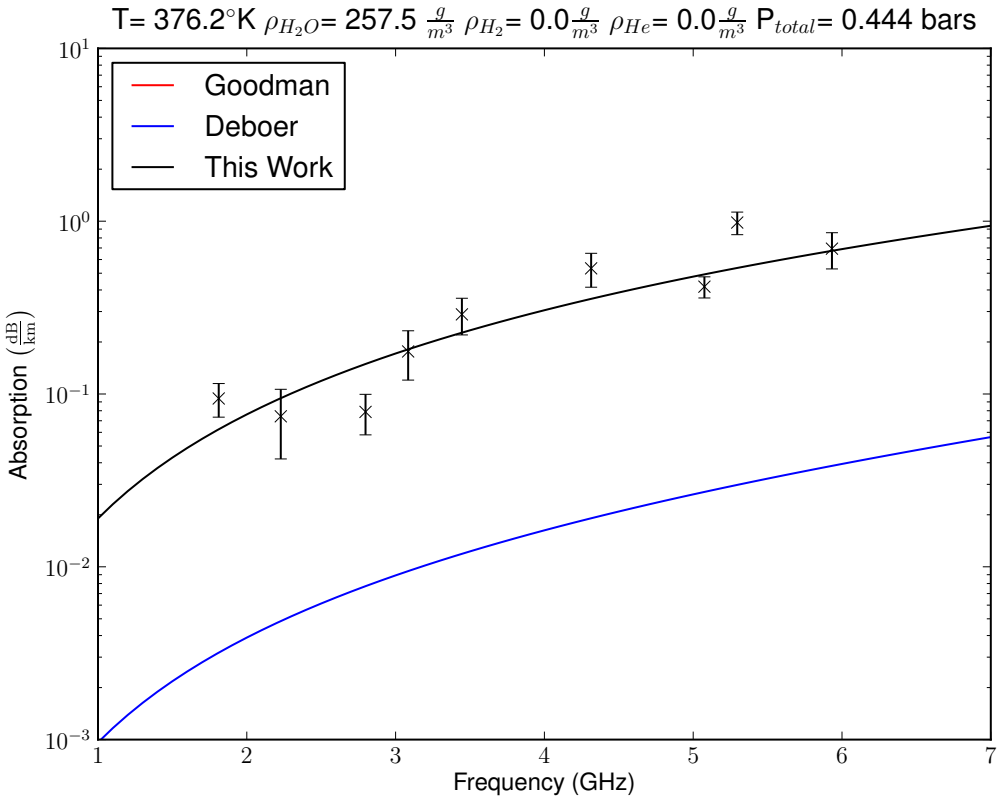

Figure 5.40: Experiment 6 with pure water vapor.

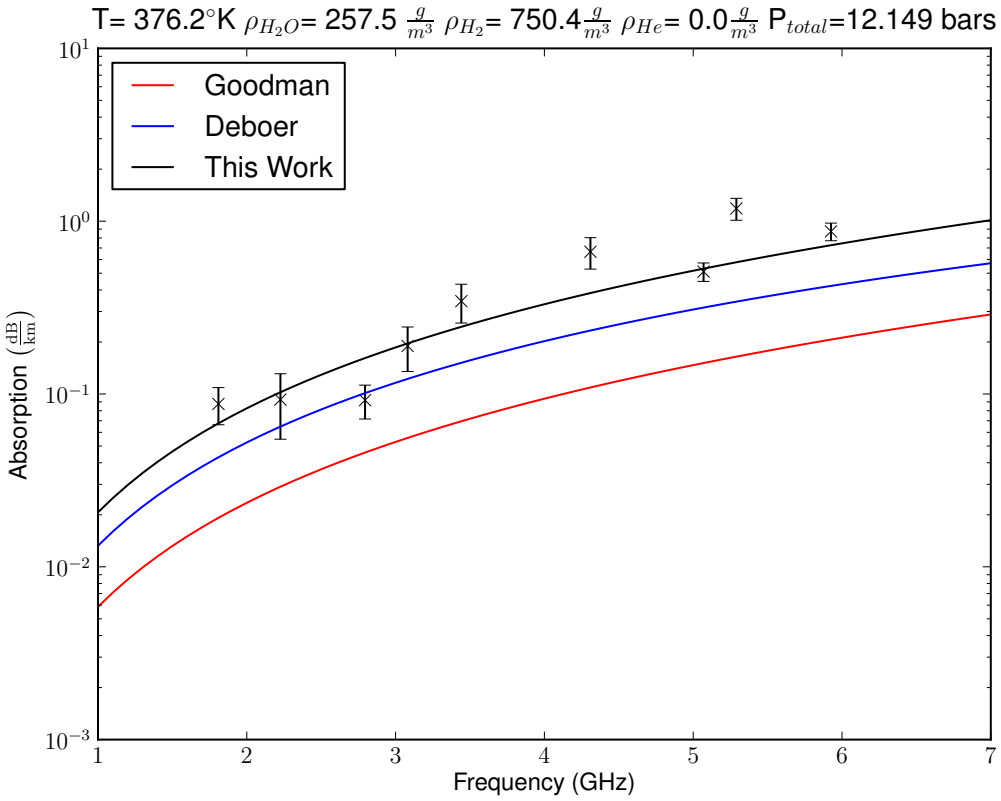

Figure 5.41: Experiment 6 with He mixture 12.1 bars total pressure

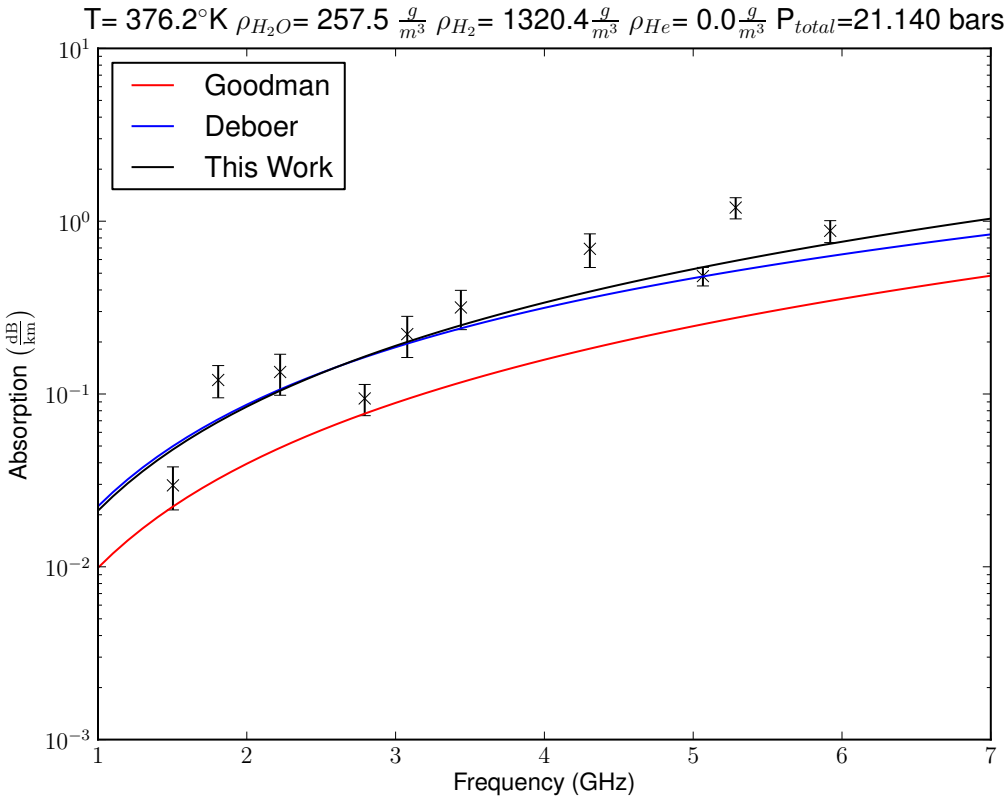

Figure 5.42: Experiment 6 with H_2/He mixture 21.1 bars total pressure

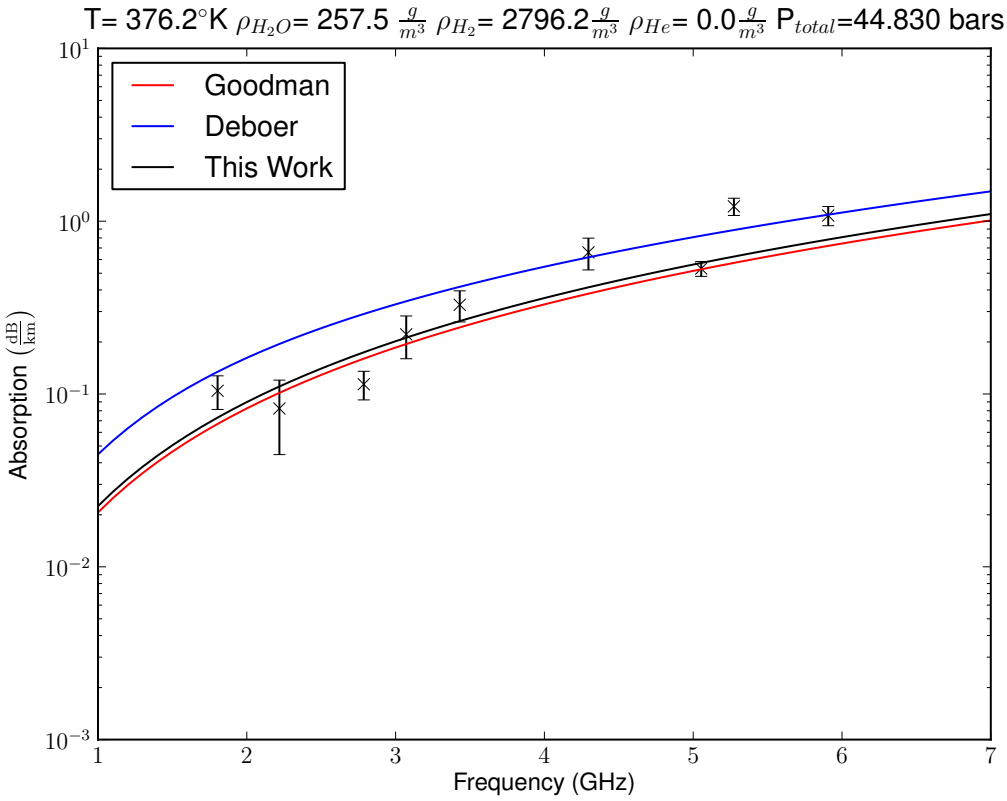

Figure 5.43: Experiment 6 with H_2/He mixture 44.8 bars total pressure.

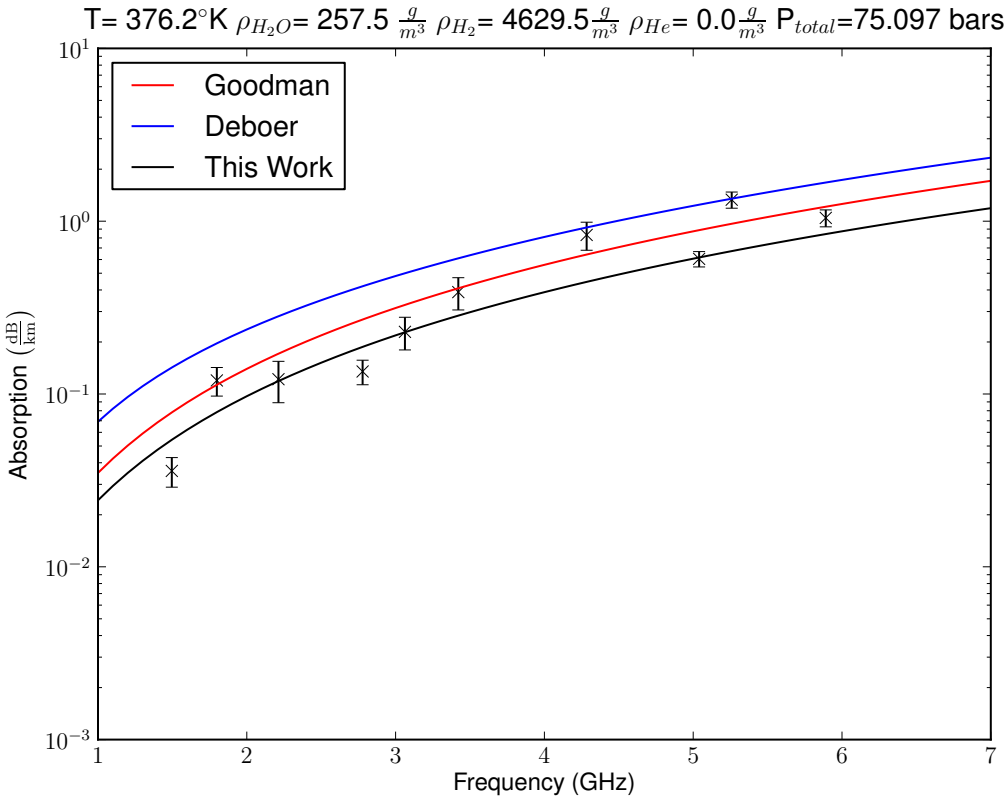

Figure 5.44: Experiment 6 with H_2/He mixture 75.1 bars total pressure.

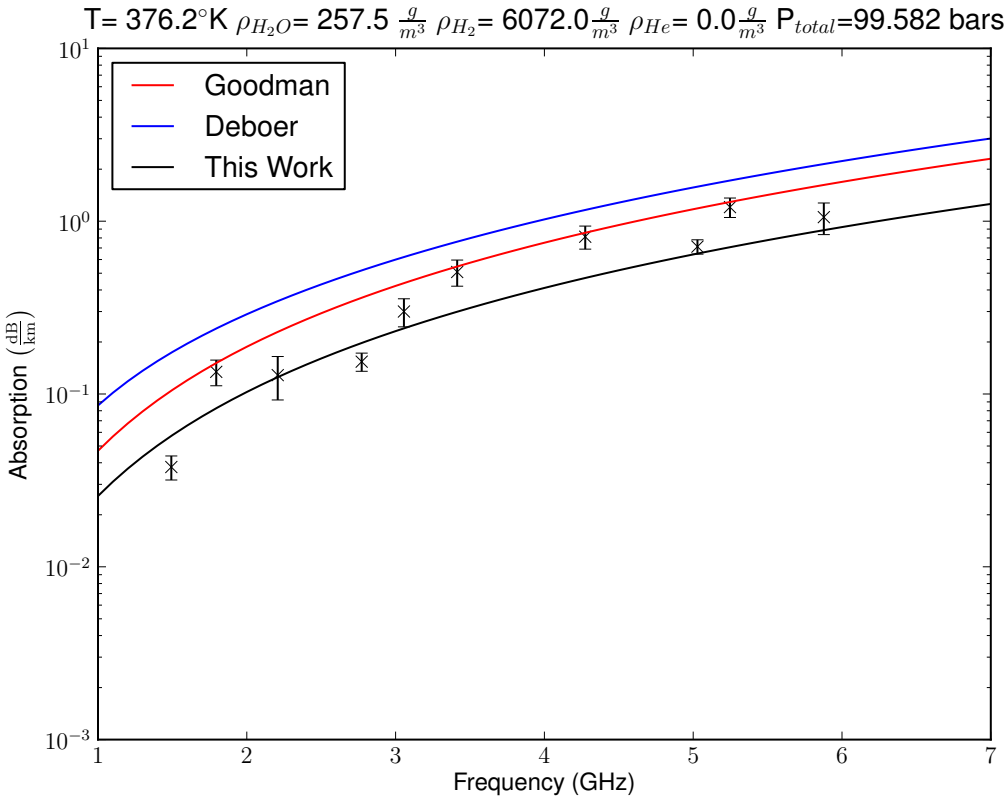

Figure 5.45: Experiment 6 with H_2/He mixture 99.6 bars total pressure.

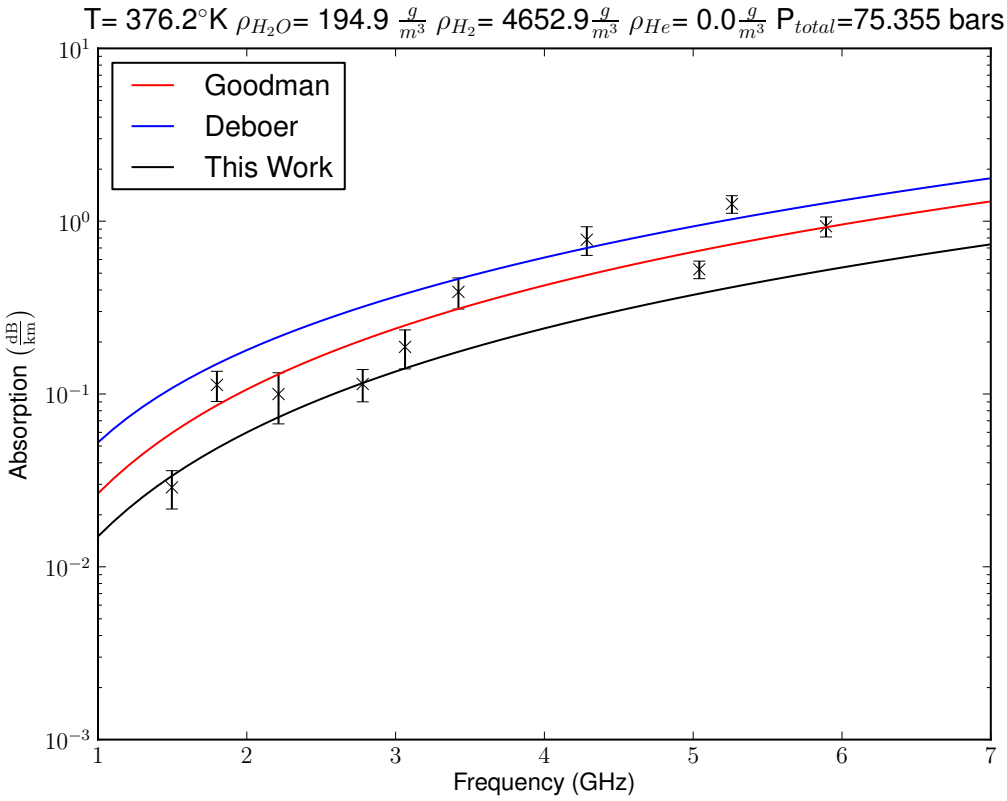

Figure 5.46: Experiment 6 with H_2/He mixture 75.4 bars total pressure (after maximum pressure).

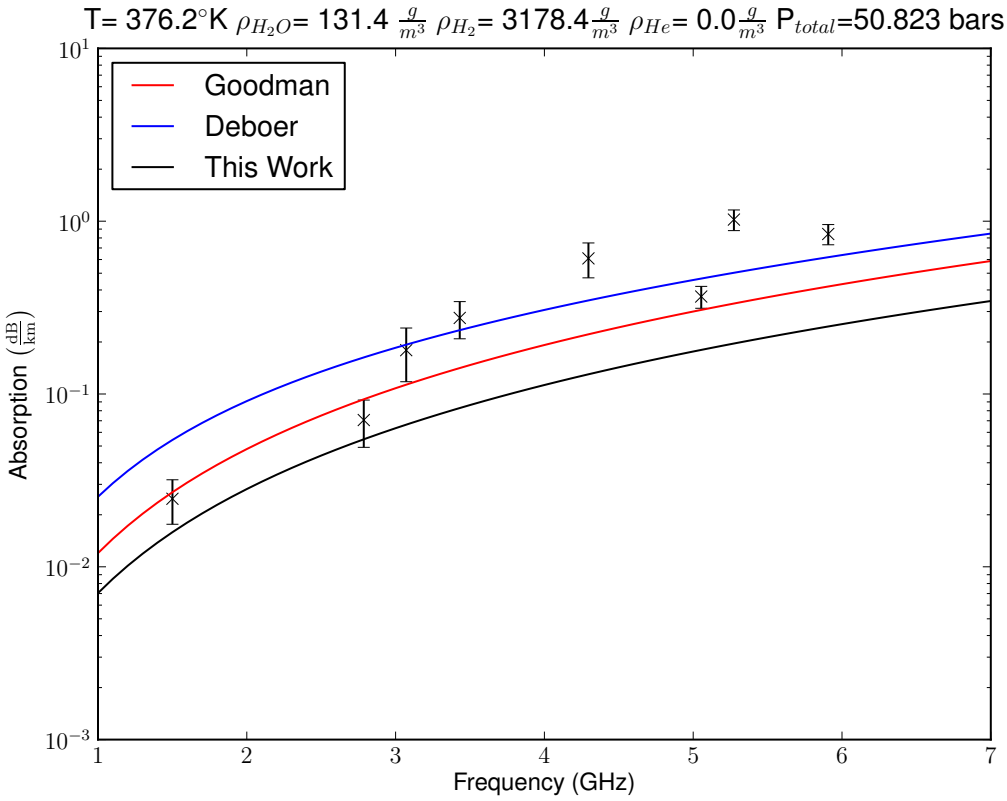

Figure 5.47: Experiment 6 with H_2/He mixture 50.8 bars total pressure (after maximum pressure).

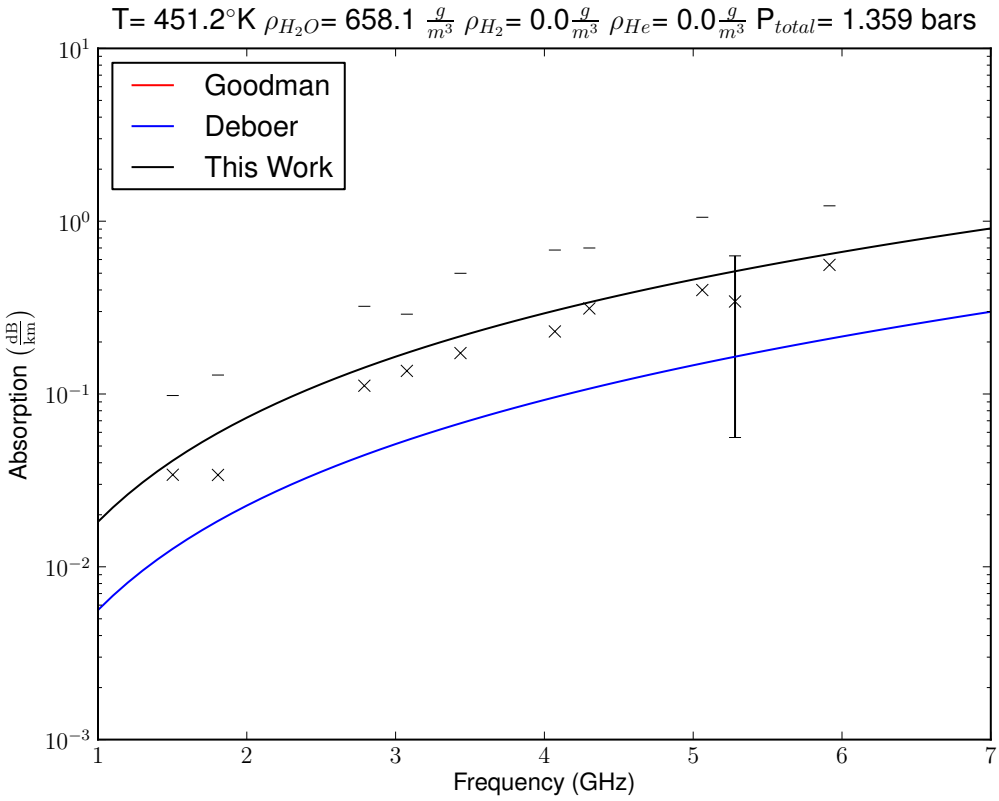

Figure 5.48: Experiment 7 with pure water vapor.

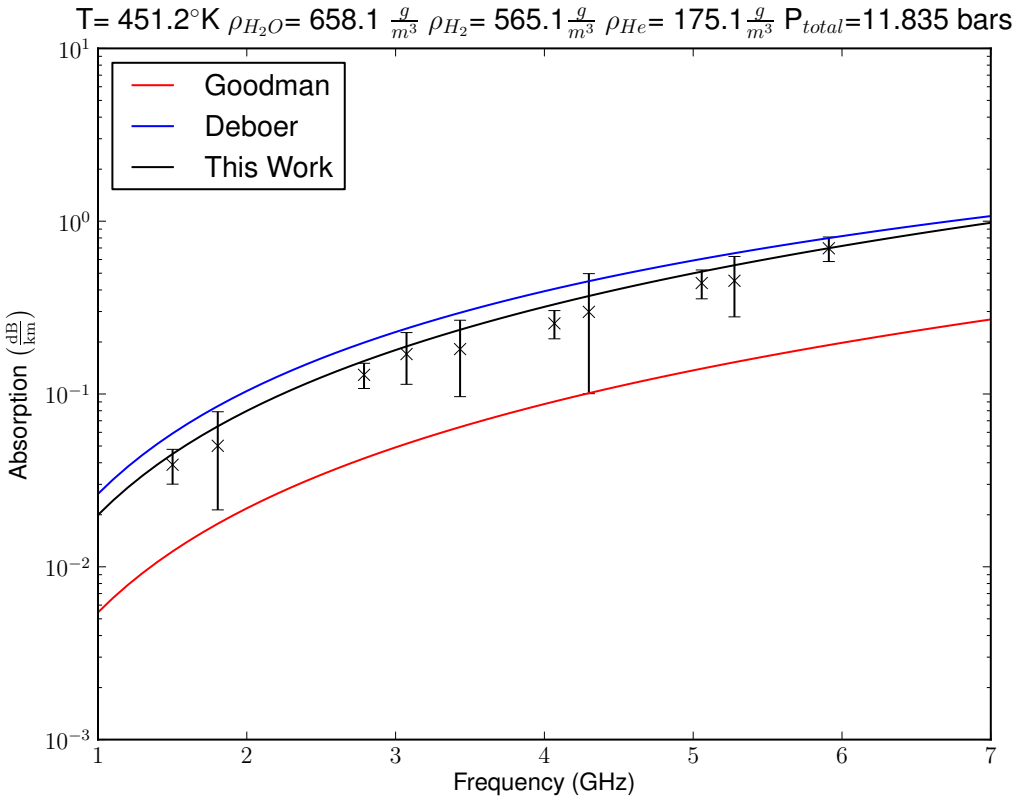

Figure 5.49: Experiment 7 with H_2/He mixture 11.8 bars total pressure

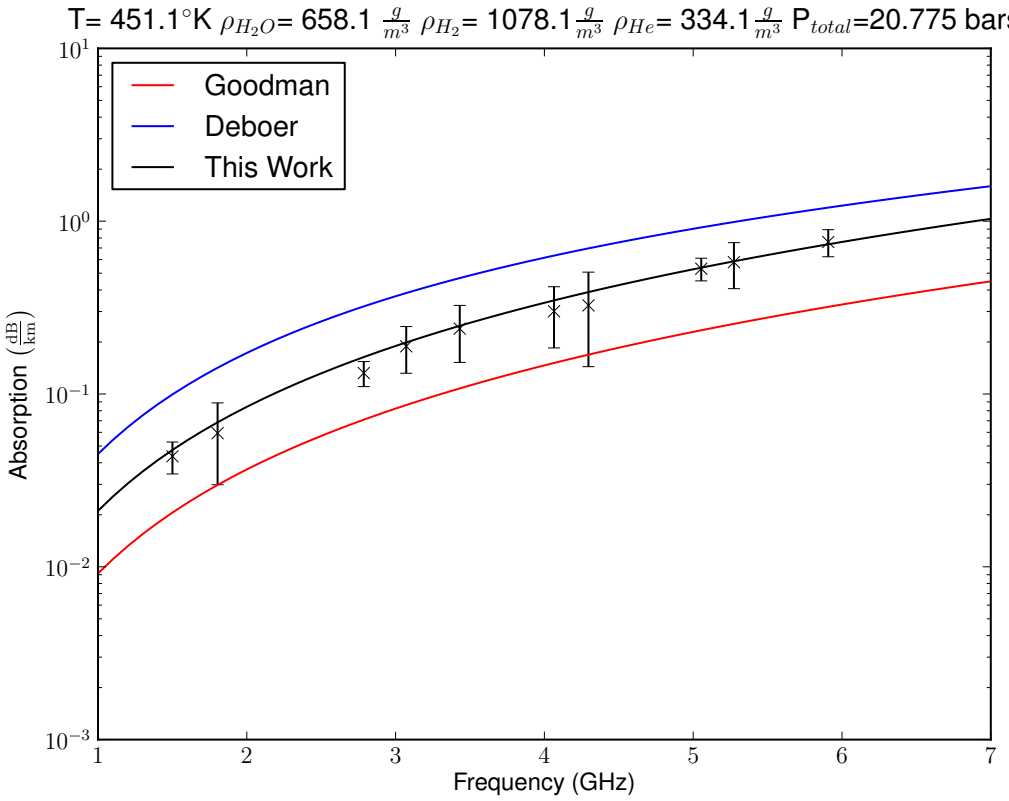

Figure 5.50: Experiment 7 with H_2/He mixture 20.8 bars total pressure

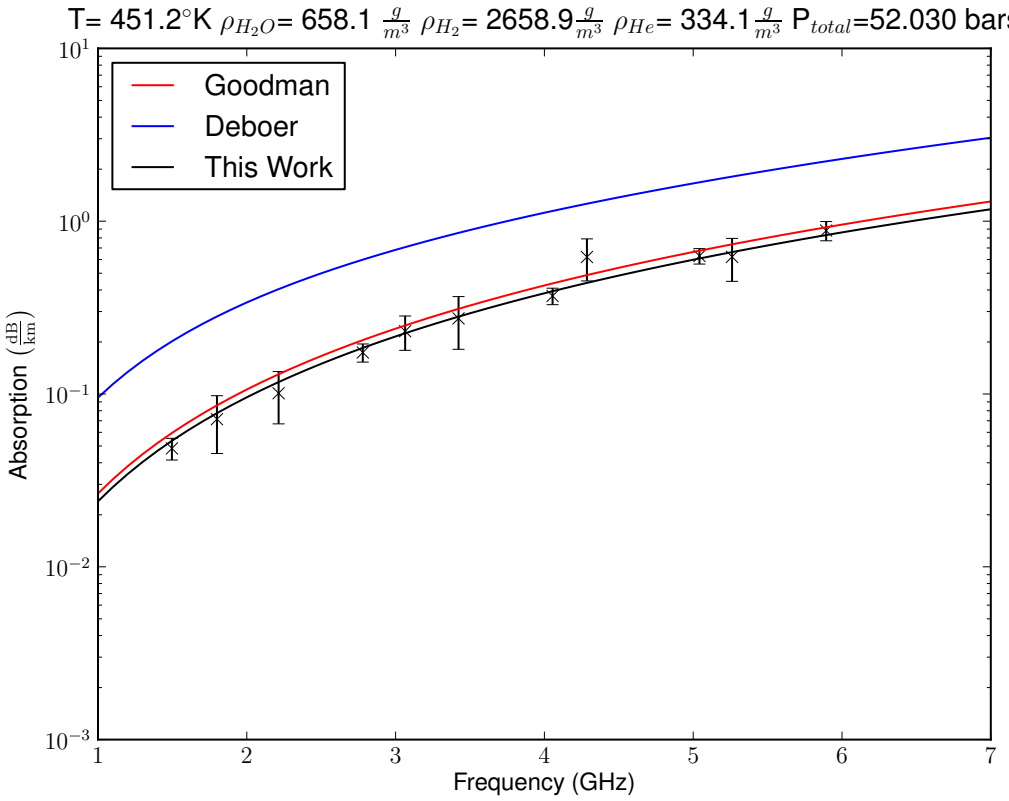

Figure 5.51: Experiment 7 with H_2/He mixture 52 bars total pressure.

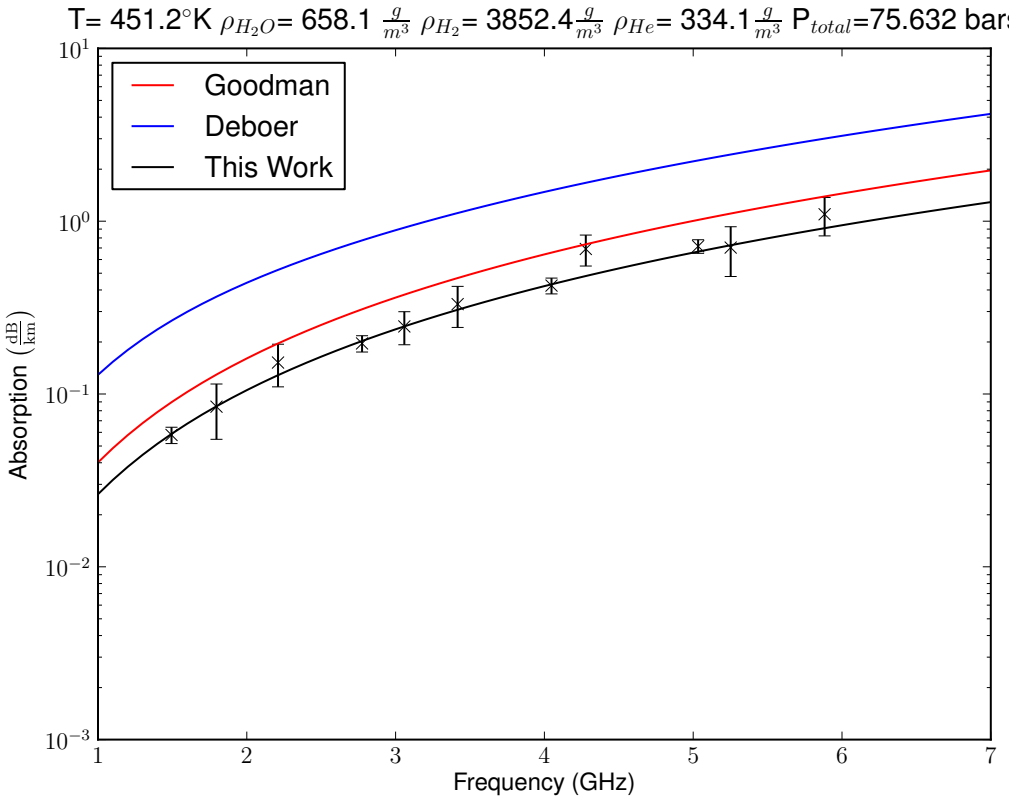

Figure 5.52: Experiment 7 with H_2/He mixture 75.6 bars total pressure.

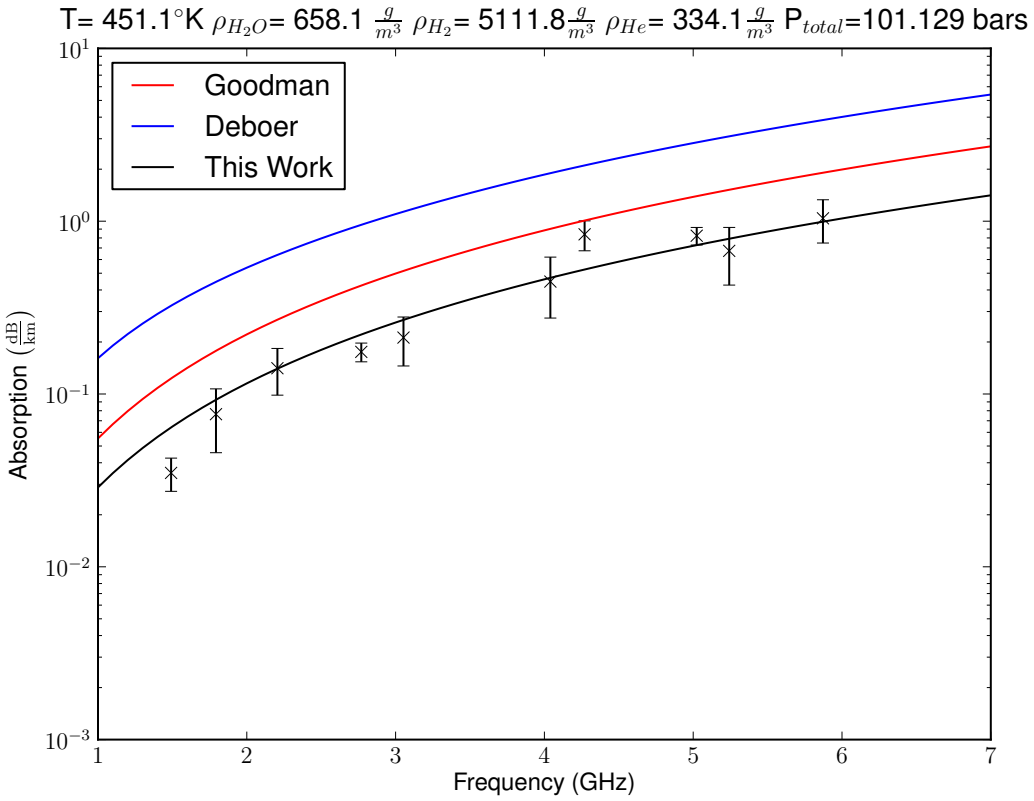

Figure 5.53: Experiment 7 with H_2/He mixture 101.1 bars total pressure.

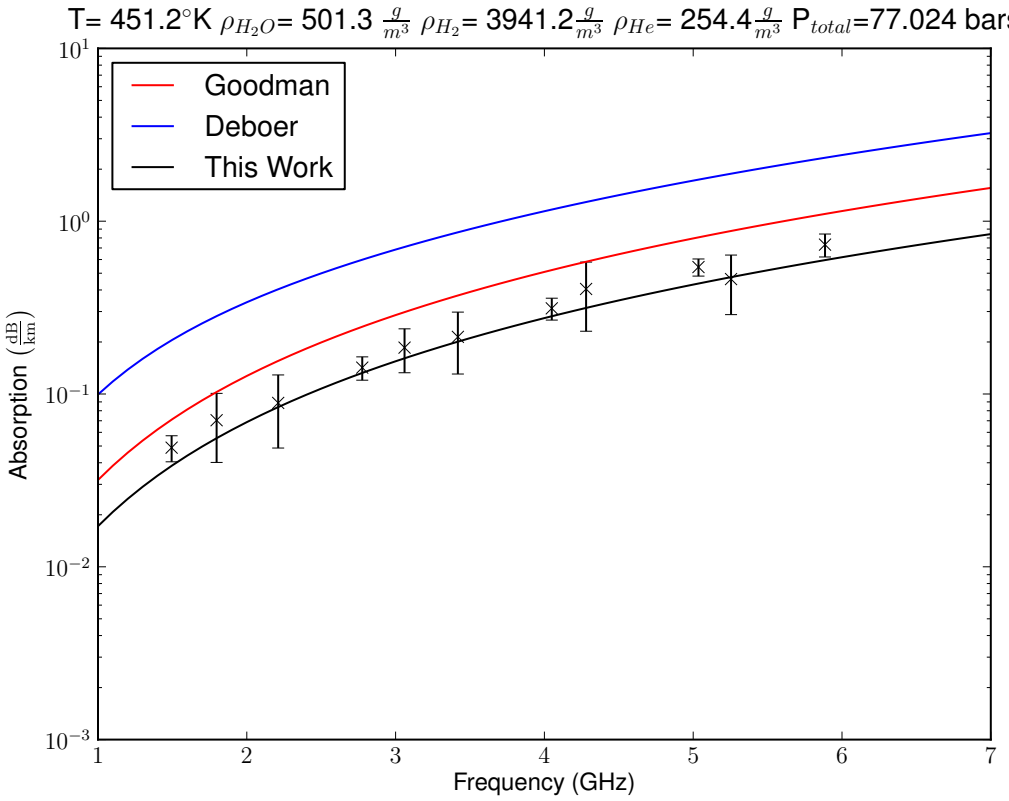

Figure 5.54: Experiment 7 with H_2/He mixture 77 bars total pressure (after maximum pressure).

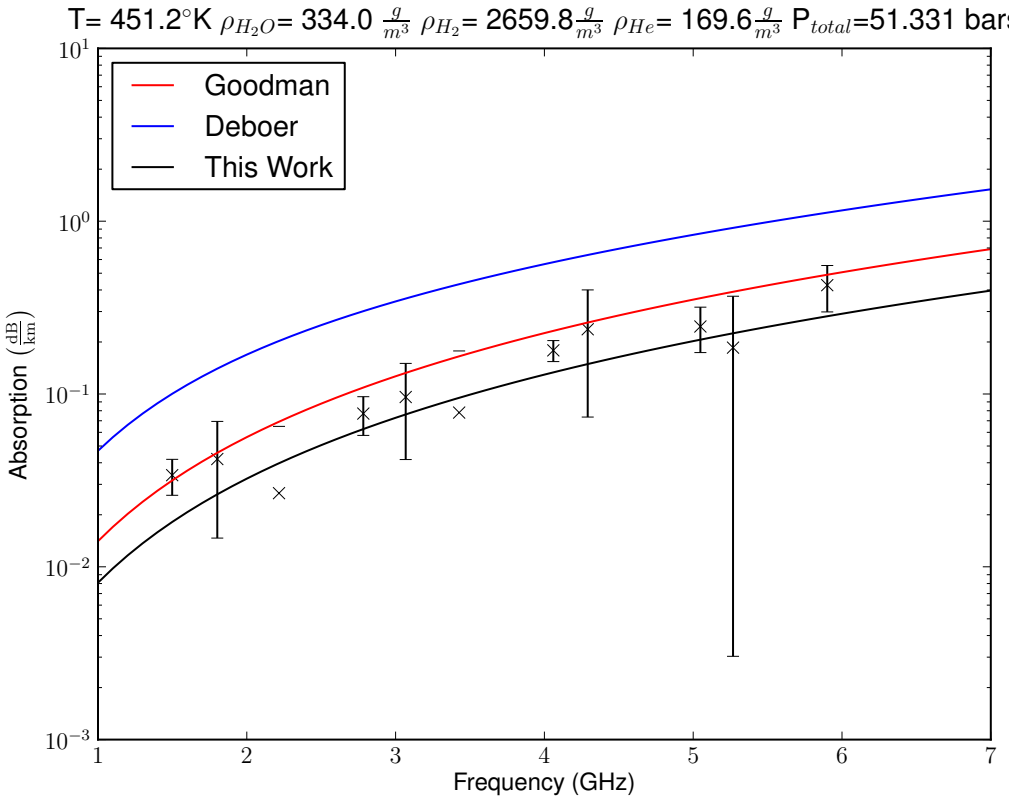

Figure 5.55: Experiment 7 with H_2/He mixture 51.3 bars total pressure (after maximum pressure).

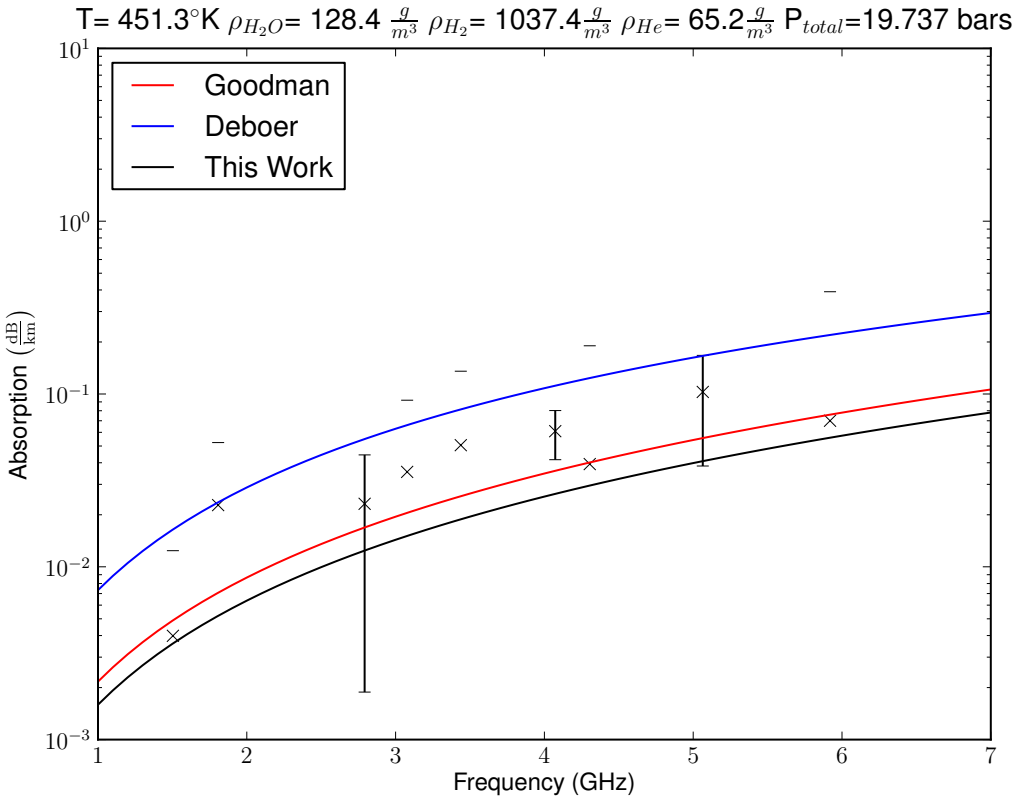

Figure 5.56: Experiment 7 with H_2/He mixture 19.7 bars total pressure (after maximum pressure).

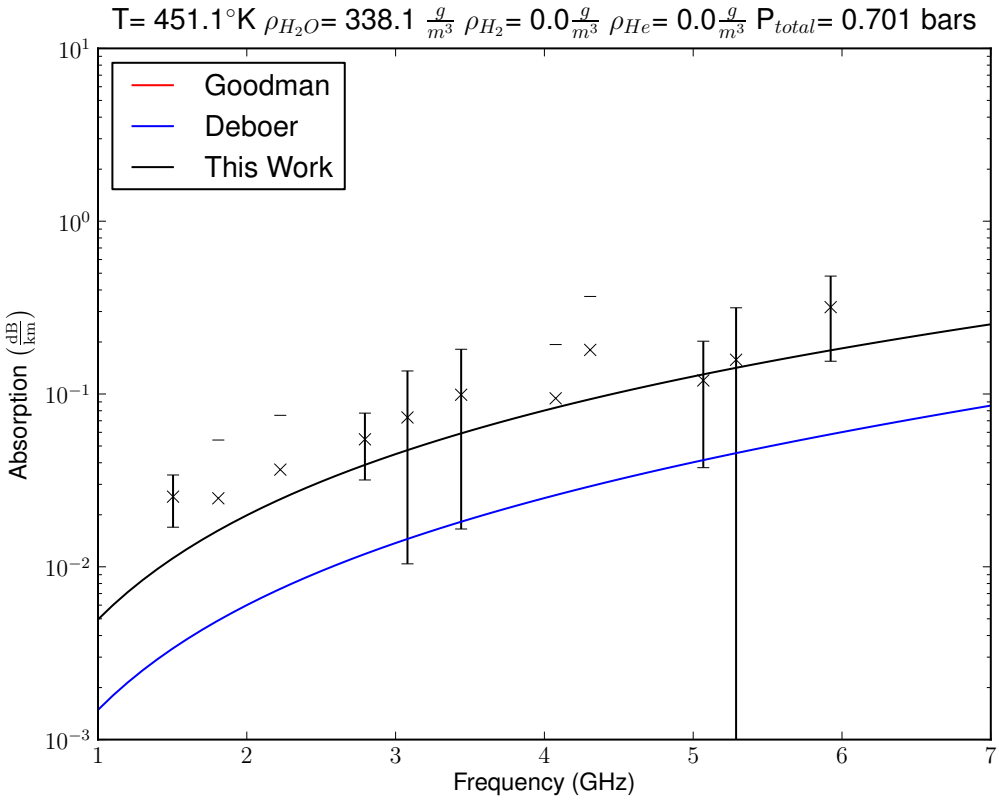

Figure 5.57: Experiment 8 with pure water vapor.

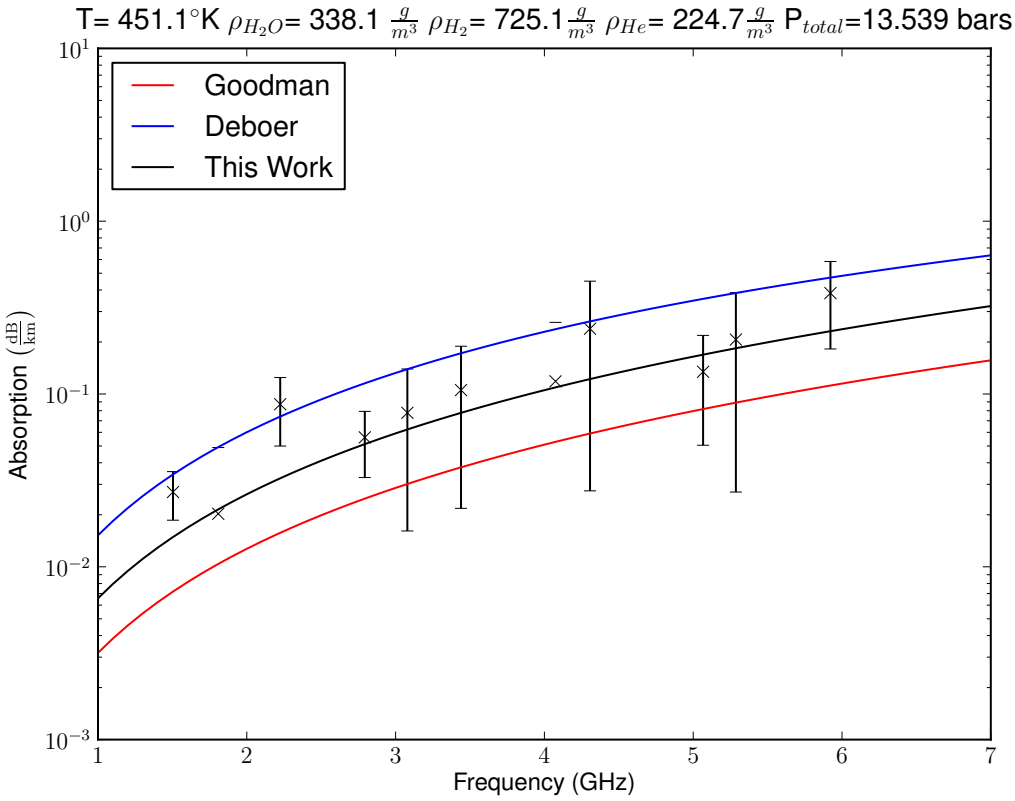

Figure 5.58: Experiment 8 with Factory H_2/He mixture 13.5 bars total pressure

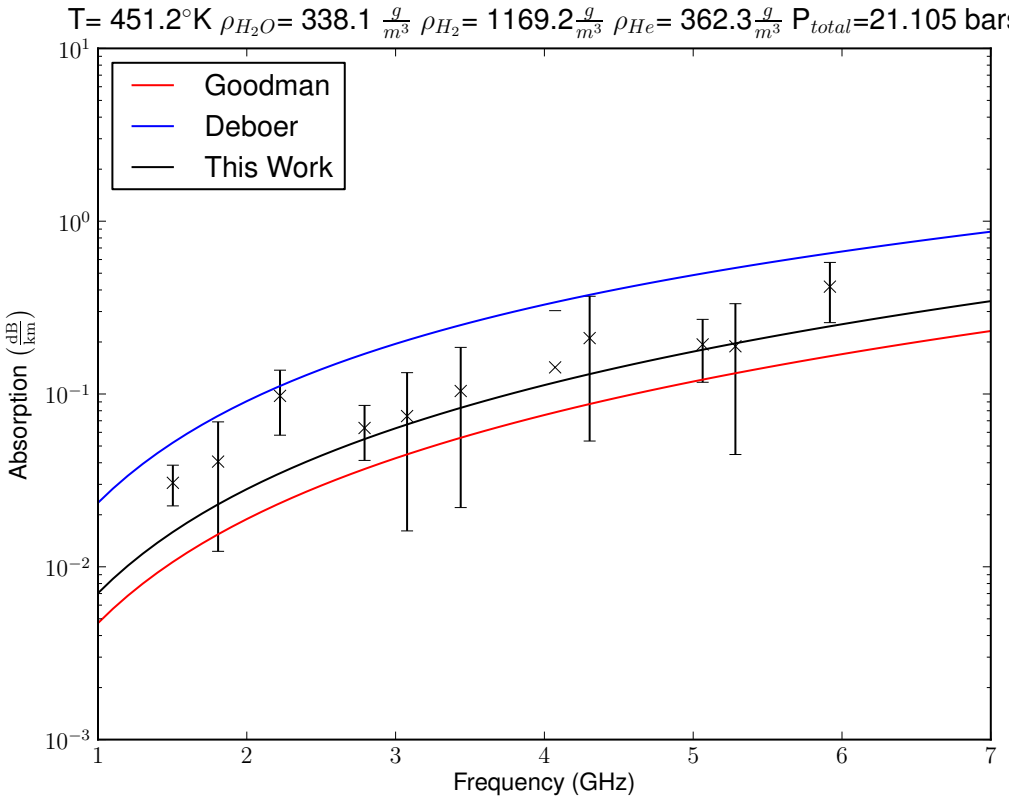

Figure 5.59: Experiment 8 with Factory H_2/He mixture 21.1 bars total pressure

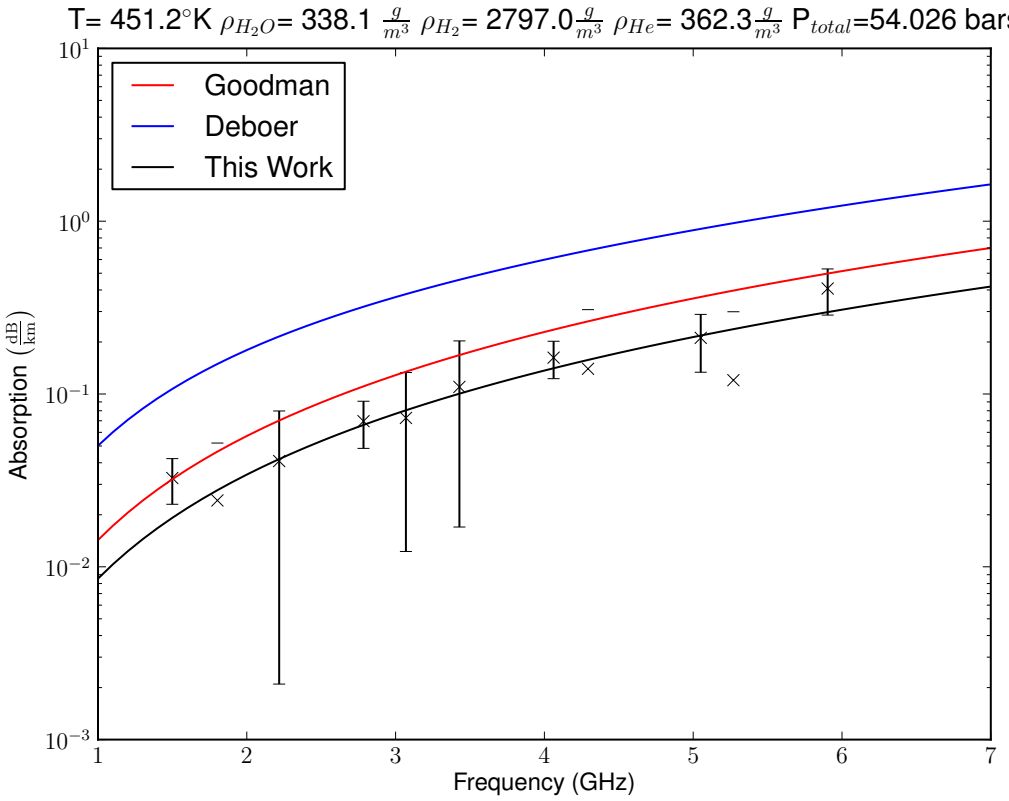

Figure 5.60: Experiment 8 with H_2/He mixture 54 bars total pressure.

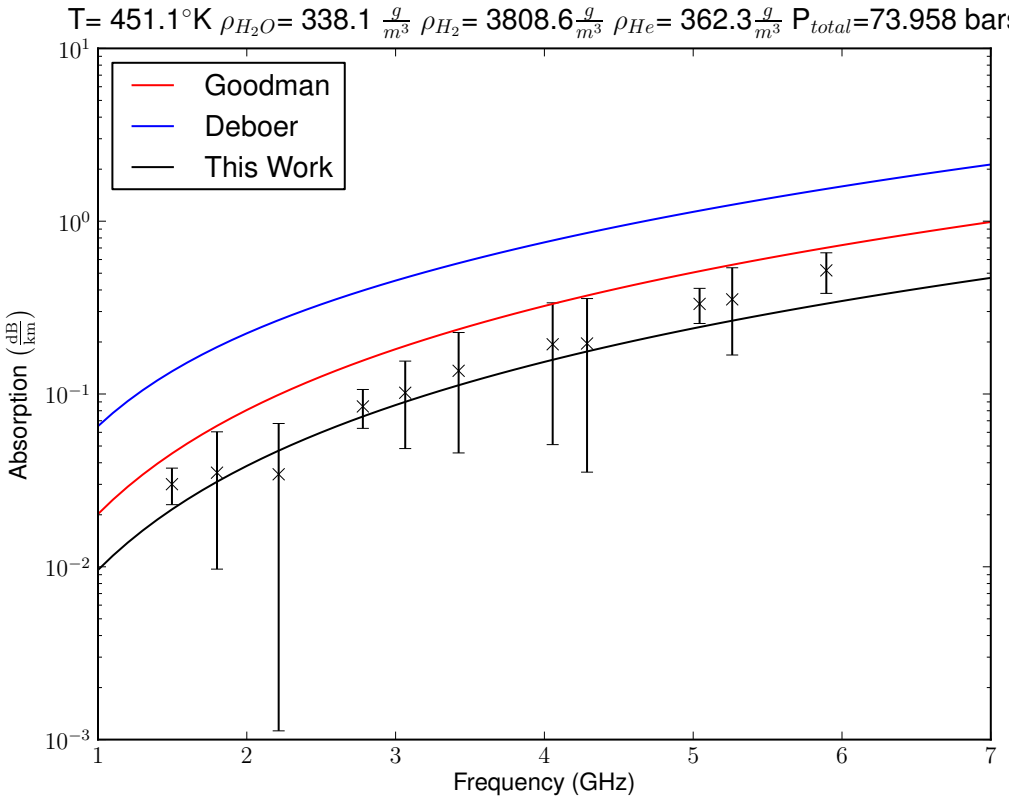

Figure 5.61: Experiment 8 with H_2/He mixture 74 bars total pressure.

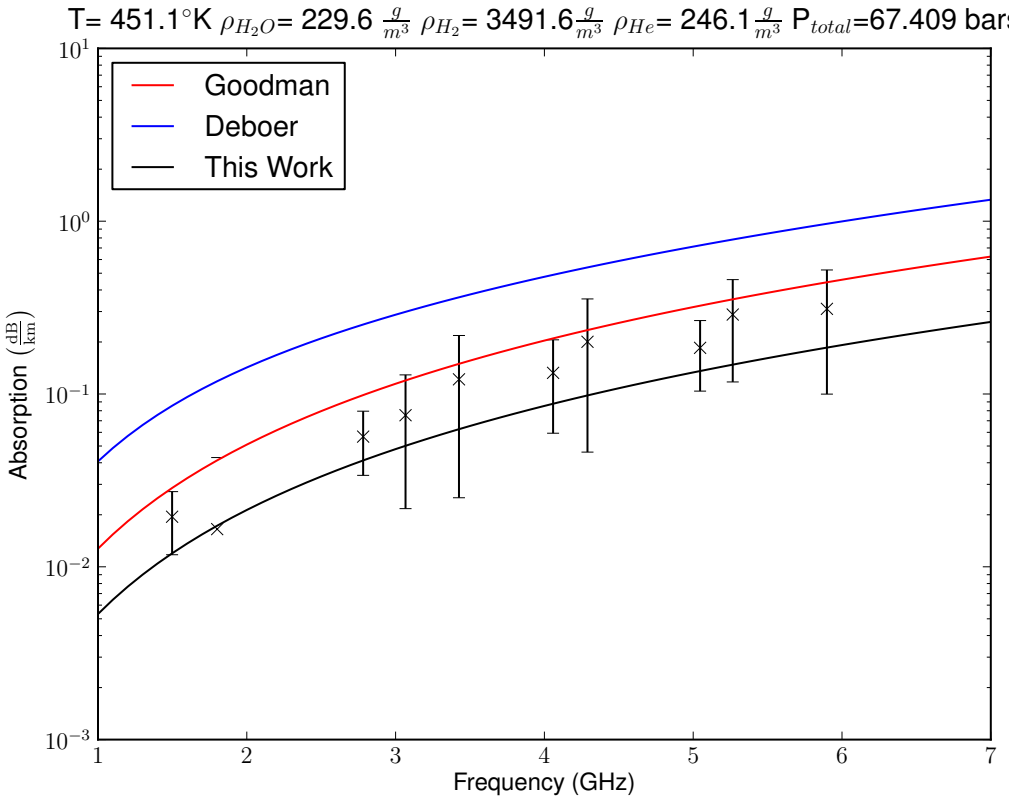

Figure 5.62: Experiment 8 with H_2/He mixture 67.4 bars total pressure (after maximum pressure).

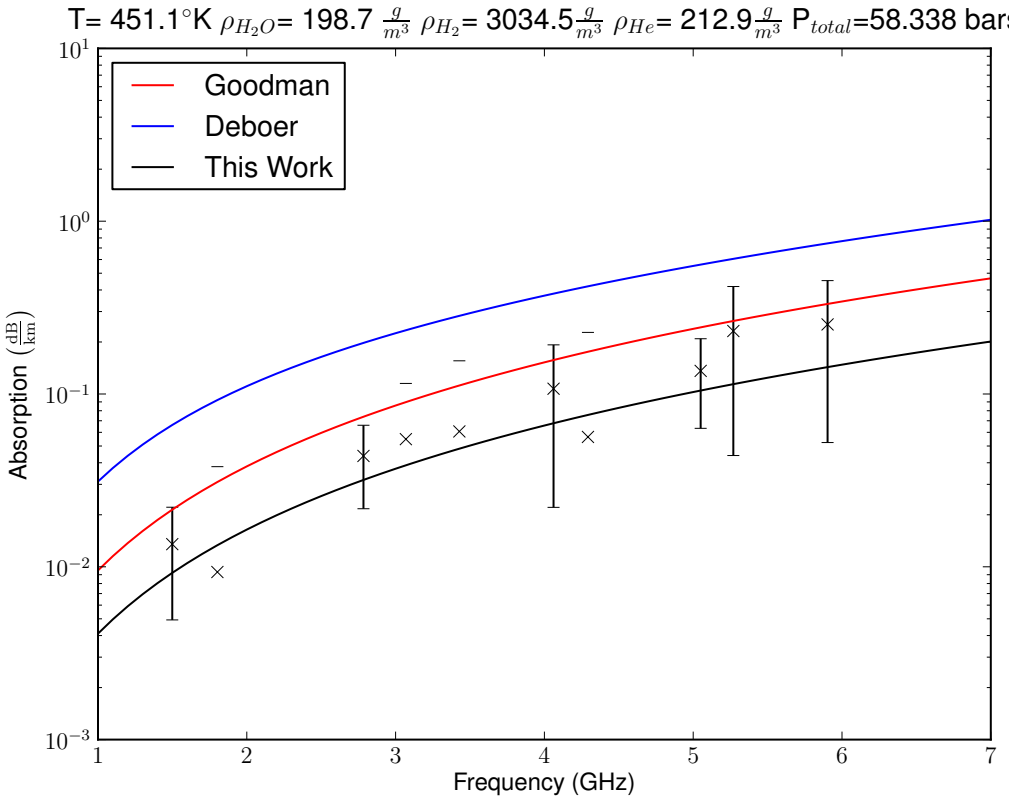

Figure 5.63: Experiment 8 with H_2/He mixture 58.3 bars total pressure (after maximum pressure).

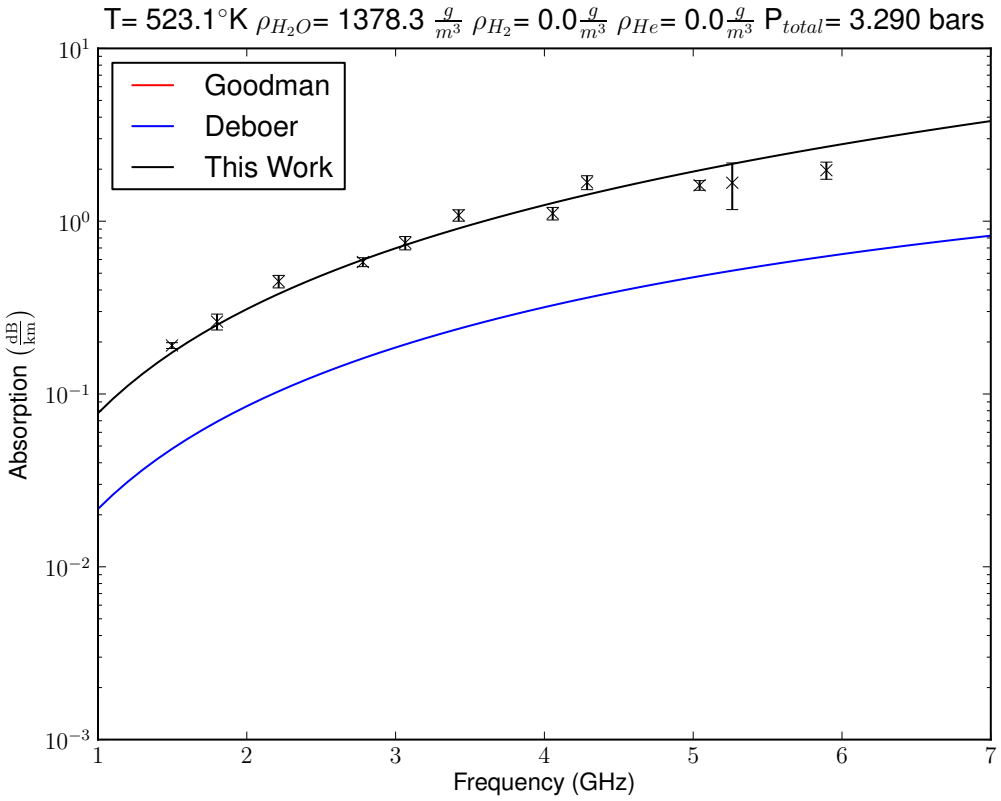

Figure 5.64: Experiment 9 with pure water vapor.

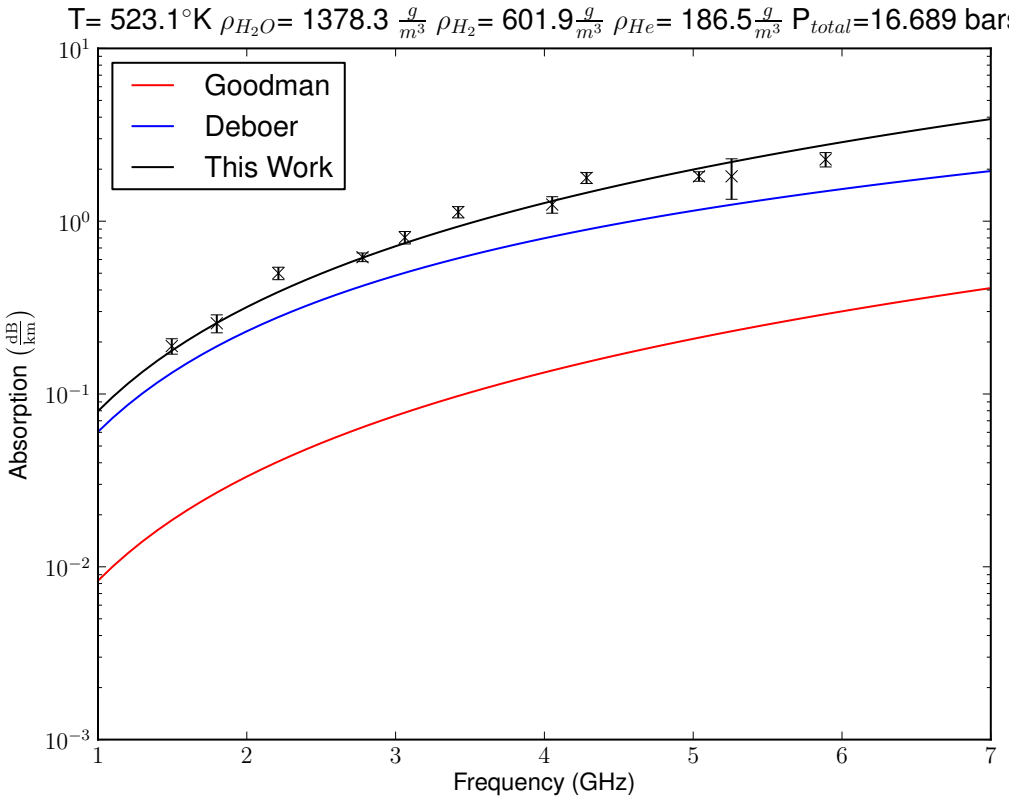

Figure 5.65: Experiment 9 with Factory H_2/He mixture 16.7 bars total pressure

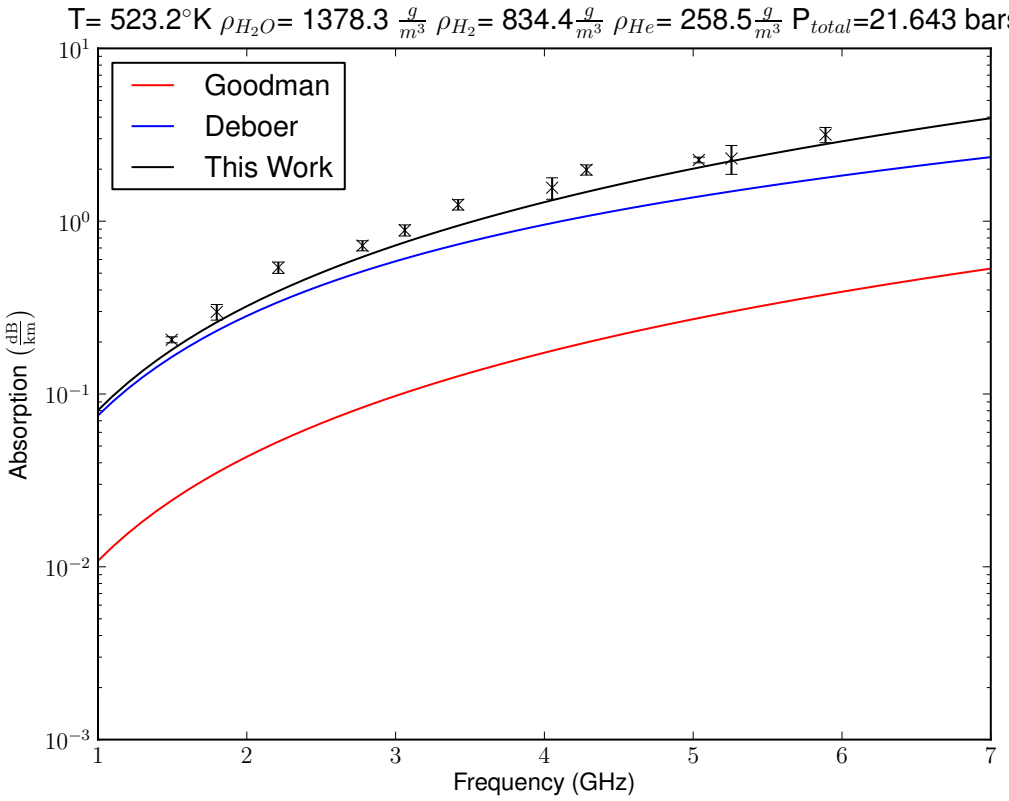

Figure 5.66: Experiment 9 with Factory H_2/He mixture 21.6 bars total pressure

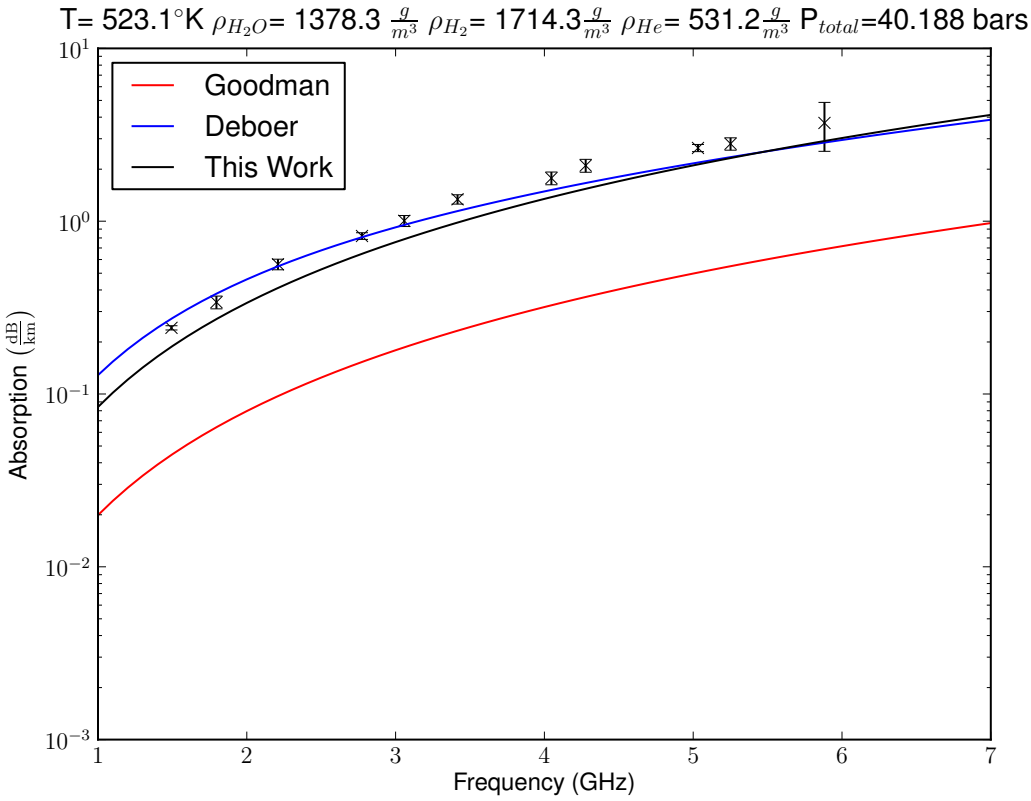

Figure 5.67: Experiment 9 with Factory H_2/He mixture 40.2 bars total pressure.

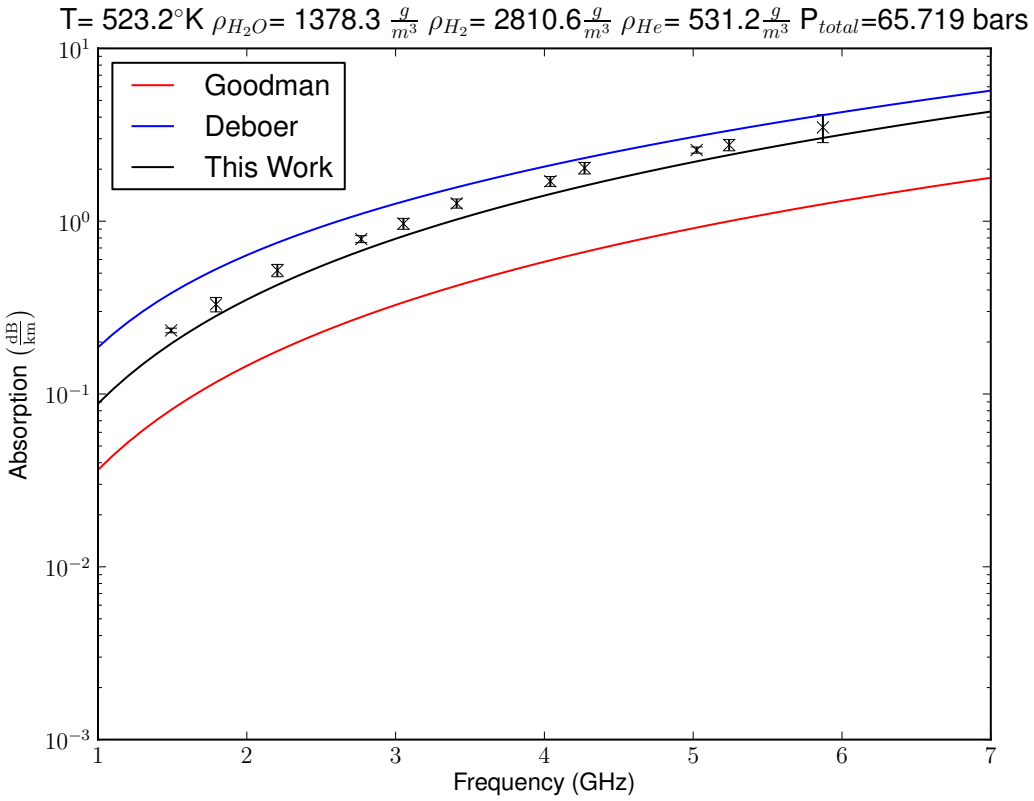

Figure 5.68: Experiment 9 with H_2/He mixture 65.7 bars total pressure.

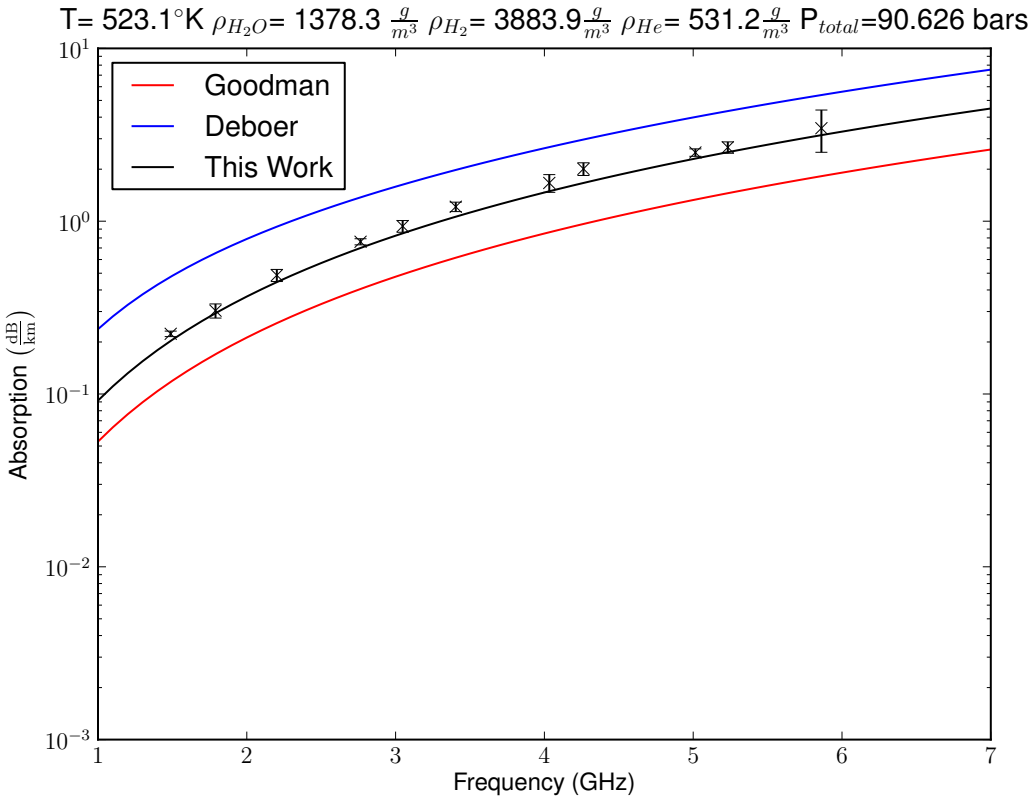

Figure 5.69: Experiment 9 with H_2/He mixture 90.6 bars total pressure.

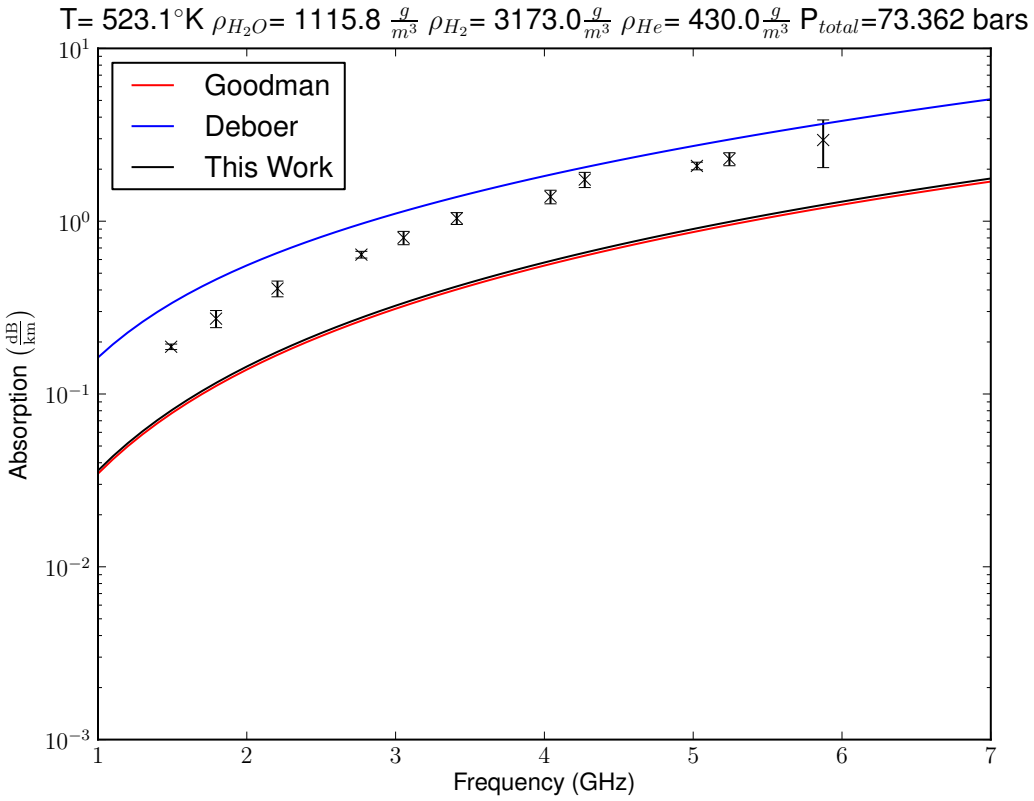

Figure 5.70: Experiment 9 with H_2/He mixture 73.4 bars total pressure (after maximum pressure).

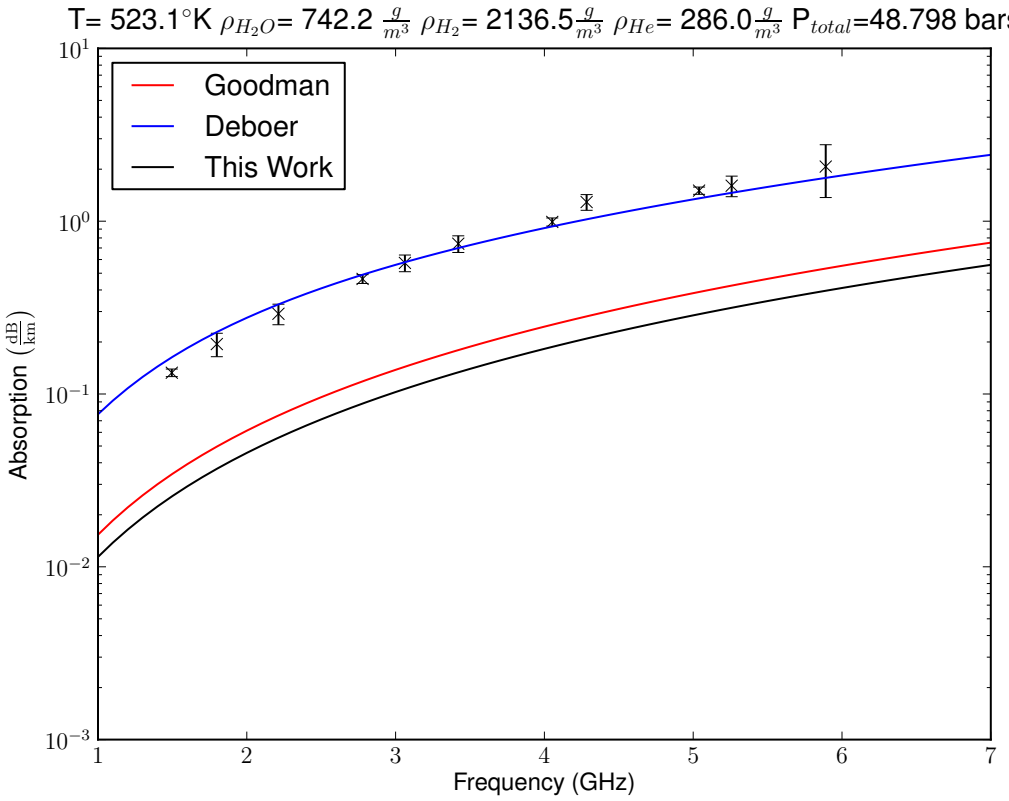

Figure 5.71: Experiment 9 with H_2/He mixture 48.8 bars total pressure (after maximum pressure).

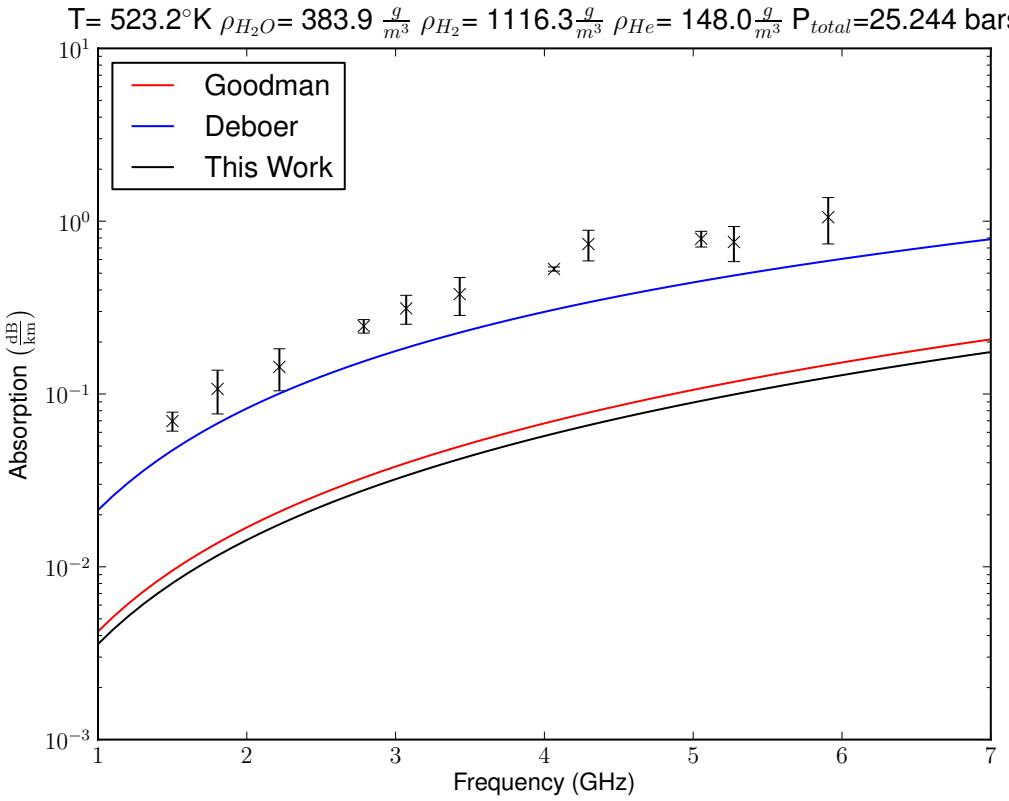

Figure 5.72: Experiment 9 with H_2/He mixture 25 bars total pressure (after maximum pressure).

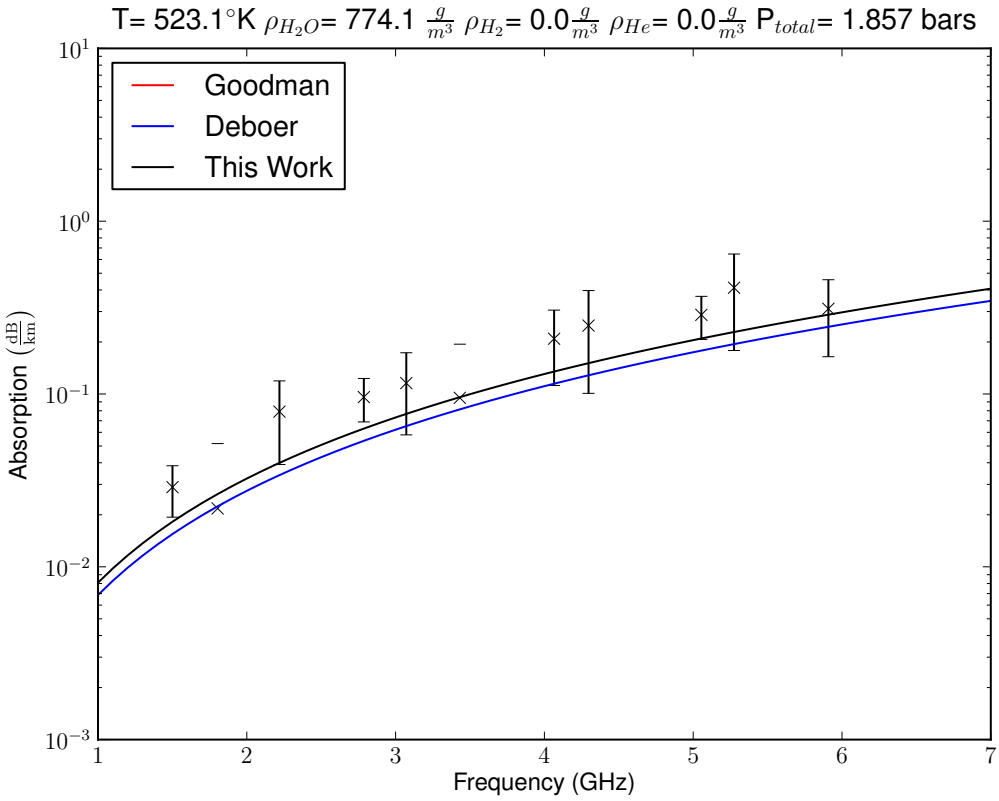

Figure 5.73: Experiment 10 with pure water vapor.

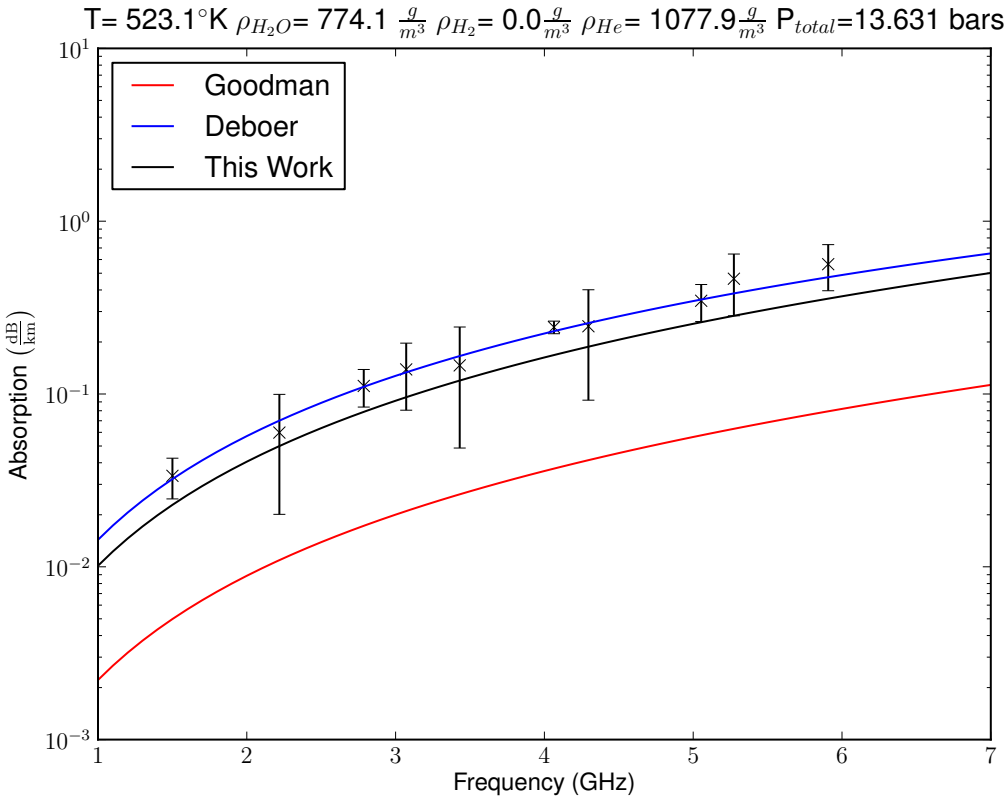

Figure 5.74: Experiment 10 with He mixture 13.6 bars total pressure

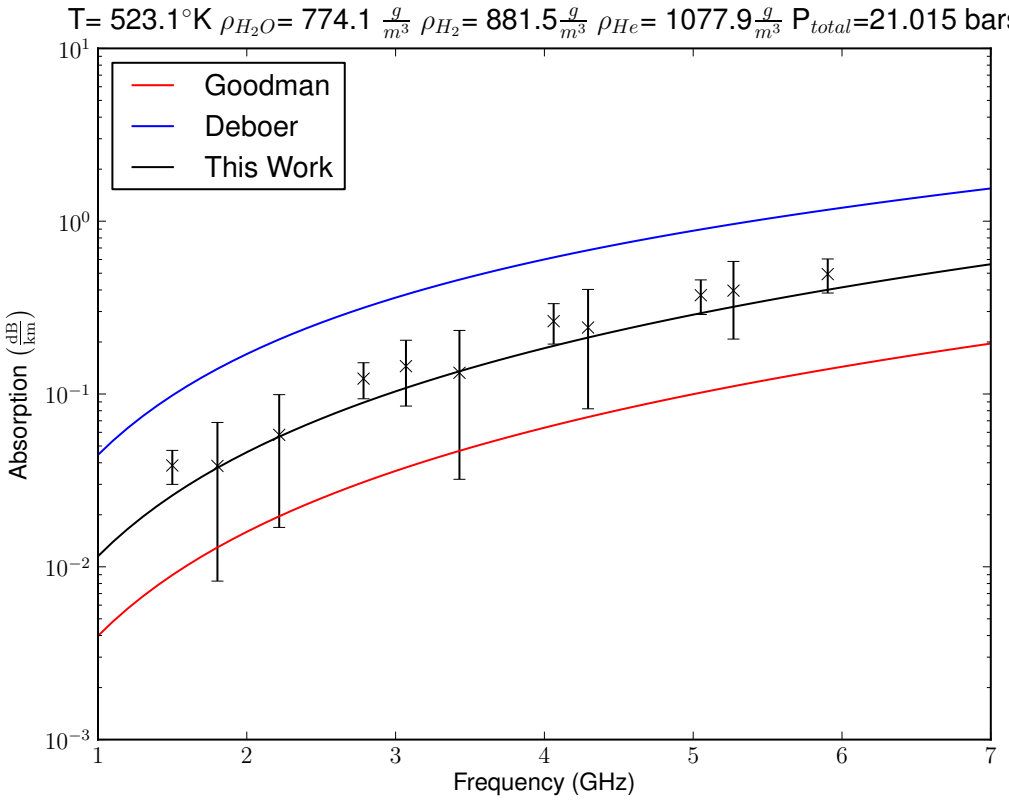

Figure 5.75: Experiment 10 with H_2/He mixture 21.0 bars total pressure

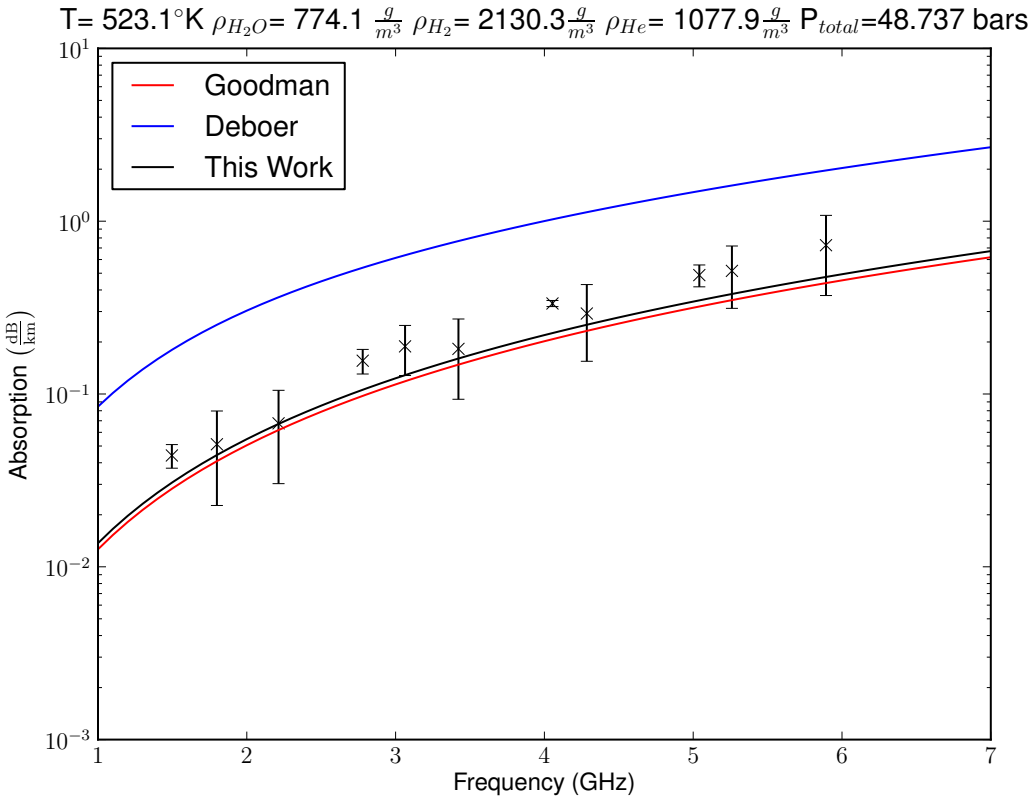

Figure 5.76: Experiment 10 with H_2/He mixture 48.7 bars total pressure.

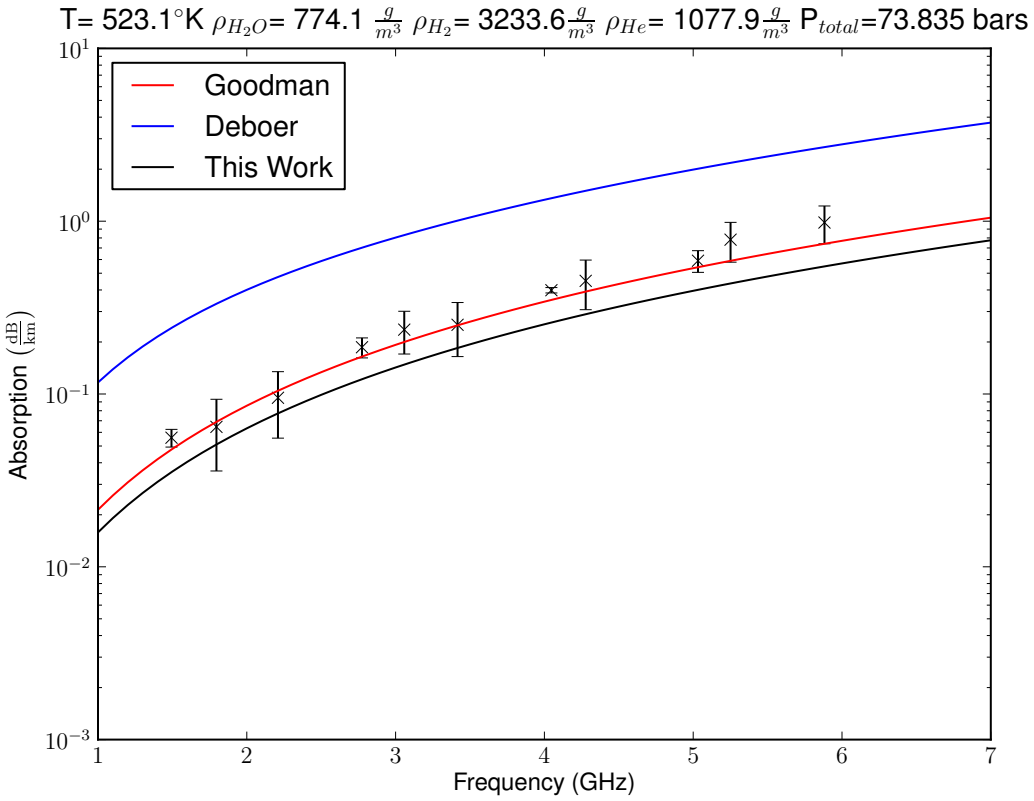

Figure 5.77: Experiment 10 with H_2/He mixture 73.8 bars total pressure.

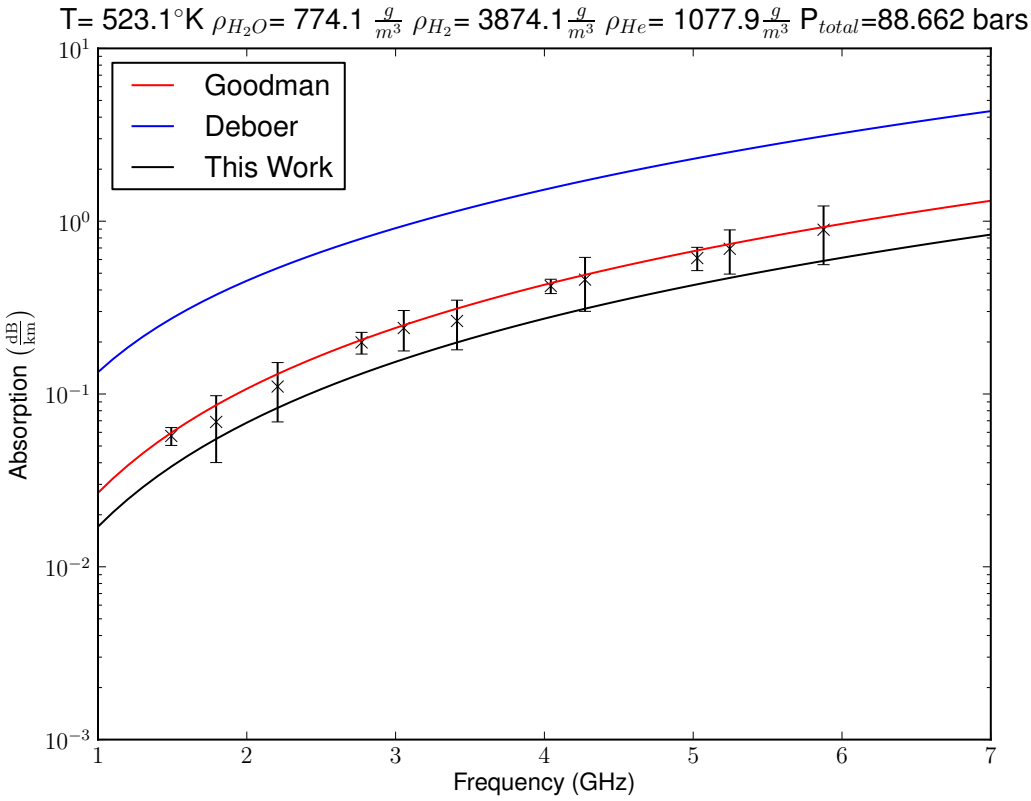

Figure 5.78: Experiment 10 with H_2/He mixture 88.6 bars total pressure.

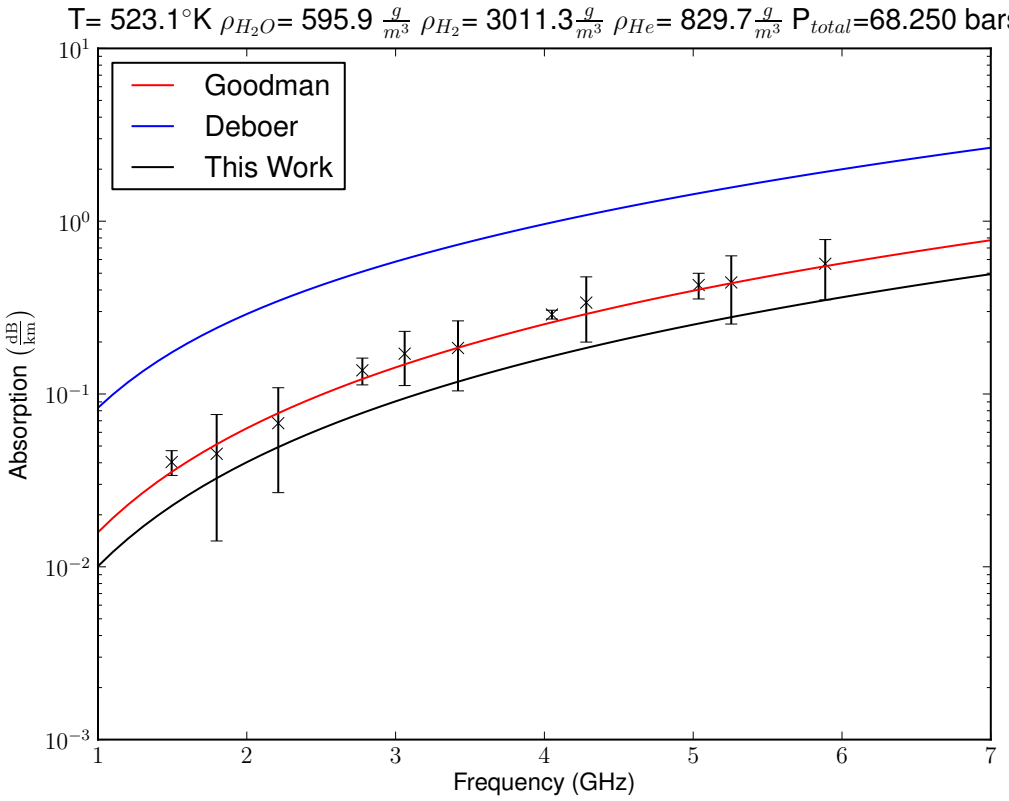

Figure 5.79: Experiment 10 with H_2/He mixture 68.3 bars total pressure (after maximum pressure).

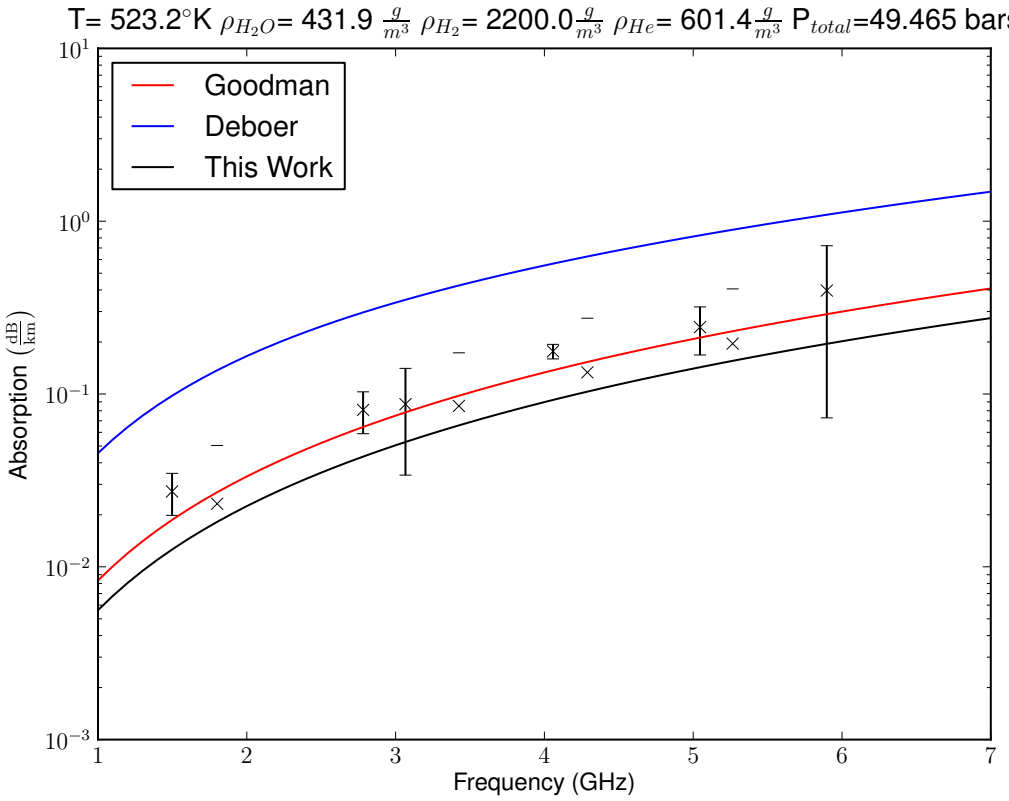

Figure 5.80: Experiment 10 with H_2/He mixture 49.5 bars total pressure (after maximum pressure).

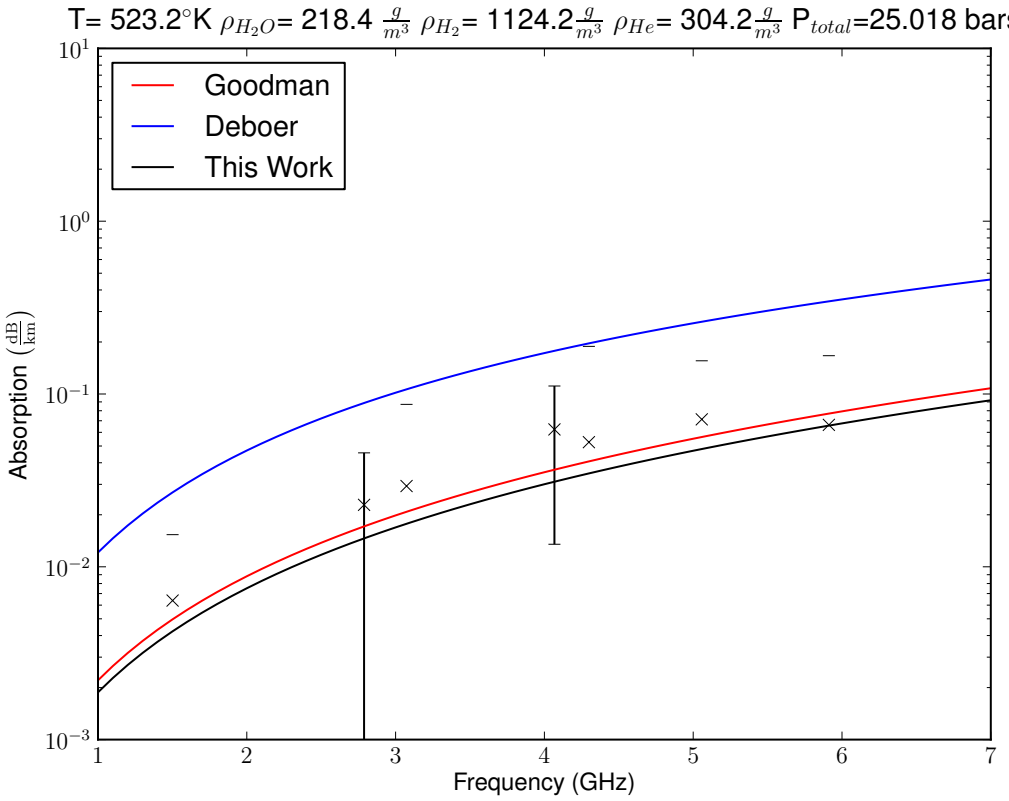

Figure 5.81: Experiment 10 with H_2/He mixture 25 bars total pressure (after maximum pressure).

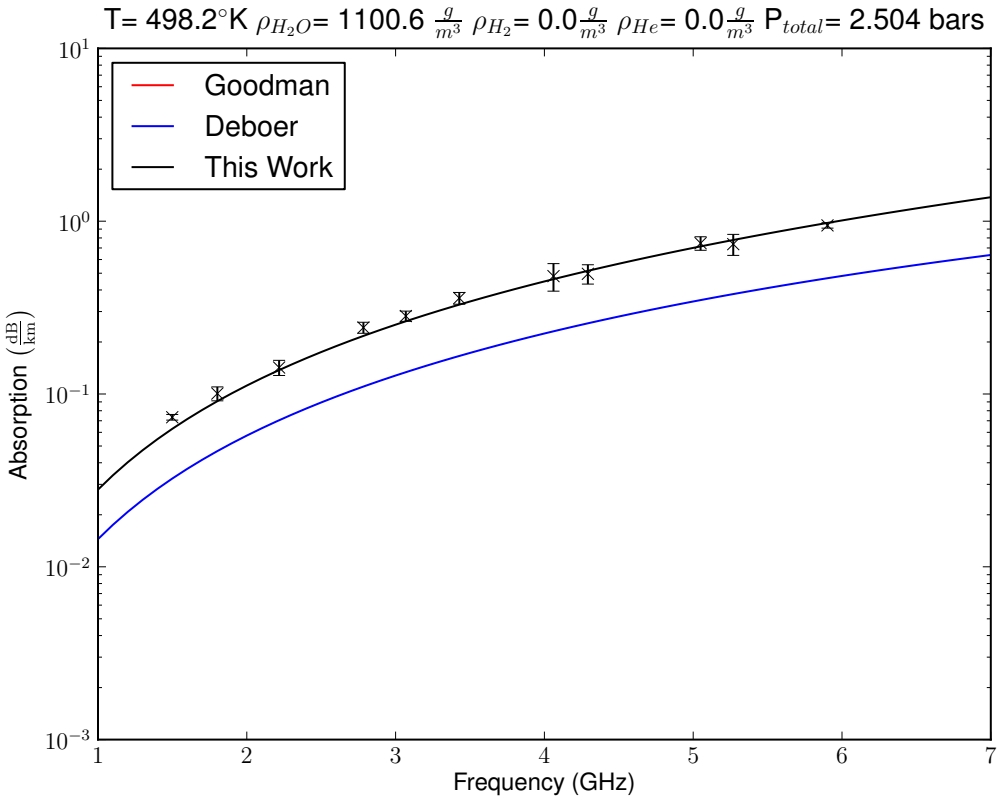

Figure 5.82: Experiment 11 with pure water vapor.

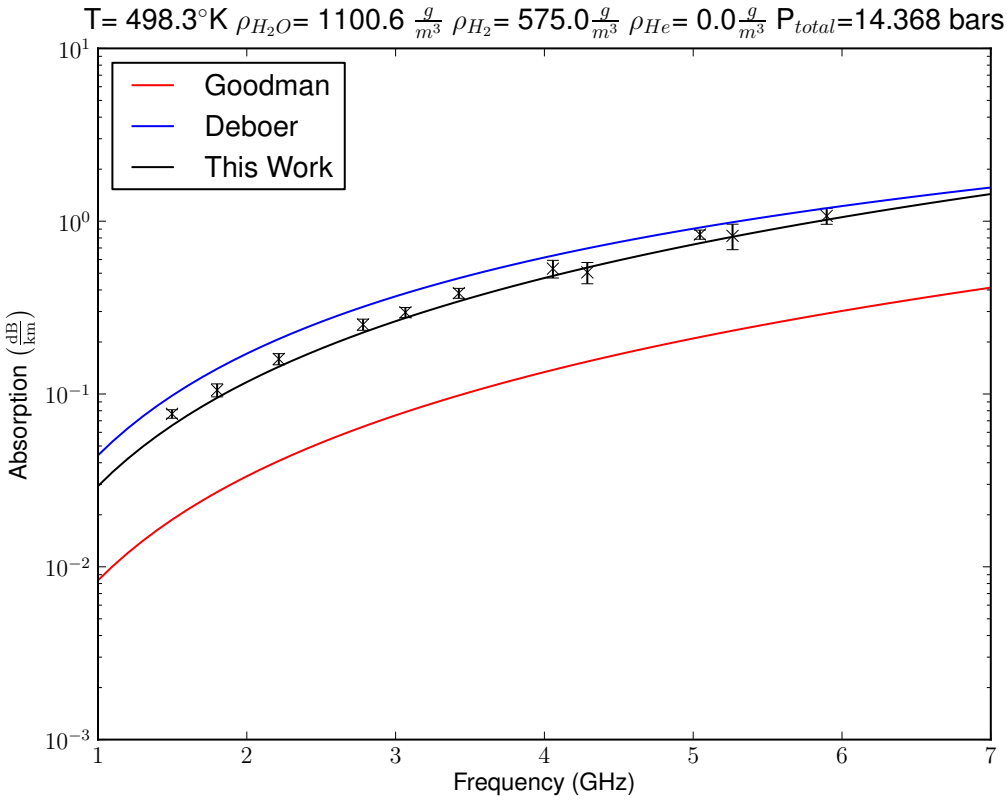

Figure 5.83: Experiment 11 with H_2 mixture 14.4 bars total pressure

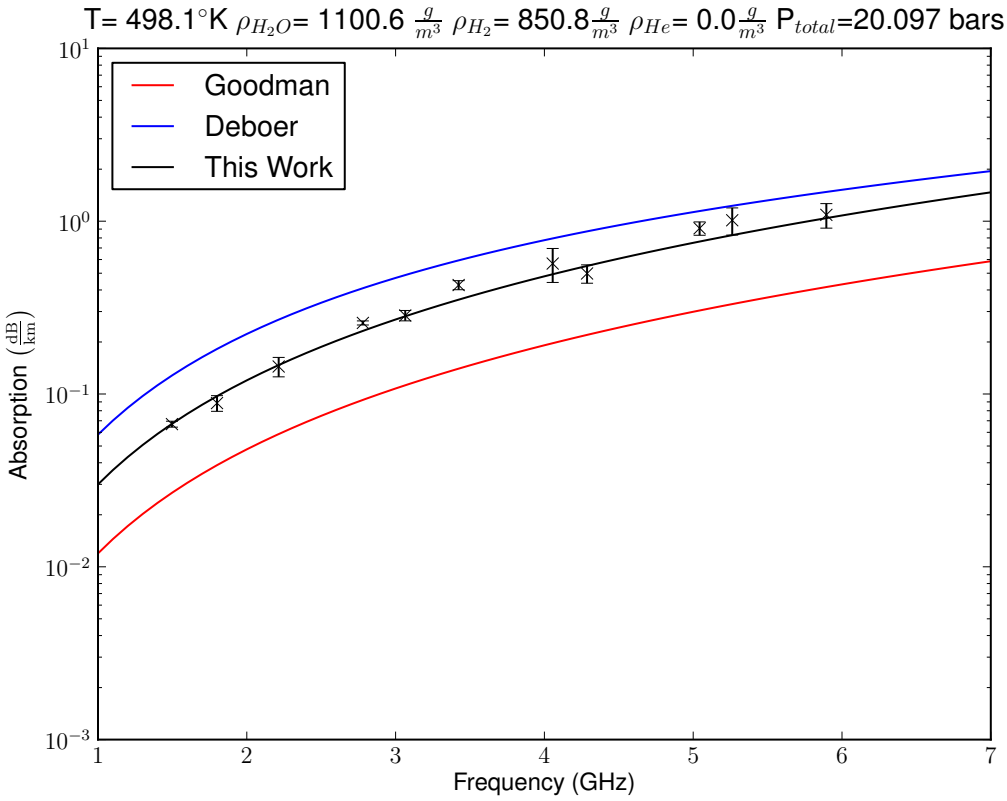

Figure 5.84: Experiment 11 with H_2 mixture 20.1 bars total pressure

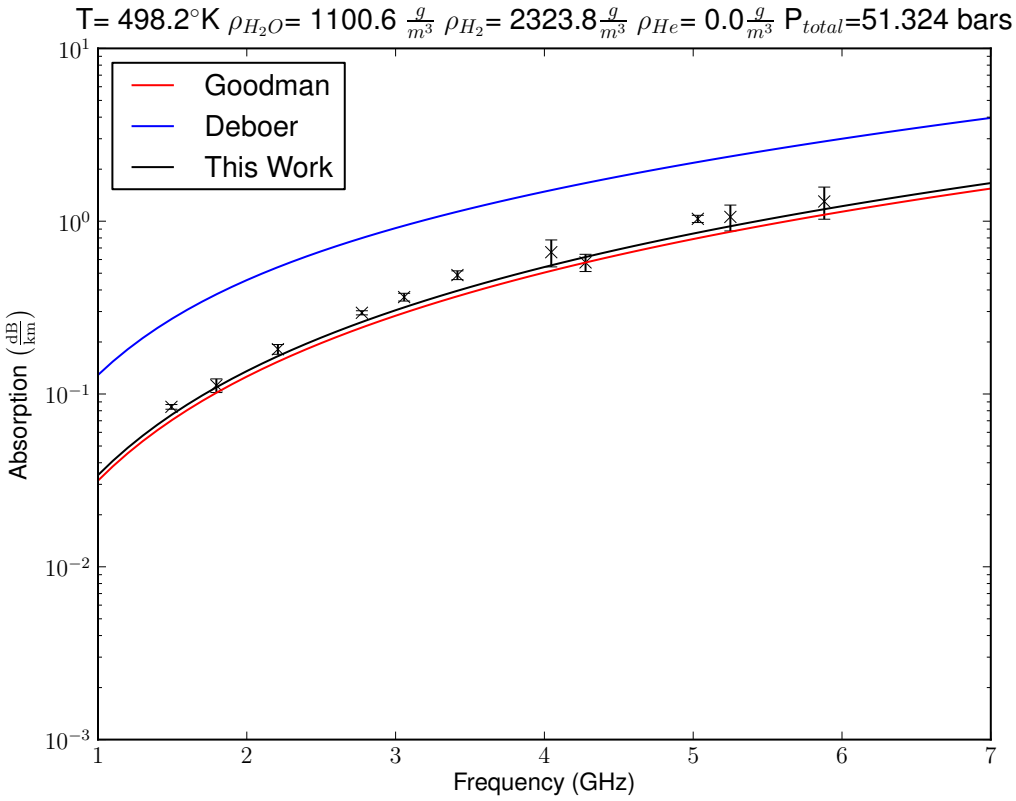

Figure 5.85: Experiment 11 with H_2 mixture 51.3 bars total pressure.

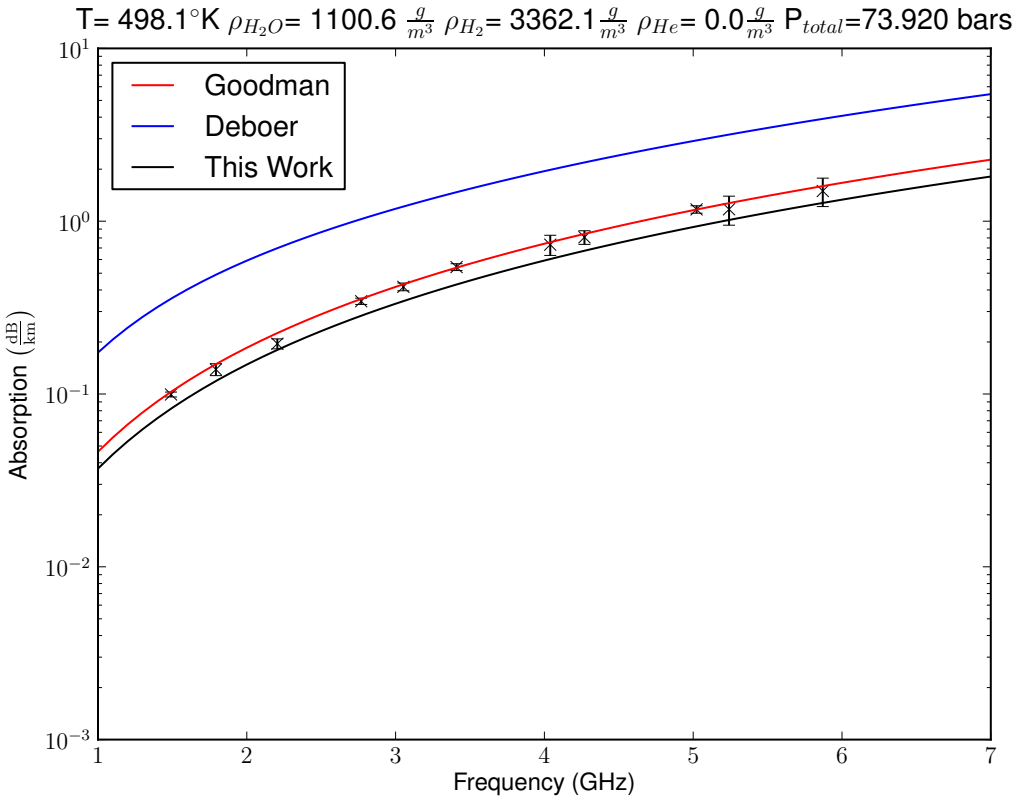

Figure 5.86: Experiment 11 with H_2mixture 73.9 bars total pressure.

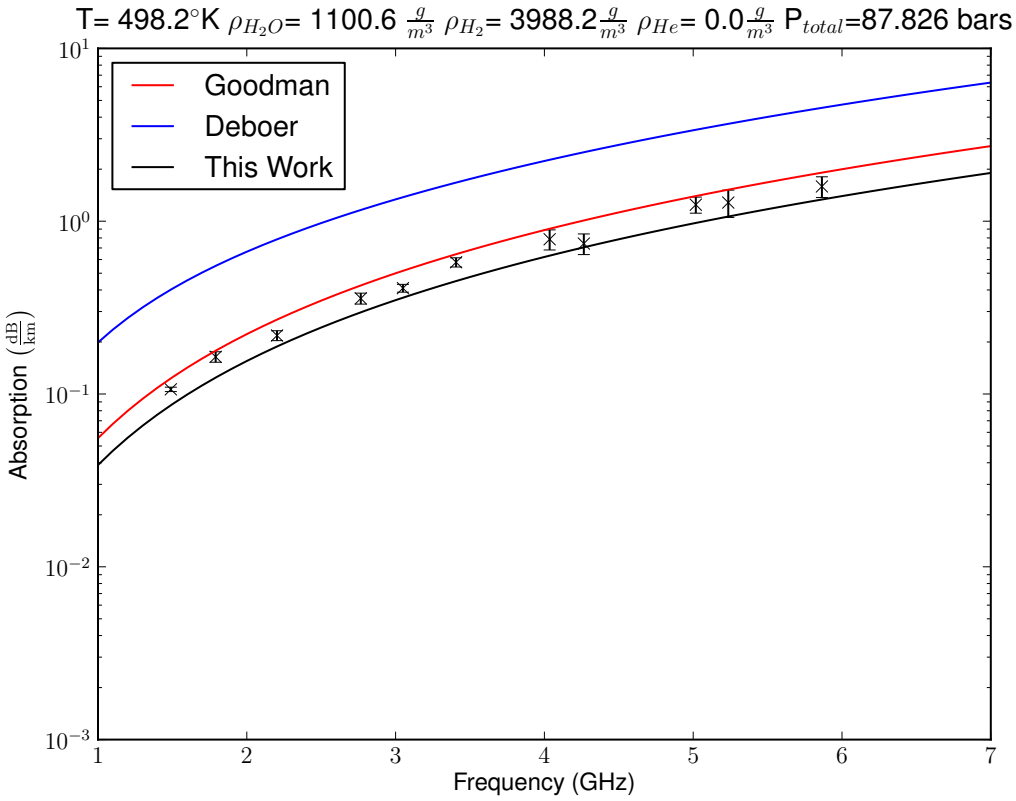

Figure 5.87: Experiment 11 with H_2 mixture 88 bars total pressure.

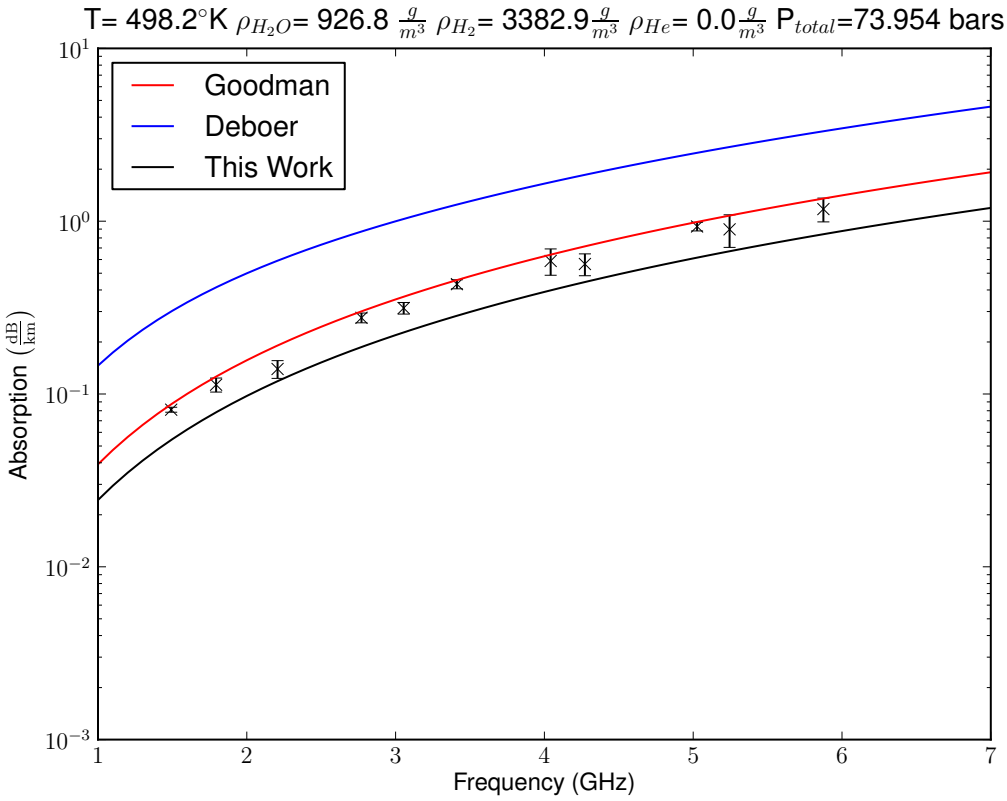

Figure 5.88: Experiment 11 with H_2 mixture 74 bars total pressure (after maximum pressure).

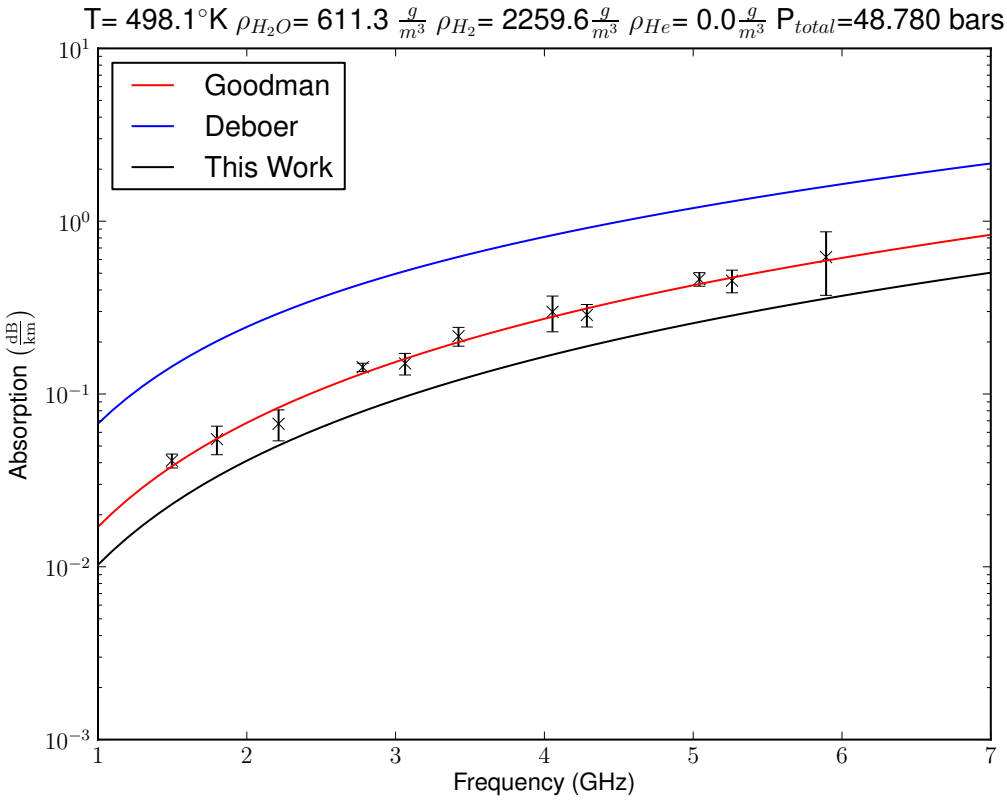

Figure 5.89: Experiment 11 with H_2 mixture 49 bars total pressure (after maximum pressure).

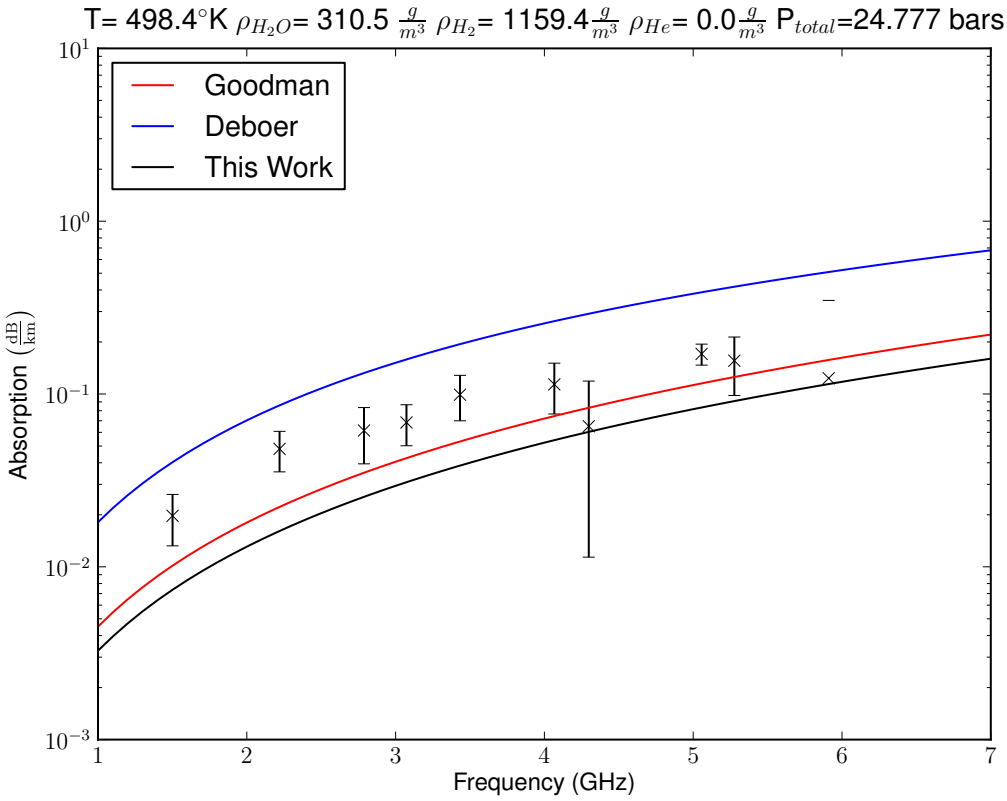

Figure 5.90: Experiment 11 with H_2 mixture 24.8 bars total pressure (after maximum pressure).

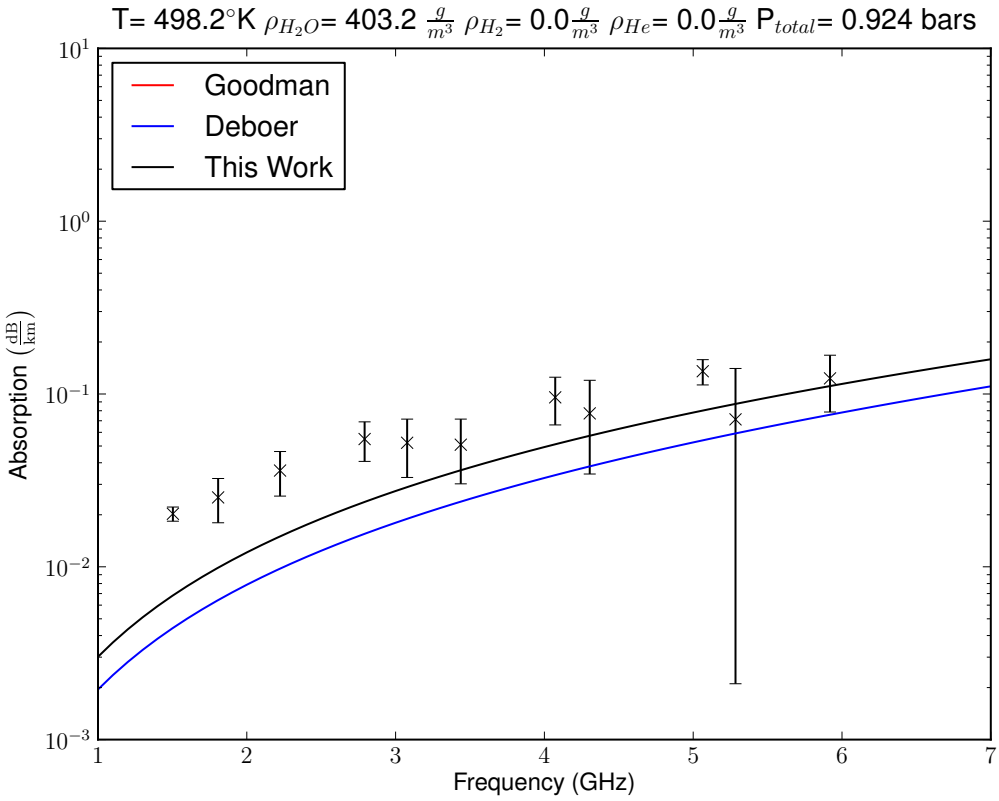

Figure 5.91: Experiment 12 with pure water vapor.

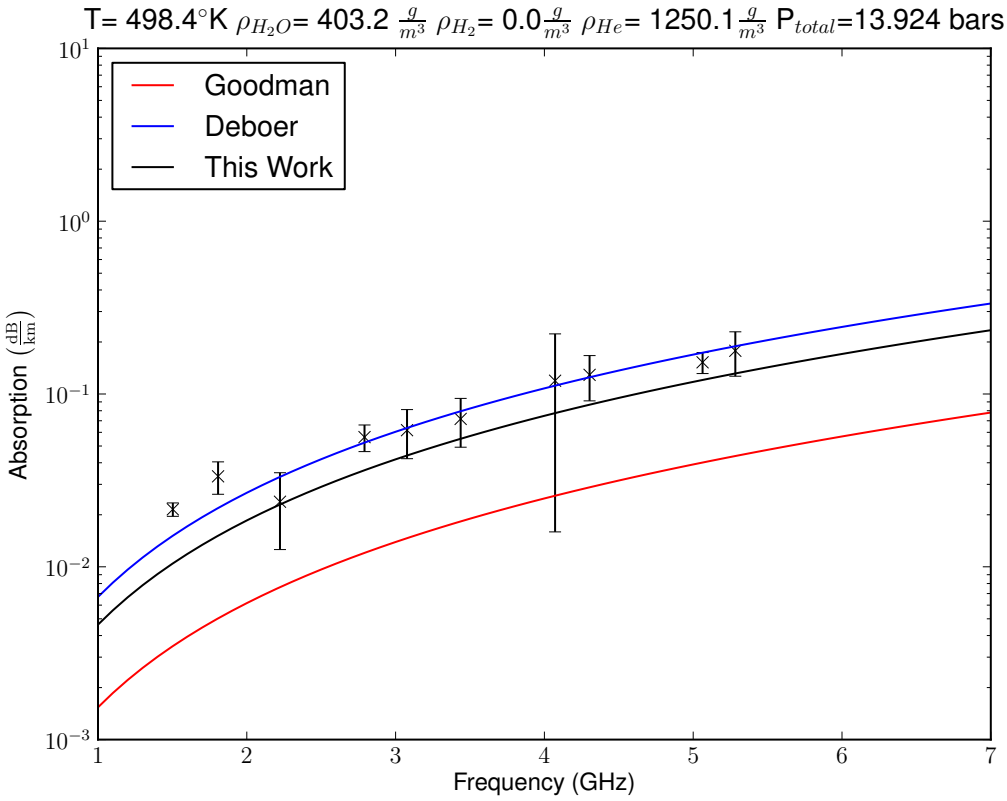

Figure 5.92: Experiment 12 with He mixture 13.9 bars total pressure

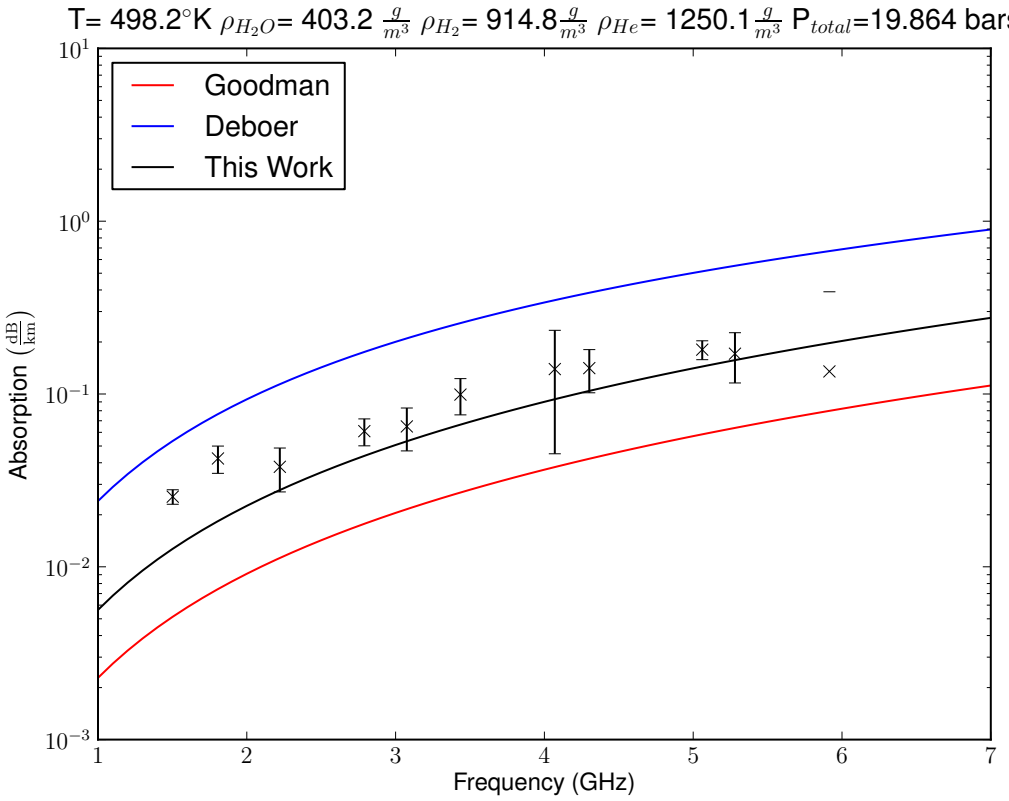

Figure 5.93: Experiment 12 with H_2/He mixture 19.9 bars total pressure

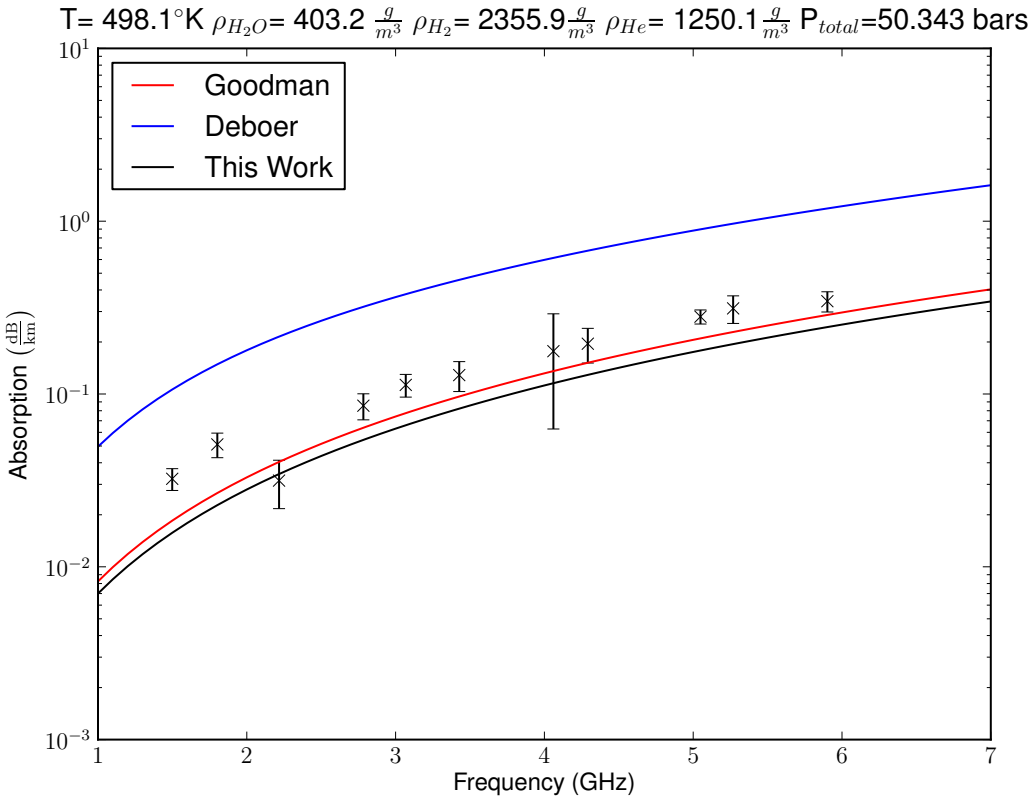

Figure 5.94: Experiment 12 with H_2/He mixture 50.3 bars total pressure.

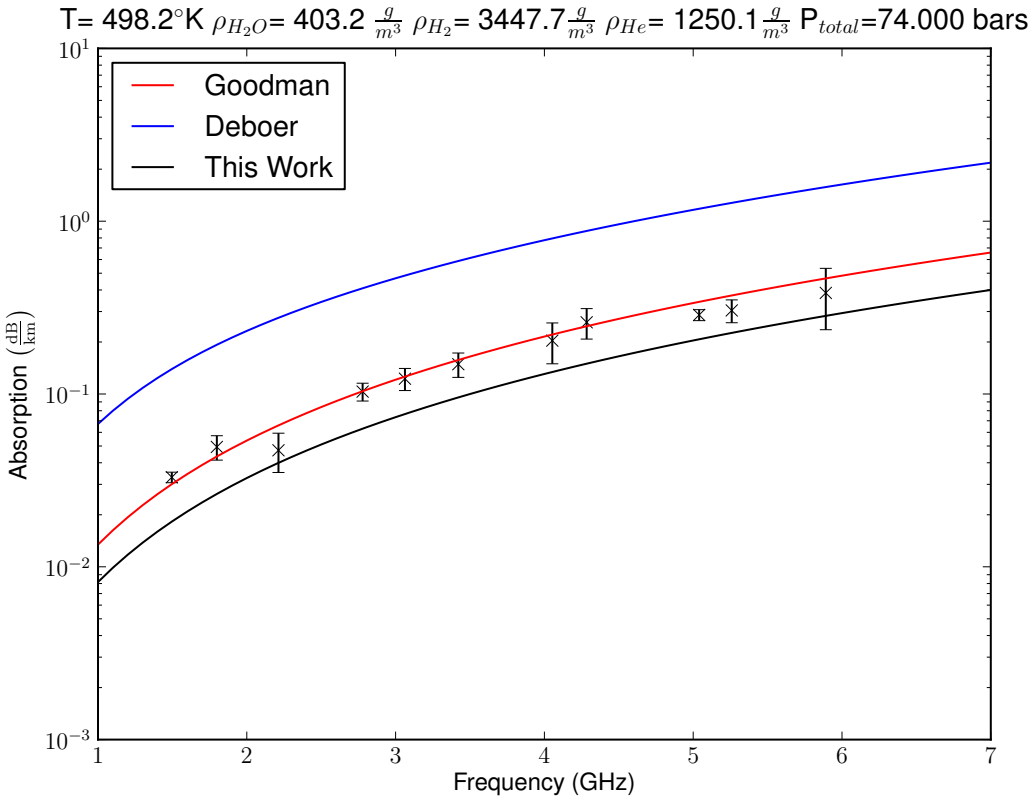

Figure 5.95: Experiment 12 with H_2/He mixture 74 bars total pressure.

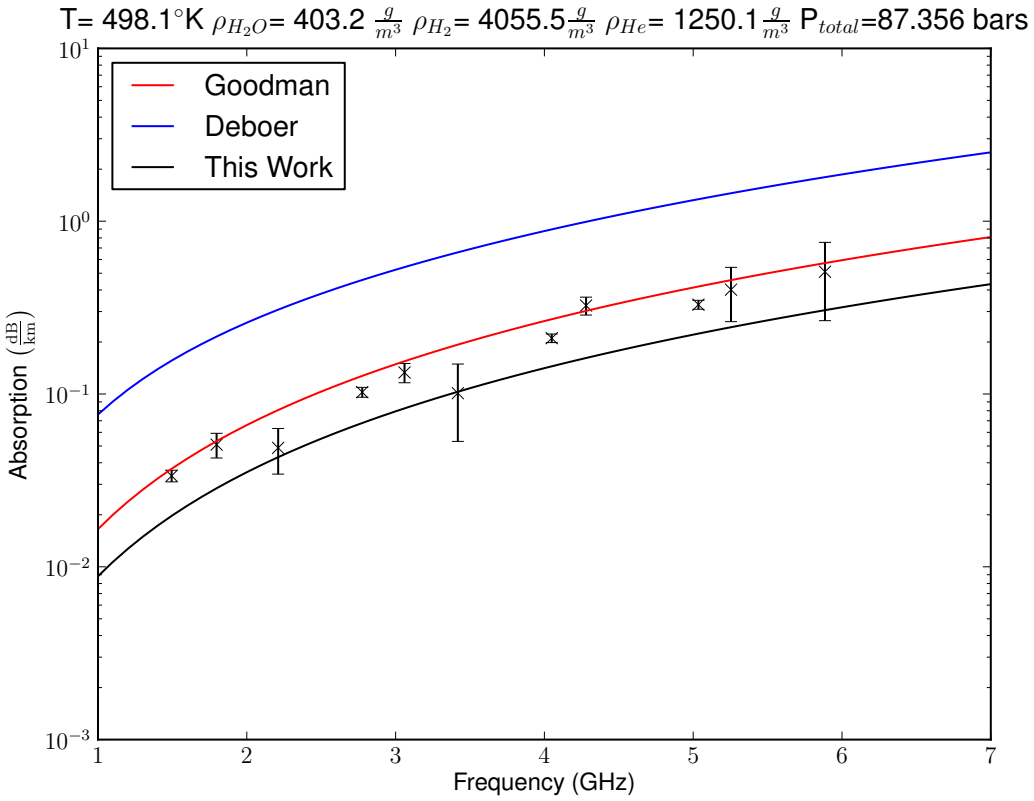

Figure 5.96: Experiment 12 with H_2/He mixture 87.3 bars total pressure.

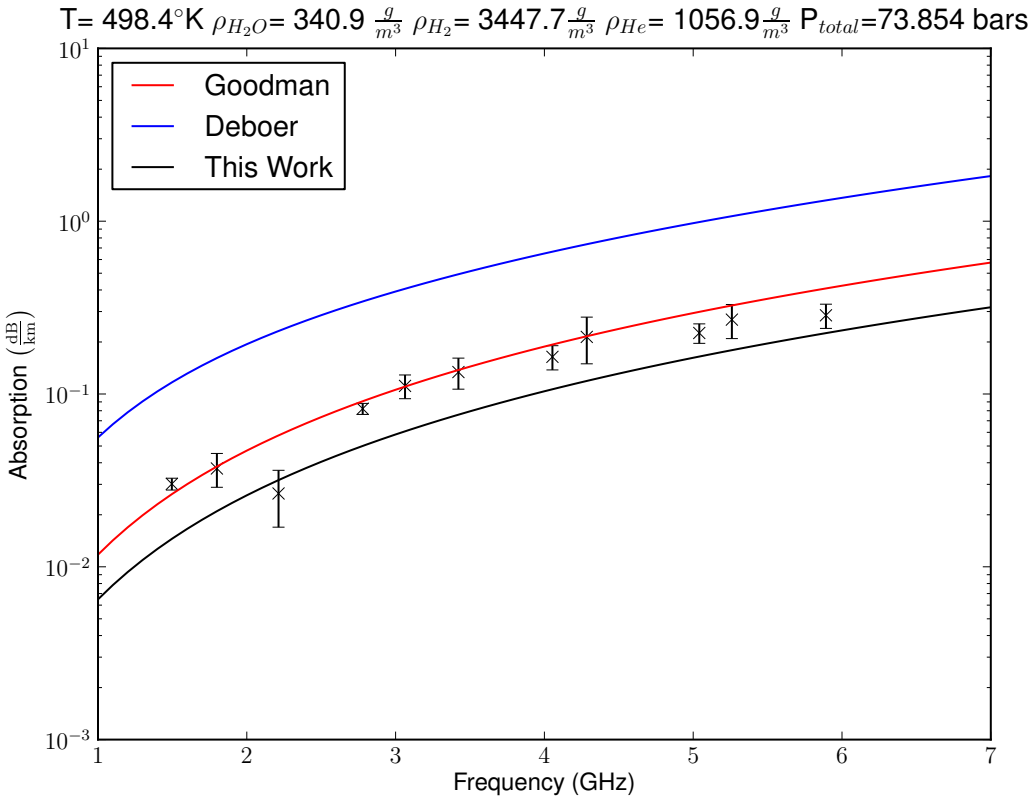

Figure 5.97: Experiment 12 with H_2/He mixture 73.8 bars total pressure (after maximum pressure).

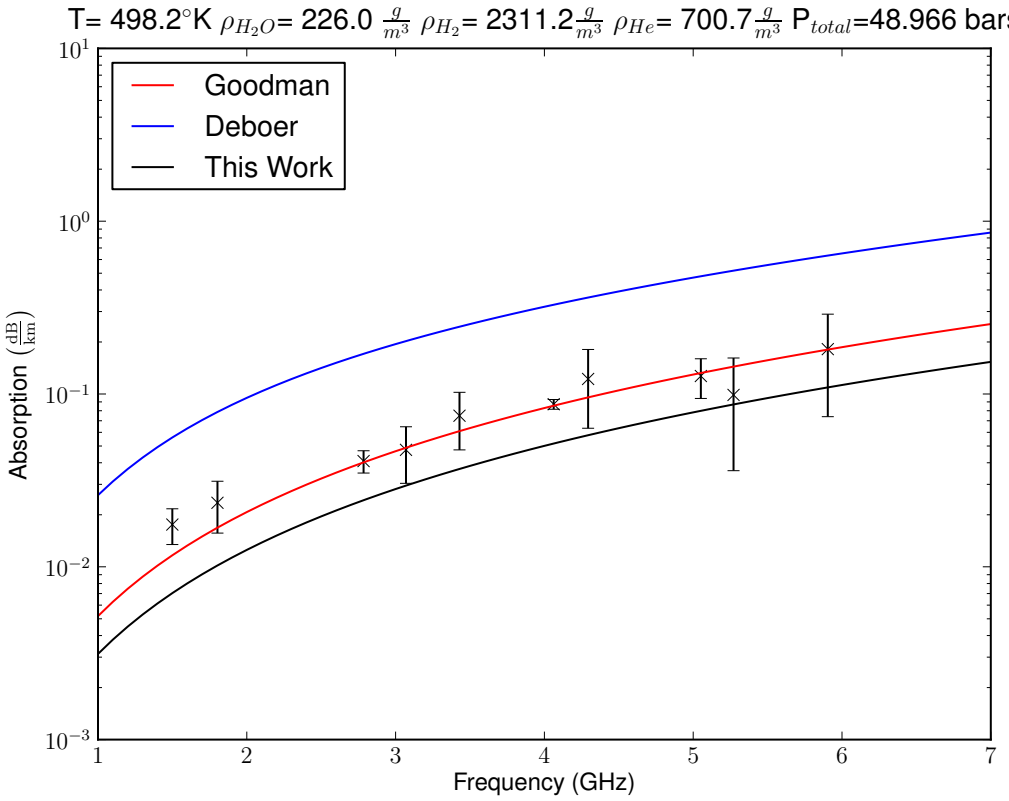

Figure 5.98: Experiment 12 with H_2/He mixture 49 bars total pressure (after maximum pressure).

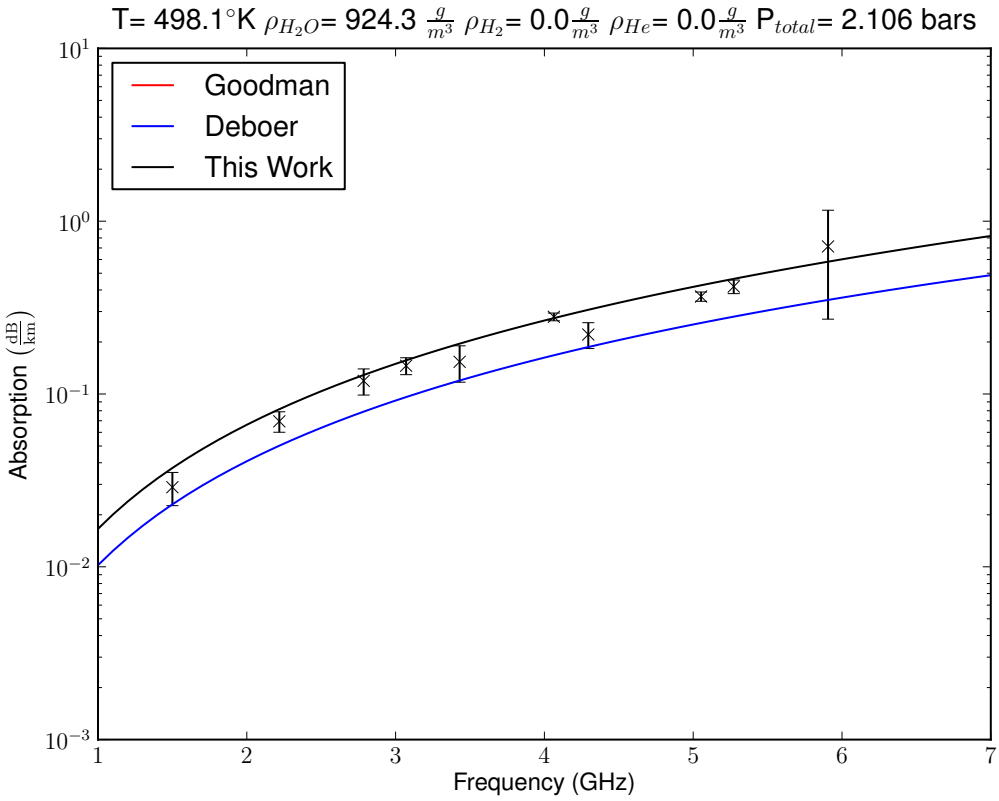

Figure 5.99: Experiment 13 with pure water vapor.

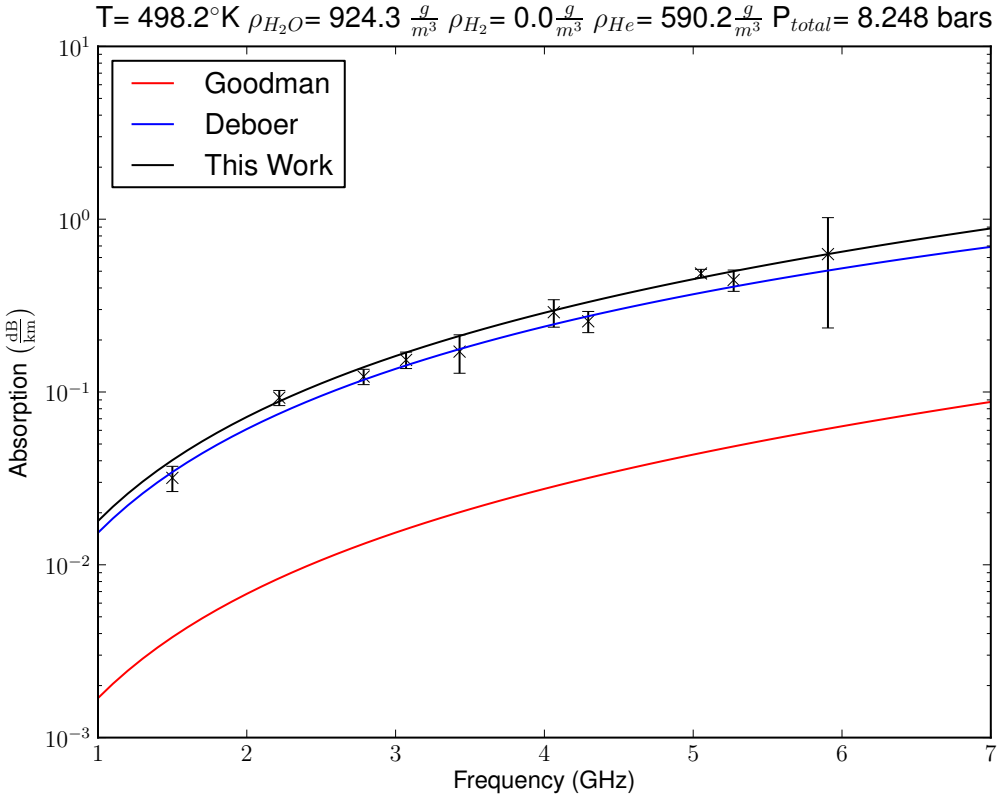

Figure 5.100: Experiment 13 with He mixture 8.2 bars total pressure

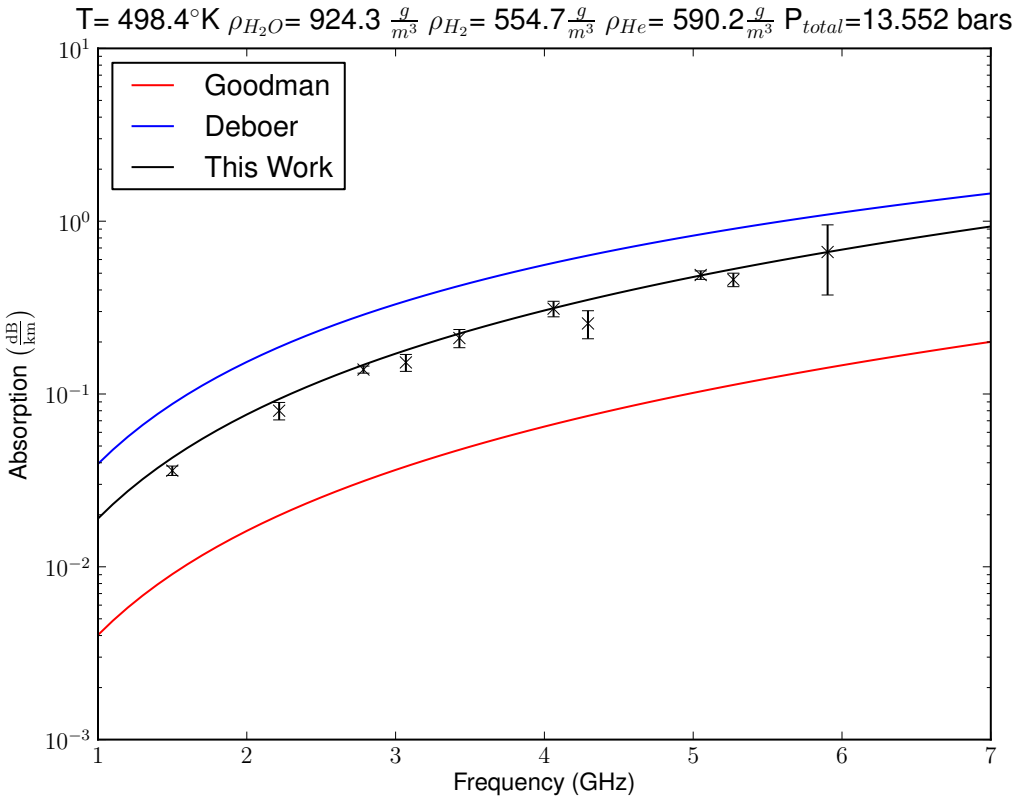

Figure 5.101: Experiment 13 with H_2/He mixture 13.5 bars total pressure

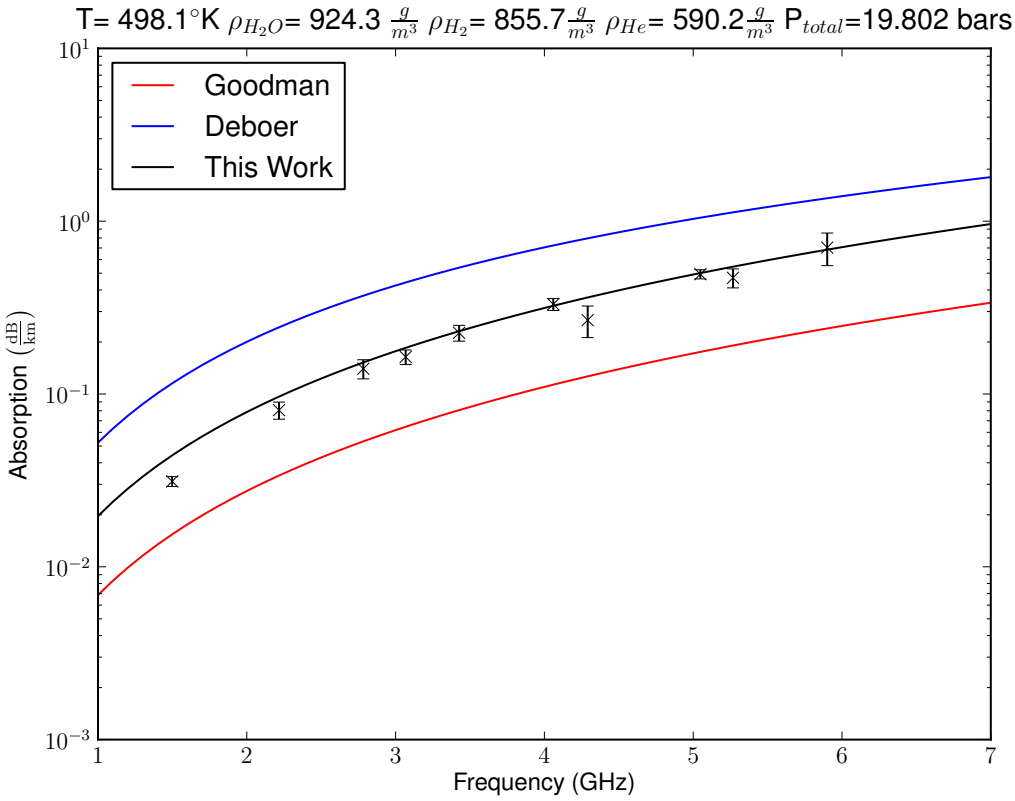

Figure 5.102: Experiment 13 with H_2/He mixture 19.8 bars total pressure.

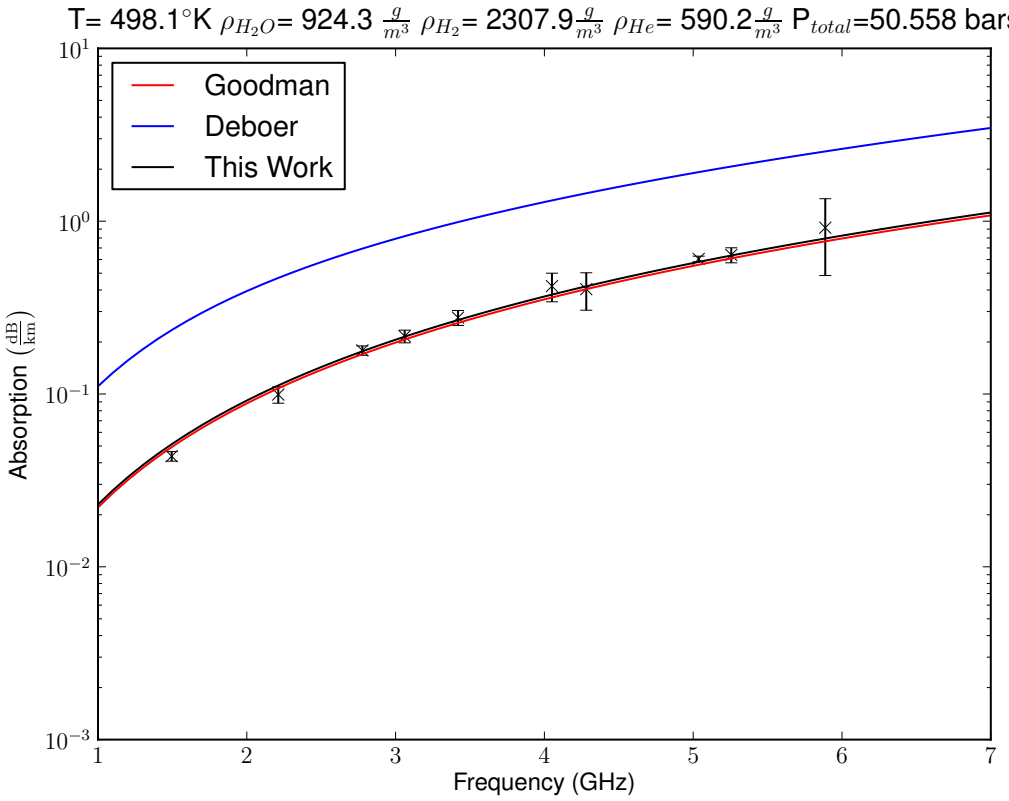

Figure 5.103: Experiment 13 with H_2/He mixture 50.5 bars total pressure.

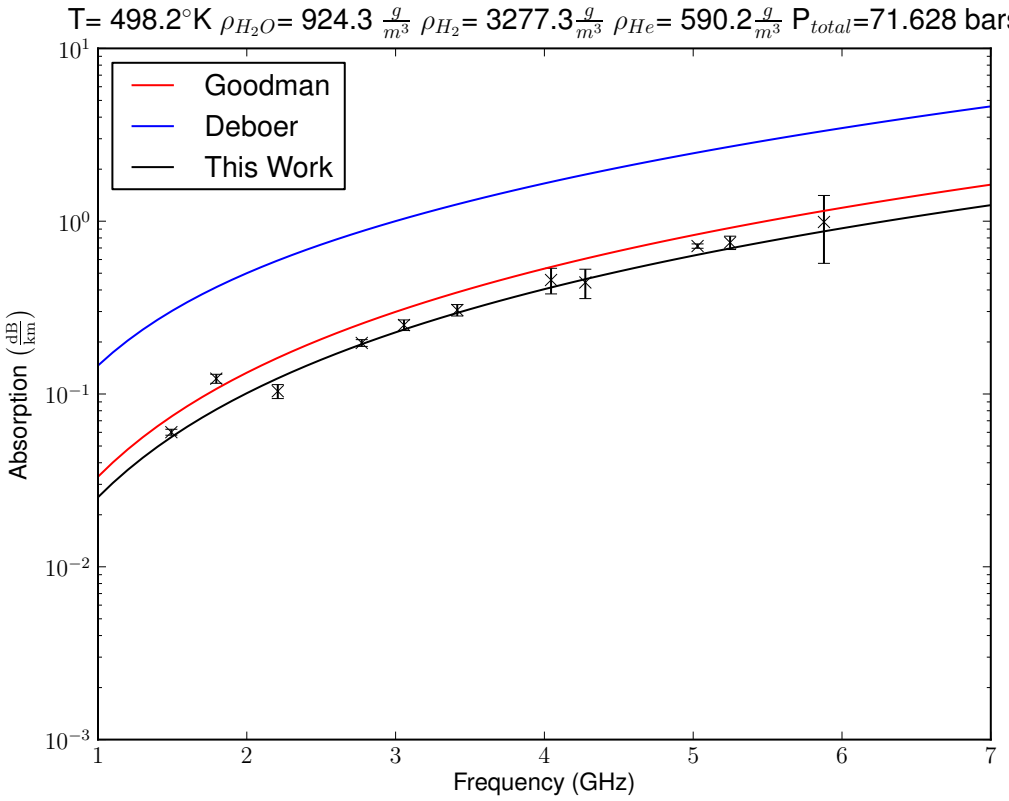

Figure 5.104: Experiment 13 with H_2/He mixture 71.6 bars total pressure.

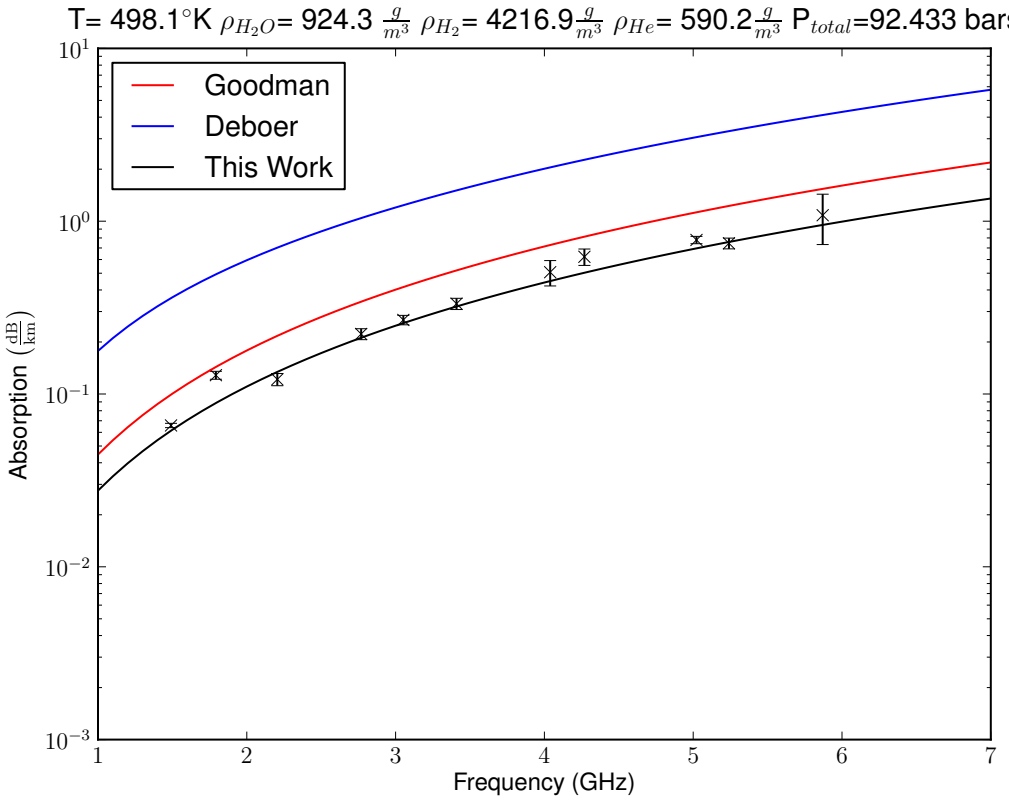

Figure 5.105: Experiment 13 with H_2/He mixture 92.4 bars total pressure.

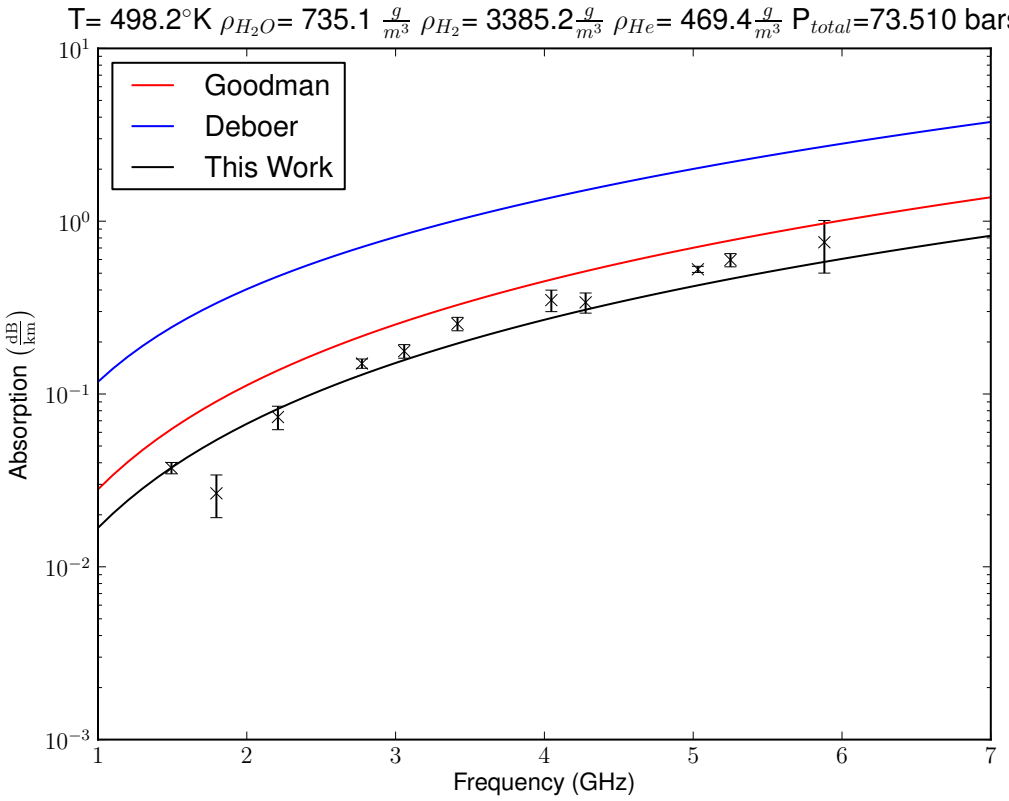

Figure 5.106: Experiment 13 with H_2/He mixture 73.5 bars total pressure (after maximum pressure).

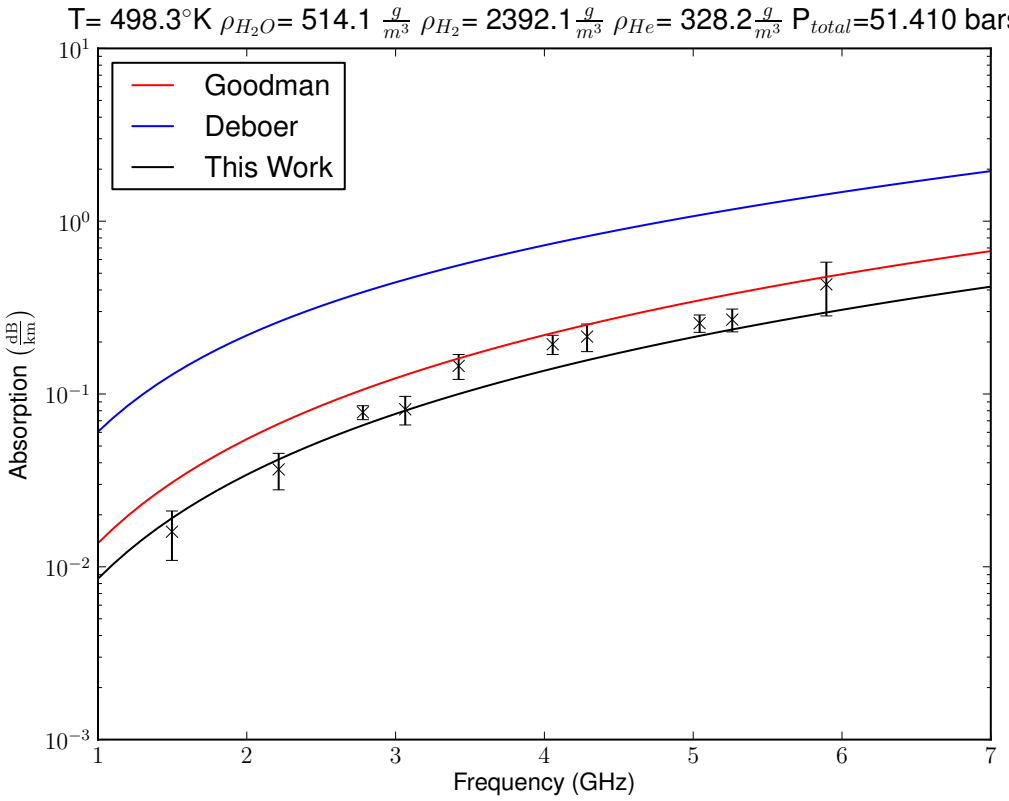

Figure 5.107: Experiment 13 with H_2/He mixture 51.4 bars total pressure (after maximum pressure).

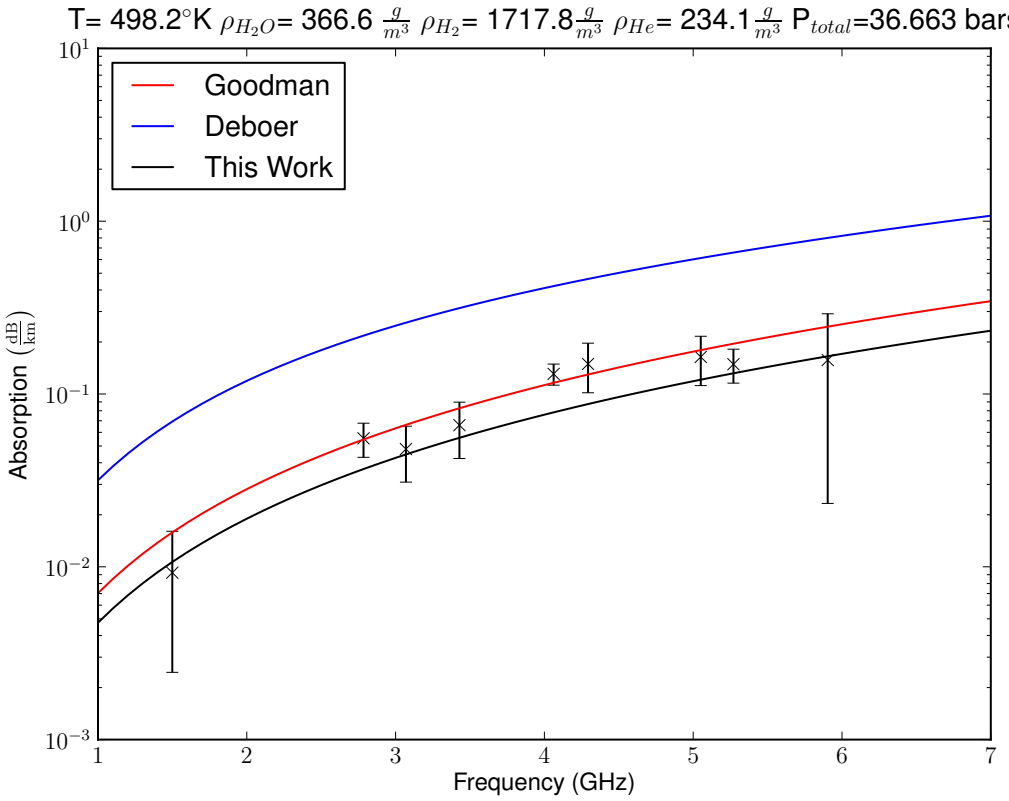

Figure 5.108: Experiment 13 with H_2/He mixture 36.6 bars total pressure (after maximum pressure).

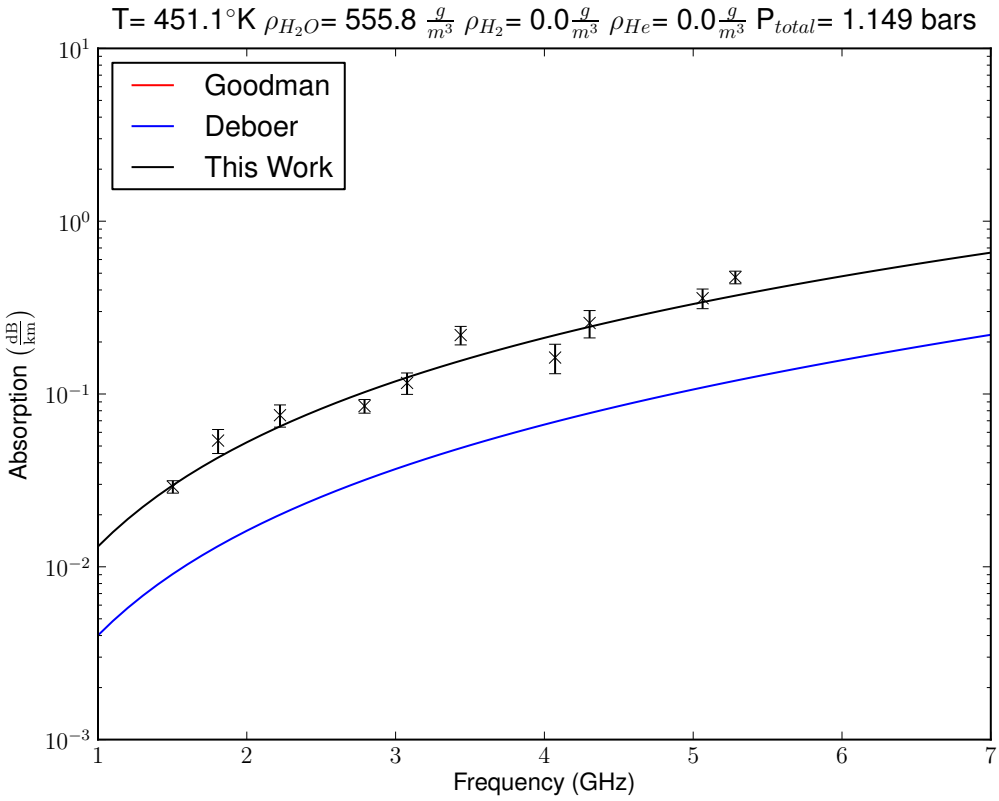

Figure 5.109: Experiment 14 with pure water vapor.

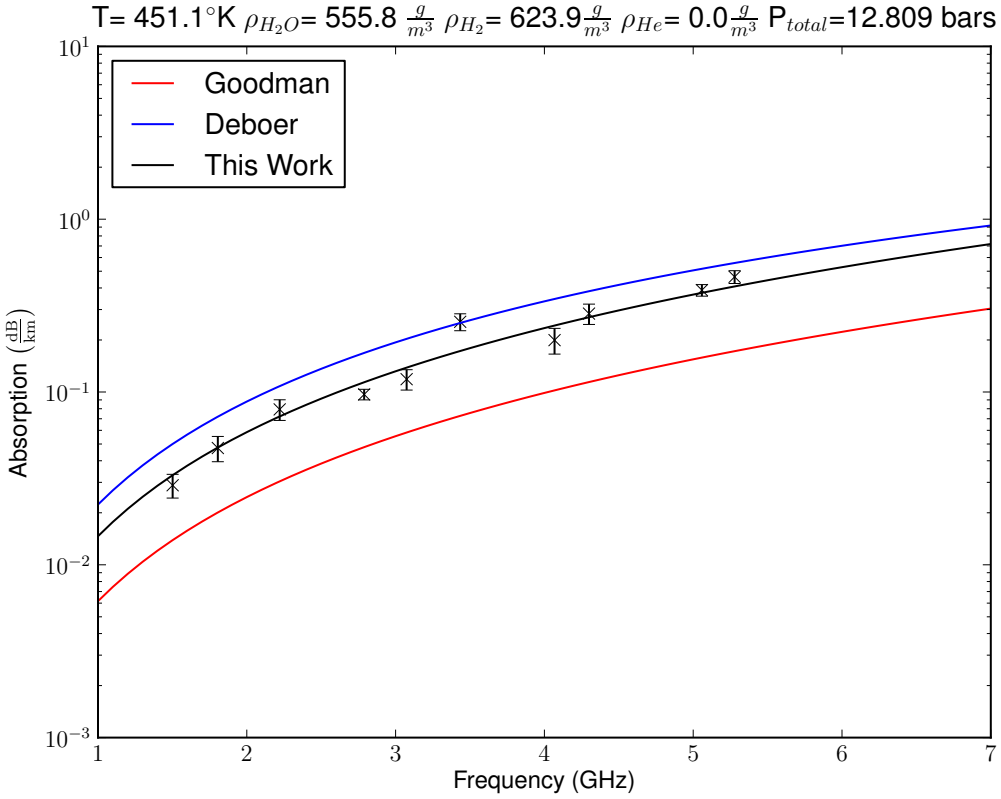

Figure 5.110: Experiment 14 with H_2 mixture 12.8 bars total pressure

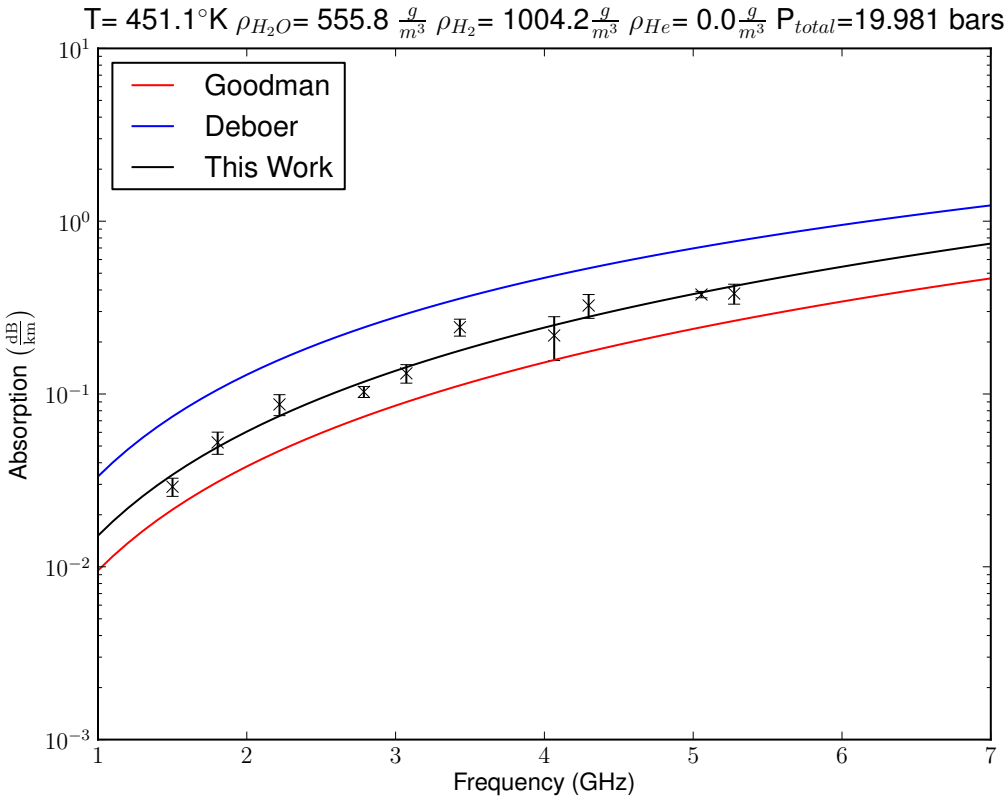

Figure 5.111: Experiment 14 with H_2 mixture 20 bars total pressure

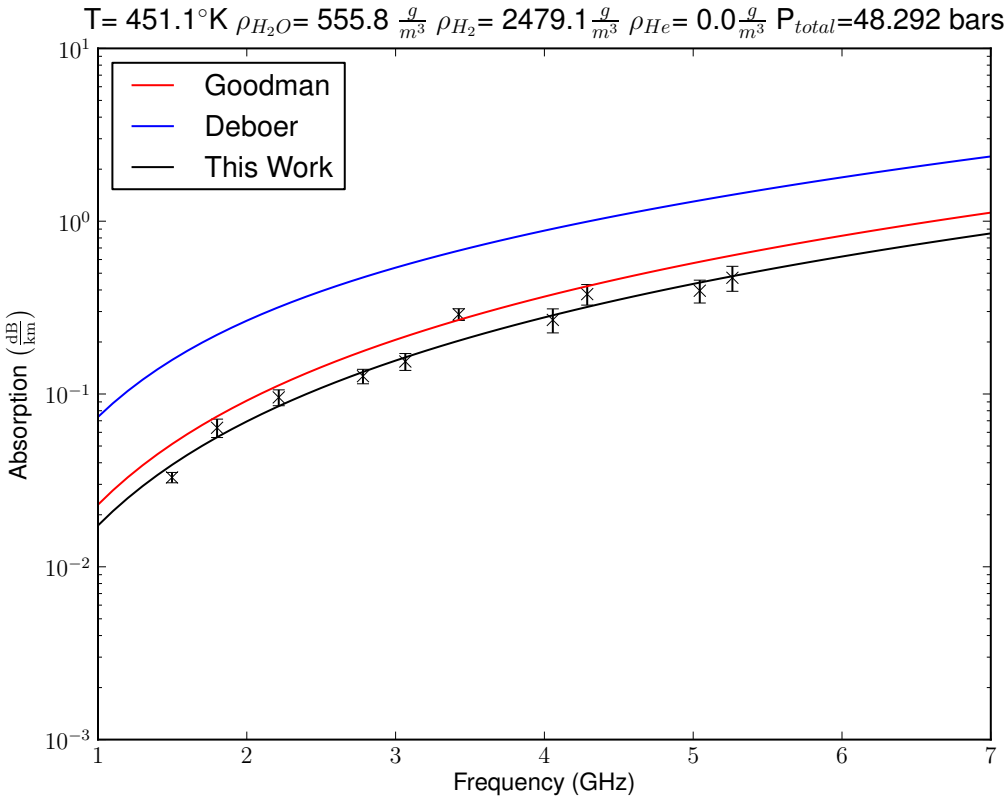

Figure 5.112: Experiment 14 with H_2 48.3 bars total pressure.

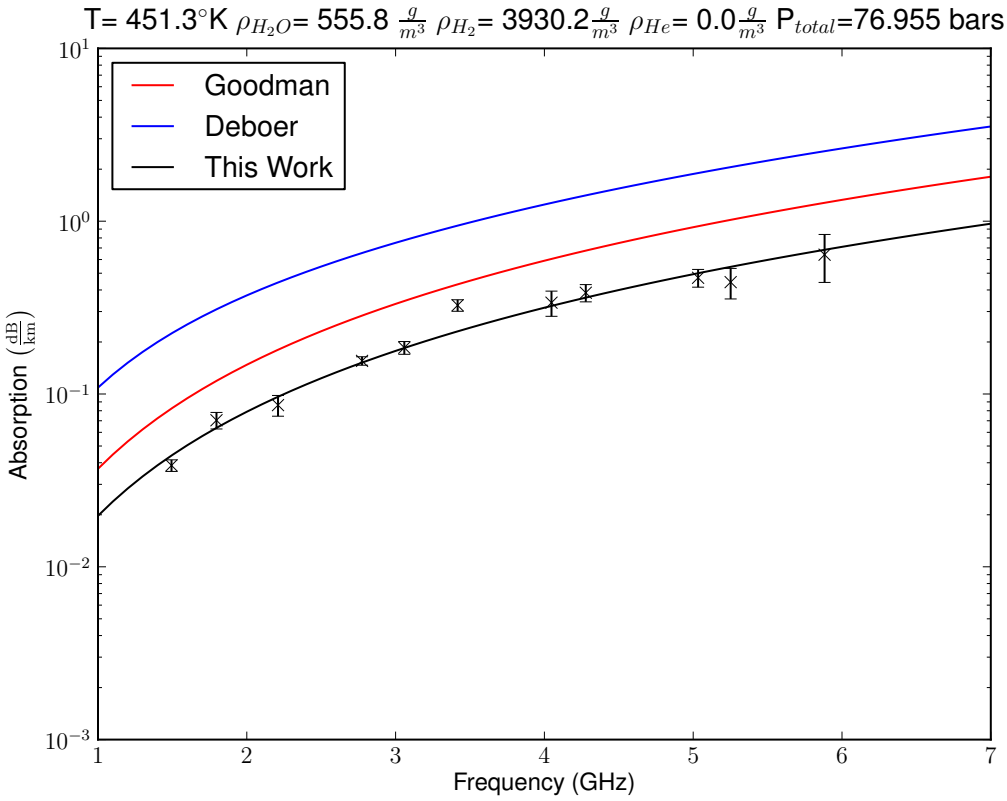

Figure 5.113: Experiment 14 with H_2 mixture 77 bars total pressure.

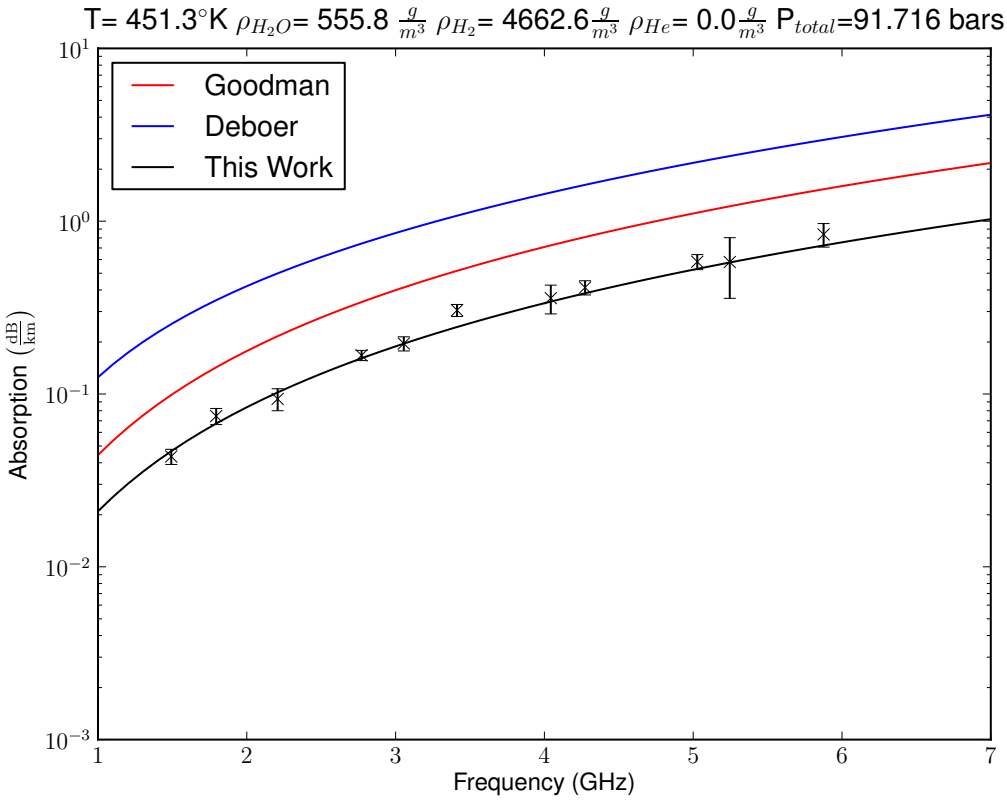

Figure 5.114: Experiment 14 with H_2 mixture 91.7 bars total pressure.

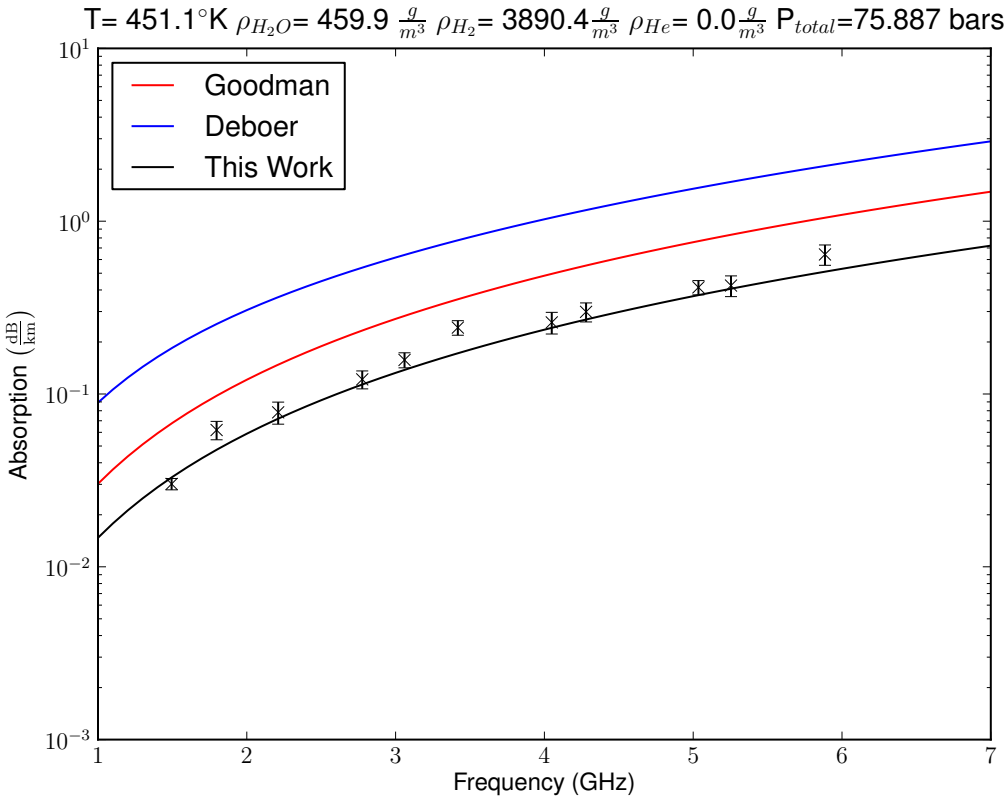

Figure 5.115: Experiment 14 with H_2 mixture 75.9 bars total pressure (after maximum pressure).

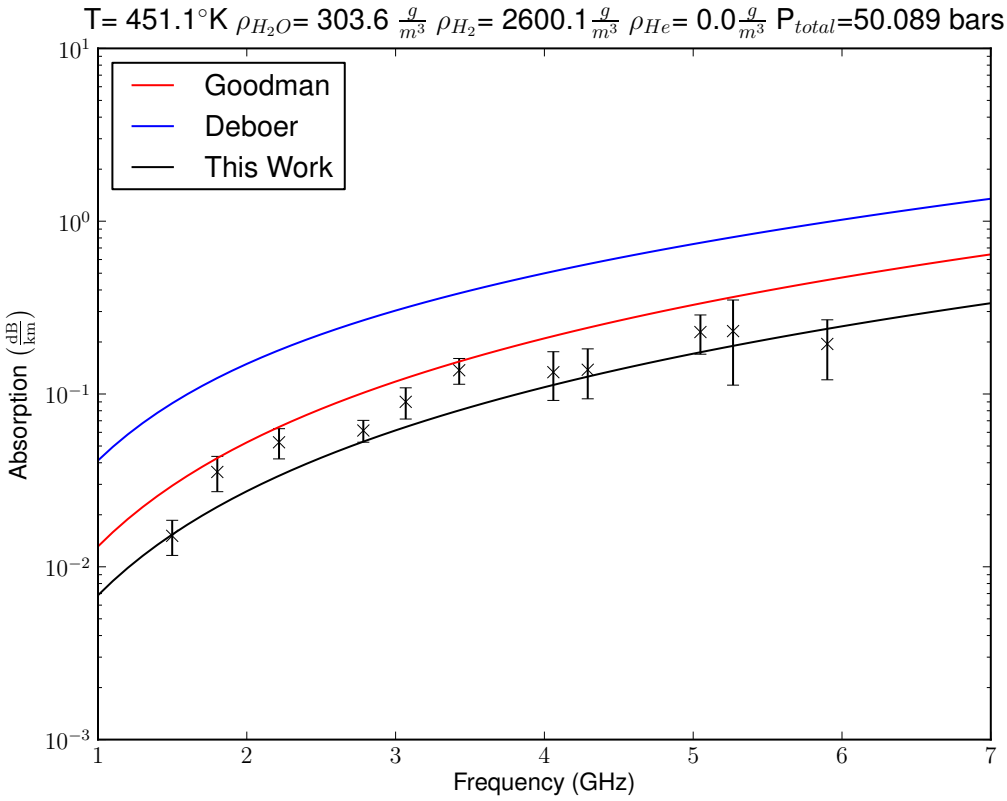

Figure 5.116: Experiment 14 with H_2 mixture 50.9 bars total pressure (after maximum pressure).

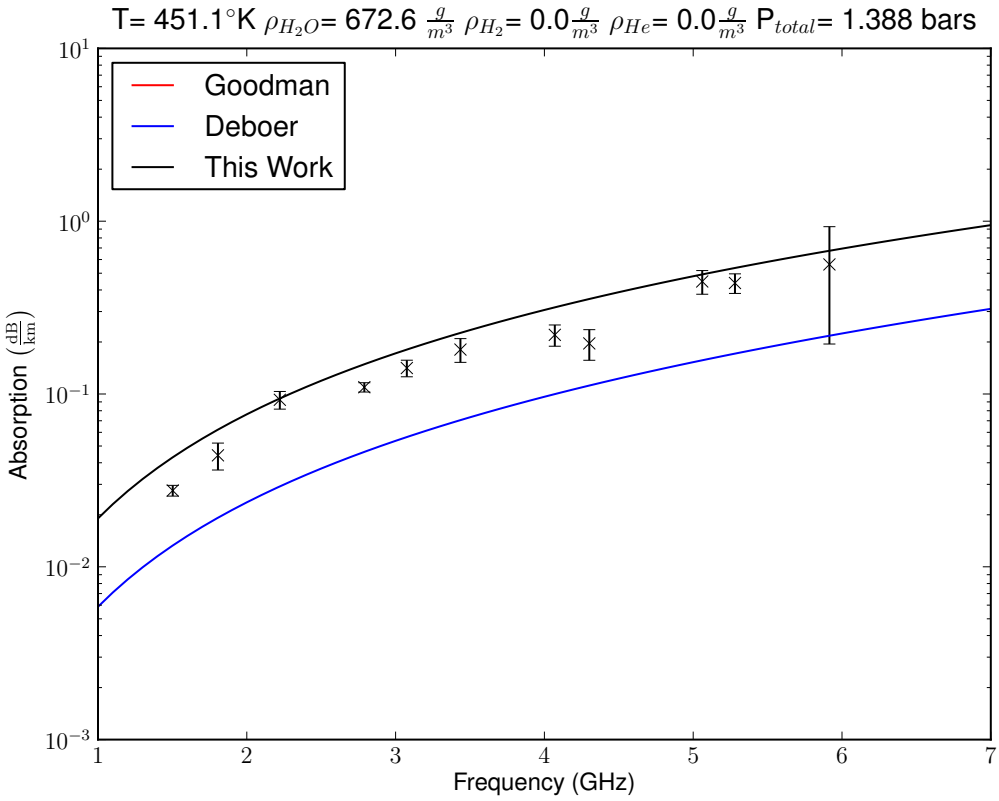

Figure 5.117: Experiment 15 with pure water vapor.

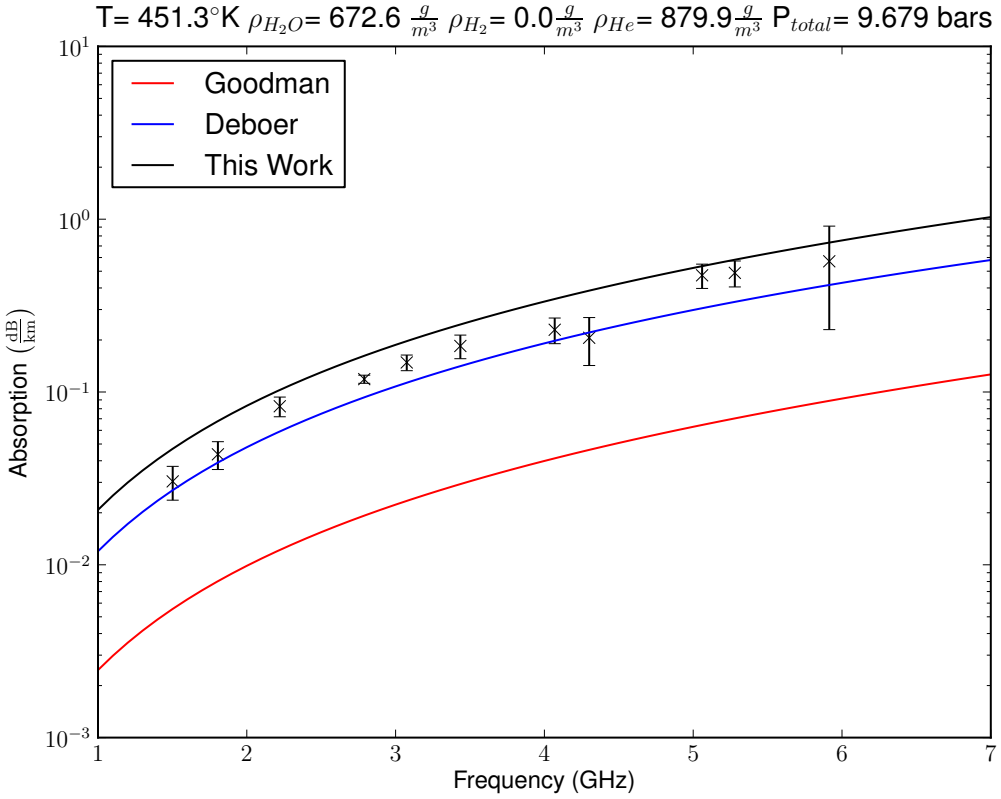

Figure 5.118: Experiment 15 with He mixture 9.7 bars total pressure

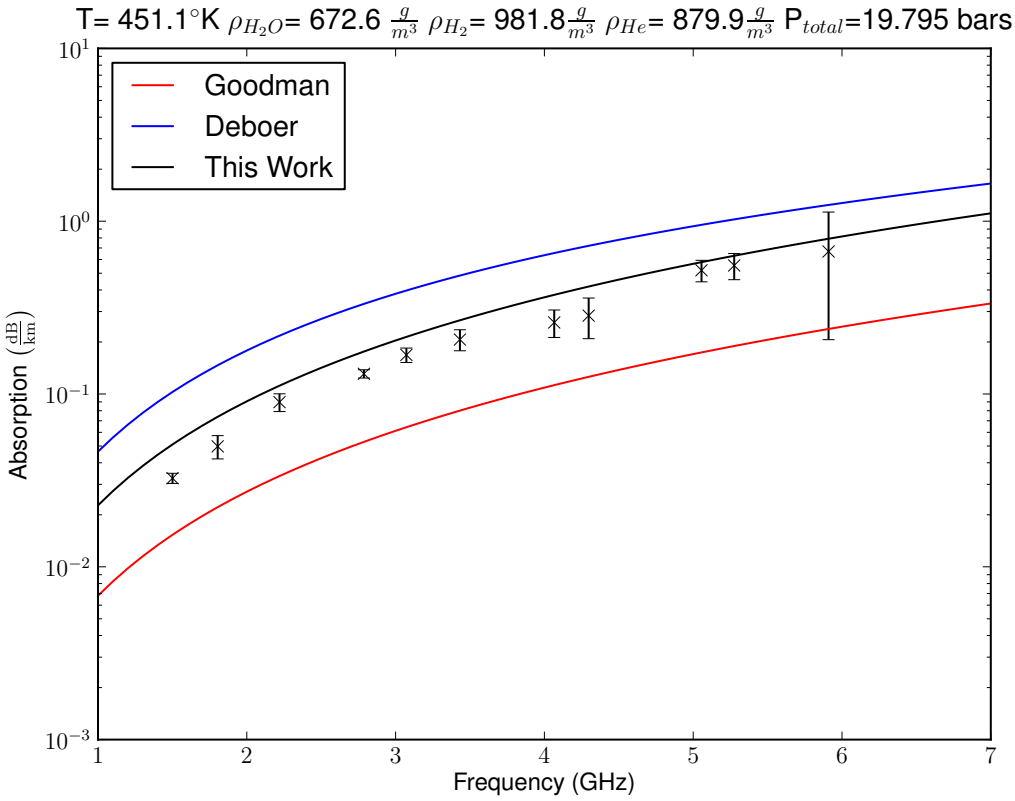

Figure 5.119: Experiment 15 with H_2/He mixture 19.8 bars total pressure

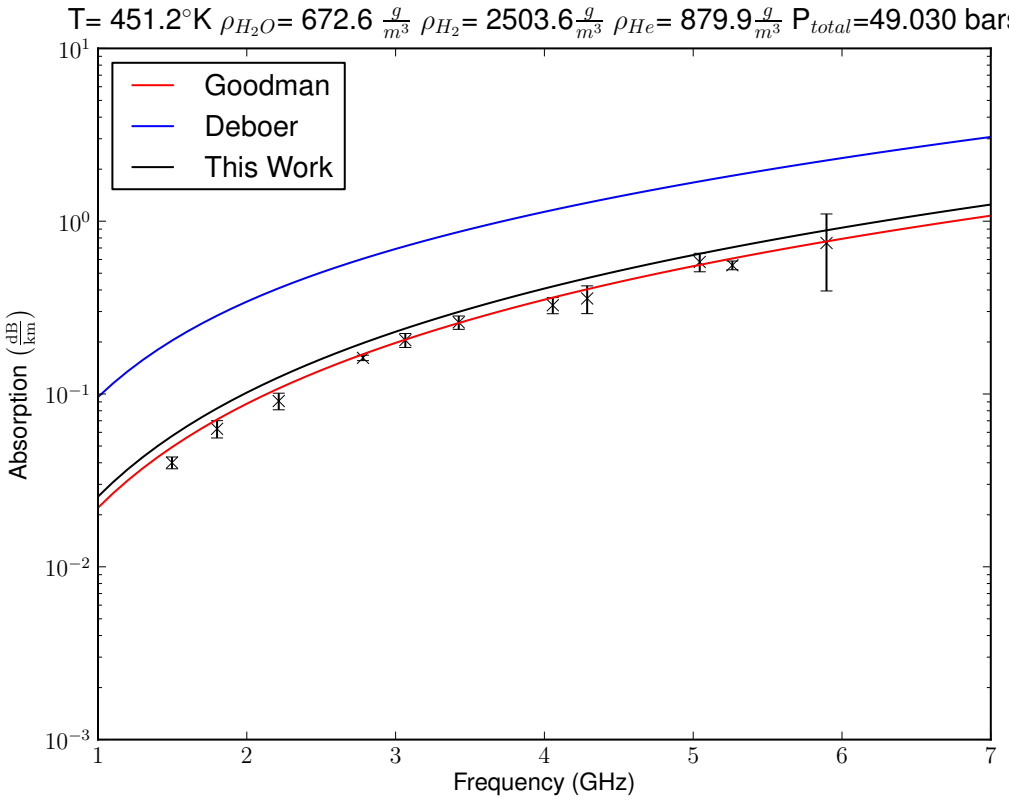

Figure 5.120: Experiment 15 with H_2/He 49 bars total pressure.

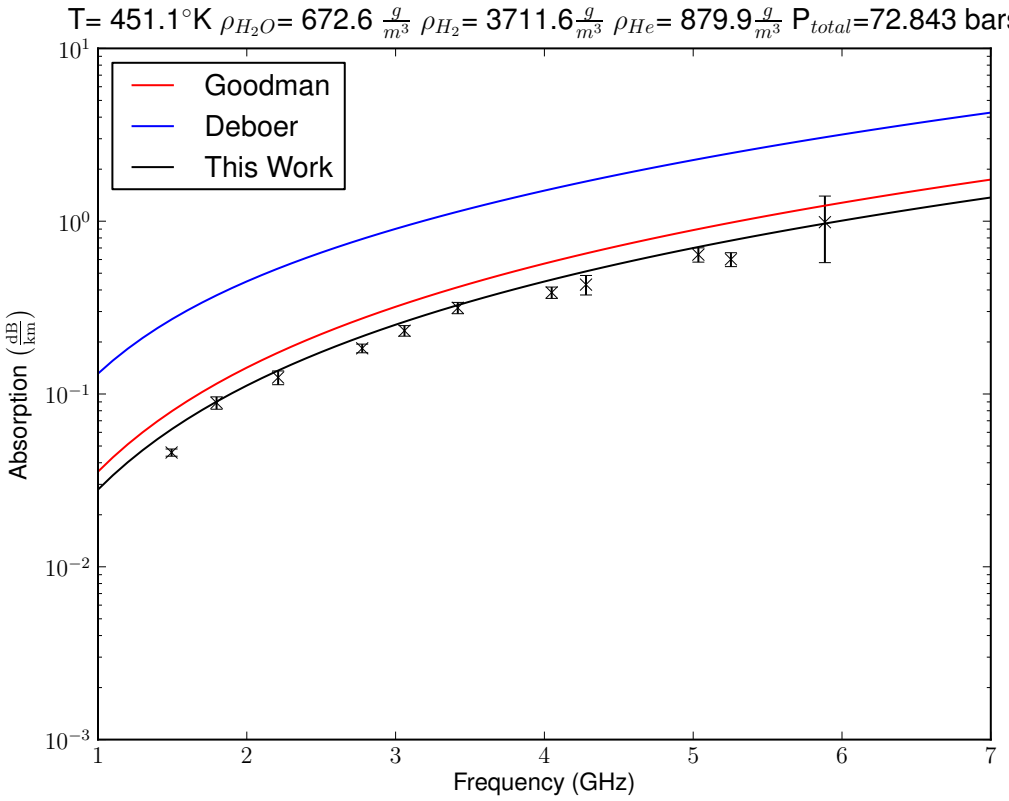

Figure 5.121: Experiment 15 with H_2 mixture 72.8 bars total pressure.

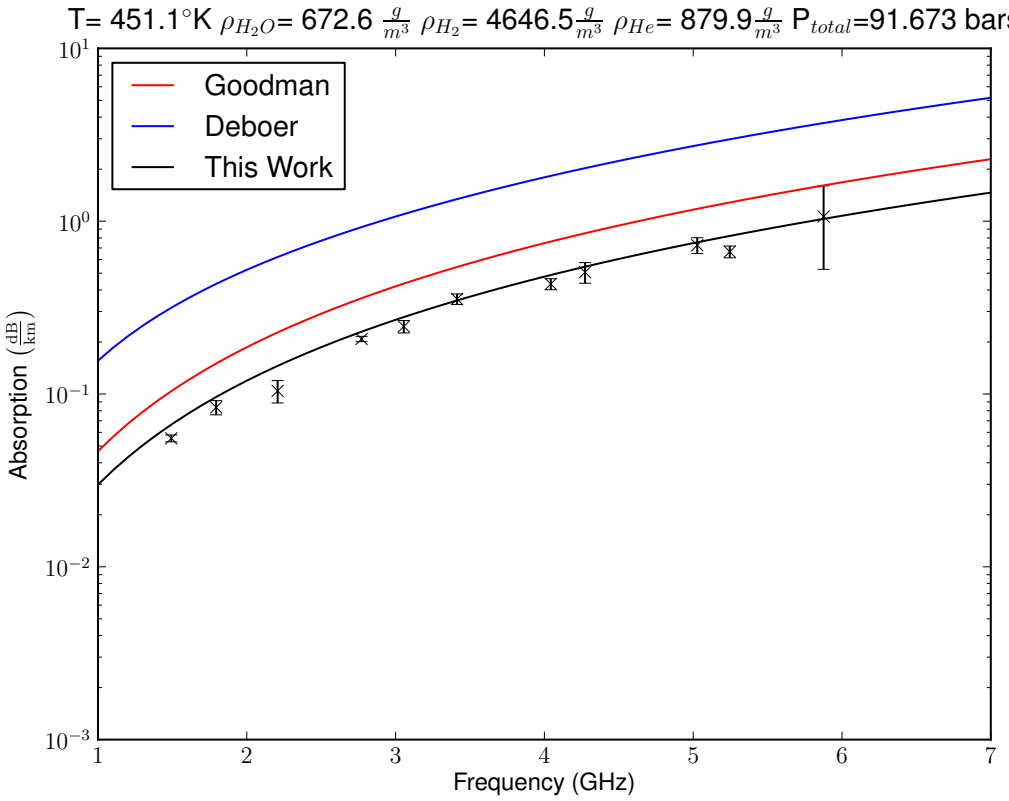

Figure 5.122: Experiment 15 with H_2 mixture 91.7 bars total pressure.

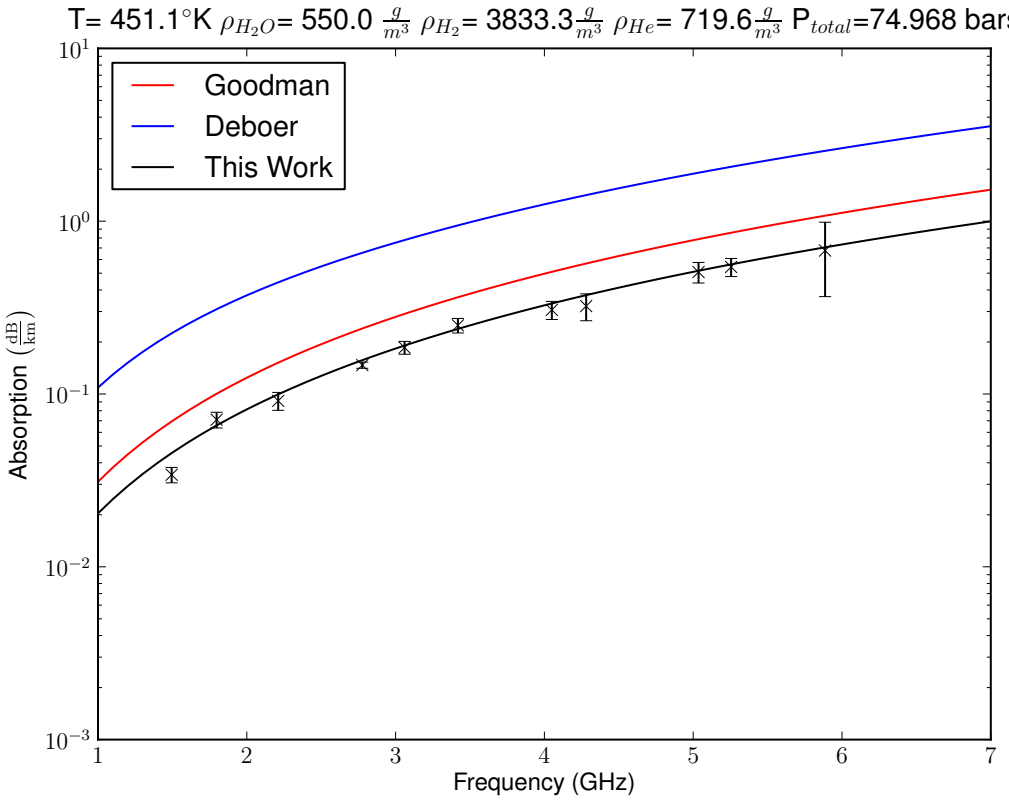

Figure 5.123: Experiment 15 with H_2 mixture 75 bars total pressure (after maximum pressure).

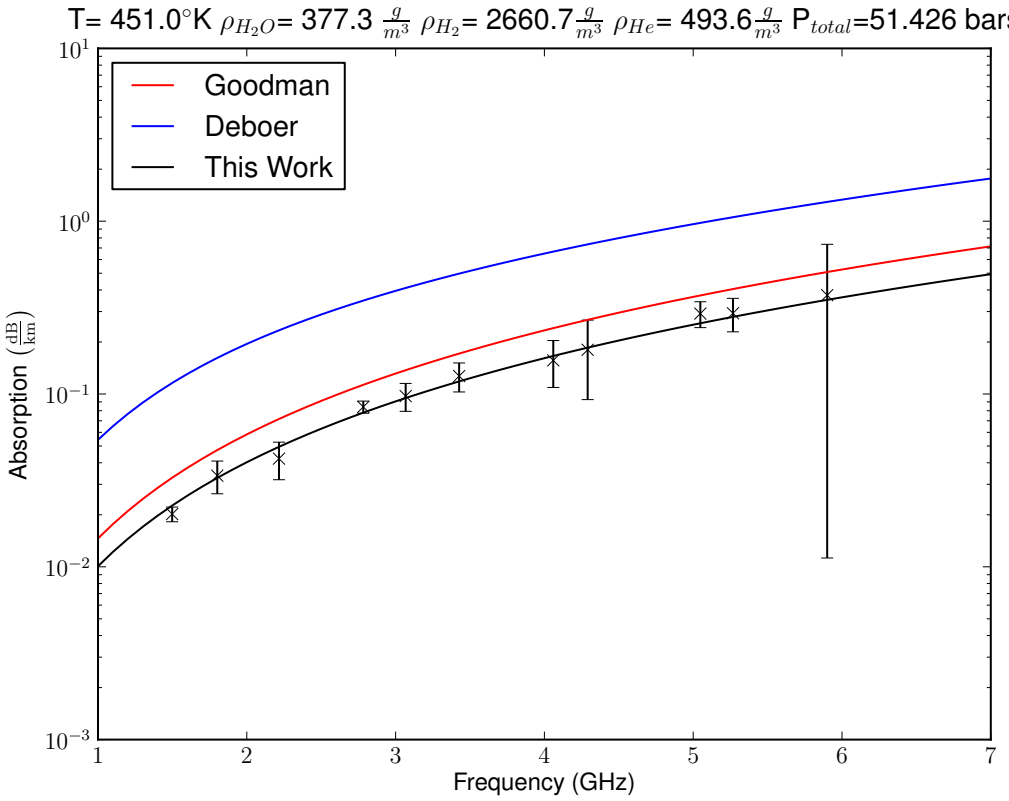

Figure 5.124: Experiment 15 with H_2/He mixture 51.4 bars total pressure (after maximum pressure).

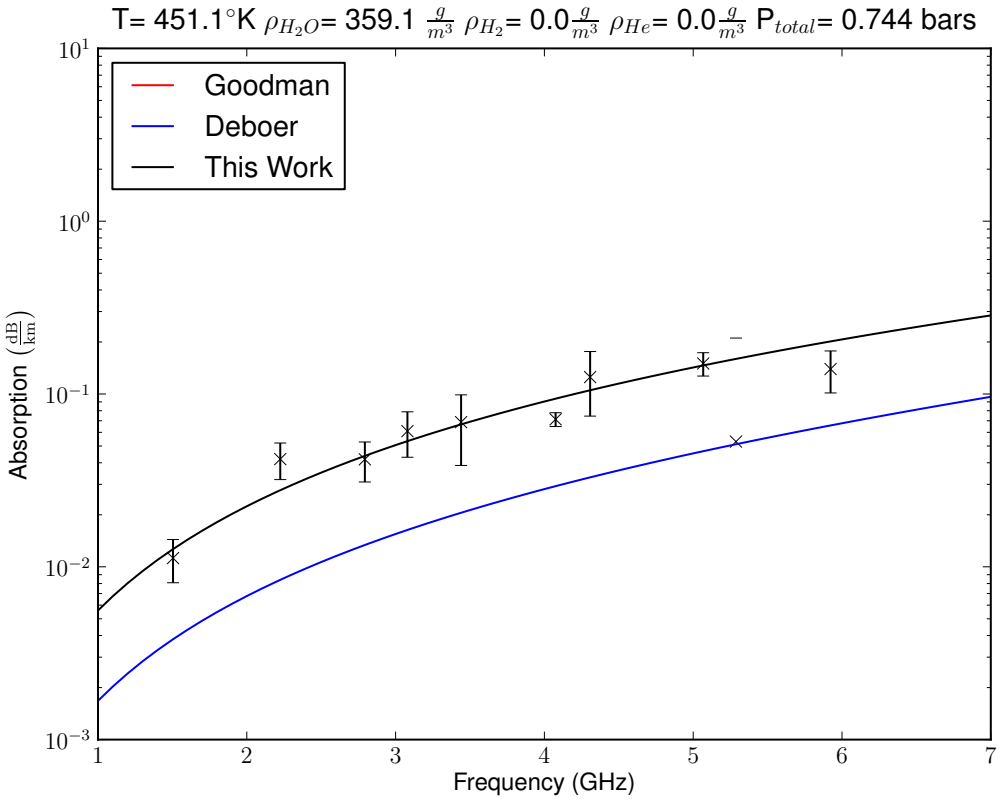

Figure 5.125: Experiment 16 with pure water vapor.

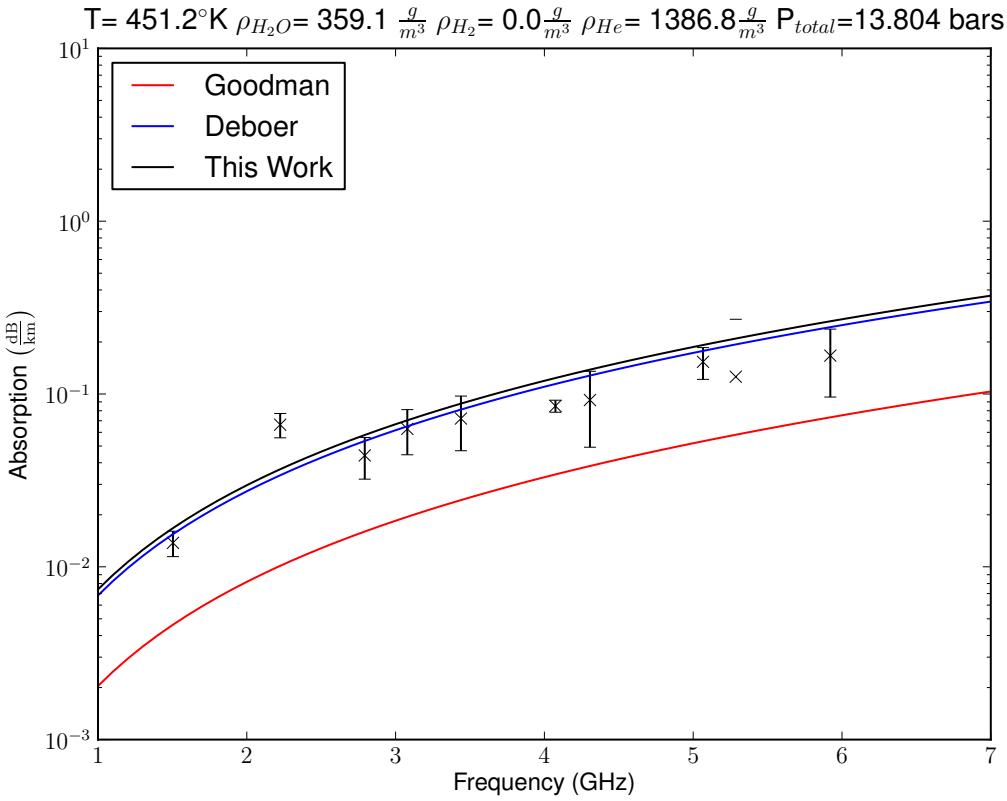

Figure 5.126: Experiment 16 with He mixture 13.8 bars total pressure

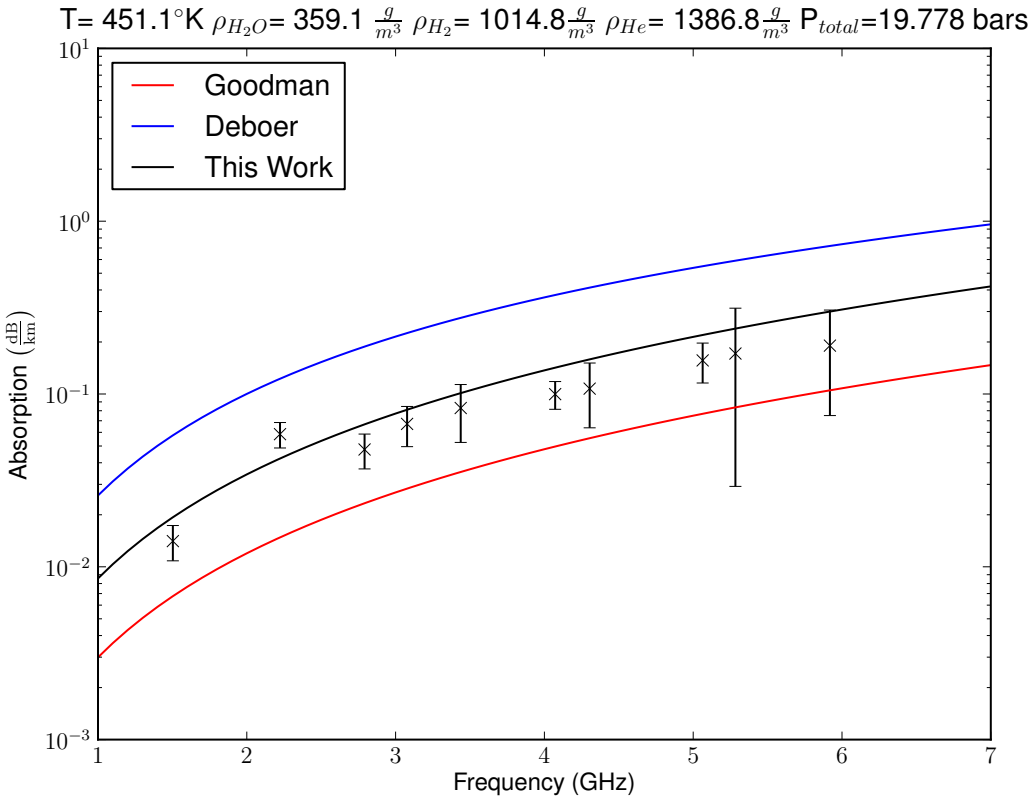

Figure 5.127: Experiment 16 with H_2/He mixture 19.8 bars total pressure

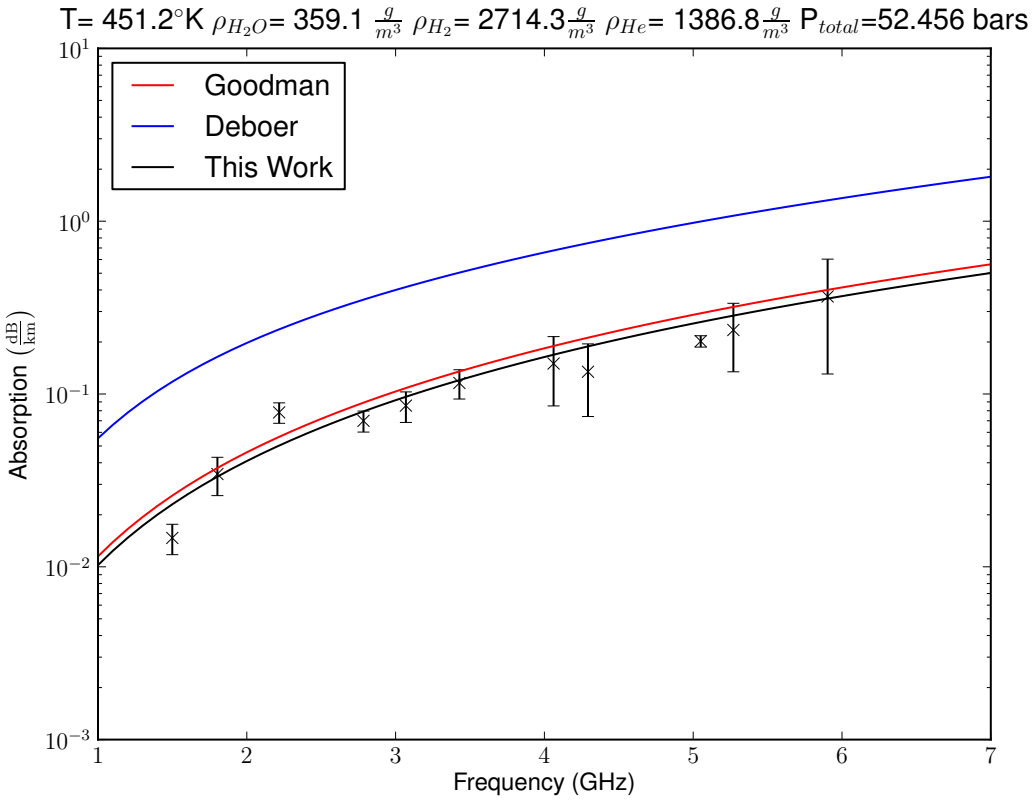

Figure 5.128: Experiment 16 with H_2/He 52.5 bars total pressure.

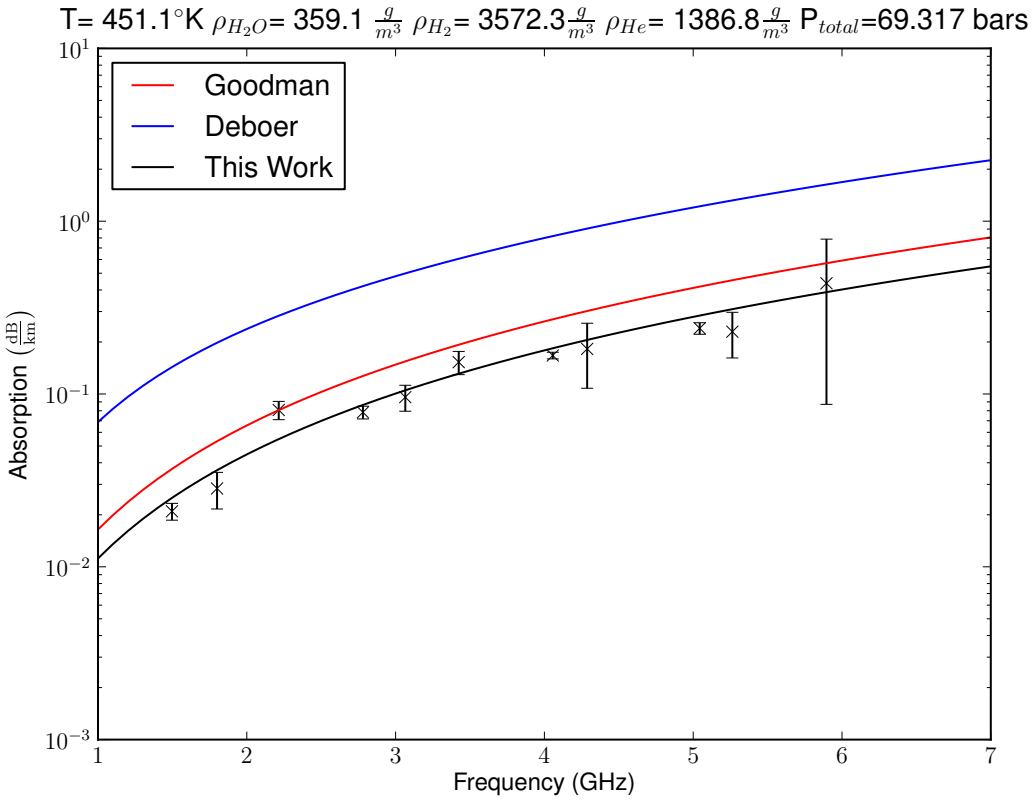

Figure 5.129: Experiment 16 with H_2 mixture 69.3 bars total pressure.

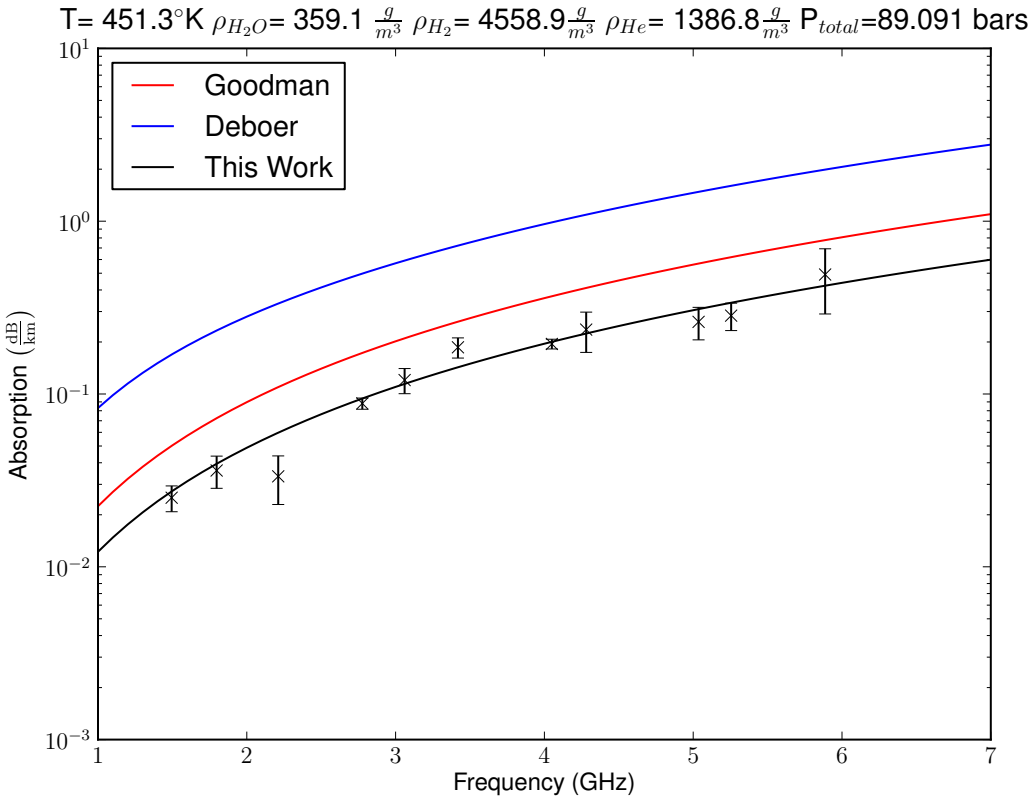

Figure 5.130: Experiment 16 with H_2 mixture 89 bars total pressure.

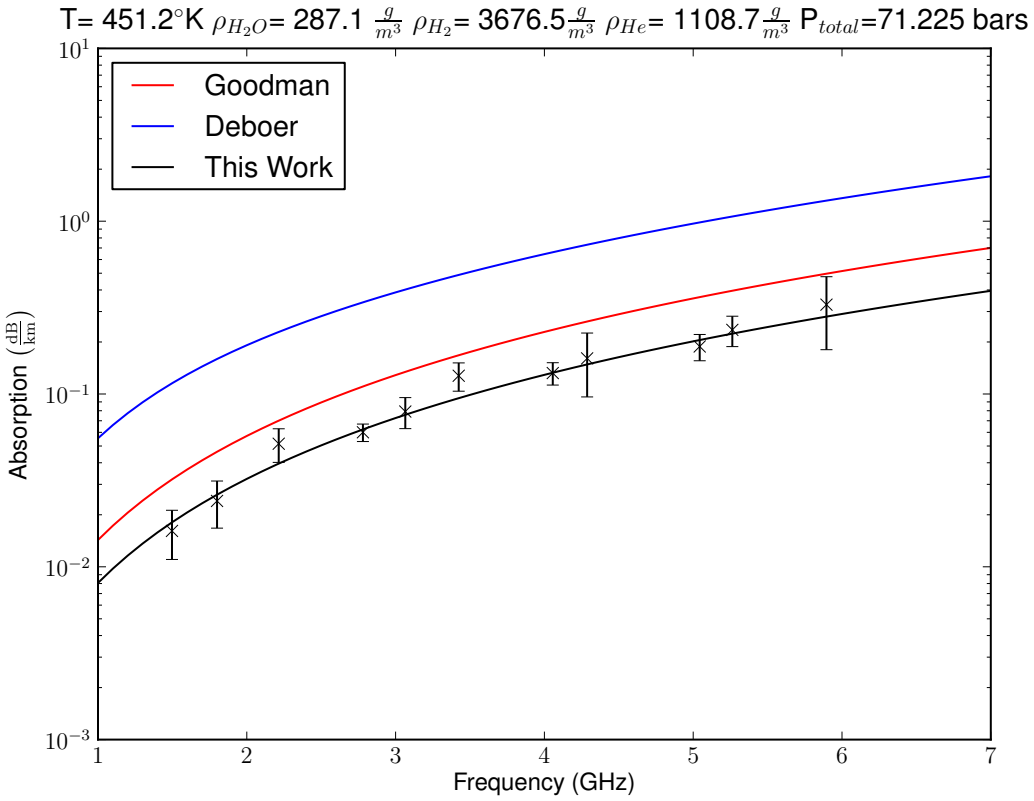

Figure 5.131: Experiment 16 with H_2 mixture 71.2 bars total pressure (after maximum pressure).

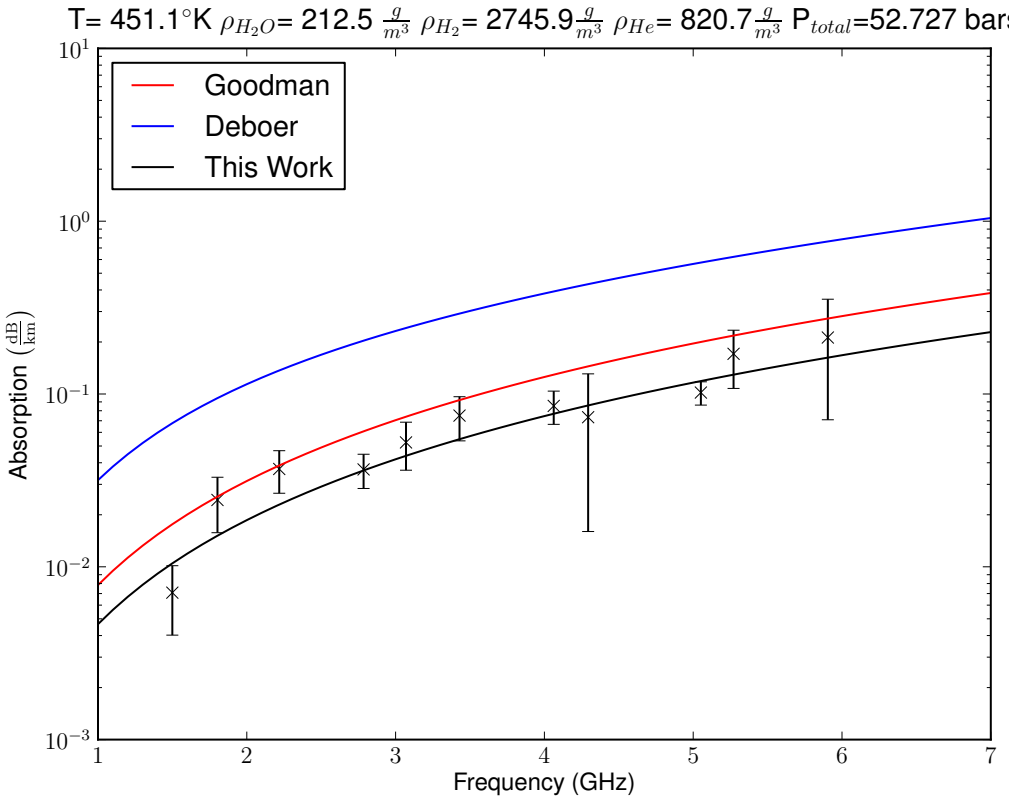

Figure 5.132: Experiment 16 with H_2/He mixture 52.7 bars total pressure (after maximum pressure).

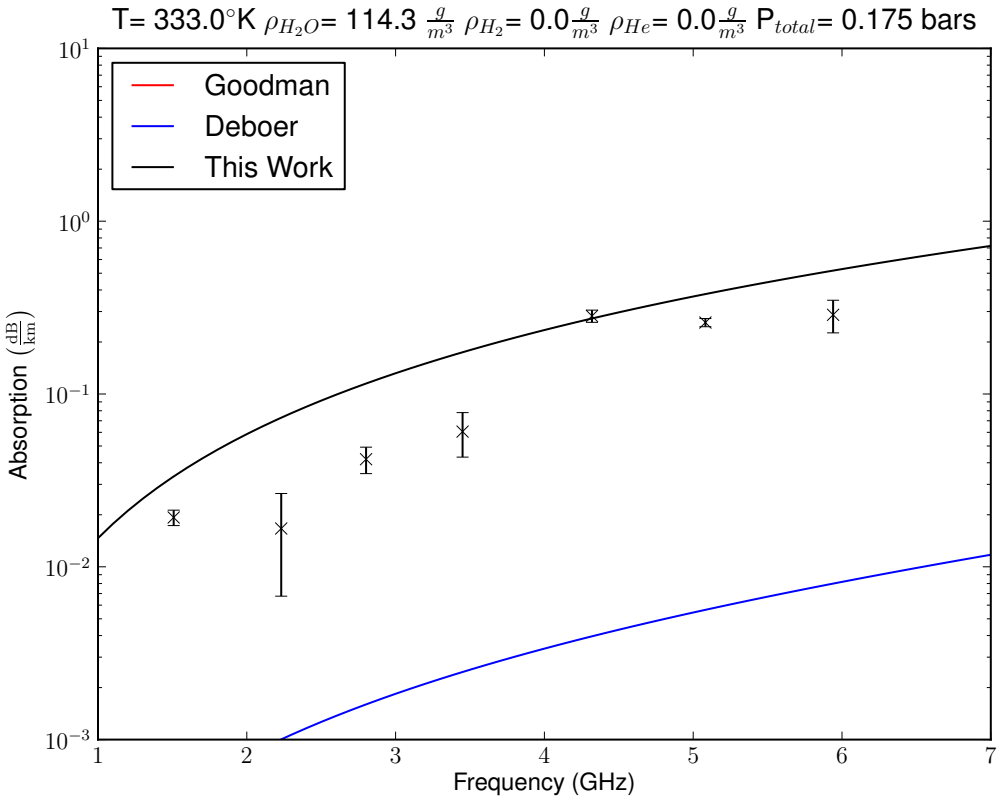

Figure 5.133: Experiment 17 with pure water vapor.

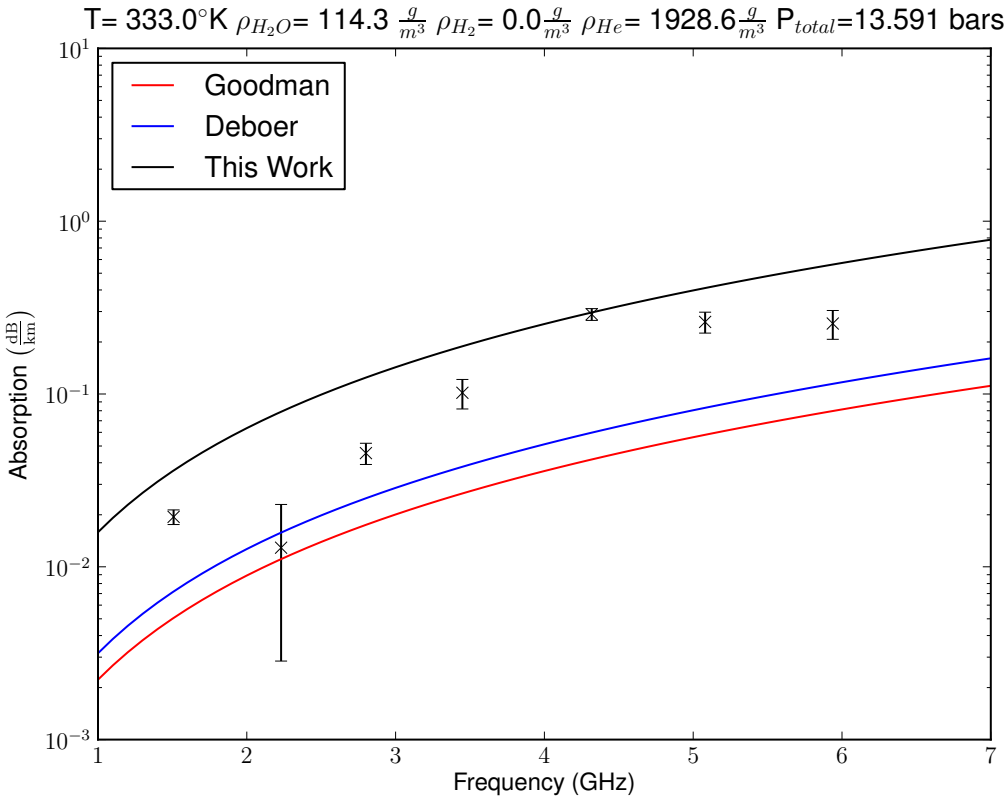

Figure 5.134: Experiment 17 with He mixture 13.6 bars total pressure

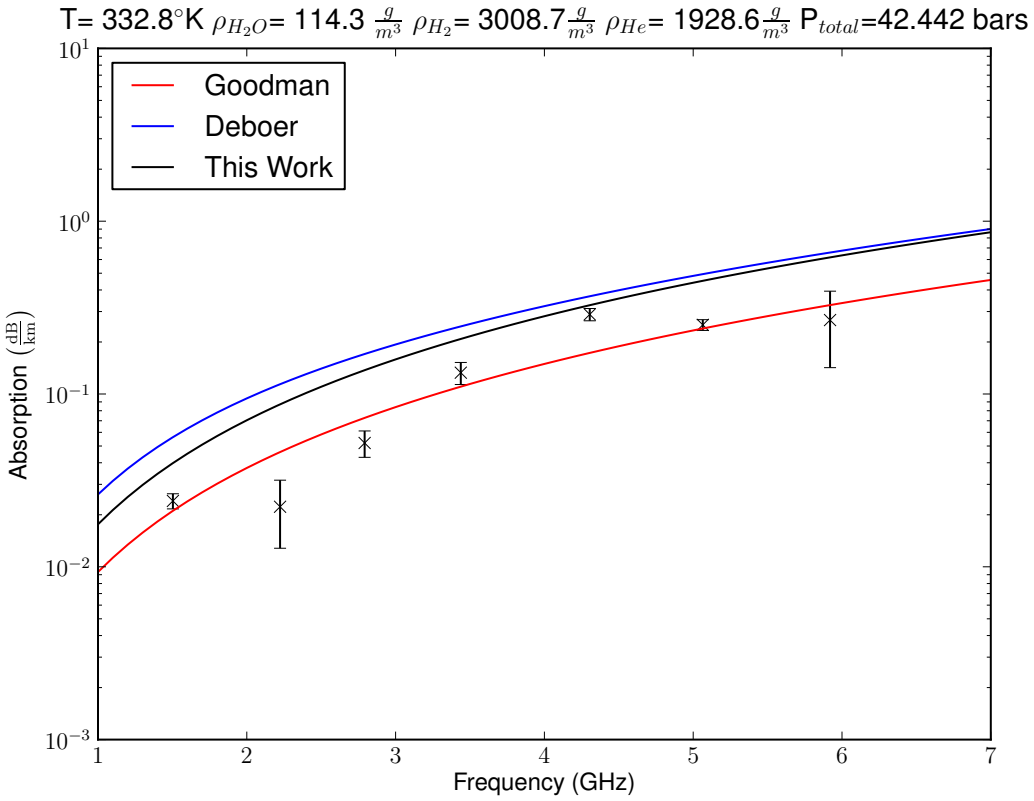

Figure 5.135: Experiment 17 with H_2/He mixture 42.4 bars total pressure

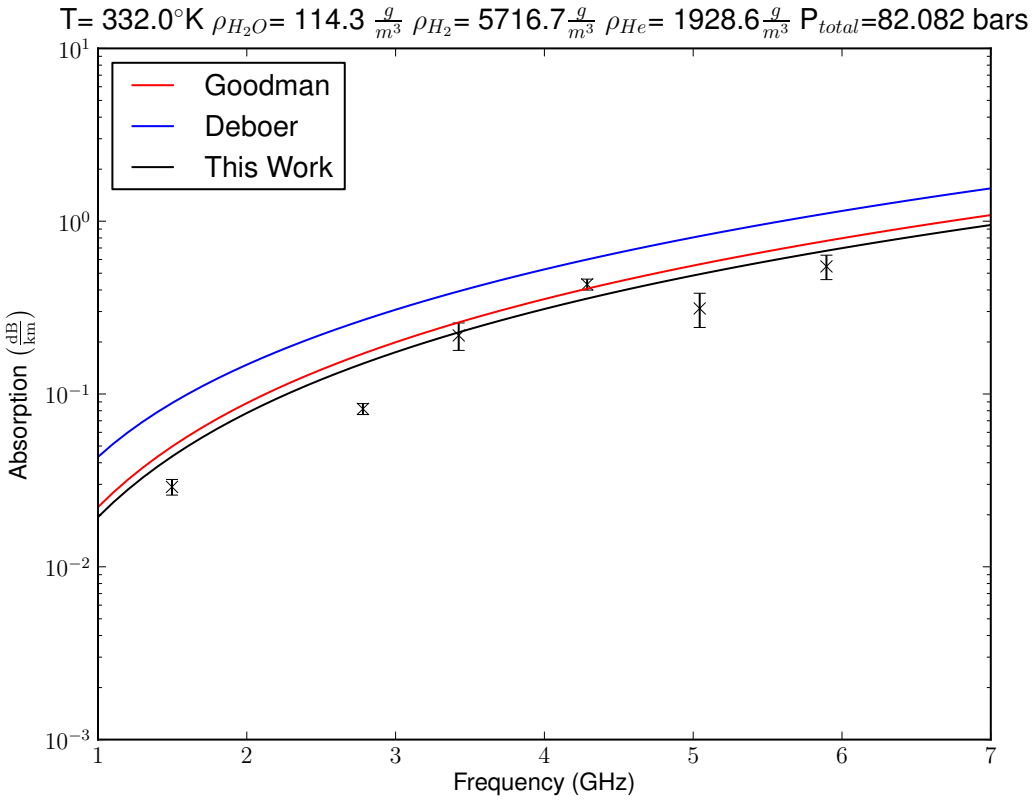

Figure 5.136: Experiment 17 with H_2/He 82 bars total pressure.

CHAPTER VI

THERMODYNAMICS OF THE JOVIAN ATMOSPHERE

The thermodynamics of the Jovian Atmosphere are a diverse, complex, and growing area of study. One of primary goals of the Juno MWR is to determine the deep abundance of water vapor (if it exists), and ammonia. If this is to be done accurately, one must have a thorough understanding of the atmospheric structure, and thermodynamic processes which govern the deep troposphere. Previous studies which have made attempts to observe, or infer the atmospheric structure of Jupiter either focus upon the upper troposphere (i.e., *Atreya et al.*, 2003; *Atreya et al.*, 1995), the deep interior structure (i.e., *Guillot*, 1999), or deep atmospheric composition inferences potentially contaminated by synchrotron radiation (i.e., *de Pater et al.*, 2001). Since the goal is to retrieve water vapor and ammonia in the 10-100 bar levels in the Jovian atmosphere using the Juno MWR, a new framework incorporating the most up to date information regarding the equation of state of the gas mixture in the 10-100 bar region is critical (perhaps even to the 1000 bar level).

Previous works using thermochemical equilibrium models (i.e., *DeBoer and Steffes*, 1996b; *Romani et al.*, 1989; *Weidenschilling and Lewis*, 1973) need to be updated to include an appropriate equation of state in place of the ideal gas law. Some models have included a basic Van der Waals correction for hydrogen (i.e., *Atreya and Wong*, 2004); however, this neglects the possibility that other less abundant species, and their mixing interactions can play a role under high pressures. In this chapter the work of *DeBoer and Steffes* (1996b) is updated to include mixing interactions between H_2-CH_4, and H_2-H_2O. The interactions between H_2-He, He-H_2O, H_2-NH_3 are ignored

largely due to the lack of measurements to constrain the interactions in the appropriate temperature-pressure regime. In reviewing the literature, there are measurements of the H_2-He (i.e., *Ree*, 1983) and He-H_2O systems (i.e., *Sretenskaja et al.*, 1995); however, neither reference alone provides enough data to enable the development of new interaction terms for a Jovian equation of state. The equations of state for the individual components H_2, He, H_2O, CH_4 are currently included. In this new model, only NH_3 and H_2S are considered ideal constituents, due to their low mole fraction in the Jovian atmosphere. However, future work should be pursued to include both their individual equations of state, and interaction terms with other constituents.

Understanding the equation of state of the fluid mixture deep within the Jovian atmosphere is also critical to understanding the formation of the water-ammonia cloud which assuming no sedimentation, or super-saturation, can reach bulk densities up to 100 $\frac{\mathrm{g}}{\mathrm{m}^3}$ (*Atreya et al.*, 2005). In Earth's atmosphere it has been widely acknowledged that cloud formation is in part controlled by the availability of cloud condensation nuclei (CCN), and there is a growing effort to include the aerosol-cloud interactions into models of Earth's Atmosphere (i.e., *Barahona and Nenes*, 2009). Understanding the aerosol-cloud interaction in the Jovian atmosphere is quite a bit more complicated given that the availability, or even the composition of aerosols that might act as nuclei at the 10 bar level are highly speculative. *Sagan and Salpeter* (1976) have made reference to the possibility of compounds containing Na and Cl as possible cloud nuclei for the water-ammonia cloud in an attempt to analyze to possibility for life on Jupiter. Lighting-generated black carbon has been suggested as a possibility on Saturn (*Baines et al.*, 2009), since lightning has been frequently observed on Jupiter (*Baines et al.*, 2007). The ability of black carbon to act as a CCN would of course require some inefficient combustion process whereby there is a coating of hydroscopic material, as black carbon itself is hydrophobic. The convective activity resulting in lightning could also play a role in the ability to form such large cloud bulk densities.

In any case, it is clear that assuming thermodynamic equilibrium for cloud formation is unlikely, some form of sedimentation process should be considered. In this work we explore a range of cloud bulk densities using a simple cloud sedimentation model following *Ackerman and Marley* (2001).

The thermodynamic model presented in this work should only be considered as a work-in-progress as the uncertainties regarding thermodynamics in the Jovian atmosphere are quite large, and warrant further study.

6.1 Defining Pressure and Altitude Steps

The Jovian atmosphere is composed of a complex fluid which varies in composition, density, temperature, and pressure. While these variations take place as a function of latitude, longitude, and altitude as continuous functions, some level of discretization is necessary to develop a computer simulation. While a full three-dimensional thermodynamic model which incorporates all dimensions would be desirable, such a model is not necessary to investigate the fundamental sensitivities relevant to the Juno MWR. Our model starts with two fundamental assumptions: hydrostatic equilibrium, and that in a localized sense the atmosphere can be assumed to be variable only along the altitude dimension, which can be divided into discrete layers.

In our current model for the Jovian atmosphere, there are three methods to generate discrete layers: the first is the original method used in *DeBoer and Steffes* (1996b) which uses an upper and lower boundary in pressure, and steps according to altitude (dz). To do this, one only needs to assume the atmosphere is in hydrostatic equilibrium, and recall the hydrostatic law where,

$$dP = \rho g dz \tag{6.1}$$

where ρ is the atmospheric density, g is acceleration due to gravity, and dz is the change in altitude. If it is assumed the gas is ideal, the equation of state becomes

$$P = \frac{\rho RT}{M_{mix}} \tag{6.2}$$

where M_{mix} is the molecular weight of the fluid mixture. The equation of state and hydrostatic law may then be combined to give

$$\frac{dP}{dz} = \frac{M_{mix}P}{RT}H \tag{6.3}$$

where $H = RT/M_{mix}g$ is the pressure scale height. Solving this for the desired pressure step in the discrete form, this gives

$$\Delta P = \Delta z \frac{P}{H} \tag{6.4}$$

where Δz is the altitude step entered by the user, and P and H are the pressure and pressure scale height at a particular level. Alternatively, the step in Δz can be solved for a given ΔP where

$$\Delta z = \frac{H}{P}\Delta P. \tag{6.5}$$

The second formulation, where the step size is specified in terms of pressure, is more convenient in the Jovian atmosphere, given most studies refer to pressure levels, rather than altitude levels. While this approach was an improvement over previous ones, it does not account for the fact that the atmosphere is not an ideal gas. To account for the non-ideality of the gas, the third method treats P as a proxy for density. That is the density for each component is specified by

$$\rho_i = X_i P \frac{R}{M_{i,gas}} T \tag{6.6}$$

where ρ_i is the density of the constituent i, X_i is the mole fraction of the constituent i. In this work, constituents i include H_2, He, CH_4, and H_2O, and the density of this group of components is computed along with the mole fractions of the group and then combined with

$$P_{real} = \rho_m RT \left(1 + \delta \frac{d\alpha^r(X_i)}{d\delta}\right) + X_{NH_3}P + X_{H_2S}P \tag{6.7}$$

where ρ_m is the density of the subset including H_2, CH_4, and H_2O, with X_{NH_3} and X_{H_2S} as the mole fractions of NH_3 and H_2S, respectively. The value of P_{real} is stored

separately as to not to interfere with cloud formulations (discussed in the next section), and can be used as a more accurate method to compute dz. The final method to compute Δz takes advantage of P_{real} using

$$\Delta z = \frac{H}{P_{real}} \Delta P \tag{6.8}$$

where ΔP is the user specified pressure step, and P_{real} is the value calculated using the equation of state.

6.2 Calculations based upon Saturation Vapor Pressure

The method used in the current thermodynamic model uses the formulation of *DeBoer and Steffes* (1996b) to compute cloud densities, and "wet" adiabatic lapse rate. The method uses a Thermo-Chemical Model (TCM) to check for condensation of various species. As a first step, the TCM steps in pressure from the deepest layer (highest pressure), and steps up to lower pressures. Along the way the TCM checks for condensation for a given step in pressure, dP. The criteria for condensate forming at a particular level is

$$P_i - P_{sat,i}(1 + F_{super}) > P_{sat,i} \tag{6.9}$$

where P_i is the partial pressure of constituent i, $P_{sat,i}$ is the saturation vapor pressure of constituent i, and F_{super} is the fraction of constituent i which is under supersaturation. The saturation vapor pressure is calculated using,

$$P_{sat} = \exp\left(\frac{a_1}{T} + a_2 + a_3 \ln(T) + a_4 T + a_5 T^2\right) \tag{6.10}$$

where T is the temperature in Kelvin, and a_1–a_5 are equilibrium coefficients for a given gaseous species over a particular condensate. The values for each gaseous species/condensate pair is given in Table 6.1.

For convenience we express constituent partial pressures in terms of mole fraction where,

$$X_i = \frac{P_i}{P} \tag{6.11}$$

Table 6.1: Coefficients for saturation pressure and latent heat

Condensation Process	a_1	a_2	a_3	a_4	a_5
NH_3(s)	-4122	27.8632	-1.8163	0	0
NH_3(aq)	-4409.3512	63.0487	-8.4598	5.51×10^{-3}	6.80×10^{-6}
H_2S (s)	-2920.6	14.156	0	0	0
H_2S (aq)	-2434.62	11.4718	0	0	0
CH_4 (s)	-1168.1	10.710	0	0	0
CH_4 (l)	-1032.5	9.216	0	0	0
H_2O (s)	-5631.1206	-22.1791	8.2312	-3.861449×10^{-2}	2.77494×10^{-5}
H_2O (l)	-2313.0338	-177.848	38.053682	-0.1344344	7.4465367×10^{-5}
PH_3 (s)	-1830.0	9.8225	0	0	0
$NH_3+H_2S \rightarrow NH_4SH$ (s)	-10834.0	34.151	0	0	0

where i is a given constituent, P_i is the partial pressure of the constituent i, and P is the atmospheric pressure.

The change in mole fraction of a given constituent from the previous pressure step (j-1) to the current pressure step (j) can be calculate by,

$$dX_{i,j} = \frac{P_{i,j} - P_{i,j-1}}{P_j} - \frac{X_{i,j-1}}{P} dP \tag{6.12}$$

To calculate $dX_{i,j}$ for a given change in temperature, the Clausius-Clapeyron equation can be considered where

$$\frac{dP_i}{dT} = \frac{L_i P_i}{RT} \tag{6.13}$$

where L_i is the latent heat from constituent i, and R is the universal gas constant ($8.3143 \times 10^7 \ \frac{erg}{K\,mole}$). Considering this the change in mole fraction for layer j can be computed as,

$$dX_{i,j} = \frac{X_{i,j-1} L_{i,j}}{RT^2}(T_j - T_{j-1}) - \frac{X_{i,j-1}}{P}(P_j - P_{j-1}) \tag{6.14}$$

The latent heat can be found by solving the Clausius-Clapeyron equation for L and substituting equation 6.10,

$$L_i = (-a_1 + a_3 T + a_4 T^2 + 2a_5 T^3) R \tag{6.15}$$

The condensate density can then be calculated as,

$$D_{i,j} = 10^6 \frac{\mu_i dX_{i,j} P_j^2}{RT(P_j - P_{j-1})} \quad \frac{g}{cm^3} \tag{6.16}$$

where μ_i is the mass of the species i (in AMU). For multi-component condensates $D_{i,j}$ is summed over i. Another key parameter that needs to be calculated is the moist adiabatic lapse rate. Using the first law of thermodynamics, the adiabatic expansion/compression of one mole of gas must satisfy,

$$c_p dT - \frac{RT}{P} dP + \sum_{i=1}^{N_{cond}} L_i dX_i = 0 \tag{6.17}$$

where c_p is molar specific heat at a constant pressure, and N_{cond} is the number of condensates. The lapse rate ($\frac{dT}{dP}$) is calculated as

$$\frac{dT}{dP} = \frac{RT + \sum_{i=1}^{N_{cond}} L_i X_i}{P(c_p \frac{1}{RT^2} \sum_{i=1}^{N_{cond}} L_i^2 X_i)} \tag{6.18}$$

The mole fraction remaining in a layer, if condensation occurs will be governed by,

$$X_{i,j} = \frac{P_{sat,i,j}}{P_j} + \frac{F_{super,i} P_{sat,i,j}}{P_j} \tag{6.19}$$

where $P_{sat,i,j}$ is the saturation vapor pressure of constituent i at the current pressure step j, P is the atmospheric pressure, and $F_{super,i}$ is the supersaturation fraction of constituent i. Otherwise the mole fraction is computed as,

$$X_{i,j} = X_{i,j-1} \tag{6.20}$$

where $X_{i,j}$ is the mole fraction of species i at pressure level j., and $X_{i,j-1}$ is the mole fraction of constituent i at the previous pressure level step $j-1$. If no condensation has occurred, the lapse rate is either computed as

$$\frac{dT}{dP} = \frac{RT}{c_p P} \tag{6.21}$$

or if the pressure level reaches that of a given pre-set temperature pressure profile (i.e., *Lindal et al.* (1987)), the lapse rate will be set/forced by that given TP profile. The value for c_p is computed as to be consistent with the equation of state using

$$\begin{aligned} c_p(\tau,\delta) &= -R\tau^2 \left(\frac{d^2\alpha^o}{d\tau^2} + \frac{d^2\alpha^r}{d\tau^2} \right) + R \left(\frac{\left(1 + \delta \frac{d\alpha^r}{d\delta} - \delta\tau \frac{dd\alpha^r}{d\tau d\delta}\right)^2}{1 + 2\delta \frac{d\alpha^r}{d\delta} + \delta^2 \frac{d^2\alpha^r}{d\delta^2}} \right) \\ &\quad + 4.459 R X_{NH_3} + 4.013 R X_{H_2S} \end{aligned} \tag{6.22}$$

where the appropriate derivatives of the Helmholtz energy are computed using the mole fractions, and densities associated with H_2, He, CH_4 and H_2O. The original *DeBoer and Steffes* (1996b) model used a curve fit for H_2 based upon the ortho/para fraction at a given temperature, with the values of He, CH_4 and H_2O calculated by taking the specific heat of each component weighted by mole fraction (values of $\frac{c_p}{R}$ of 2.5, 4.5, and 4.00, respectively).

One final condensate which must be considered is that of ammonium hydrosulfide. The ammonium hydrosulfide cloud has a unique treatment, because it has a more complex method of formation. The reaction process for this cloud is given by the reaction:

$$NH_3 + H_2S \rightarrow NH_4SH \tag{6.23}$$

The equilibrium constant for this reaction is given by,

$$\ln(K) = \ln(P_{NH_3} P_{H_2S}) = 34.150 - \frac{10834}{T} \tag{6.24}$$

where P_{NH_3}, and P_{H_2S} are the partial pressures of ammonia and hydrogen sulfide, respectively (*Weidenschilling and Lewis*, 1973). The latent heat of this reaction is assumed to be temperature independent where L_{NH_4SH}=1.6×10^{12} erg/mole (*Briggs and Sackett*, 1989). Note, that the change in ammonia and hydrogen sulfide will be equal, since they react in equal proportions. Therefore, the change in ammonia or hydrogen sulfide may be written as,

$$dX_{NH_3} = dX_{H_2S} = \left(\frac{X_{NH_3} X_{H_2S}}{X_{NH_3} + X_{H_2S}}\right)\left(\frac{10834 dT}{T^2} - \frac{2dP}{P}\right) \tag{6.25}$$

A more useful expression can be derived using the partial pressures of NH_3 and H_2S at the NH_4SH cloud base ($P^o_{NH_3}$,and $P^o_{H_2S}$), and the fact that the partial pressure at any altitude above the cloud base will follow,

$$P^o_{H_2S} - P_{H_2S} = P^o_{H_2S} - P_{NH_3} \tag{6.26}$$

Assuming this reaction is in equilibrium, and no there are no sources or sinks for each constituent, the value for the partial pressure of ammonia and hydrogen sulfide are found by,

$$P_{NH_3} = \frac{1}{2}\left[P^o_{NH_3} - P^o_{H_2S} + \sqrt{(P^o_{NH_3} - P^o_{H_2S})^2 + 4\exp\left(34.150 - \frac{10834}{T}\right)}\right] \quad (6.27)$$

and,

$$P_{H_2S} = \frac{1}{2}\left[P^o_{H_2S} - P^o_{NH_3} + \sqrt{(P^o_{NH_3} - P^o_{H_2S})^2 + 4\exp\left(34.150 - \frac{10834}{T}\right)}\right] \quad (6.28)$$

The equation for moist adiabatic lapse rate is modified to account for the NH_4SH cloud formation, and is represented by,

$$\frac{dT}{dP} = \frac{RT + \sum_{i=1}^{N_{cond}} L_i X_i + 2L_{NH_4SH}\left(\frac{X_{NH_3}X_{H_2S}}{X_{NH_3}+X_{H_2S}}\right)}{P\left[c_p\frac{1}{RT^2}\sum_{i=1}^{N_{cond}} L_i^2 X_i + L_{NH_4SH}\left(\frac{X_{NH_3}X_{H_2S}}{X_{NH_3}+X_{H_2S}}\right)\frac{10834}{T^2}\right]} \quad (6.29)$$

While two different expressions have been presented here for lapse rate (Equations 6.18 and, 6.29) only the more complicated and complete expression given by Equation 6.29 is implemented in the TCM.

A sample Temperature-Pressure profile, cloud density profile, and a profile of mole fraction of different constituents using the original DeBoer TCM are shown in Figures 6.1,6.2 and 6.3, respectively. The impact of the updated TCM using the new equation of state is shown in Figure 6.4 where the Temperature-Pressure profile has changed significantly below the cloud condensation region.

6.3 A Simplified Sedimentation Process

Up to this point the TCM assumes an atmosphere is static, and that all condensible material in excess of saturation will form a condensate. While this is a possibility, this is certainly not the case for water, or ice clouds in Earth's atmosphere. The availability of Cloud Condensation Nuclei (CCN) plays a critical role in this formation process. When CCN are readily available, clouds with large bulk densities may form (i.e.,

cumulus clouds on Earth). However, when CCN aren't readily available, only a small fraction of saturated condensible species actually form a condensate (i.e., cirrus clouds on Earth). The amount, size, or even the composition of CCN in Jovian atmosphere are largely unknown. While this seriously limits one's ability to accurately represent Jovian cloud bulk densities, there are a few ways one can improve cloud bulk density representation in a TCM.

The approach adopted here is taken from *Ackerman and Marley* (2001). The approach begins with a balance between the upward turbulent mixing of condensate and condensible species, and the downward transport of condensate defined as,

$$-K\frac{dX_t}{dz} - f_{sed}w^*X_c = 0 \tag{6.30}$$

where K is the vertical eddy diffusion coefficient, X_t is the mole fraction of both condensate, and condensible species, X_c is the mole fraction of the condensate, w^* is the convective velocity scale, and f_{sed} is an adjustable parameter rigorously defined as the ratio of the mass-weighted droplet sedimentation velocity to $w*$. Since the parameters which define f_{sed} are poorly understood for Jovian atmospheres, we will treat this as an adjustable parameter. The value for eddy diffusion coefficient is calculated using

$$K = \frac{H}{3}\left(\frac{L}{H}\right)^{4/3}\left(\frac{RF}{\mu\rho_a c_p}\right)^{1/3} \quad (\mathrm{cm}^2/\mathrm{sec}) \tag{6.31}$$

where H is the scale height, L is the turbulent mixing length, R is the universal gas constant, F is the convective heat flux, μ is the molecular weight, ρ_a is the atmospheric density, and c_p is the specific heat of the atmosphere at constant pressure. The convective heat flux is calculated using the Stefan-Boltzmann law which is defined as

$$F = \sigma T^4 \tag{6.32}$$

where σ is the Stefan-Boltzmann constant (5.6704×10^{-12} Watts/cm^2/°K^4), and T is taken to be the effective temperature of the planet (124°K for Jupiter). The turbulent

mixing length is calculated using:

$$L = H \max(0.1, \Gamma_{moist}/\Gamma_{dry}) \tag{6.33}$$

where Γ_{moist}, and Γ_{dry} are the moist and dry adiabatic lapse rates, respectively. The convective velocity is found via

$$w^* = \frac{K}{L} \quad \text{(cm/sec)} \tag{6.34}$$

Finally, the solution to equation 6.30 in terms of X_c is found to be

$$X_{c,j} = -\frac{K(X_{g,j} - X_{g,j-1} - X_{c,j-1})}{K + f_{sed} w^* (z_{j-1} - z_j)} \tag{6.35}$$

where $X_{g,j}$ is the mole fraction of the condensible species (gas) for the current level j, $X_{g,j-1}$ is the mole fraction of the condensible species (gas) for the previous level $j-1$, $X_{c,j-1}$ is the mole fraction of the condensate for the previous level, z_{j-1} is the altitude of the previous level, and z_j is the altitude of the current level. For the initial condition (at the base of the cloud) the value of X_c will be defined by equation 6.19. Once 6.35 has been solved, the lapse rate for level j is updated using equation 6.29. This is necessary to maintain a consistent temperature pressure profile, since there will be a significant change in the lapse rate from the change in cloud material.

For reference, three cases with different values of f_{sed} are shown in Figure 6.5. The sedimentation process allows for a mechanism to remove cloud material using f_{sed} as an adjustable parameter. While this is not the most rigorous method to do so in the Jovian atmosphere, it provides at least some physically based mechanism to investigate the role that the water-ammonia solution cloud could plays in the microwave emission from Jupiter as viewed by the Juno MWR.

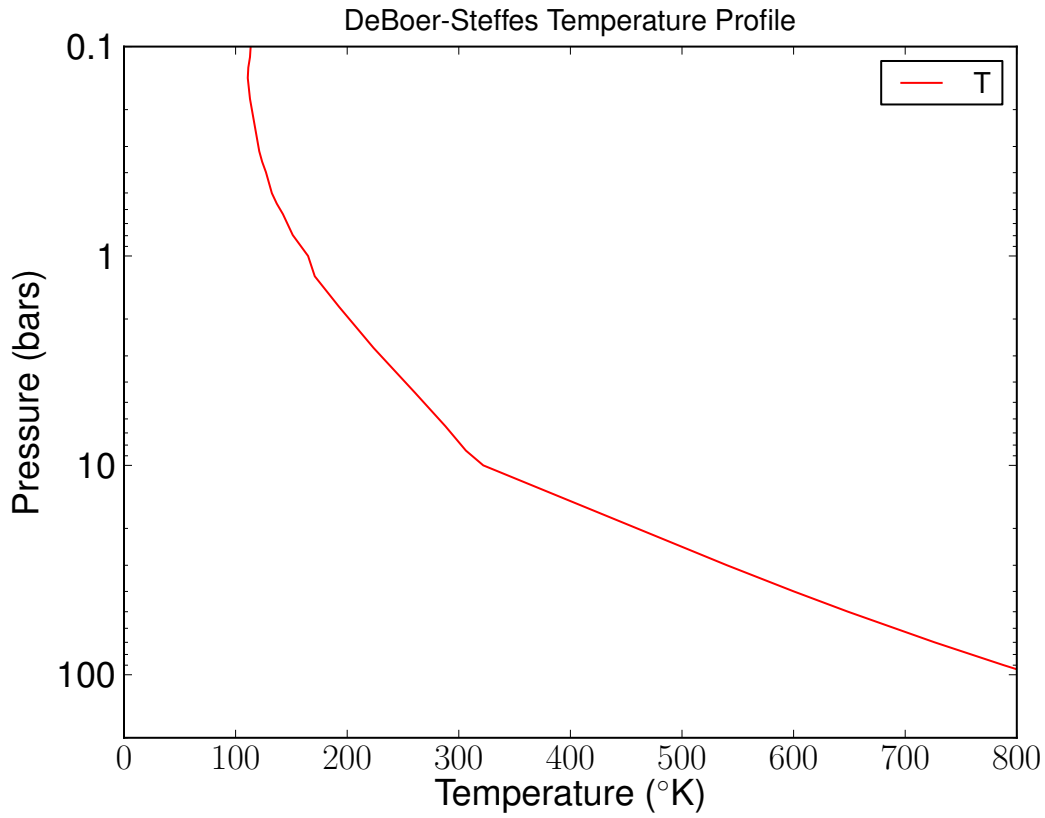

Figure 6.1: DeBoer-Steffes TCM Temperature-Pressure Profile under Mean Jovian conditions.

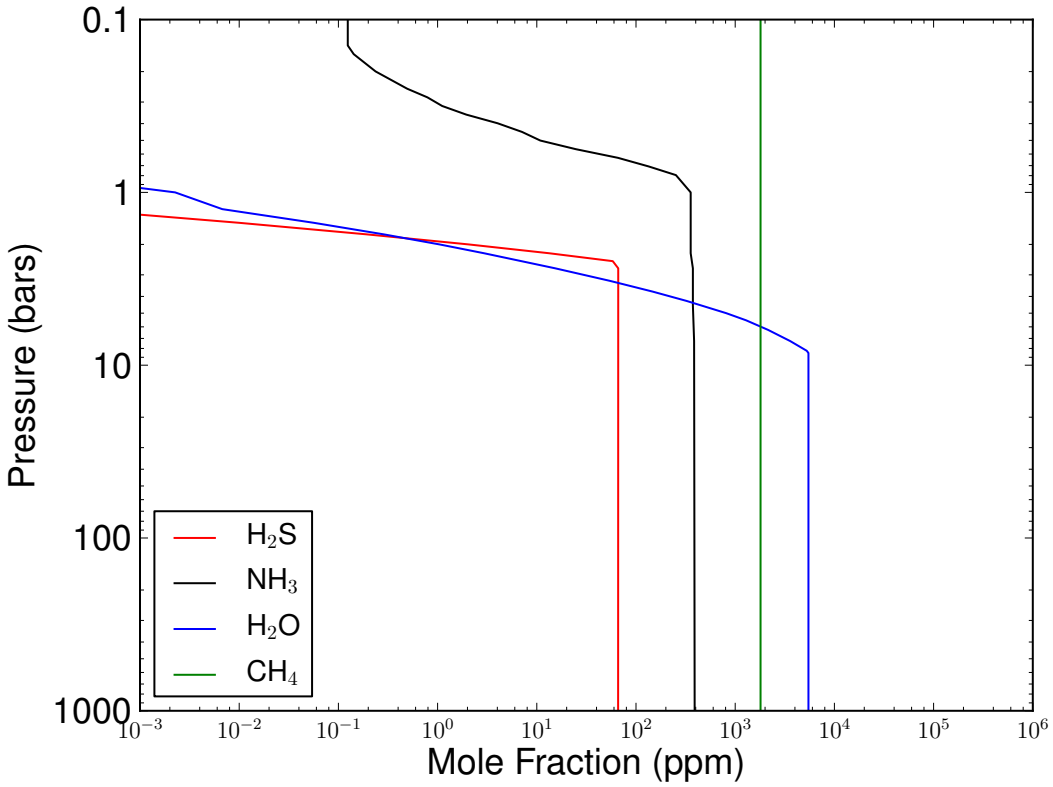

Figure 6.2: DeBoer-Steffes TCM Cloud Density Profile under Mean Jovian conditions.

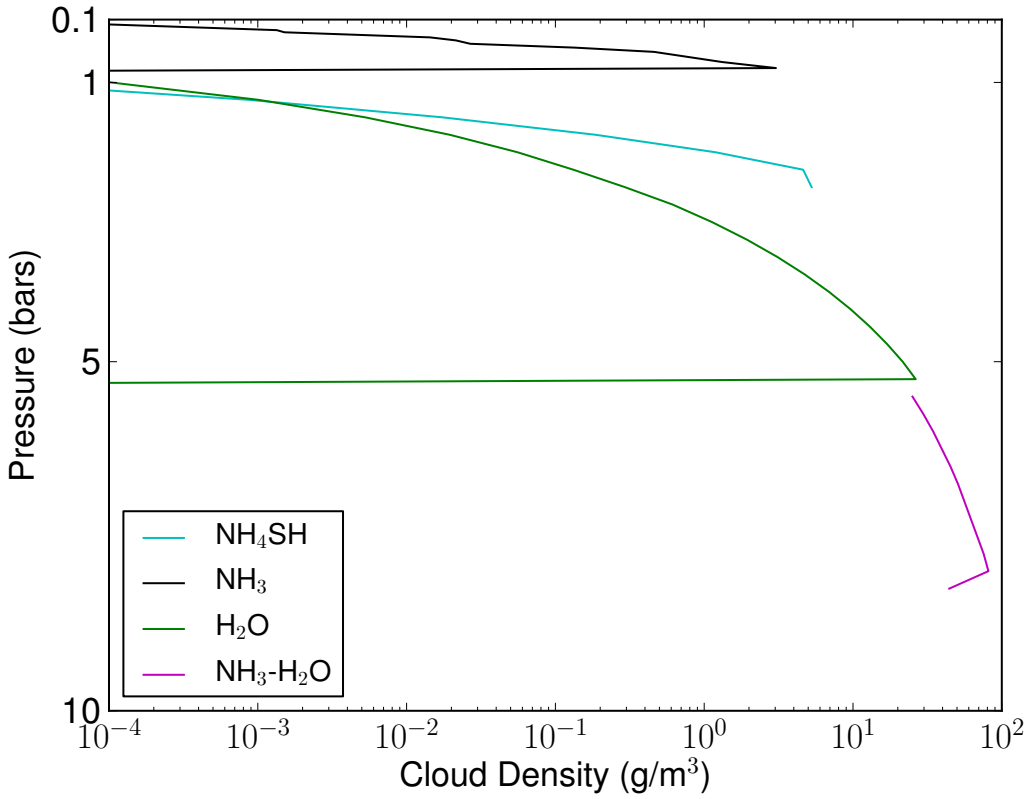

Figure 6.3: DeBoer-Steffes TCM Mole Fraction profile of Jovian gaseous constituents.

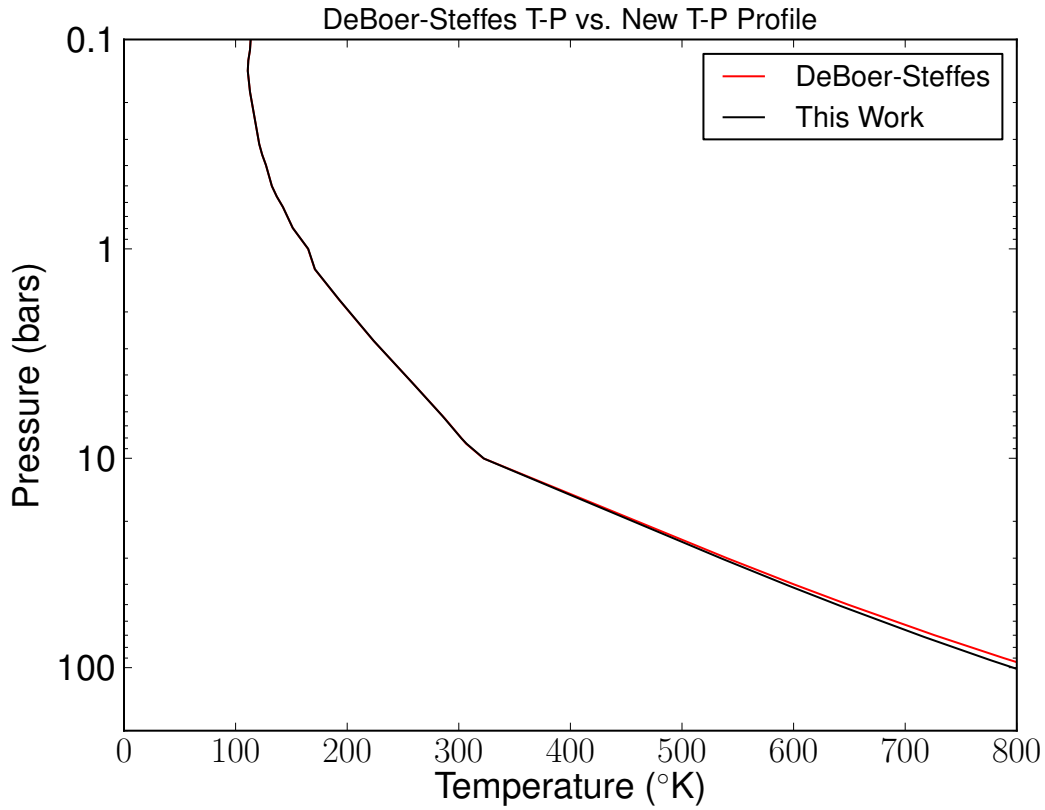

Figure 6.4: DeBoer-Steffes TCM temperature pressure profile vs. new model using the new equation of state.

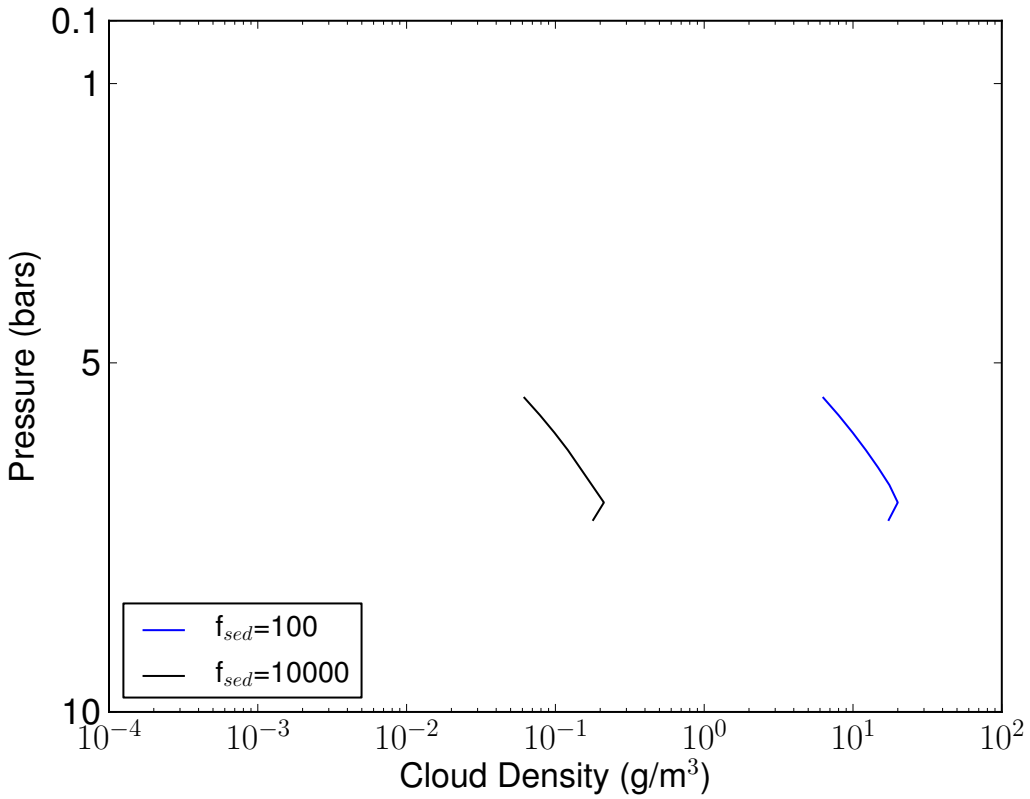

Figure 6.5: Cloud Density profile showing the effect of adjusting f_{sed}.

CHAPTER VII

RADIATIVE TRANSFER IN THE JOVIAN ATMOSPHERE

7.1 Microwave Radiative Transfer in Jovian Atmospheres: For a single ray

Radiative transfer is in essence a method to solve for the distribution of electromagnetic energy in a medium. There are two main assumptions in the development of the radiative transfer equation. First, it is a solution for intensity (or brightness temperature) along an infinitely thin (pencil beam) of radiation emerging from an atmosphere. The other assumption is that the atmosphere is in local thermodynamic equilibrium (LTE). LTE assumes that for a given moment or snapshot in time, the atmosphere is static, and atmospheric dynamics are not considered while solving the radiative transfer equation. The differential form of the radiative transfer equation is simply stated as,

$$dI_\nu = -\alpha I_\nu ds + \alpha J ds \tag{7.1}$$

where dI_ν is the change in intensity at a given frequency ν, over a path length ds, α is the absorption coefficient, or attenuation over a path length ds, and J is the source function (*Liou*, 2002). The value $-\alpha I_\nu$ds is often referred to as the loss term, whereas $\alpha J ds$ is referred to as the source term. In the microwave regime, effects from scattering approach the Rayleigh limit, and may be neglected without introducing significant error. Therefore, the source function J becomes the Planck function,

$$J_\nu = B_\nu(T) = \frac{h\nu^3}{c^2}\frac{1}{\exp(\frac{h\nu}{kT}) - 1} \tag{7.2}$$

where T is the temperature in °K, h is Planck's constant, k is Boltzman's constant. The solution for radiative transfer over a path length s_1 from a planet's surface to

the top of the atmosphere can then be written as,

$$I_\nu^\uparrow(s_1) = I_{\nu,o}^\uparrow \exp(-\tau_\nu(s_1)) + \int_0^{s_1} \alpha B_\nu(T) \exp(-\tau_\nu(s)) ds \tag{7.3}$$

where $I_\nu^\uparrow(s_1)$ is the upwelling intensity at a s_1 from the surface, $I_{\nu,o}$ represents the intensity of radiation at the surface, and $\tau(s)$ is the optical optical depth defined as,

$$\tau_\nu(s) = \int_0^s \alpha_\nu(s') ds' \tag{7.4}$$

In solving the radiative transfer equation for Jovian atmospheres (Gas, and Ice Giants), the first term may be ignored since there is no boundary which one may consider to be a surface. Therefore, the equation simplifies to

$$I_\nu(s_1) = \int_0^{s_1} \alpha B_\nu(T) \exp(-\tau_\nu(s)) ds \tag{7.5}$$

While intensity is a quantity often used in solar and ultra-violet remote sensing, it is far more common to use brightness temperature for longer wavelengths such as infrared and microwave. This quantity is found taking Equation 7.2 and solving for T. Brightness temperature is defined as,

$$T_b = \frac{h\nu}{k \ln(B_\nu(T) + 1)} \tag{7.6}$$

The long wavelength approximation (also know as the Rayleigh-Jean's approximation), can be used to simplify Equation 7.6. This is done by considering a Taylor series expansion about the exponent term in the planck function,

$$B_\nu(T) \approx \frac{h\nu^3}{c^2} \frac{1}{\left(1 + \frac{h\nu}{kT} + \frac{\frac{h\nu}{kT}}{2} ...\right) - 1} \tag{7.7}$$

If the term in the exponent is $\frac{h\nu}{kT} << 1$, the entire exponent term will simplify to $\frac{h\nu}{kT}$, and thus the Planck function simplifies to

$$B_\nu(T) = \frac{2kT\nu^2}{c^2}. \tag{7.8}$$

This approximation of the Planck function holds to within 1% given that $\frac{\nu}{T} < 3.9 \times 10^8\,\mathrm{Hz\,K^{-1}}$ (*Ulaby et al.*, 1981). Inserting Equation 7.8 into Equation 7.6 gives a much simpler expression for brightness temperature in the microwave regime:

$$T_b = \frac{Tc^2}{2\nu^2 k} \tag{7.9}$$

Then, substituting Equations 7.8, and 7.9 into 7.5, and solving for brightness temperature, the equation for radiative transfer becomes,

$$T_b(\nu) = \int_0^{s_1} \alpha T(s) \exp(-\tau_\nu(s)) ds \tag{7.10}$$

The discrete form of 7.10 can be expressed as,

$$T_b = \sum_{i=1}^{N} T_i (1 - \exp(-\tau_{\nu,i})) \exp(-\tau_{\nu,i}) \tag{7.11}$$

where $\tau_{\nu,i}$ is the optical depth in layer i, and T_i is the physical temperature in layer i. It should be noted that the optical depth is the total absorption coefficient multiplied by the path length through each layer. The path length through each layer is calculated via the ray tracing method described in the next section.

A useful quantity which is derived from 7.11 is the weighting function,

$$W_i = (1 - \exp(-\tau_i)) \exp(-\tau_i) \tag{7.12}$$

If the weighting function is compared against altitude, or pressure level, this indicates which level contributes most to the brightness temperature at a particular frequency.

7.2 Simulating Brightness Temperature as Observed by a Microwave Radiometer: Ray Tracing Approach

While the radiative transfer equation can be used to solve for brightness temperature as observed by an orbiting spacecraft, the formalism developed in the previous section would only hold true for a radiometer with an infinitely narrow beamwidth. The formalism would also neglect the effect of refraction (ray bending) between atmospheric layers. Here we present the ray tracing approach used in LRTM (*Hoffman*, 2001).

7.2.1 Ray Ellipsoid Intersections

The path lengths (values for ds) are calculated by breaking up the planet described by an ellipsoid into several shells. The method by which these paths are calculated is by using a ray-ellipsoid intersection test. This is done by first specifying two vectors the spacecraft location (R_{origin}), and the Antenna/Spacecraft direction ($R_{direction}$):

$$R_{origin} \equiv R_o \equiv \begin{bmatrix} X_o & Y_o & Z_o \end{bmatrix} \tag{7.13}$$

$$R_{direction} \equiv R_d \equiv \begin{bmatrix} X_d & Y_d & Z_d \end{bmatrix} \tag{7.14}$$

where

$$X_d^2 + Y_d^2 + Z_d^2 = 1 \tag{7.15}$$

which defines a ray as a set of points described by the equation for a line,

$$R(t) = R + R_d \times t \tag{7.16}$$

where t>0. The Ellipsoid is defined by,

$$S_{center} \equiv S_c \equiv \begin{bmatrix} X_c & Y_c & Z_c \end{bmatrix} \tag{7.17}$$

$$S_{surface} \equiv \begin{bmatrix} X_s & Y_s & Z_s \end{bmatrix} \tag{7.18}$$

where

$$\left(\frac{X_s}{a}\right)^2 + \left(\frac{Y_s}{b}\right)^2 + \left(\frac{Z_s}{c}\right)^2 = 1 \tag{7.19}$$

To find the intersection between ray and ellipsoid the ray is expressed as,

$$\begin{aligned} X &= X_o + X_d t \\ Y &= Y_o + Y_d t \\ Z &= Z_o + Z_d t \end{aligned} \tag{7.20}$$

and is substituted into the surface vector [X_s Y_s Z_s] resulting in,

$$\left(\frac{X_o + X_d t}{a}\right)^2 + \left(\frac{Y_o + Y_d t}{b}\right)^2 + \left(\frac{Z_o + Z_d t}{c}\right)^2 = 1 \tag{7.21}$$

This can be simplified to a quadratic expression of the form:

$$At^2 + Bt + C = 0 \tag{7.22}$$

where,

$$A = \Lambda X_d^2 + \Upsilon Y_d^2 + K Z_d^2$$

$$B = 2(\Lambda X_o X_d + \Upsilon Y_o Y_d + K Z_o Z_d) \tag{7.23}$$

$$C = \Lambda X_o^2 + \Upsilon Y_o^2 + K Z_o^2 - 1$$

where,

$$\Lambda = \tfrac{1}{a^2}$$

$$\Upsilon = \tfrac{1}{b^2} \tag{7.24}$$

$$K = \tfrac{1}{c^2}\,.$$

The solutions to this equation are the quadratic solutions,

$$t_{0,1} = \tfrac{-B \mp \sqrt{B^2 - 4AC}}{2A} \tag{7.25}$$

where values for t_0, t_1 are solutions for the distance from the ray origin to the intersection point with the ellipsoid. If the discriminant of these equations is negative, the ray misses the ellipsoid. The smallest positive value of t is the correct solution. Once t is found, the vector location of the intersection is,

$$r_{int} \equiv r_i = \begin{bmatrix} X_o + X_d t & Y_o + Y_d t & Z_o + Z_d t \end{bmatrix} \tag{7.26}$$

To find the local surface normal at the location of the intersection, the gradient of the ellipsoid surface is calculated with the surface denoted as G,

$$r_{normal} \equiv n = \frac{\nabla G}{|\nabla G|} \tag{7.27}$$

where,

$$\nabla G = \frac{2x}{a^2}i + \frac{2y}{b^2}j + \frac{2z}{c^2}k \tag{7.28}$$

and,

$$|\nabla G| = 2\sqrt{\frac{x^2}{a^4} + \frac{y^2}{b^4} + \frac{z^2}{c^4}} \tag{7.29}$$

The above equations give the key values need to solve radiative transfer along the ray path: t (or ds) through a layer, the intersection vector r_{int}, and the surface normal, r_{normal}. The values r_{int} and r_{normal} are used in combination with Snell's law to calculate the direction of the transmitted ray, or the ray emerging from the boundary.

The angle between the incident ray (I) and surface normal (N) is given by,

$$\theta_1 = \cos^{-1}(-I \bullet N). \tag{7.30}$$

The relative index of refraction is,

$$\eta = \frac{\sin(\theta_2)}{\sin(\theta_1)} = \frac{\eta_1}{\eta_2}. \tag{7.31}$$

The angle of the transmitted ray (θ_2) can be computed from,

$$\theta_2 = \cos^{-1}(\sqrt{1 - \sin^2(\theta)}) = \cos^{-1}(\sqrt{1 - \eta^2 \sin^2(\theta_1)}) = \cos^{-1}(\sqrt{1 - \eta^2(1 - \cos^2(\theta_1))}) \tag{7.32}$$

The vector direction of the transmitted ray is computed as,

$$T = \eta I + (\eta \cos(\theta_1) - \cos(\theta_2))\, N. \tag{7.33}$$

The mathematics describing the ray path are repeated for each ray that is transmitted through the Jovian atmosphere.

7.2.2 Antenna Pattern: Beam Sampling

An accurate simulation of brightness temperature as viewed by a radiometer requires sampling the antenna beam space by using several rays, or infinitely small beams of

radiation. The width of the overall beam is governed by the 3 dB beamwidth of the antenna, or the Beam Width Half Maximum (BWHM). The strategy used to sample the beam is to take one boresight ray, and several cocentric rings of rays about the boresight ray. The sampled angle ($\Delta\phi$) is governed by the number of rings, and the BWHM, where

$$\Delta\phi = \frac{BWHM}{N_{\phi\, rings}} \tag{7.34}$$

The number of rays within each $\Delta\phi$ ring along θ is governed by

$$N_{\theta,k} = N_{1st\ ring} \times (2k-1) \tag{7.35}$$

where $N_{1st\ ring}$ is the number of rays within the first ring, and k is the index of the $\Delta\phi$ ring. The user has the ability to change the number of samples by changing $N_{1st\ ring}$, and $N_{\phi\, rings}$. The spacing in θ along each ring in ϕ is governed by,

$$\theta_{last} = 2\pi - \frac{2\pi}{N_{\theta,k}} \tag{7.36}$$

where for $\theta > 0$,

$$\theta_{i,k} = \theta_{i-1,k} + \frac{\theta_{last}}{N_{\theta,k}} \tag{7.37}$$

Once the ϕ and θ of each ray has been computed, it is converted from spherical, to cartesian coordinates to define ray samples in the form of several unit vectors. These unit vectors are then rotated along the $R_{direction}$ vector using,

$$Beamsamples_{rotated} = R_x \times R_y \times R_z \times R_y^{-1} \times R_x^{-1} Beamsamples_{original} \tag{7.38}$$

where,

$$R_x = \begin{bmatrix} 1 & 0 & 0 \\ 0 & \cos(\alpha) & -\sin(\alpha) \\ 0 & \sin(\alpha) & \cos(\alpha) \end{bmatrix}$$

$$R_y = \begin{bmatrix} \cos(\alpha) & 0 & \sin(\alpha) \\ 0 & 1 & 0 \\ -\sin(\alpha) & 0 & \cos(\alpha) \end{bmatrix} \tag{7.39}$$

$$R_z = \begin{bmatrix} \cos(\alpha) & -\sin(\alpha) & 0 \\ \sin(\alpha) & \cos(\alpha) & 0 \\ 0 & 0 & 1 \end{bmatrix}$$

where α is the angle between the respective axis, and the boresight vector ($R_{direction}$). The rays which hit the ellipsoid are computed following the procedure described previously giving values for $T_{boresight}$ and for each sampled ray temperature $T_{i,k}$.

Next, the weights of each beam sample are computed by,

$$b_{i,k}(\Delta\phi) = \exp\left(-2.76\left(\frac{\Delta\phi_{i,k}}{BWHM}\right)^2\right). \tag{7.40}$$

Next, the sum of all beam pattern weights must be computed to ensure proper scaling where,

$$b_{sum} = \sum_{k=1}^{N_{\phi\, rings}} N_{1st\, ring}(2k-1)b_k \tag{7.41}$$

The Brightness temperature of the beam is then computed as,

$$T_{beam} = \frac{T_{boresight} + \sum_{i=1}^{N_\theta}\sum_{k=1}^{N_{\phi\, rings}} b_{i,k}T_{i,k}}{1 + b_{sum}} \tag{7.42}$$

where $T_{boresight}$ is the brightness temperature using a beam sample at boresight, and $T_{i,k}$ are the brightness temperatures calculated along each sample in ϕ and θ.

The beam weighting procedure stated up until this point is for an antenna that is assumed to have a gaussian pattern, and only includes contributions from the main lobe of the antenna. If a measured antenna pattern is available for a given sensor (i.e., the Cassini radiometer), the procedure is the same with a few exceptions. First, the weights of each beam sample ($b_{i,k}$) are given by the normalized antenna pattern (maximum scaled to 1, and where units of gain are a linear quantity). The values of $\phi_{i,k}$ and $\theta_{i,k}$ are constrained by the measurement sampling space of the antenna pattern measurement. Finally the value of b_{sum} is computed using,

$$b_{sum} = \sum_{m=1}^{N_{samples}} b_m \tag{7.43}$$

where m is the antenna pattern sample, and $N_{samples}$ is the total number of sample points. The values in b_m strictly speaking are those given in $b_{i,k}$ only re-dimensioned such that b is a vector rather than a matrix of values. This reduces time to calculate b_{sum} in Matlab.

The calculation of the antenna temperature T_{beam} in equation 7.42 is the discrete form of the more familiar definition of antenna temperature defined as:

$$T_A = \frac{\int\int_{4\pi} T_{AP}(\theta,\phi) F_n(\theta) d\Omega}{\int\int_{4\pi} F_n(\theta,\phi) d\Omega} \tag{7.44}$$

where T_{AP} is the apparent temperature distribution, and F_n is the antenna weighting function (gain/antenna pattern) (*Ulaby et al.*, 1981).

CHAPTER VIII

SIMULATIONS OF JUPITER'S EMISSION AS VIEWED FROM THE JUNO MWR

The Microwave Radiometer (MWR) instrument, part of the NASA Juno mission will allow for unprecedented microwave observations of the thermal emission from Jupiter. The MWR is composed of 6 channels including: a 600 MHz (50 cm), 1.25 GHz (24 cm), 2.6 GHz (11.7 cm), 5.2 GHz (5.7 cm), 10 GHz (3.0 cm), and a 22 GHz channel (1.3 cm). The spacecraft will orbit with a highly elliptical orbit with a perijove of 4500 km above the 1 bar level near the the equator. This allows for the radiometer to view the thermal emission from Jupiter without contamination from the strong synchrotron radiation belts which contaminate Earth based observations in the microwave. While this is an exciting step forward in planetary radio astronomy, the ambitious goal of the Juno mission to determine a planet-wide distribution of water vapor would be impossible without the measurements conducted in this work. As shown in Chapter 5, neither absorption model originally proposed for use in Jovian atmospheres (i.e., *DeBoer*, 1995; *Goodman*, 1969) fit the laboratory measurements conducted in this work. Given that a new Ammonia opacity model based upon extensive laboratory measurements has recently been published *Hanley et al.* (2009), the question which begs for an answer is: What will the MWR observe? The answer to this question is far beyond the scope of this work; however, some initial estimates of brightness temperature, and limb darkening can be made based upon the radiative transfer model developed in this work, combined with the new H_2O opacity model.

To make any estimate as to what the MWR can observe, one needs to assume a possible range of composition in the deep Jovian atmosphere. A traditional method

often employed by planetary scientists involves normalizing key species relative to a reference "proto-solar" abundance. That is, one normalizes constituent abundances containing heavy elements such as Nitrogen bound in NH_3 molecules and Oxygen bound in water molecules, and normalizing each by the amount of nitrogen, and oxygen hypothesized to exist early in the formation of our solar system. While knowing the amount of NH_3, and H_2O in the deep Jovian atmosphere can serve as a method to better understand early solar system formation, this practice can only be described as a "bad habit". The goal of this work has been to provide the Juno mission with the most precise estimates of the microwave absorption from water vapor, thus to normalize observations by an imprecise and subjective number has little merit. The uncertainty regarding solar composition is readily observed in looking at "standard" solar abundances over the past few decades (i.e., *Anders and Grevesse*, 1989; *Grevesse and Sauval*, 1998; *Asplund et al.*, 2006). In this Chapter a brief discussion of how dramatic the projections of solar composition has changed is presented. As an alternative to describing increases or decreases in NH_3 and H_2O in terms of solar abundance, a thorough literature search of measurements and constituent abundances is presented and referred to as *depleted*, *mean* and *enhanced*. Using the results of the literature survey, we derive a set of cases of deep constituent abundances, and compute using the radiative transfer model, what the Juno MWR might observe at perijove when orbiting Jupiter.

8.1 Solar Abundance: Just Say NO*!*

As mentioned, the values for "reference" solar abundances have varied greatly over the years. Of most concern is the needless confusion, and error propagation among studies. Take for example, *DeBoer* (1995). The values for solar composition are computed from *Anders and Grevesse* (1989) by taking the values for mass abundance in Table 1 of *Anders and Grevesse* (1989). These values instead should be corrected

for proto-solar composition (the composition of the solar system at its "birth") using photospheric abundance (in Table 2 of *Anders and Grevesse* (1989)). In *Grevesse et al.* (2005) the method given is to add 0.057 dex to the He abundance while adding 0.05 dex to all other elemental abundance values. To obtain each value of proto-solar composition presented in Table 8.1, values are first converted from units of dex to number concentration relative to H:

$$N_i = 10^{(N_{i,dex}-12)} \tag{8.1}$$

where $N_{i,dex}$ is the photospheric abundance for each element i in units of dex, and N_i is the value expressed in units of concentration. Next, the total concentration of all abundances relative to H are found using:

$$N_{total} = \sum_{i=1}^{n_{elements}} N_i \tag{8.2}$$

The relative abundances of each molecule of interest is found by first calculating the solar abundance of H_2:

$$X_{H_2} = \frac{1}{1 + 2N_{total}} \tag{8.3}$$

where X_{H_2} is the solar mole fraction of H_2. Next each molecular species of interest is found by assuming that all the heavy elements are associated with a particular molecular species of interest (i.e., all nitrogen is locked away in NH_3). The mole fraction of each species is found by:

$$X_j = 2N_j X_{H_2} \tag{8.4}$$

where X_j is the mole fraction of each molecular species j, and N_j is the heavy element associated with X_j. Many authors prefer to consider values of q, or concentration relative to H_2. This can be simply found by dividing all values of X_j by X_{H_2}. For reference, values obtained using the outlined procedure are given in Tables 8.1 and 8.2.

Table 8.1: Solar Composition as stated in *DeBoer* (1995) and calculated using proto-solar composition (*Anders and Grevesse*, 1989)

	X_i *DeBoer* (1995)	X_i Proto-solar	q_i *DeBoer* (1995)	q_i Proto-solar
H_2	0.8346	0.8321	1	1
He	0.1623	0.1653	0.19446	0.19862
H_2O	1.424×10^{-3}	1.416×10^{-3}	1.7062×10^{-3}	1.7023×10^{-3}
CH_4	6.043×10^{-4}	6.0421×10^{-4}	7.2046×10^{-4}	7.2616×10^{-4}
NH_3	1.873×10^{-4}	1.8671×10^{-4}	2.2442×10^{-4}	2.2440×10^{-4}
H_2S	3.081×10^{-5}	2.6989×10^{-5}	3.691×10^{-5}	3.2436×10^{-5}
PH_3	6.222×10^{-7}	6.1828×10^{-7}	7.4551×10^{-7}	7.4307×10^{-7}

Table 8.2: Solar Abundance Values using *Grevesse et al.* (2005) compared to those above from *Anders and Grevesse* (1989)

	X_i	q_i	% Change from *Anders and Grevesse* (1989)
H_2	0.83596	1	0
He	0.1623	0.1941	2.2757
H_2O	0.8574×10^{-3}	1.0257×10^{-3}	39.746
CH_4	4.6048×10^{-4}	5.5084×10^{-4}	24.143
NH_3	1.1304×10^{-4}	1.3522×10^{-4}	39.742
H_2S	2.5895×10^{-5}	3.0976×10^{-5}	4.5012
PH_3	4.2975×10^{-7}	5.1408×10^{-7}	30.817

8.2 Jupiter's composition: A survey of recent observations

While some measurements have given estimates for the values of constituent abundances in the deep Jovian atmosphere, an orbiting multi-wavelength microwave radiometer could provide unique insight. In place of assuming an arbitrary 1X, 3X, or 6X solar abundance, we have conducted a recent survey of measurements of Jupiter's chemical composition, and used these to guide our modeling study.

8.2.1 He Abundance

Recent measurements by the Galileo Entry probe have provided the most accurate measurements to date of the Helium abundance in Jupiter's atmosphere. While the Entry probe trajectory placed it in a 5 μm "hot spot", the value given for Helium abundance can be considered representative of the planet given that Helium is well mixed throughout most of Jupiter's atmosphere. The Helium Abundance Detector (HAD) on Galileo's entry probe measured a mole fraction of 0.1359 (*von Zahn et al.*, 1998) (He/H_2=0.157), while the Galileo Probe Mass Spectrometer (GPMS) gave nearly identical results with a reading of mole fraction 0.136 (He/H_2=0.157) (*Niemann et al.*, 1998). Given this reliable information we will adopt this value for all cases simulating Jupiter.

8.2.2 H_2S Abundance

Prior to the Galileo entry probe the amount of H_2S had never been measured *in-situ*. The only remote measurement was conducted during the impact of Shoemaker-Levy 9 where H_2S was found to be on the order of 5×10^{-8} (*Yelle and McGrath*, 1996). This value is not quoted in Table 8.3, due to some controversy as to whether or not H_2S can be uniquely detected in the presence of aerosols (*Atreya et al.*, 1995). It is for this reason that we adopt the H_2S/H_2 value of 7.7×10^{-5} (*Niemann et al.*, 1998).

8.2.3 NH_3 Abundance

A critical species to study from a microwave perspective is NH_3, due to its strong absorption features and its abundance on Jupiter. Studies have found deep abundances ranging from 2×10^{-4} to 2×10^{-3}. However, the upper limit of 2×10^{-3} was later modified by *Atreya et al.* (2003) after calibration of the Galileo Probe Mass Spectrometer to 7.1×10^{-4}. Given the importance of this species at microwave wavelengths and the variability shown in Table 8.3 we use an NH_3/H_2 abundance range of 2 (*Kunde et al.*, 1982) to 7.1 (*Atreya et al.*, 2003) $\times 10^{-4}$.

8.2.4 H_2O Abundance

In this study we have generally accepted the constituent abundance values measured by the Galileo Probe Mass Spectrometer (GPMS). While we do consider the measurements by the GPMS to be accurate, the GPMS did enter a 5 μm "hot spot", and therefore we do not consider the water vapor abundance measured by GPMS to be representative of Jupiter's entire atmosphere. We therefore only consider the value measured by GPMS for our "hot spot" model. Unfortunately in looking away from the GPMS for sources of information, our options are limited since all IR measurements of water in the deep atmosphere of Jupiter are made through observations of 5 μm hot spots, and give values on the same order as the GPMS. While (*de Pater and Massie*, 1985) cite an abundance value for H_2O vapor, they do not actually include water vapor in their retrieval technique and only include it as a method to produce clouds in their thermo-chemical model. In out model we reluctantly derive our range of water vapor relative to solar abundance calculations. (While it may seem attractive to use the latest estimates for solar abundance to be consistent with others in the astronomy field, this adoption and referral to H_2O abundance values in these terms has and will continue to cause confusion). Therefore we derive the "3 $\times$ Solar value" for H_2O/H_2 of 5.1069×10^{-3} based upon *Anders and Grevesse* (1989) . We then

consider a range of H_2O/H_2 of 2.5535×10^{-3}–1.0214×10^{-2}. It should be emphasized that this is the most consistent way to describe a "3 × Solar" abundance that would be consistent with the GPMS measurement of other heavy elements which were all approximately "3 × Solar" using *Anders and Grevesse* (1989) as a reference for Solar composition.

8.2.5 CH_4 Abundance

Methane is a species which has been well measured by IR measurements along with the *in-situ* measurements from the Galileo entry prope. While values for CH_4 do vary slightly from study to study, a CH_4/H_2 value of 2.1×10^{-3} is generally accepted, and is adopted for all our modeling cases (*Niemann et al.*, 1998).

8.2.6 PH_3 Abundance

Phosphine has also been measured both in the IR along with measurements made by the Galileo entry probe. Most studies adopt the original value retrieved from the Voyager's IRIS (*Kunde et al.*, 1982) of 6×10^{-7}. The Galileo entry probe measured an amount between 0 and 2×10^{-7} at pressures below 12 bars, above 12 bars this estimate is raised to between 0 and 6×10^{-6}. While there seems to be the potential for a large amount of Phosphine on Jupiter on the order of 10^{-6}, this only reflects the upper limit given by the mass spectrometer, and shouldn't be considered an actual measurement. For this reason we will adopt the widely accepted PH_3/H_2 value of 6×10^{-7}.

8.3 Simulated Juno MWR observations

By evaluating recent studies on the composition of Jupiter, we have determined a set of atmospheric conditions for sensitivity analysis. Each atmospheric condition is summarized in Tables 8.4, and 8.5. The two constituent abundances we use for sensitivity analysis are NH_3 and H_2O. We use a mean condition which corresponds to

Table 8.3: Recent studies on the composition of Jupiter

Reference	He	H_2S	NH_3	H_2O	CH_4	PH_3	Additional References
Atreya et al. (2003)	0.157	7.7×10^{-5}	7.1×10^{-4}	6.0×10^{-4}	2.1×10^{-3}	6×10^{-7}	He (*Niemann et al.*, 1998; *von Zahn et al.*, 1998),H_2S (*Niemann et al.*, 1998), NH_3 (*Mahaffy et al.*, 1999)
de Pater et al. (2001)	N/A	2.5 × Solar	3.6 × Solar	2.5 × Solar	N/A	N/A	For ammonia values to match observations, must reduce ammonia >4 bars to 0.3 × Solar Solar N=1.97×10^{-4}
Lellouch et al. (2001)	N/A	N/A	N/A	N/A	2.1×10^{-3}	N/A	CH_4 (*Niemann et al.*, 1998)
Fouchet et al. (2000)	N/A	N/A	2.8×10^{-4}	8 % of sat	2.1×10^{-4}	7×10^{-7}	CH_4 (*Niemann et al.*, 1998),PH_3 (*Kunde et al.*, 1982)
Atreya et al. (1999)	0.157	7.7×10^{-5}	8.1×10^{-4}	6×10^{-4}	2.1×10^{-3}	6×10^{-7}	He (*Niemann et al.*, 1998; *von Zahn et al.*, 1998), H_2S (*Niemann et al.*, 1998), NH_3 (*Folkner et al.*, 1998), H_2O (*Niemann et al.*, 1998), PH_3 (*Kunde et al.*, 1982)
Niemann et al. (1998)	0.157	7.7×10^{-5}	2.3×10^{-3}	6×10^{-4}	2.1×10^{-3}	$\leq 6 \times 10^{-6}$	He values nearly identical to *von Zahn et al.* (1998), H_2S values at >16 bars, NH_3 15 bars considered an upper limit estimate, H_2O 19 bars, PH_3 > 16 bars
Sromovsky et al. (1998)	N/A	N/A	2.5×10^{-4}	$\sim 1.5 \times 10^{-4}$	1.81×10^{-3}	6.0×10^{-7}	use mixing ratio (the real one!), Everything except NH_3 and H_2O is fixed, keep deep NH_3 of *de Pater and Massie* (1985), but decrease amount up top to match model/measurements, CH4 (*Niemann et al.*, 1996), PH_3 (*Carlson et al.*, 1993), NH_3 and H_2O (*de Pater and Massie*, 1985)
von Zahn et al. (1998)	0.157	N/A	N/A	N/A	N/A	N/A	He values nearly identical to *Niemann et al.* (1998)
Folkner et al. (1998)	N/A	N/A	4×10^{-4}	N/A	N/A	N/A	This abundance is for below 7 bars or "4 times the solar nitrogen abundance"
Carlson et al. (1993)	<10 × Solar		$4.4–4.6 \times 10^{-4}$	$\sim 2 \times 10^{-3}$	2.2×10^{-3}	6×10^{-7}	values based upon analysis of IRIS data, they are very vague on how much H_2S they use. They discuss that 10 × Solar is too much, but neglect to say how much. Best treatment of clouds modeling out of all papers
Joiner (1991)	∼ 10 %	2.9×10^{-3}–2.2×10^{-4}	2.5×10^{-4}	1.5×10^{-3}	N/A	6×10^{-7}	
de Pater and Massie (1985)	11 %	solar	2.5×10^{-4}	1×10^{-6}	solar	solar	They only really consider absorption from clouds or ammonia on Jupiter, all other species are basically ignored
Kunde et al. (1982)	N/A	N/A	$\sim 2 \times 10^{-4}$	1×10^{-6}	1.75×10^{-3}	6×10^{-7}	From Voyager IRIS data CH_4 value is assumed.

a mean value found for each of the two species. For each species we use a depleted, and an enhanced condition which correspond to the upper and lower limits we consider reasonable for each species based upon recent measurements. In addition to varying constituent abundance each simulation considers the effect of cloud absorption by including/excluding cloud absorption when calculating the microwave emission from the planet.

Table 8.4: Conditions modeled with LRTM in conjunction with DeBoer and Steffes Thermo-Chemical Model (q_i, where $q_i = X_i/X_{H_2}$)

Case	He	H_2S	NH_3	H_2O	CH_4	PH_3
Mean	0.157	7.7×10^{-5}	4.55×10^{-4}	6.3838×10^{-3}	2.1×10^{-3}	6×10^{-7}
Depleted NH_3	0.157	7.7×10^{-5}	2.0×10^{-4}	6.3838×10^{-3}	2.1×10^{-3}	6×10^{-7}
Enhanced NH_3	0.157	7.7×10^{-5}	7.1×10^{-4}	6.3838×10^{-3}	2.1×10^{-3}	6×10^{-7}
Depleted H_2O	0.157	7.7×10^{-5}	4.55×10^{-4}	2.5535×10^{-3}	2.1×10^{-3}	6×10^{-7}
Enhanced H_2O	0.157	7.7×10^{-5}	4.55×10^{-4}	1.0214×10^{-2}	2.1×10^{-3}	6×10^{-7}

Table 8.5: Conditions modeled with LRTM in conjunction with DeBoer and Steffes Thermo-Chemical Model expressed in mole fraction

Case	H_2	He	H_2S (ppm)	NH_3 (ppm)	H_2O (ppm)	CH_4 (ppm)	PH_3 (ppm)
Mean	0.8576	0.1346	66.0368	390.2175	5474.8801	1801.0038	0.5146
Depleted NH_3	0.8578	0.1347	66.0513	171.5617	5476.0777	1801.3978	0.5147
Enhanced NH_3	0.8574	0.1346	66.0224	608.7777	5473.6831	1800.6100	0.5145
Depleted H_2O	0.8604	0.1351	66.2544	391.5036	2197.1524	1806.9395	0.5163
Enhanced H_2O	0.8548	0.1342	65.8206	388.9399	8731.0593	1795.1072	0.5129

The wavelength range we consider valid for study at this time ranges from 1.3 cm (22 GHz) up to 30 cm. The reason for this is readily observed in Figure 8.1. The weighting function of the 30 cm wavelength does not terminate until nearly the 1000 bar level. One could easily increase the depth of the model to support wavelengths up to 50 cm (the longest wavelength on the Juno MWR), however, the additional opacity necessary to terminate weighting functions at these frequencies requires including pressures up to thousands of bars. None of the microwave opacity formalisms can be considered valid at these elevated temperatures and pressures. The laboratory

measurements in this work only extend over a few hundred degrees Kelvin and up to 100 bars (see Figure 5.1). There is no evidence that these measurements, and the resulting opacity models will remain valid over *thousands* of degrees kelvin, and *thousands* of bars.

The viewing geometry of the simulation assumes the spacecraft is 4500 km above to 1 bar pressure level, with a gaussian antenna pattern of beamwidth 10°. Two observations are made with the spacecraft at the equator: one at nadir, and the other 60° emission angle (which corresponds to an angle of 54 ° off nadir for the spacecraft). This allows for the computation of limb darkening defined as:

$$R = 100 \times \frac{T_{b,nadir} - T_{b,limb}}{T_{b,nadir}} \ (\%) \tag{8.5}$$

where $T_{b,nadir}$ is the brightness temperature observed at nadir, and $T_{b,limb}$ is the brightness temperature observed at the limb (60° emission angle).

The effect of changing the deep water vapor abundance upon simulated brightness temperature and limb darkening are shown in Figures 8.2 and 8.3, respectively. In most cases limb darkening decreases with an increase in H_2O abundance. A decrease in brightness temperature can be observed for an increase in deep H_2O abundance. The one exception is the depleted H_2O case including cloud absorption. The reason for this becomes clear in Figure 8.4, where a large cloud forms at an altitude much higher than either the enhanced, or mean cases. In Figure 8.5 the corresponding decrease in H_2O mole fraction is shown with the thin blue line corresponding to the depleted H_2O case.

The effect of changing the deep ammonia abundance upon simulated brightness temperature and limb darkening are shown in Figures 8.6 and 8.7. Again, generally speaking, limb darkening decreases with an increase in abundance, and the brightness temperature decreases. The spectral variation in limb darkening at shorter wavelengths is very different from that observed from varying H_2O abundance. The reason

for this is evident when comparing the weighting functions in Figure 8.1, and the vertical distribution of ammonia, and water vapor abundance in Figure 8.5. In the thermo-chemical model all water has condensed out above the 1 bar level, whereas the NH_3 abundance never quite goes to zero, but reaches a minimum at the 0.1 bar level. It is important to note that the short wavelength spectrum is very much constrained by the thermochemical model, which does not include potential dynamical processes. If either ammonia or water vapor were transported to either higher or lower layers in the model by a dynamical process, a much different spectral signature in both brightness temperature and limb darkening would result.

The importance of the new H_2O opacity model is highlighted in Figure 8.8. The case using the new H_2O model displays a similar pattern to that using the *DeBoer* (1995), and *Goodman* (1969) models, but the limb darkening computed using the new H_2O model shows less limb darkening in the 10-20 cm wavelength region, but increased limb darkeing in the 20-30 cm wavelength region. While these effects are relatively small, they are well above the Juno MWR limb darkening measurement precision of 0.01%.

Given the dramatic change upon limb darkening when including or omitting the microwave opacity of the H_2O-NH_3 solution cloud, an exploration of the effect of changing the cloud bulk density of the cloud is warranted. Some cases using the sedimentation scheme developed in Chapter 6 have been used to show what limb darkening pattern would result when varying the f_{sed} parameter, which controls the cloud bulk density of the solution cloud. In Figures 8.9 and 8.10, simulations using two values of f_{sed} along with the mean Jovian case (including and excluding cloud absorption). Upon careful inspection of Figure 8.9, the values computed using a value of 100, and 10000 for f_{sed} do not lie between the mean cases both including and excluding cloud absorption. The primary reason for this is that the parameterization using f_{sed} is thermodynamically consistent. That is, the amount of cloud material

that condenses and remains at a particular layer is used to compute the lapse rate, whereas the cases where cloud absorption is "turned off" is not. The differences observed between the mean cases with and without cloud absorption to the cases using the sedimentation scheme is a combined effect of changing the lapse rate, and the amount of cloud material. We consider this to be a more physically realistic approach, and should be considered for future sensitivity studies, and retrievals by the MWR team.

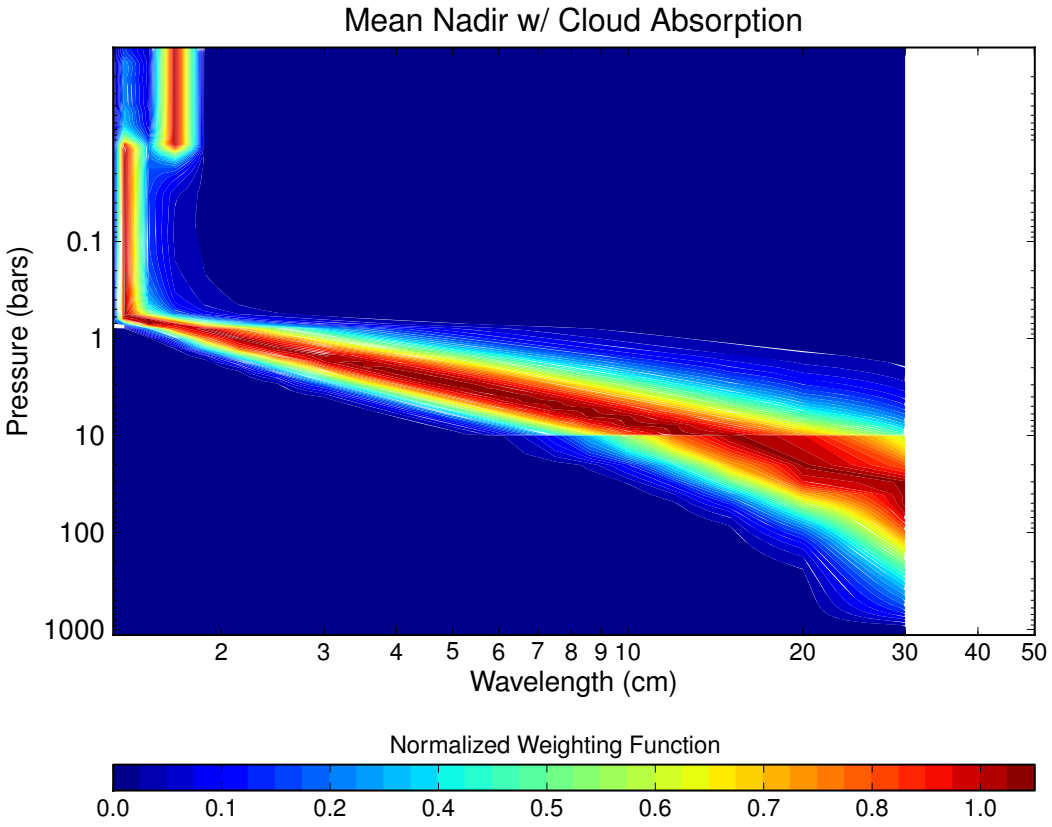

Figure 8.1: Normalized weighting functions for Nadir viewing geometry under mean Jovian conditions.

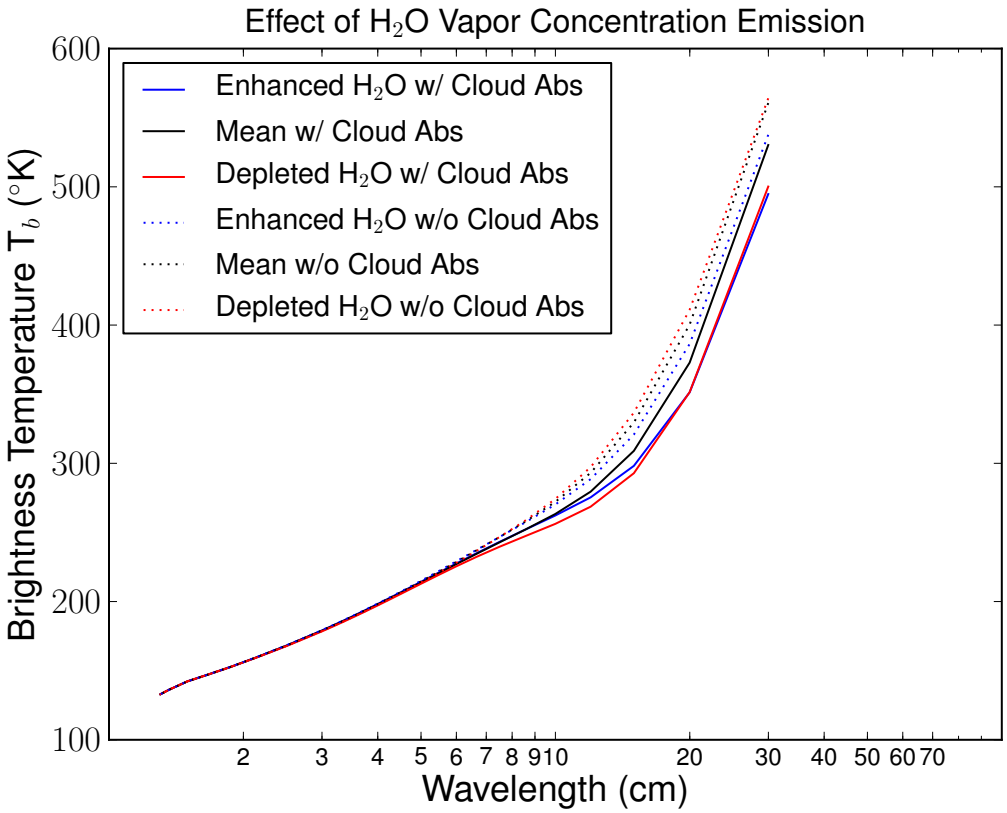

Figure 8.2: Simulated nadir brightness temperature for cases of varying deep H_2O abundance.

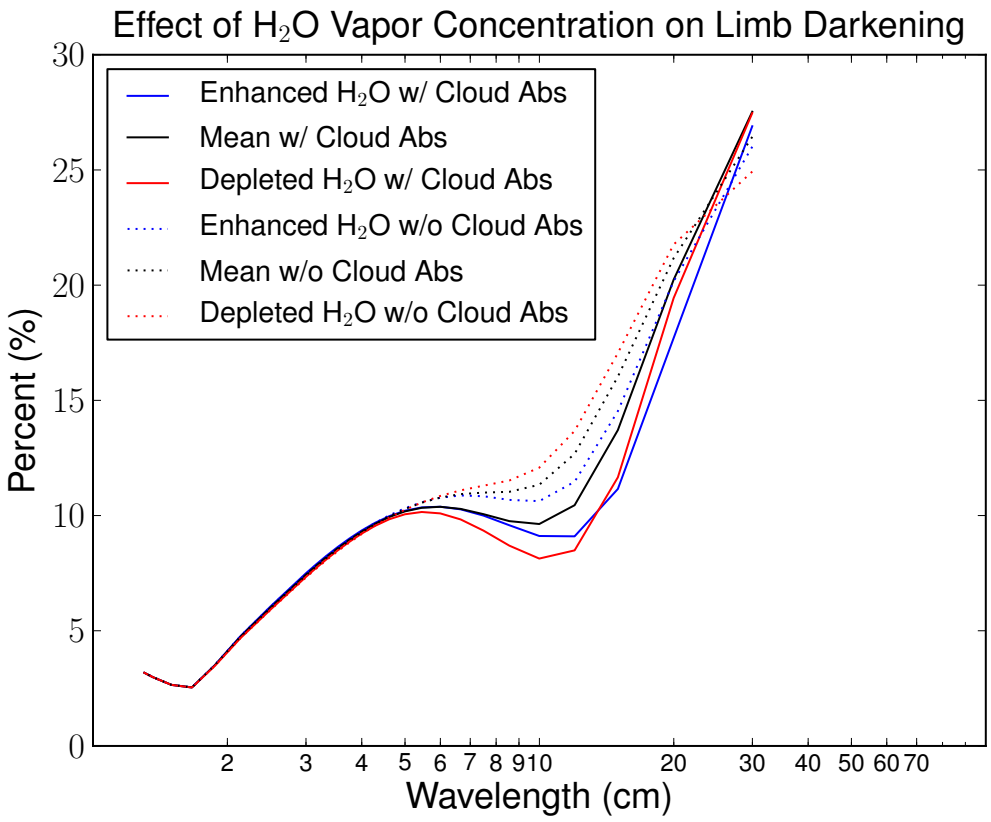

Figure 8.3: Simulated limb darkening for cases of varying deep H_2O abundance.

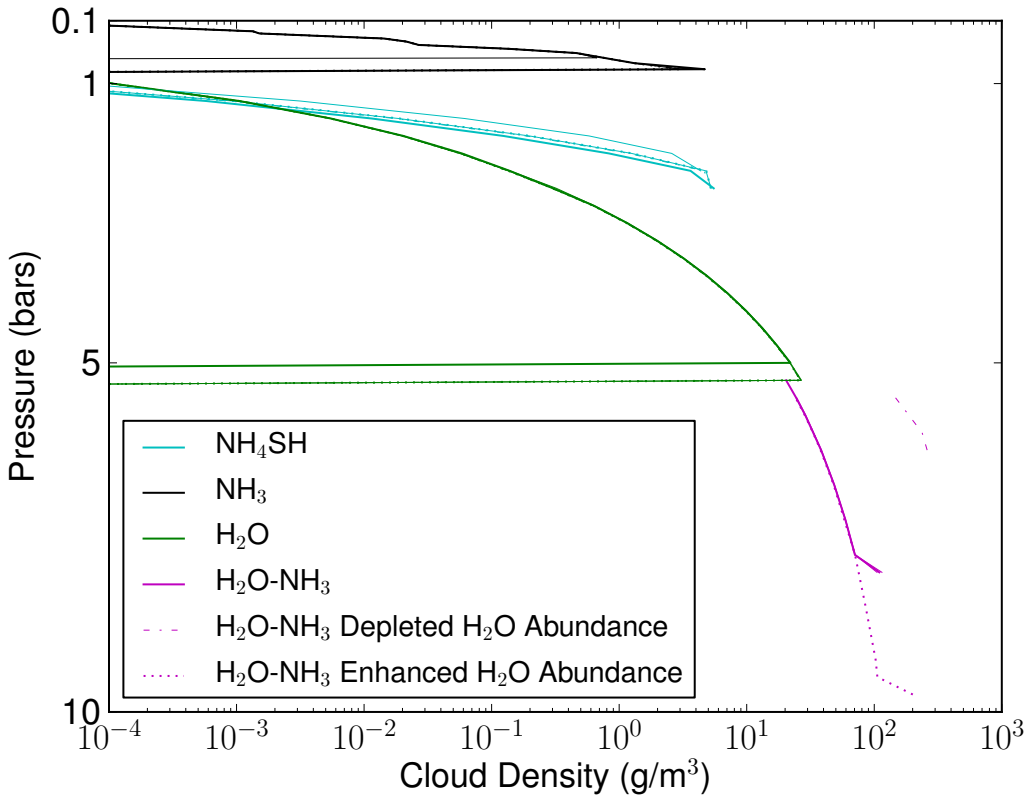

Figure 8.4: Cloud densities for under various Jovian conditions.

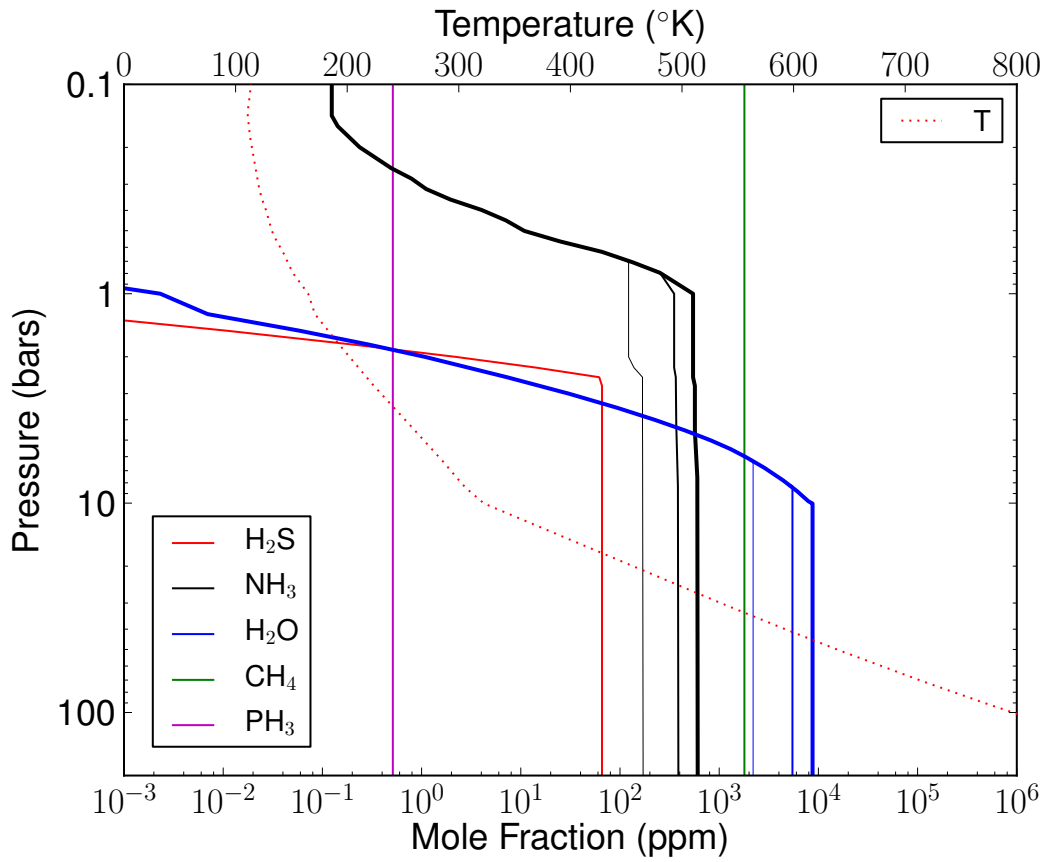

Figure 8.5: Constituent abundance profiles under various Jovian conditions along with a temperature pressure profile (Line weight indicates, depleted, mean and enhanced conditions).

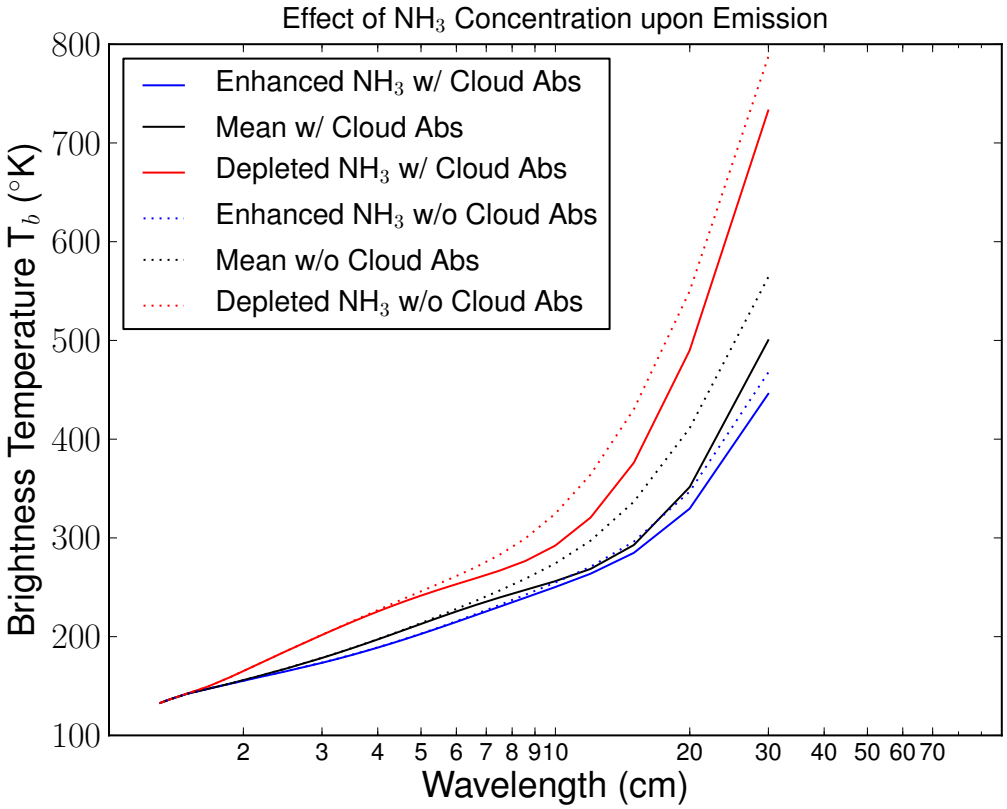

Figure 8.6: Simulated nadir brightness temperature for cases of varying deep NH_3abundance.

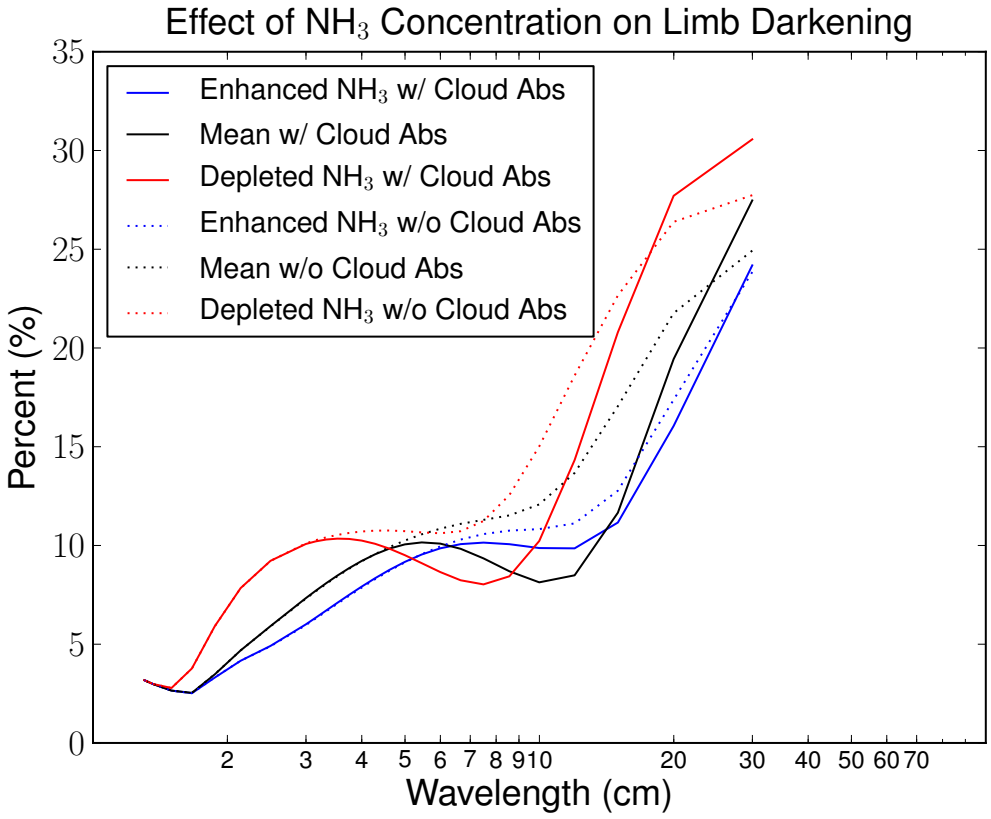

Figure 8.7: Simulated limb darkening for cases of varying deep NH_3 abundance.

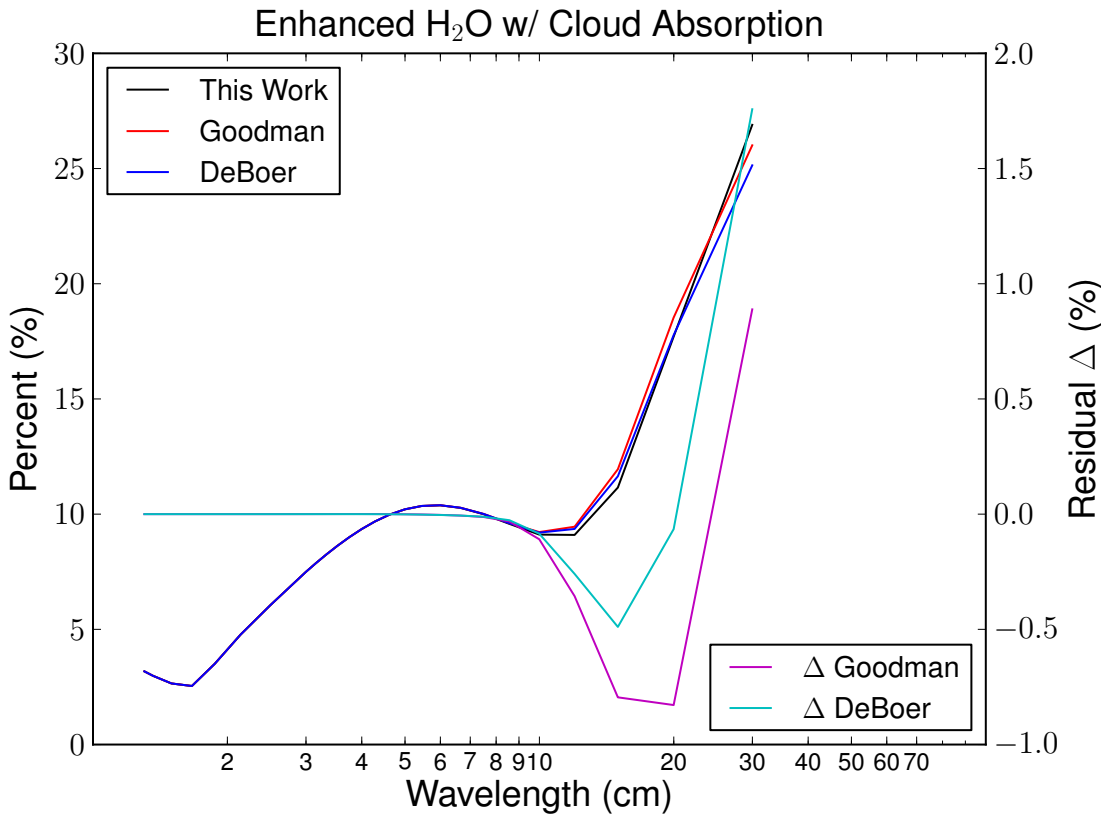

Figure 8.8: Simulated limb darkening for the enhanced H_2O case using various opacity models, along with residuals (ΔGoodman $= R_{\text{This Work}} - R_{\text{Goodman}}$, ΔDeBoer $= R_{\text{This Work}} - R_{\text{DeBoer}}$).

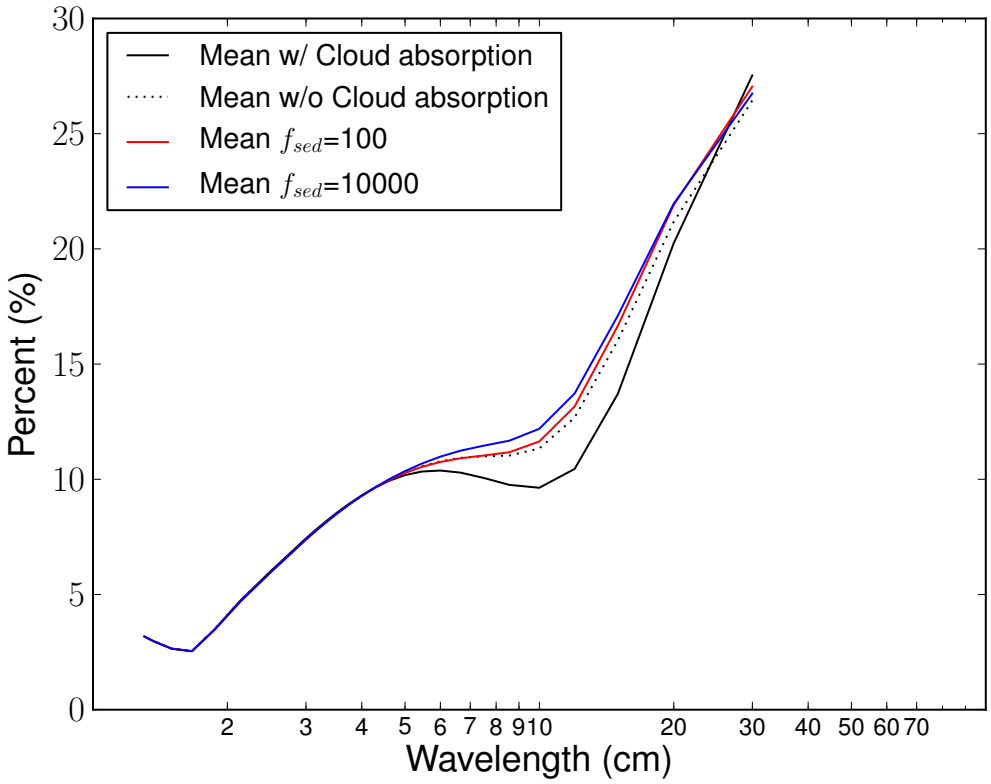

Figure 8.9: Simulated limb darkening for varying values of f_{sed} along with the Mean Jovian case with cloud absorption considered, and ignored.

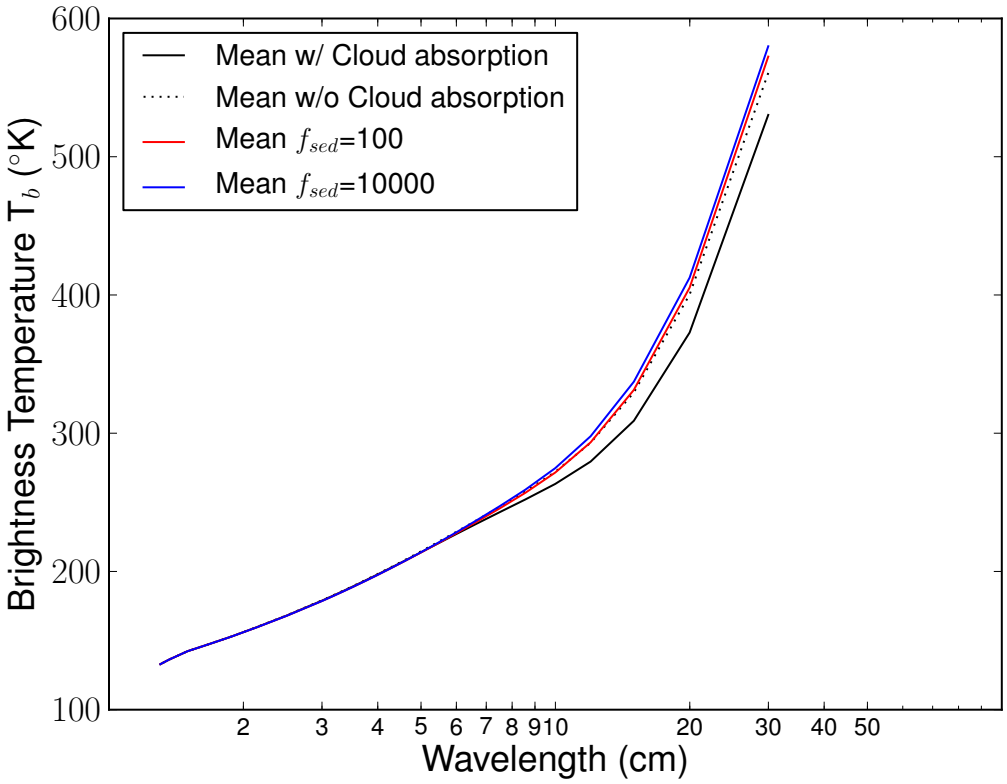

Figure 8.10: Simulated nadir emission for varying values of f_{sed} along with the Mean Jovian case with cloud absorption considered, and ignored.

CHAPTER IX

SUMMARY AND CONCLUSIONS

The primary objective of this work has been to derive a centimeter-wave opacity model for water vapor under deep Jovian conditions. The water vapor opacity model is based upon extensive laboratory measurements conducted under temperatures ranging from 375-525°K and pressures up to 100 bars. The model developed provides a good fit with experimental data, and is the first centimeter wave opacity model developed for water vapor under Jovian conditions to be verified by laboratory experiments. Use of previous models (i.e., *Goodman*, 1969; *DeBoer*, 1995) should be discontinued, as neither of these models come close to fitting the data taken in the laboratory experiments. This work will allow the MWR team to interpret observations of centimeter-wave emission from Jupiter as viewed by the Microwave Radiometer (MWR) instrument of the NASA Juno Mission. The complexity, and highly non-ideal nature of the H_2-H_2O mixture required that an equation of state be developed to correctly interpret the microwave opacity measurements. Unfortunately, the data set regarding this mixture was quite sparse, and we found it necessary to conduct our own measurements of pVT to derive constraints on the equation of state. While the measurements provided a constraint to derive an equation of state which was valid, the measurements are only accurate at the 3 % level. The equation of state also is verified by previously conducted thermodynamic measurements.

In addition to providing both a centimeter wave water vapor opacity model, and an equation of state for the deep Jovian atmosphere, several simulations of the microwave emission as observed from the Juno MWR were conducted using a 1D thermochemical model mapped onto a 3D ray tracing radiative transfer model. Analysis showed

results similar to that of *Janssen et al.* (2005), however, inclusion of the newly developed water vapor opacity model in the analysis shows, that the water vapor opacity model of *Goodman* (1969) model does not provide accurate representations of thermal emission, or limb darkening. The work of *Janssen et al.* (2005) also neglects the effects of the non-ideal behavior of H_2, CH_4, and H_2O, along with the non-ideal mixture effects from H_2-H_2O and H_2-CH_4. The current work includes these effects in the thermochemical model, and further work should continue to include non-ideal behavior of other constituents, along with non-ideal mixing effects. In our analysis we are unable to draw conclusions regarding the performance of the 600 MHz channel in its ability to detect water vapor. In order to accurately retrieve results from the 600 MHz channel a more thorough analysis of the performance of absorption models under pressures greater than 1000 bars and 1000°K should be performed, as there is no way to verify that current opacity models will remain valid at these extreme temperatures and pressures. In addition the effect of cloud absorption was investigated both by the traditional method of "turning off" the microwave opacity from the water-ammonia solution cloud, and using a modification of the thermochemical model to include a scheme for sedimentation of cloud material. The second method is included so as to be consistent with the thermodynamic state of the atmosphere. That is, the lapse rate is computed so as to be consistent with the loss of cloud material. The traditional method of "turning off" cloud absorption generates a temperature pressure profile that follows a saturated "wet" adiabat, but assumes that no condensate forms absorb or emit centimeter waves. The second method is common among sensitivity studies, and should be used only as a diagnostic tool to test how a radiative transfer model handles cloud absorption.

9.1 Suggestions for Future Work

While this work is extensive, it is by no means complete. The effort which will be required to make the Juno MWR successful will require an unprecedented multi-disciplinary approach. Understanding the fundamental thermodynamics beyond what is presented in this work should be pursued. New thermodynamic measurements should be conducted to better understand the mixing effects of H_2, He, CH_4, and H_2O. This is especially true, if one desires to use the 600 MHz channel whose weighting function extends below the 1000 bar level. Otherwise it will be impossible to decouple effects of temperature and composition. Either extensive *ab-initio* calculations of microwave absorbtion, or *extreme* high pressure/temperature microwave measurements should be conducted near the 1000 bar level, as there is no evidence to support that any absorption model can perform over the temperature and pressure range required for the 600 MHz channel. A water vapor absorption model including theory included in the MT_CKD (*Payne et al.*, 2010) *could* provide for a more sound interpretation of the 600 MHz channel, however, without laboratory measurements or supporting *ab-initio* calculations, the uncertainties would be much larger than for other MWR channels. A major improvement that could be made to the thermochemical model would be to include an integration routine to compute the cloud bulk densities from the equation of state. This could be done by applying the Maxwell criterion to individual components of the equation of state (*Span*, 2000) in place of using the rather old coefficients used to compute cloud bulk densities in the current thermochemical model. Next, measurements of NH_3 under the same conditions in this work would be highly desirable, and are currently being conducted by another student working in this laboratory. A subtle, but potentially difficult process to understand is the enhanced opacity of ammonia due to the presence of water vapor. At least one laboratory measurement study has indicated that water vapor can efficiently broaden the 572 GHz line of ammonia (*Belov et al.*, 1983), and this could be true of

other ammonia lines as well. Laboratory measurements of the opacity of mixtures of ammonia and water vapor using the ultra high pressure measurement system could provide a unique insight into this problem as it relates to the Juno MWR observation. High pressure measurements of other microwave absorbers with relatively large abundances such as H_2S would also help to limit uncertainties in retrievals. Finally, most studies currently use the absorption coefficient of pure liquid water to compute the absorption coefficient of the H_2O-NH_3 cloud. While the fraction of NH_3 dissolved in H_2O is likely to be small, it may result in an increase in microwave opacity. Laboratory measurements of the dielectric constant of liquid H_2O with dissolved NH_3 could provide a better estimate of cloud opacity.

9.2 Contributions

In this work several contributions have been made to the fields of microwave spectroscopy, planetary science, and remote sensing. A new ultra-high pressure system was developed to measure microwave and thermodynamic properties of water vapor in a H_2-He atmosphere up to 100 bars pressure, and temperatures up to 525°K. This required an extensive effort to update hardware, and include the latest and best available sensors to monitor pressure, temperature, relative humidity, and a method to control the temperature system remotely. A new framework for understanding the deep atmosphere of Jupiter has been established using the newly developed equation of state, the first laboratory verified Jovian microwave opacity model for water vapor, a new thermo-chemical model including the non-ideal effects upon pressure and specific heat, and a new radiative transfer model based upon the work of (*Hoffman*, 2001).

APPENDIX A

ADDITIONAL ABSORPTION MODELS

A.1 H_2, He, CH_4 Collisionally Induced Absorption

In LRTM one may select either a H_2-He collisionally induced H_2 absorption with a formalism from *Goodman* (1969), a H_2-He formalism given by *Joiner* (1991), a H_2-He-CH_4 collisionally induced absorption (*Joiner*, 1991), a H_2-He model derived from *Goodman* (1969), a H_2 model from *Borysow et al.* (1985), or a H_2 model from *Orton et al.* (2007). The deviation between the formalisms is negligible for microwave frequencies, but can start to deviate at millimeter-wave frequencies as shown in Figures A.1, and A.2. The formalism adopted for collisionally induced absorption using only H_2 and He is taken from *Goodman* (1969).*Goodman* (1969) uses a slightly different notation for absorption coefficient where μ is the total absorption coefficient (units of cm^{-1}) and α is the atomic absorption coefficient (units of cm^2). The difference between μ and α in *Goodman* (1969) is a factor of the number density of H_2. Here we will adopt a notation where α is the absorption coefficient (in units of cm^{-1}) from the H_2-He contribution including the additional term for number density.

$$\alpha_{H_2/He} = N_{H_2} \frac{1}{c} \times 10^{-38} \left[0.377 N_{H_2} \left(\frac{T}{100} \right)^{-0.8} + 0.535 N_{He} \left(\frac{T}{100} \right)^{-0.61} \right] \nu^2 \quad \text{(A.1)}$$

where c is the speed of light (units of cm/sec), T is temperature in °K, ν is wavenumber in units cm^{-1}, and where N_{H_2} and N_{He} are the number density of each species given by:

$$N_i = P_i \left(\frac{273}{T} \right) L_o \quad \text{(A.2)}$$

where P_i is the partial pressure of the species in atmospheres, T is the temperature in °K, and L_o is Loschimdt's number (air concentration at STP 2.687×10^{19} cm^{-3}).

Note that pressure is converted from units of bars to atmospheres for this formalism.

There are two formalisms available in LRTM referenced by *Joiner* (1991). The first is a formalism which is derived from *Goodman* (1969). The opacity from collisionally induced absorption from H_2-He is taken to be:

$$\alpha_{H_2/He} = \frac{4.0 \times 10^{-11}}{\lambda^2} P_{H_2} \left[P_{H_2} \left(\frac{273}{T} \right)^{2.8} + 1.7 P_{He} \left(\frac{273}{T} \right)^{2.61} \right] \tag{A.3}$$

where P_{H2} is the partial pressure of hydrogen, P_{He} is the partial pressure of helium, T is temperature in °K, and λ is the wavelength in cm. While this expression is similar to that of *Goodman* (1969), it is not identical as there are some round off errors between the expressions. The second formalism from *Joiner* (1991) accounts for the collisionally induced absorption from H_2 with He and CH_4, and is a simplified fit to the *Borysow et al.* (1985) model. The formalism is given as

$$\begin{aligned} \alpha_{H_2/He/CH_4} &= \frac{3.557 \times 10^{-11}}{\lambda^2} P_{H_2} \left[P_{H_2} \left(\frac{273}{T} \right)^{3.12} + 1.382 P_{He} \left(\frac{273}{T} \right)^{2.24} \right. \\ &\quad \left. + 9.322 P_{CH_4} \left(\frac{273}{T} \right)^{3.34} \right] \end{aligned} \tag{A.4}$$

where λ is the wavelength in cm, T is the temperature in °K, and P_{H_2}, P_{He}, and P_{CH_4} are the partial pressures of H_2, He, and CH_4 in atmospheres, respectively.

Both the *Borysow et al.* (1985) and *Orton et al.* (2007) formalisms available in LRTM are based upon the FORTRAN code used in *Borysow et al.* (1985) (available for dowload at `http://www.astro.ku.dk/~aborysow/programs/index.html`). The *Orton et al.* (2007) formalism is not given directly in the paper, but states that reducing the $\lambda_1\lambda_2\Lambda L$ 2233 dipole component by a factor of 1/2 in the *Borysow et al.* (1985) FORTRAN code results in a close fit to their model. We have developed two routines based upon the *Borysow et al.* (1985) code, one which represents the original *Borysow et al.* (1985) routine, and another which represents the routine proposed by *Orton et al.* (2007). Figure A.3 shows the absorption coefficient in units of 10^{-6}cm^{-1} per amagat^2. The amagat is a normalized unit of density commonly

used by spectroscopists (rarely by radio-astronomers):

$$\rho_{amagat} = \frac{\rho}{\rho_{stp}} \tag{A.5}$$

where ρ is the density of the species, and ρ_{stp} is the density of an ideal gas at STP(Loschimdt's number 2.687 $\times$ 10^{19} cm^{-3}). Figure 1 shows that there is very little (if any) difference between between formalisms at microwave frequencies. To show how well we have replicated the results of *Orton et al.* (2007) we include an overlay from Figure 1 of *Orton et al.* (2007) in Figure A.4.

The approach to modeling collisionally-induced hydrogen absorption given in *Borysow et al.* (1985) is to reduce the quantum mechanical formulas down to a computationally affordable level by curve fitting several physically based functions against a full quantum mechanical formalism. The equation used to calculate absorption coefficient is:

$$\begin{aligned} \alpha(\omega) &= \frac{2\pi^2}{3hc} n^2 \omega (1 - e^{-h\omega/kT}) \\ &\quad \times \Sigma_{\lambda_1\lambda_2\Lambda L} \Sigma_{j_1 j_1' j_2 j_2'} (2j_1+1) P_{j_1} C(j_1 \lambda_1 j_1'; 00)^2 \\ &\quad \times (2j_2+1) P_{j_2} C(j_2 \lambda_2 j_2'; 00)^2 \\ &\quad \times G_{\lambda_1\lambda_2\Lambda L}(\omega) \end{aligned} \tag{A.6}$$

where n is the number density of molecular hydrogen, T is the temperature, $C(j\lambda j';00)$ are the Clebsch-Gordan coefficients, j_i are the rotational quantum numbers of molecule i=1,2 where the prime indicates the final state, $\omega_{j_i j_i'}$ are 2π times the rotational transition frequencies, P_{j_i} are normalized Boltzmann factors,$G_{\lambda_1\lambda_2\Lambda L}(\omega)$ are the unshifted translational profiles, and λ_1,λ_2, Λ are all summation indices. The value for $G_{\lambda_1\lambda_2\Lambda L}(\omega)$ is found using a six parameter Extended Birnbaum and Cohen model (EBC) ($G_{\lambda_1\lambda_2\Lambda L}(\omega) \approx S\Gamma(\omega)$):

$$\begin{aligned} S\Gamma(\omega) &= \frac{S}{1+\epsilon} \left[\frac{\tau_1}{\pi} \frac{z K_1(z)}{1+\omega^2\tau_1^2} \exp\left(\frac{\tau_2}{\tau_1} + \tau_o\omega\right) \right. \\ &\quad \left. + \epsilon \frac{\tau_3}{\pi} K_o(z') \exp\left(\frac{\tau_3}{\tau_4} + \tau_o\omega\right) \right] \end{aligned} \tag{A.7}$$

with

$$z = [(1 + \omega^2\tau_1^2)(\tau_2^2 + \tau_0^2)]^{1/2}/\tau_1 \tag{A.8}$$

and

$$z' = [(1 + \omega^2\tau_4^2)(\tau_3^2 + \tau_o^2)]^{1/2}/\tau_4 \tag{A.9}$$

This model has been shown to be in agreement with models which incorporate all quantum mechanics within an error of 0.3–2% depending upon temperature and the spectral range. *Orton et al.* (2007) reduce the $\lambda_1\lambda_2\Lambda L$ 2233 component by a factor of 1/2 (multiplying the value of S by 1/2 on line 123 of the original FORTRAN source code provided by Borysow at `http://www.astro.ku.dk/~aborysow/programs/index.html`) which better models the spectrum of Uranus, and matches their quantum scattering code results. The output from the FORTRAN code is in units of $\mathrm{cm}^{-1}/\mathrm{amagat}^2$. To find the absorption at a given layer, our routine multiplies this quantity by a factor of ρ^2_{amagat}.

To compare the hydrogen formalisms we consider the Jovian coditions used in *DeBoer* (1995) which are slightly different in that abundances are 78% for H_2, 19% for He, and 3% for CH_4. The results using these mixing ratios in conjunction with the various H_2 collisionally induced absorption models are shown in Figure A.5. In Figure A.6 it is clear that significant deviation between the Joiner H_2-He-CH_4 model and the various other models occurs only at millimeter wavelengths.

A.2 NH_3 Absorption

There are several NH_3 models which may be used with LRTM. The models available are the *Mohammed and Steffes* (2003) model, the *Joiner and Steffes* (1991b), the *Spilker* (1993) model, and the *Berge and Gulkis* (1976) model. Each model uses a formalism based of the BR lineshape.

A.2.1 Mohammed-Steffes Ka Band model

The *Mohammed and Steffes* (2003) Ka band model uses a BR lineshape with the coupling term found by

$$\zeta_j = 1.92 P_{H_2} \left(\frac{300}{T}\right)^{2/3} + 0.49 P_{He} \left(\frac{300}{T}\right)^{2/3} + 0.49 P_{NH_3} \left(\frac{300}{T}\right) \Delta\nu_j^o \quad \text{(GHz)} \quad \text{(A.10)}$$

where P_{H_2}, P_{He},and P_{NH_3} are the partial pressures (in bars) from hydrogen, helium and ammonia, repectively. The self broadening parameters ($\Delta\nu_j^o$) are taken from *Poynter and Kakar* (1975). The pressure broadened linewidth is given as,

$$\Delta\nu_j = 2.318 \left(\frac{300}{T}\right)^{2/3} P_{H_2} + 0.79 \left(\frac{300}{T}\right)^{2/3} P_{He} + 0.75 \left(\frac{300}{T}\right) P_{NH_3} \Delta\nu_j^o \quad \text{(GHz)} \quad \text{(A.11)}$$

where again P_{H_2}, P_{He},and P_{NH_3} are the partial pressures (in bars) from hydrogen, helium and ammonia, repectively. Again, the self broadening parameters ($\Delta\nu_j^o$) are taken from *Poynter and Kakar* (1975). The pressure shift term is given by

$$\delta = -0.45 P_{NH_3} \quad \text{(GHz)} \quad \text{(A.12)}$$

where P_{NH_3} is the partial pressure of ammonia. Also *Mohammed and Steffes* (2003) use a correction factor (D),

$$D_j = \frac{1.71797 \nu^{0.0619}}{(5.4015 + |\nu - \nu_j^o|)^{0.266}} \quad \text{(A.13)}$$

Using the parameters presented here in conjunction with Equation 2.6 with D_j inserted as a factor, the absorption coefficient for ammonia can be calculated for a given constituent, temperature and pressure profile.

A.2.2 Joiner-Steffes Model

The *Joiner and Steffes* (1991b) model is similar to the *Mohammed and Steffes* (2003) model, but without the D_j correction term. *Joiner and Steffes* (1991b) use a Ben-Reuven lineshape, however, it is of a slightly different form, along with the line center

center absorption. The overall absorption is found by:

$$\alpha(\nu) = \sum_{J=0} \sum_{K=1} A(J,K) F(J,K,\Delta\nu,\delta,\zeta,\nu) \quad (\mathrm{cm}^{-1}) \tag{A.14}$$

where $A(J,K)$ is the line center absorption with the rotational state J,K, and $F(J,K,\Delta\nu,\delta,\zeta,\nu)$ represents the BR lineshape. The values for line center absorption are found by:

$$A(J,K) = 1214 \frac{(2J+1)K^2}{J(J+1)} \nu_o^2(J,K) S(K) \frac{P_{NH_3}}{T^{7/2}} \exp\left(\frac{4.8}{T[1.09K^2 - 2.98J(J+1)]}\right) \tag{A.15}$$

where $\nu_o(J,K)$ are the center frequencies of the absorption lines (presented in MHz converted to GHz), P_{NH_3} is the partial pressure of ammonia in bars, T is the temperature in °K, and $S(K)$ is the line intensity which is 3 for a K of multiple 3, and 1.5 otherwise. The BR lineshape is also in a slightly different form than presented earlier

$$F(J,K,\Delta\nu,\delta,\zeta,\nu) = 2\left(\frac{\nu}{\nu_o}\right)^2 \frac{(\Delta\nu - \zeta)\nu^2 + (\Delta\nu + \zeta)[(\nu_o+\delta)^2 + \nu^2 - \zeta^2]}{[\nu^2 - (\nu_o+\delta)^2 - \nu^2 + \zeta^2]^2 + 4.0\nu^2\Delta\nu^2} \tag{A.16}$$

where all terms are the same as in Equation 2.5, with removal of the $1/\pi$ factor. The The coupling term is found by

$$\zeta(J,K) = 1.92 P_{H_2}\left(\frac{300}{T}\right)^{2/3} + 0.49 P_{He}\left(\frac{300}{T}\right)^{2/3} + 0.49 P_{NH_3}\left(\frac{300}{T}\right)\Delta\nu^o(J,K) \tag{A.17}$$

where P_{H_2}, P_{He},and P_{NH_3} are the partial pressures (in bars) from hydrogen, helium and ammonia, repectively. The self broadening parameters ($\Delta\nu^o(J,K)$) are taken from *Poynter and Kakar* (1975). The pressure broadened linewidth is given as,

$$\Delta\nu(J,K) = 2.318\left(\frac{300}{T}\right)^{2/3} P_{H_2} + 0.79\left(\frac{300}{T}\right)^{2/3} P_{He} + 0.75\left(\frac{300}{T}\right) P_{NH_3}\Delta\nu^o(J,K) \tag{A.18}$$

where again P_{H_2}, P_{He},and P_{NH_3} are the partial pressures (in bars) from hydrogen, helium and ammonia, repectively. Again, the self broadening parameters ($\Delta\nu^o(J,K)$)

are taken from *Poynter and Kakar* (1975). The pressure shift term is given by

$$\delta = -0.45 P_{NH_3} \quad \text{(GHz)} \tag{A.19}$$

where P_{NH_3} is the partial pressure of ammonia.

Using the parameters presented here in conjunction with Equation A.14, the absorption coefficient for ammonia can be calculated for a given constituent, temperature and pressure profile.

A.2.3 Spilker Model

The *Spilker* (1993) model is the most complex of the formalisms available in LRTM. It uses a Ben-Reuven lineshape with a more complex set of parameters. The pressure broadened linewidth for hydrogen is given as,

$$\Delta\nu_{H_2} = 2.34 \left[1 - \frac{2.122 \exp\left(\frac{-T}{116.8}\right)}{\left(\exp\left(9.024 - \frac{T}{20.3}\right) - 0.9918 + P_{H_2}\right)^r} \right] P_{H_2} \left(\frac{300}{T}\right)^{2/3} \text{(GHz)} \tag{A.20}$$

where,

$$r = 8.79 \exp\left(-\frac{T}{83}\right) \tag{A.21}$$

where P_{H_2} is the partial pressure of hydrogen in bars, and T is the temperature in °K.

The pressure broadened linewidth for helium is given by,

$$\Delta\nu_{He} = \left(0.46 + \frac{T}{3000}\right) P_{He} \left(\frac{300}{T}\right)^{2/3} \quad \text{(GHz)} \tag{A.22}$$

where P_{He} is the partial pressure of helium in bars, and T is the temperature in °K.

The pressure broadened linewidth of ammonia is given by

$$\Delta\nu_{NH_3,j} = 0.74 \Delta\nu_j^o P_{NH_3} \left(\frac{300}{T}\right) \quad \text{(GHz)} \tag{A.23}$$

where P_{NH_3} is the partial pressure of ammonia in bars, T is the temperature in °K, and $\Delta\nu_j^o$ are the self broadening parameters for ammonia.

The coupling parameter for hydrogen in the *Spilker* (1993) formalism is

$$\zeta_{H_2} = (5.746 - 7.764\Delta\nu_{H_2} + 9.193\Delta\nu_{H_2}^2 - 5.682\Delta\nu_{H_2}^3 + 1.231\Delta\nu_{H_2}^4) P_{H_2} \left(\frac{300}{T}\right)^{2/3} \quad \text{(GHz)} \tag{A.24}$$

where $\Delta\nu_{H_2}$ is the pressure broadened linewidth from H_2, P_{H_2} is the partial pressure of hydrogen in bars, and T is the temperature in °K.

The coupling parameter for helium in the *Spilker* (1993) formalism is

$$\zeta_{He} = \left(0.28 - \frac{T}{1750}\right) P_{He} \left(\frac{300}{T}\right)^{2/3} \quad \text{(GHz)} \tag{A.25}$$

where P_{He} is the partial pressure of helium in bars, and T is the temperature in °K.

The coupling parameter for ammonia in the *Spilker* (1993) formalism is

$$\zeta_{NH_3,j} = 0.50\Delta\nu_{NH_3,j}^o P_{NH_3} \left(\frac{300}{T}\right) \quad \text{(GHz)} \tag{A.26}$$

where P_{NH_3} is the partial pressure of ammonia in bars, T is the temperature in °K, and $\Delta\nu_j^o$ are the self broadening parameters for ammonia.

The pressure shift term is

$$\delta = -0.45 P_{NH_3} \quad \text{(GHz)} \tag{A.27}$$

where P_{NH_3} is the partial pressure of ammonia.

Finally, *Spilker* (1993) uses a correction factor of

$$C = -0.337 + \frac{T}{110.4} - \frac{T^2}{70600} \tag{A.28}$$

where T is the temperature in °K. It should be carefully noted that this correction factor will result in non-physical values for higher temperatures (as in the deep atmosphere of Jupiter). There are also known singularities in this formalism.

Using the parameters presented here in conjunction with Equation 2.6 with C inserted as a factor, the absorption coefficient for ammonia can be calculated for a given constituent, temperature and pressure profile. It should be noted that this

formalism is not suitable for the atmosphere of Jupiter due to the negative values of absorption coefficient it can yield for high temperatures typical deep within Jupiter's atmosphere.

A.2.4 Berge-Gulkis Model

The final ammonia formalism in LRTM is that of *Berge and Gulkis* (1976). The formalism is similar to *Joiner and Steffes* (1991b), but with a value for line center absorption given as,

$$A(J,K) = 1230\frac{(2J+1)K^2}{J(J+1)}\nu_o^2(J,K)S(K)\frac{P_{NH_3}}{T^{7/2}}\exp\left(\frac{4.8}{T}[1.09K^2 - 2.98J(J+1)]\right) \tag{A.29}$$

The *Berge and Gulkis* (1976) model uses the BR line shape with the pressure broadened linewidth given by

$$\Delta\nu_j = 2.318\left(\frac{300}{T}\right)^{2/3}P_{H_2} + 0.79\left(\frac{300}{T}\right)^{2/3}P_{He} + 0.75\left(\frac{300}{T}\right)P_{NH_3}\Delta\nu_j^o \quad \text{(GHz)} \tag{A.30}$$

where P_{H_2}, P_{He},and P_{NH_3} are the partial pressures (in bars) from hydrogen, helium and ammonia, repectively. The self broadening parameters ($\Delta\nu_j^o$) are taken from *Poynter and Kakar* (1975).

The coupling parameter is given by,

$$\zeta_j = 1.92P_{H_2}\left(\frac{300}{T}\right)^{2/3} + 0.49P_{He}\left(\frac{300}{T}\right)^{2/3} + 0.49P_{NH_3}\left(\frac{300}{T}\right)\Delta\nu_j^o \quad \text{(GHz)} \tag{A.31}$$

where P_{H_2}, P_{He},and P_{NH_3} are the partial pressures (in bars) from hydrogen, helium and ammonia, repectively. Again, the self broadening parameters ($\Delta\nu_j^o$) are taken from *Poynter and Kakar* (1975). The pressure shift term is given by

$$\delta = -0.45P_{NH_3} \quad \text{(GHz)} \tag{A.32}$$

where P_{NH_3} is the partial pressure of ammonia.

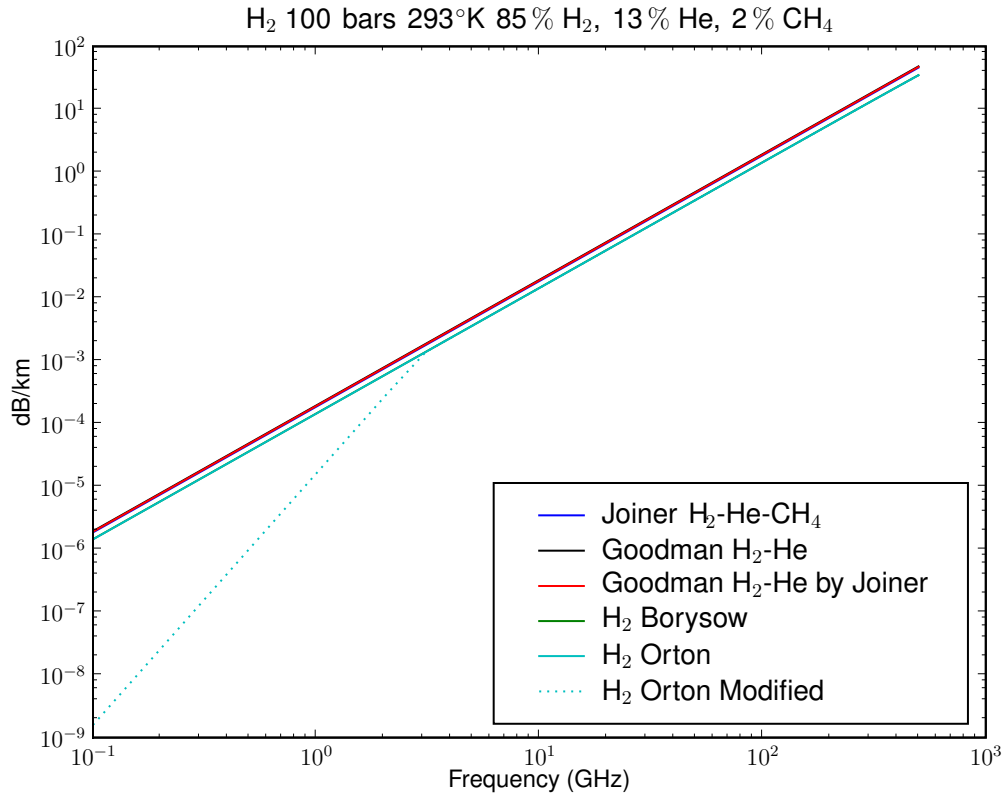

Figure A.1: H_2 collisionally induced absorption using a variety of Formalisms.

Finally, *Berge and Gulkis* (1976) uses a correction factor of

$$C = 1.0075 + (0.0308 + 0.0552\frac{P_{H2}}{T})\frac{P_{H_2}}{T} \tag{A.33}$$

where T is the temperature in °K, and P_{H_2} is the partial pressure of hydrogen.

Using the parameters presented here in conjunction with Equation A.14 with C inserted as a factor, the absorption coefficient for ammonia can be calculated for a given constituent, temperature and pressure profile.

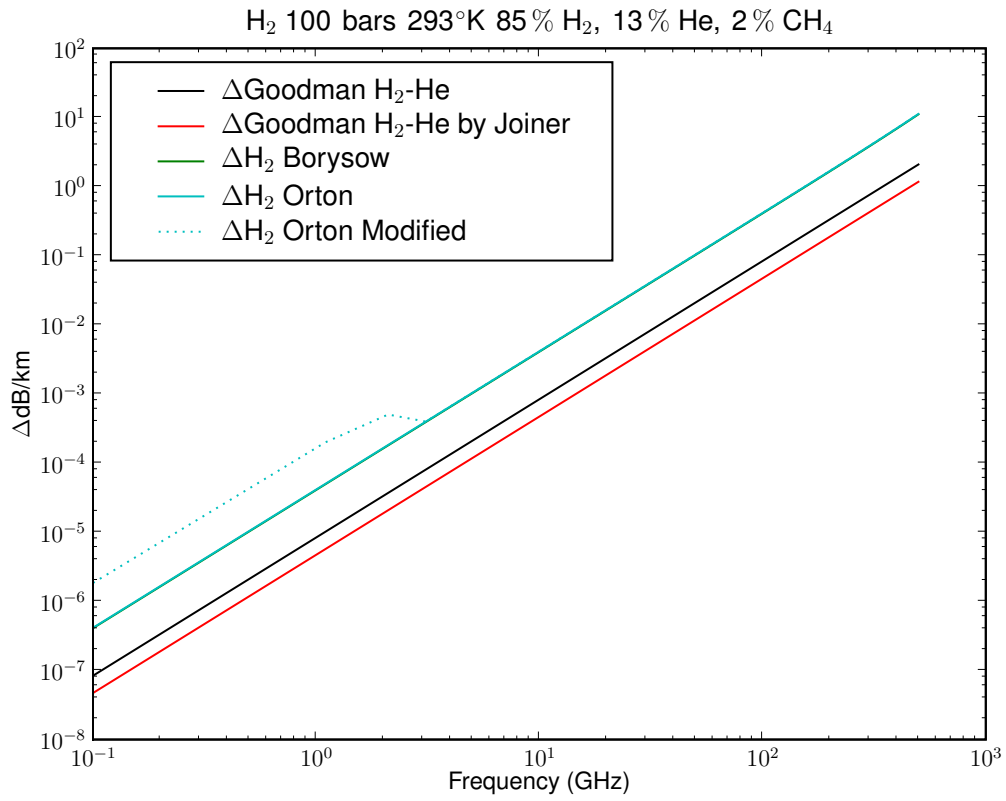

Figure A.2: Change in Absorption for a given formalism relative to the Joiner H_2-He-CH_4 formalism. Note the sign of ΔdB/km for Orton cases are negative (ie. the value for the Joiner formalism is larger, than that of Orton) .

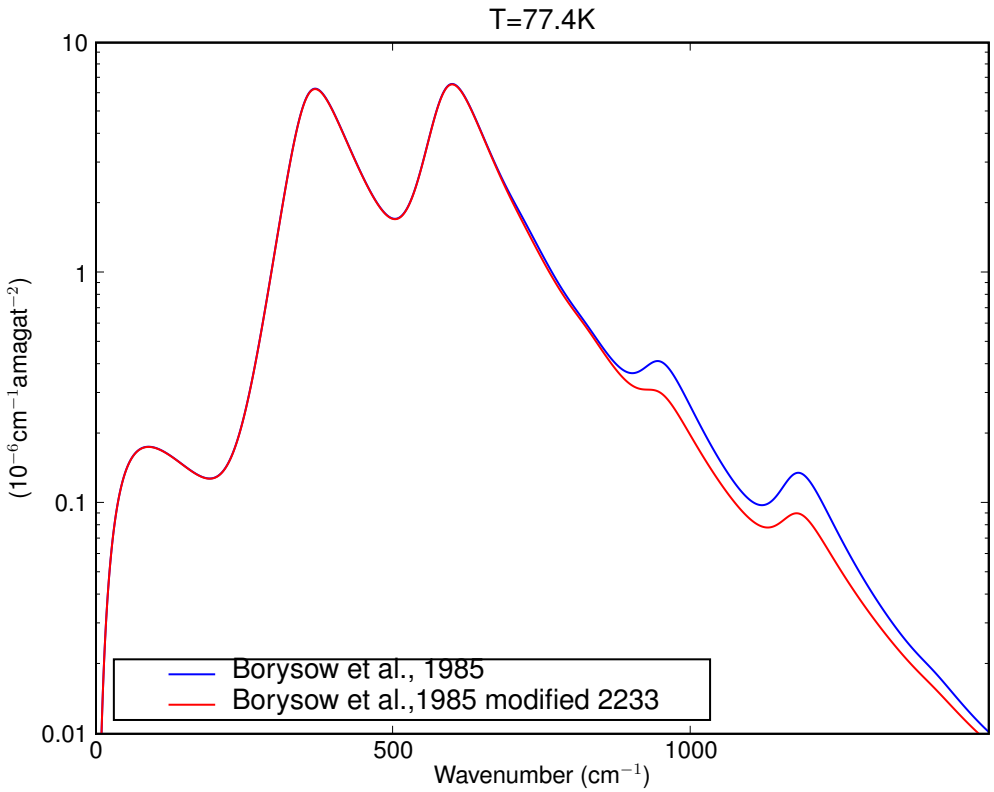

Figure A.3: The absorption coefficient for collisionally induced H_2 absorption for 0-1500 cm^{-1} as shown in *Orton et al.* (2007).

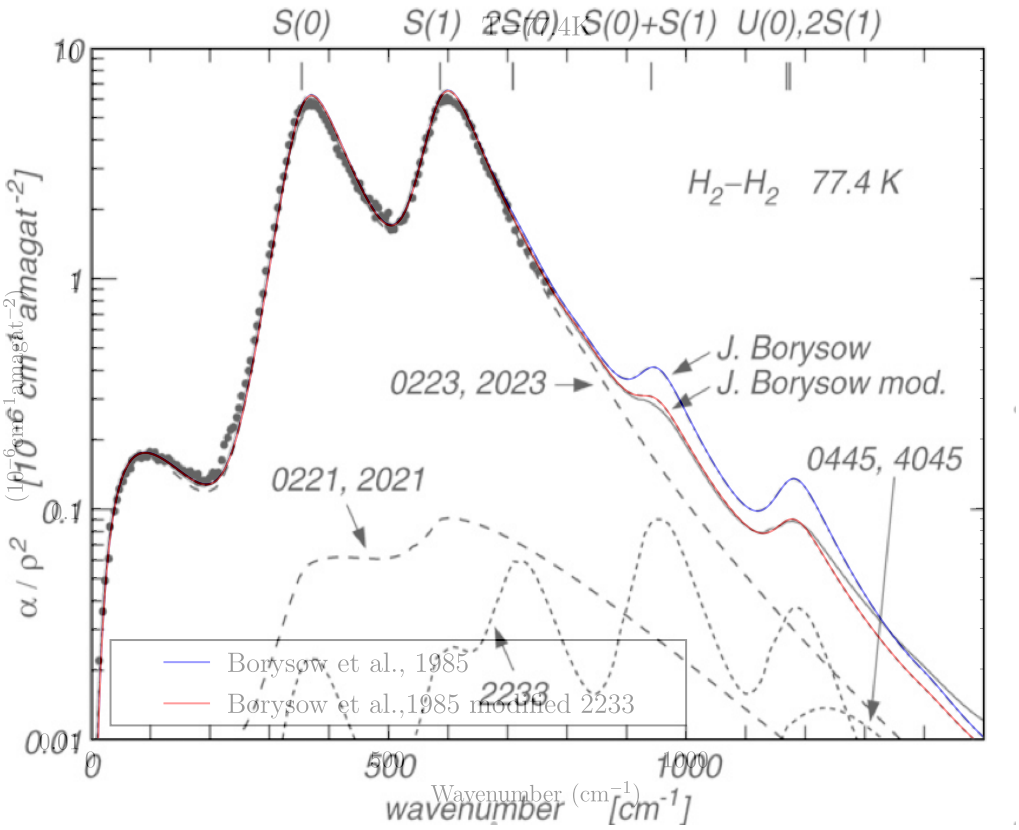

Figure A.4: The absorption coefficient for collisionally induced H_2 absorption for 0-1500 cm^{-1} with overlay from Figure 1 of *Orton et al.* (2007).

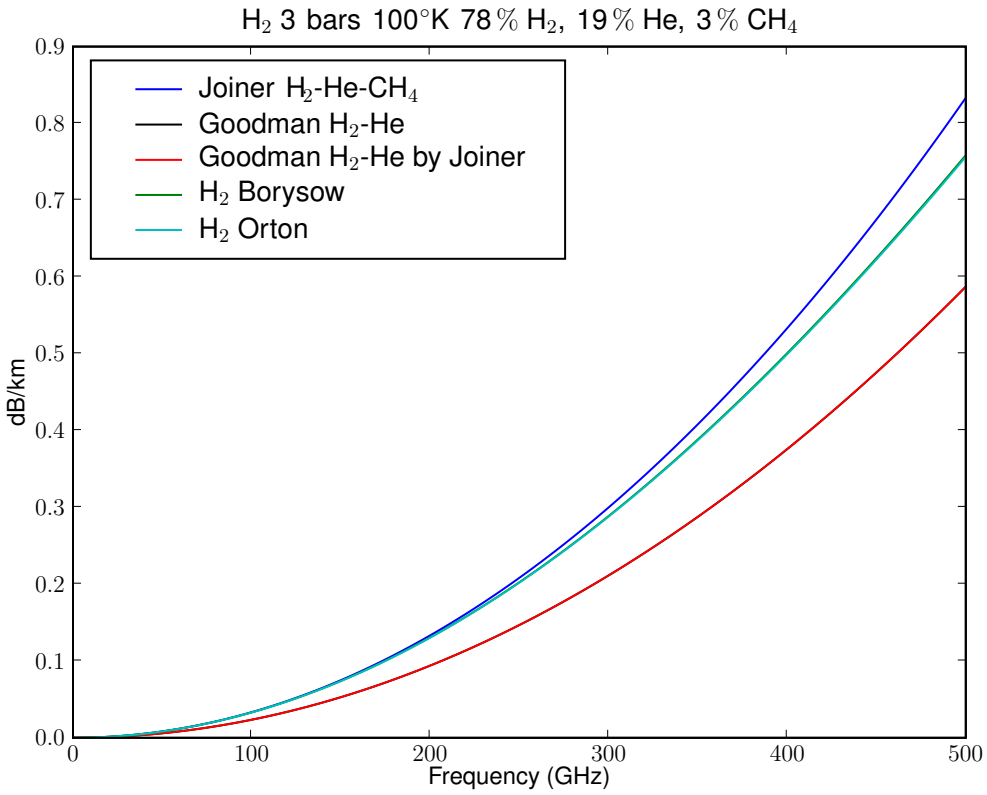

Figure A.5: The absorption coefficient for collisionally induced H_2 absorption between 0–500 GHz

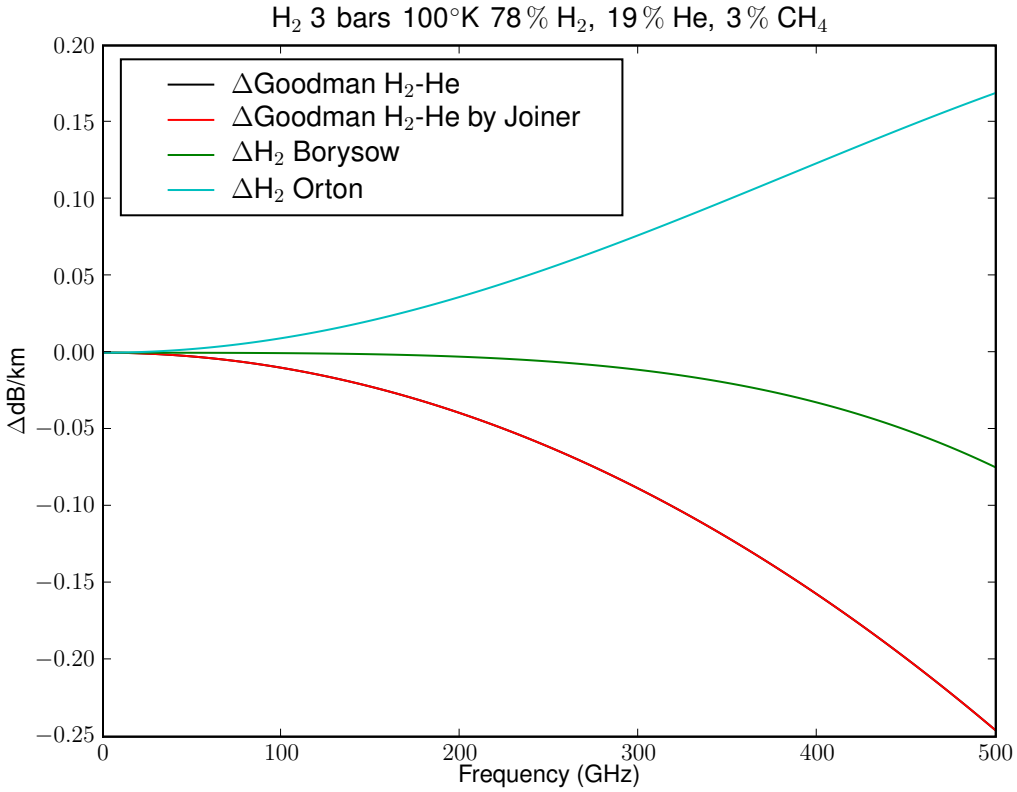

Figure A.6: The change in absorption coefficient relative to the Joiner H_2-He-CH_4 formalism for collisionally induced H_2 absorption between 0–500 GHz

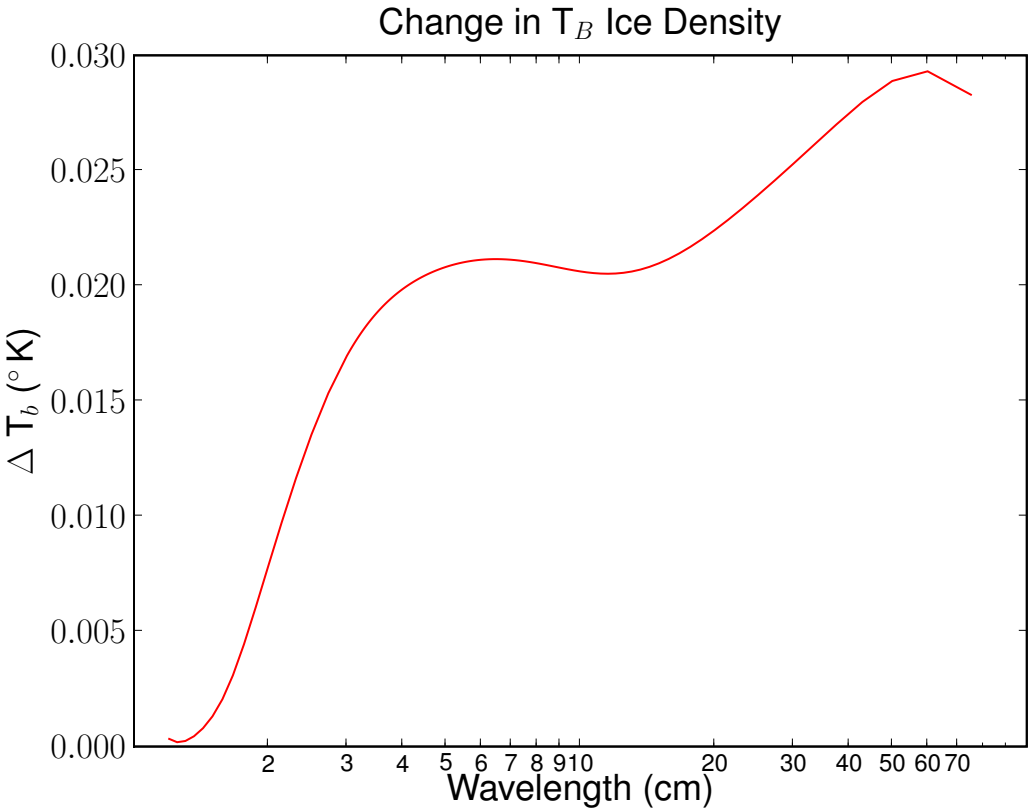

Figure A.7: Change in brightness temperature ($\Delta T = T^{\rho=1}_{Enhanced} - T^{\rho_m}_{Enhanced}$) replacing a value of $\rho = 1\frac{g}{cm^3}$, for an appropriate value associated with the material (see text).

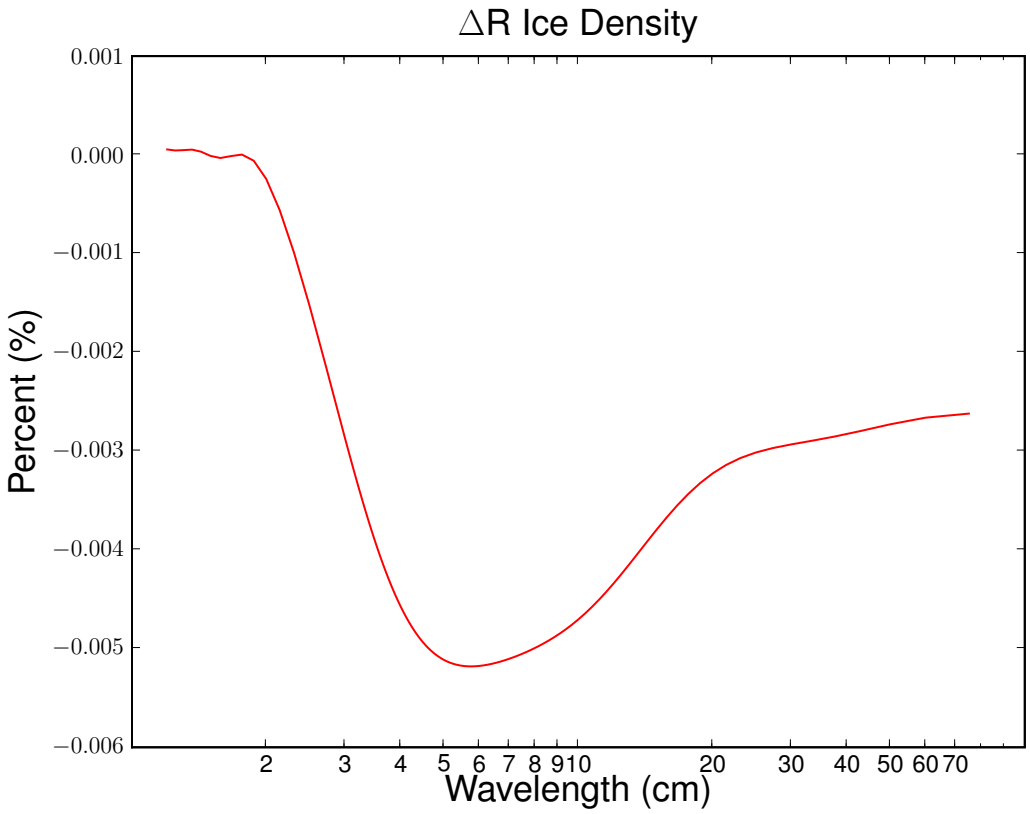

Figure A.8: Change in limb darkening ($\Delta R = R^{\rho=1}_{Enhanced} - R^{\rho_m}_{Enhanced}$) replacing a value of $\rho = 1\frac{g}{cm^3}$, for an appropriate value associated with the material (see text).

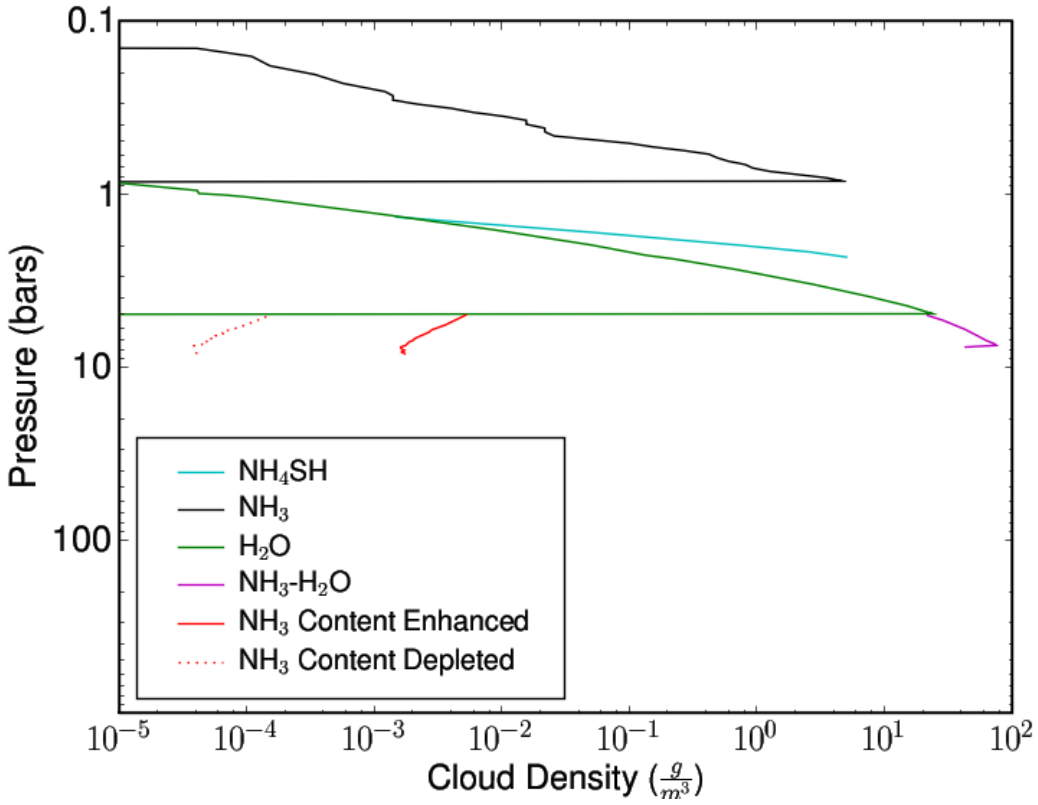

Figure A.9: Cloud Density plot for enhanced ammonia case with an ammonia content for the case of enhanced ammonia, and depleted ammonia.

APPENDIX B

PRESSURE CORRECTION FOR TELEDYNE-HASTINGS HFM-I-104 FLOWMETER

The pressure correction method suggested by Teledyne-Hastings for the HFM-I-104 flowmeter uses a pressure coefficient of 0.001%/psi. This coefficient is based upon older models derived from NIST's webbook (`http://webbook.nist.gov/chemistry/fluid/`). A simpler method is to replace the internal scale factor used by the flowmeter, and replace it with a scale factor adjusted for pressure. The Gas Correction Factor (GCF) as defined by Teledyne-Hastings is

$$GCF = \frac{c_{p_{p_{N_2}}}}{c_{test\,gas}}, \tag{B.1}$$

where $c_{p_{test\,gas}}$ is the specific heat under constant pressure for the gas under test, and $c_{p_{N_2}}$ is the specific heat under constant pressure for nitrogen. For normal H_2 the flowmeter's internal value for GCF (1.03509998) is replaced with a look-up table. The look-up table is generated using equation B.1 combined with values of $c_{p_{H_2}}$ defined by the H_2 equation of state (*Leachman*, 2007) along with values of $c_{p_{N_2}}$ defined by the N_2 equation of state (*Span et al.*, 2000) at 273.15°K in a pressure range from 0-100 bars in pressure increments of 0.01 bars. The GCF for a given pressure is found by linearly interpolating the GCF generated using equation B.1 for the final line pressure when H_2 is added to the system.

To obtain the highest accuracy within reason, hydrogen was added slowly in steps of 10 bars. This ensured that the difference in pressure across the flowmeter was not radically different from the line pressure. A pressure gradient is inevitable by definition, but is minimized by both the slow addition of H_2 and by minimizing the

pressure delivered to the flowmeter. While the flowmeter was only used in this work for pVT measurements, it can be used in for future measurements which simultaneously measure microwave opacity and pVT. For future experiments using other gases such as Helium and Argon, a table of values have been generated and stored in the following location: `http://users.ece.gatech.edu/~psteffes/palpapers/karpowicz_data/flowmeter_cal/`. The data contained in the file is tab delimited and contains columns of temperature (in° C), pressure (in bars), density (in $\frac{mol}{dm^3}$), and specific heat at constant pressure (in $\frac{kJ}{^\circ K\, mol}$). In this work, only the second and fourth columns of the files associated with H_2 and N_2 were used. Once the GCF is computed it can be used to either calculate the correct flowrate, or totalized flow. For this work, totalized flow was needed for pVT measurements of both pure hydrogen and hydrogen-water vapor mixtures. This was computed using

$$Total\,Flow = \frac{Measured Total\,Flow}{1.03509998} \times GCF \tag{B.2}$$

where both the $Total\,Flow$ and $Measured Total\,Flow$ are in units of Standard Liters (SL). The totalized flow can be converted to total mass in grams using

$$M_{H_2} = \frac{Total\,Flow \times 1.01325}{R_{H_2} \times 273.15} \tag{B.3}$$

where R_{H_2} is the specific gas constant for hydrogen ($8.314472 \times 10^{-2}\, \frac{L\,atm}{K\,mol}$ divided by the molecular mass of normal H_2 $2.01594\, \frac{g}{mol}$). The number of moles of H_2 is computed using

$$N_{H_2} = \frac{M_{H_2}}{2.01494} \tag{B.4}$$

where N_{H_2} is the number of Moles (with units mol). For other gases one must be careful to use constants consistent with the referenced equation of state. A prime example is the Helium equation of state (*McCarty*, 1990) which uses a value of $8.314310 \times 10^{-2}\, \frac{L\,atm}{K\,mol}$ for the ideal gas constant, and a molecular mass of $4.0026\, \frac{g}{mol}$.

APPENDIX C

GRIEVE 650 OVEN SCHEMATIC

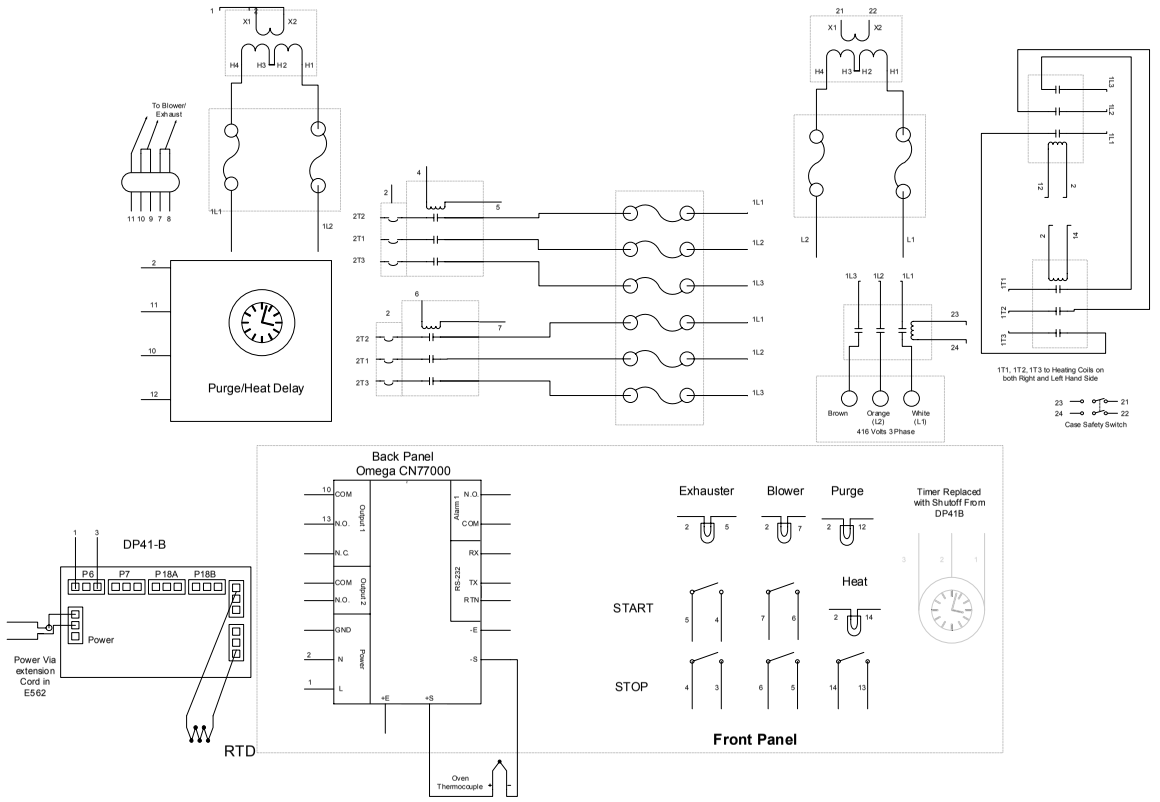

Figure C.1: Schematic Diagram of Greive 650 Oven.

References

Ackerman, A. S., and M. S. Marley (2001), Precipitating condensation clouds in substellar atmospheres, *The Astrophysical Journal*, *556*, 872–884.

Anders, E., and N. Grevesse (1989), Abundances of the elements: Meteoric and solar, *Geochemica et Cosmochimica Acta*, *53*, 197–214.

ASME (Ed.) (2007), *2007 ASME Boiler and Pressure Vessel Code, Section II - Materials*, American Society of Mechanical Engineers.

Asplund, M., N. Grevesse, and A. J. Sauval (2006), The solar chemical composition, *Nuclear Physics A*, *777*, 1–4.

Atreya, S. K., and A.-S. Wong (2004), Clouds of neptune and uranus, in *Proceedings, International Planetary Probe Workshop*.

Atreya, S. K., S. G. Edgington, L. M. Trafton, J. J. Caldwell, K. S. Noll, and H. A. Weaver (1995), Abundances of ammonia and carbon disulfide in the Jovian stratosphere following the impact of comet Shoemaker-Levy 9, *Geophysical Research Letters*, *22*, 1625–1628, doi:10.1029/95GL01718.

Atreya, S. K., M. H. Wong, T. C. Owen, P. R. Mahaffy, H. B. Niemann, I. de Pater, P. Drossart, and T. Encrenaz (1999), A comparison of the atmospheres of Jupiter and Saturn: deep atmospheric composition, cloud structure, vertical mixing, and origin, *Planetary and Space Science*, *47*, 1243–1262.

Atreya, S. K., P. R. Mahaffy, H. B. Niemann, M. H. Wong, and T. C. Owen (2003), Composition and origin of the atmosphere of Jupiter–an update, and implications for the extrasolar giant planets, *Planetary and Space Science*, *51*, 105–112.

Atreya, S. K., A. S. Wong, K. H. Baines, M. H. Wong, and T. C. Owen (2005), Jupiter's ammonia clouds–localized or ubiquitous?, *Planetary and Space Science*, *53*, 498–507.

Baines, K. H., J. H. Kim, T. W. Momary, B. J. Buratti, M. L. Delitsky, R. N. Clark, R. H. Brown, P. D. Nicholson, and Cassini/VIMS Science Team (2009), The Thunderstorm-related Clouds of Saturn: Composition, Structure, and Origin as Constrained from Cassini/VIMS Spectral Imagery, in *AAS/Division for Planetary Sciences Meeting Abstracts*, *AAS/Division for Planetary Sciences Meeting Abstracts*, vol. 41, pp. 28.07–+.

Baines, K. H., et al. (2007), Polar Lightning and Decadal-Scale Cloud Variability on Jupiter, *Science*, *318*, 226–, doi:10.1126/science.1147912.

Barahona, D., and A. Nenes (2009), Parameterizing the competition between homogeneous and heterogeneous freezing in cirrus cloud formation, *Atmos. Chem. Phys.*, *9*, 369–381.

Belov, S. P., A. F. Krupnov, V. N. Markov, A. A. Mel'Nikov, V. A. Skvortsov, and M. Y. Tret'yakov (1983), Study of microwave pressure lineshifts: Dynamic and isotopic dependences, *Journal of Molecular Spectroscopy*, *101*, 258–270, doi: 10.1016/0022-2852(83)90131-5.

Berge, G. L., and S. Gulkis (1976), Earth-based radio observations of Jupiter - Millimeter to meter wavelengths, in *IAU Colloq. 30: Jupiter: Studies of the Interior, Atmosphere, Magnetosphere and Satellites*, edited by T. Gehrels, pp. 621–692.

Borysow, J., L. Trafton, L. Frommhold, and G. Birnbaum (1985), Modeling of pressure-induced far-infrared absorption spectra Molecular hydrogen pairs, *The Astrophysical Journal*, *296*, 644–654, doi:10.1086/163482.

Boss, A. P. (1998), Evolution of the solar nebula IV. Giant gaseous protoplanet formation, *The Astrophysical Journal*, *503*, 923–937.

Boss, A. P. (2002), Formation of gas and ice giant planets, *Earth and Planetary Science Letters*, *202*, 513–523.

Briggs, F. H., and P. D. Sackett (1989), Radio observations of Saturn as a probe of its atmophere and cloud structure, *Icarus*, *80*, 77–103.

Carlson, B. E., A. A. Lacis, and W. B. Rossow (1993), Tropospheric gas composition and cloud structure of the Jovian North Equatorial Belt, *Journal of Geophysical Research*, *98*, 5251–5290.

de Pater, I., and S. T. Massie (1985), Models of the millimeter–centimeter spectra of the giant planets, *Icarus*, *62*, 143–171.

de Pater, I., D. Dunn, P. Romani, and K. Zahnle (2001), Reconciling Galileo Probe Data and Ground-Based Radio Observations of Ammonia on Jupiter, *Icarus*, *149*, 66–78, doi:10.1006/icar.2000.6527.

de Pater, I., D. Deboer, M. Marley, R. Freedman, and R. Young (2005), Retrieval of water in Jupiter's deep atmosphere using microwave spectra of its brightness temerature, *Icarus*, *173*(2), 425–447.

DeBoer, D. R. (1995), The microwave opacity of H_2S with applications to the tropospheric vertical structure of the Jovian planets, Ph.D. thesis, Georgia Institute of Technology.

Deboer, D. R., and P. G. Steffes (1994), Laboratory measurements of the microwave properties of H_2S under simulated Jovian conditions with an application to Neptune, *Icarus*, *109*, 352–366, doi:10.1006/icar.1994.1099.

DeBoer, D. R., and P. G. Steffes (1996a), The Georgia Tech high sensitivity microwave measurement system, *Astrophysics and Space Science*, *236*, 111–124.

DeBoer, D. R., and P. G. Steffes (1996b), Estimates of the tropospheric vertical structure of Neptune based on microwave radiative transfer studies, *Icarus*, *123*, 324–335.

Debye, P. (1929), *Polar Molecules*, The Chemical Catalog Company, Inc., New York.

Dutta, J. M., C. R. Jones, T. M. Goyette, and F. C. De Lucia (1993), The hydrogen and helium pressure broadening at planetary temperatures of the 183 and 380 GHz transitions of water vapor, *Icarus*, *102*, 232–239, doi:10.1006/icar.1993.1046.

Essen, L. (1953), The Refractive Indices of Water Vapour, Air, Oxygen, Nitrogen, Hydrogen, Deuterium and Helium , *Proceedings of the Physical Society B*, *66*, 189–193.

Folkner, W. M., R. Woo, and S. Nandi (1998), Ammonia abundance in Jupiter's atmosphere derived from the attenuation of the Galileo probe's radio signal, *Journal of Geophysical Research*, *103*, 22,847–22,856, doi:10.1029/98JE01635.

Fouchet, T., E. Lellouch, B. Bézard, T. Encrenaz, P. Drossart, H. Feuchtgruber, and T. de Graauw (2000), ISO-SWS Observations of Jupiter: Measurement of the Ammonia Tropospheric Profile and of the $^{15}N/^{14}N$ Isotopic Ratio, *Icarus*, *143*, 223–243, doi:10.1006/icar.1999.6255.

Gillespie, P., and G. Wilson (Eds.) (1980), *Vapor-liquid equilibrium data on water-substitute gas components: N_2—H_2O, H_2—H_2O, CO—H_2O, H_2—CO—H_2O and H_2S—H_2O*, 41, Gas Processors Association, Gas Processors Association Research Report, Provo, UT.

Goodman, G. C. (1969), Models of Jupiter's atmosphere, Ph.D. thesis, University of Illinois.

Grevesse, N., and A. J. Sauval (1998), Standard solar composition, *Space Science Reviews*, *85*.

Grevesse, N., M. Asplund, and A. J. Sauval (2005), The new solar chemical composition, in *Element Stratification in Stars: 40 Years of Atomic Diffusion*, vol. 17, pp. 21–30, EDP Sciences, Les Ulis Cedex A, F-91944, France.

Gross, E. P. (1955), Shape of collision-broadened spectral lines, *Physical Review*, *97*, 395–403.

Guillot, T. (1999), A comparison of the interiors of Jupiter and Saturn, *Planetary and Space Science*, *47*, 1183–1200.

Hanley, T. R. (2007), The microwave opacity of ammonia and water vapor: Application to remote sensing of the atmosphere of Jupiter, Ph.D. thesis, Georgia Institute of Technology.

Hanley, T. R., and P. G. Steffes (2007), A high-sensitivity laboratory system for measuring the microwave properties of gases under simulated conditions for planetary atmospheres, *Radio Science*, *42*, doi:10.1029/2007RS003693.

Hanley, T. R., P. G. Steffes, and B. M. Karpowicz (2009), A new model of the hydrogen and helium broadened microwave opacity of ammonia based on extensive laboratory measurements, *Icarus*, *202*, 316–335.

Ho, W., I. A. Kaufman, and P. Thaddeus (1966), Laboratory measurement of microwave absorption in models of the atmosphere of Venus, *J. Geophys. Res.*, *71*(21), 5091–5108.

Hodges, M. P., R. J. Wheatley, G. K. Schenter, and A. H. Harvey (2004), Intermolecular potential and second virial coefficient of the water – hydrogen complex, *Journal of Chemical Physics*, *120*(2), 710–720.

Hoffman, J. P. (2001), Microwave opacity of phosphine: Application to remote sensing of the atmospheres of the outer planets, Ph.D. thesis, Georgia Institute of Technology.

Hoffman, J. P., and P. G. Steffes (2001), Laboratory measurements of the microwave opacity of phosphine: Opacity formalism and application to the atmospheres of the outer planets, *Icarus*, *152*, 172–184.

Howett, C. J. A., R. W. Carlson, P. G. J. Irwin, and S. B. Calcutt (2007), Optical constants of ammonium hydrosulfide ice and ammonia ice, *J. Opt. Soc. Am. B*, *24*(1), 126–136.

Janssen, M. A., M. D. Hofstadter, S. Gulkis, A. P. Ingersoll, M. Allison, S. J. Bolton, S. M. Levin, and L. W. Kamp (2005), Microwave remote sensing of Jupiter's atmosphere from an orbiting spacecraft, *Icarus*, *173*(2), 447–453.

Jenkins, J. M., M. A. Kolodner, B. J. Butler, S. H. Suleiman, and P. G. Steffes (2001), Microwave remote sensing of the temperature distribution of sulfur compounds in the lower atmosphere of Venus, *Icarus*, *158*, 312–328.

Joiner, J. (1991), Millimeter-wave spectra of the Jovian planets, Ph.D. thesis, Georgia Institute of Technology.

Joiner, J., and P. G. Steffes (1991a), Modeling of Jupiter's millimeter wave emission utilizing laboratory measurements of ammonia (NH3) opacity, *Journal of Geophysical Research*, *96*, 17,463–+.

Joiner, J., and P. G. Steffes (1991b), Modeling of Jupiter's millimeter wave emission utilizing laboratory measurements of ammonia (NH3) opacity, *Journal of Geophysical Research*, *96*, 17,463–+.

Kell, G. S., and E. Whalley (1965), The PVT properties of water i. liquid water in the temperature range 0 to 150 degrees c and pressures up to 1 kb, *Phlisophical Transactions of the Royal Society of London*, *258*(1094), 565–614.

Kunde, V., R. Hanel, W. Maguire, D. Gautier, J. P. Baluteau, A. Marten, A. Chedin, N. Husson, and N. Scott (1982), The tropospheric gas composition of Jupiter's north equatorial belt (NH_3, PH_3, CH_3D, GeH_4, H_2O) and the Jovian D/H isotopic ratio, *Astrophys. J.*, *263*, 443–467, doi:10.1086/160516.

Kunz, O., R. Klimeck, W. Wagner, and M. Jaeschke (2006), The GERG-2004 wide-range reference equation of state for natural gases and other mixtures, *Technical monograph*, VDI-Verlag.

Lancaster, N. M., and C. J. Wormald (1990), Excess molar enthalpies of nine binary steam mixtures: New and corrected values, *Journal of Chemical Engineering Data*, *35*, 11–16.

Leachman, J. (2007), Fundamental equations of state for parahydrogen, normal hydrogen, and orthohydrogen, Master's thesis, University of Idaho.

Lellouch, E., B. Bézard, T. Fouchet, H. Feuchtgruber, T. Encrenaz, and T. de Graauw (2001), The deuterium abundance in Jupiter and Saturn from ISO-SWS observations, *Astron. Astrophys.*, *670*, 610–622.

Lemmon, E., M. Huber, and M. McLinden (2007), NIST Standard Reference Database 23: Reference Fluid Thermodynamic and Transport Properties-REFPROP, *Standard Reference Data Program Version 8.0*, National Institute of Standards and Technology, Gaithersburg.

Lemmon, E. W., and V. Arp (2009), An equation of state for the calculation of the thermodynamic properties of Helium-4, in *17th Symposium on Thermophysical Properites*, Boulder, CO.

Liebe, H. J., G. A. Hufford, and M. G. Cotton (1993), Propagation modeling of moist air and suspended water/ice particles at frequencies below 1000 GHz, in *52nd Specialists' Meeting of the Electromagnetic Wave Propagation Panel*, AGARD, Palma de Mallorca, Spain.

Lindal, G. F., D. N. Sweetnam, and V. R. Eshleman (1985), The atmosphere of Saturn - an analysis of the Voyager radio occultation measurements, *Astron. J.*, *90*, 1136–1146, doi:10.1086/113820.

Lindal, G. F., J. R. Lyons, D. N. Sweetnam, V. R. Eshleman, D. P. Hinson, and G. L. Tyler (1987), The atmosphere of Uranus: Results of radio occultation measurements with Voyager 2, *J. Geophys. Res.*, *92*(A13), 14,987–15,001.

Lindal, G. F., et al. (1981), The atmosphere of Jupiter - an analysis of the Voyager radio occultation measurements, *Journal of Geophysical Research*, *86*, 8721–8727.

Liou, K. N. (2002), *An Introduction to Atmopheric Radiation*, 2nd ed., Academic Press, San Diego, California.

Lorentz, H. A. (1915), The width of spectral lines, in *Proceedings of the Royal Netherlands Academy of Arts and Sciences*, vol. 18, pp. 134–150.

Mahaffy, P. R., H. B. Niemann, and J. E. Demick (1999), Deep Atmosphere Ammonia Mixing Ratio at Jupiter from the Galileo Probe Mass Spectrometer, in *AAS/Division for Planetary Sciences Meeting Abstracts*, *AAS/Division for Planetary Sciences Meeting Abstracts*, vol. 31.

Matsuoka, T., S. Fujita, and S. Mae (1996), Effect of temperature on dielectric properties of ice in the range of 5–39 GHz, *J. Appl. Phys.*, *80*(10), 5884–5890.

Matthaei, G. L., L. Young, and E. Jones (1980), *Microwave Filters, Impedance Matching Networks and Coupling Structures*, McGraw-Hill, New York.

McCarty, R. D. (1990), A new wide range equation of state for helium, *Advances in Cryogenic Engineering*, *35*, 1465–1475.

Michels, A., W. De Graaff, J. M. H. Wassenaar, T.and Levelt, and P. Louwerse (1959), Compressibility isotherms of hydrogen and deuterium at temperatures between -175°c and +150°c (at densities up to 960 amagat), *Physica*, *25*, 25–42.

Mohammed, P. N. (2005), Laboratory measurements of the millimeter wavelength opacity of phosphine (PH_3) and ammonia (NH_3) under simulated conditions for the Cassini-Saturn encounter, Ph.D. thesis, Georgia Institute of Technology.

Mohammed, P. N., and P. G. Steffes (2003), Laboratory measurements of the Ka-band (7.5 mm to 9.2 mm) opacity of phosphine (PH_3) and ammonia (NH_3) under simulated conditions for the Cassini-Saturn encounter, *Icarus*, *166*, 425–435, doi: 10.1016/S0019-1035(03)00275-6.

Morris, E. C., and R. W. Parsons (1970), Microwave absorption by gas mixtures at pressures up to several hundred bars, *Aus. J. Phys.*, *23*, 335–349.

Namiot, A. J. (1991), *Rastvorimost' gazov v vode (Solubility of Gases in Water)*, Nedra Press, Moscow.

Niemann, H. B., et al. (1996), The Galileo Probe Mass Spectrometer: Composition of Jupiter's Atmosphere, *Science*, *272*, 846–849.

Niemann, H. B., et al. (1998), The composition of the Jovian atmosphere as determined by the Galileo probe mass spectrometer, *Journal of Geophysical Research*, *103*, 22,831–22,846, doi:10.1029/98JE01050.

Orton, G. S., M. Gustafsson, M. Burgdorf, and V. Meadows (2007), Revised ab initio models for the H_2-H_2 collision induced absorption at low temperatures, *Icarus*, *189*, 544–549.

Payne, V., E. Mlawer, K. Cady-Pereira, and J. Moncet (2010), Water vapor continuum absorption in the microwave, *IEEE Transactions on Geoscience and Remote Sensing*, *In Review*.

Pollack, J. B., O. Hubickyj, P. Bodenheimer, J. J. Lissauer, M. Podolak, and Y. Greenzweig (1996), Formation of the giant planets by concurrent accretion of solids and gas, *Icarus*, *124*, 62–85.

Poynter, R. L., and R. K. Kakar (1975), The microwave frequencies, line parameters, and spectral constants for NH3-14, *Astrophysical Journal Supplement Series*, *29*, 87–96.

Pozar, D. M. (1998), *Microwave Engineering*, 2nd ed., Wiley and Sons, New York.

Press, W. H., S. A. Teukolsky, W. T. Vetterling, and B. P. Flannery (1992), *Numerical Recipes in C: The Art of Scientific Programming*, second ed., Cambridge University Press.

Rabinovich, V. A. (1995), *Moist Gases: Thermodynamic Properties*, Begell House.

Ramo, S., J. R. Whinnery, and T. V. Duzer (1965), *Fields and Waves in Communications Electronics*, Wiley and Sons, New York.

Ree, F. H. (1983), Solubility of h_2-he mixtures in fluid phases to 1 GPa, *J. Phys. Chem.*, *87*(15), 2846–2852.

Romani, P. N., I. de Pater, and S. K. Atreya (1989), Neptune's deep atmosphere revealed, *Geophysical Research Letters*, *16*, 933–936, doi:10.1029/GL016i008p00933.

Rosenkranz, P. W. (1998), Water vapor microwave continuum absorption: A comparison of measurements and models, *Radio Science*, *33*, 919–928, doi:10.1029/98RS01182.

Rothman, L. S., et al. (2009), The HITRAN 2008 molecular spectroscopic database, *Journal of Quantitative Spectroscopy and Radiative Transfer*, *110*, 533–572, doi:10.1016/j.jqsrt.2009.02.013.

Rüeger, J. M. (2002), Refractive index formulae for radio waves, in *XXII FIG International Congress*, Washington, D.C.

Sagan, C., and E. E. Salpeter (1976), Particles, environments, and possible ecologies in the Jovian atmosphere, *Astrophysical Journal Supplement Series*, *32*, 737–755, doi:10.1086/190414.

Setzmann, U., and W. Wagner (1991), A new equation of state and tables of thermodynamic properties for methane covering the range from the melting line to 625 k at pressures up to 1000 MPa, *J. Phys. Chem. Ref. Data*, *20*(6), 1061–1151.

Seward, T. M., and E. U. Franck (1981), The system hydrogen - water up to 440°C and 2500 bar pressure, *Berichte der Bunsengesellschaft für Physikalische Chemie*, *85*, 2–7.

Seward, T. M., O. M. Suleimenov, and E. U. Franck (2000), pVT data for binary H_2-H_2O mixtures in the homogeneous region to 450°C and 2500 bar, in *Steam, water, and hydrothermal systems : physics and chemistry meeting the needs of industry : Proceedings of the 13th International Conference on the Properties of Water and Steam*, pp. 104–109, NRC Research Press.

Span, R. (2000), *Multiparameter Equations of State*, Springer, New York.

Span, R., E. W. Lemmon, R. T. Jacobsen, W. Wagner, and A. Yokozeki (2000), A reference equation of state for the thermodynamic properties of nitrogen for temperatures from 63.151 to 1000 k and pressures up to 2200 MPa, *J. Phys. Chem. Ref. Data*, *29*(6), 1361–1433.

Spilker, T. R. (1990), Laboratory measurements of microwave absorptivity and refractivity spectra of gas mixtures applicable to giant planet atmospheres, Ph.D. thesis, Stanford University.

Spilker, T. R. (1993), New laboratory measurements on ammonia's inversion spectrum, with implications for planetary atmospheres, *Journal of Geophysical Research*, *98*, 5539–5548.

Sretenskaja, N. G., R. J. Sadus, and E. U. Franck (1995), High-pressure phase equilibria and critical curve of the water+helium system to 200 mpa and 723 k, *J. Phys. Chem.*, *99*, 4273–4277.

Sromovsky, L. A., A. D. Collard, P. M. Fry, G. S. Orton, M. T. Lemmon, M. G. Tomasko, and R. S. Freedman (1998), Galileo probe measurements of thermal and solar radiation fluxes in the Jovian atmosphere, *Journal of Geophysical Research*, *103*, 22,929–22,978, doi:10.1029/98JE01048.

Thayer, G. D. (1974), An improved equation for the radio refractive index of air, *Radio Science*, *9*, 803–807.

Tyler, G. L., and H. T. Howard (1969), Refractivity of carbon dioxide under simulated Martian conditions, *Radio Science*, *4*, 899–904.

Ulaby, F. T., R. K. Moore, and A. K. Fung (1981), *Microwave Remote Sensing Active and Passive: Microwave Remote Sensing Fundamentals and Radiometry*, vol. I, Addison-Wesley.

Ulaby, F. T., R. K. Moore, and A. K. Fung (1986), *Microwave Remote Sensing Active and Passive: From Theory to Applications*, vol. III, Artech House, Inc.

van Vleck, J. H., and V. F. Weisskopf (1945), On the Shape of Collision-Broadened Lines, *Reviews of Modern Physics*, *17*, 227–236, doi:10.1103/RevModPhys.17.227.

von Zahn, U., D. M. Hunten, and G. Lehmacher (1998), Helium in Jupiter's atmosphere: Results from the Galileo probe helium interferometer experiment, *Journal of Geophysical Research*, *103*, 22,815–22,830, doi:10.1029/98JE00695.

Wagner, W., and A. Pruß (2002), The iapws formulation 1995 for the thermodynamic properties of ordinary water substance for general and scientific use, *J. Phys. Chem. Ref. Data*.

Weast, R. C., and M. J. Astle (Eds.) (1979), *CRC Handbook of Chemistry and Physics*, CRC Press.

Weidenschilling, S. J., and J. S. Lewis (1973), Atmospheric and cloud structures of the jovian planets, *Icarus*, *20*, 465–476.

Wormald, C. J. (1977), A differential-flow mixing calorimeter. the excess enthalpy of methane + benzene, methane + cyclohexane, and bezene + cyclohexane, *Journal of Chemical Thermodynamics*, *9*, 901–910.

Yelle, R. V., and M. A. McGrath (1996), Ultraviolet Spectroscopy of the SL9 Impact Sites, *Icarus*, *119*, 90–111, doi:10.1006/icar.1996.0004.

Young, R. E. (2003), The Galileo probe: How it has changed our understanding of Jupiter, *New Astronomy Reviews*, *47*, 1–51.

Younglove, B. A., and M. O. McLinden (1994), An interntaional standard equation of state for the thermodynamic properties of refrigerant 123 (2,2-dichloro-1,1,1-trifluoroethane), *J. Phys. Chem. Ref. Data*, *23*(5), 731–779.

Zander, M., and W. Thomas (1979), Some thermodynamic properties of liquid ammonia: PVT data, vapor pressure, and critical temperature, *Journal of Chemical Engineering Data*, *24*(1), 1–2.

VITA

Bryan Mills Karpowicz was Born in May of 1979 in Albany, New York. He was raised in Schenectady, NY. He Graduated from Rensselaer Polytechic Institute in May 2001 with a Bachelor's Degree in Electrical Engineering. In August of 2001 he enrolled at the Georgia Institute of Technology, where he pursued a Master's Degree in Electrical and Computer Engineering while investigating the potential for a millimeter-wavelength SCanning Ozone Radiometer (SCOR). In May of 2003, he earned a Master's degree in Electrical and Computer Engineering. In August of 2003, he transfered to the School of Earth and Atmospheric Sciences where he pursued a Master's degree while investigating the potential for polarimetry in remote sensing measurements of strongly absorbing aerosols. During the Summers of 2004, and 2005 he worked on various projects at Ball Aerospace and Technologies Corporation including a visible-wavelength scanning Polarimeter. In January of 2007, he began the work presented in this dissertation.

Under the guidance of Professor Paul G. Steffes, he investigated the absorption properties of water vapor under deep Jovian conditions. The measurements were used in a radiative transfer model to test the sensitivity to water vapor as observed from the Microwave Radiometer (MWR) aboard the soon-to-be-launched NASA Juno Mission. As a graduate student he assisted in organizing the Annual Earth and Atmospheric Sciences Graduate Student Symposium from 2006-2008. He maintained the website for the symposium, organized abstracts, and assisted in various activities associated with the symposium.

Bryan M. Karpowicz is a Junior member of the American Astronomical Society's Division for Planetary Science, American Geophysical Union, and IEEE. Upon completion of his doctorate, he will join the remote sensing group at Atmospheric Environmental Research, Inc. in Lexington, Massachusetts.